UNIVERSITY OF CALIFORNIA
RIVERSIDE

Carboranes: Engineering Ligands and Catalysts

A Dissertation submitted in partial satisfaction
of the requirements for the degree of

Doctor of Philosophy

in

Chemistry

by

Jack Finley Kleinsasser

September 2019

Dissertation Committee:
Dr, Vincent Lavallo, Chairperson
Dr. Catharine Larsen
Dr. Yadong Yin

The Dissertation of Jack Finley Kleinsasser is approved:

Committee Chairperson

University of California, Riverside

AKNOWLEDGEMENTS

To begin, I would like to thank my research advisor, Prof. Vincent Lavallo whose guidance and patience has helped me to navigate the complicated and exciting process of discovery in chemistry. I owe a great deal of my professional experience to him. Furthermore, I would like to thank all my colleagues in the Lavallo group who have struggled and persevered with me through the PhD process. I thank them for keeping my spirits high and making working in the lab a fun place. I also want to thank my mentors, Dr. Jess Estrada and Dr. Allen Chan who taught me many of the skills needed to be a successful chemist. Lastly, and certainly most importantly, I want to thank my ever loving and supporting wife, Kristine. Her unwavering dedication and endless encouragement means more to me than she will ever imagine. Kristine, this process would have been impossible to complete if it were not for you. I love you more than you could ever comprehend and I dedicate this thesis to you.

ABSTRACT OF THE DISSERTATION

Carboranes: Engineering Ligands and Catalysts

by

Jack Finley Kleinsasser

Doctor of Philosophy, Graduate Program in Chemistry
University of California, Riverside, September 2019
Dr. Vincent Lavallo, Chairperson

Carborane anions have been increasingly utilized as a vital tool in the study of reactive compounds as a result of their exceptional stability and weakly coordinating properties. These unique properties have anchored them into the toolbox of any chemist pursing unique and novel chemistry. Though they have been mainly used as counter anions to stabilize reactive cations, their application in organometallic chemistry is still in its infancy. In this report, we provide an in depth study on their impact within organometallic chemistry. Specifically, we studied their reactivity with the trityl cation and found that it does not react the way it has historically been explained. Moreover, we sought to use these compunds as phosphine ligand substituents. As phosphine ligands, their use in the hydroamination of alkynes with gold was explored where moderate activity was found with TONs as high as 900. Furthermore, their incorporation into a series of zwitterionic Ru complexes was examined. We also investigated how carboranyl phosphines affect the activity of Drent-type palladium polymerization of ethylene which produced oligomers and low molecular weight polyethylene. Lastly, we probed an exotic palladium dimer bearing a carboranyl phosphine with its reactivity with ethylene and obtained the first ever organometallic structure determined by MicroED.

The text, figures, and schemes for the following chapters have been reproduced, in part or in their entirety from the following published manuscripts.

Chapter 1: Nonclassical Applications of *closo*-Carborane Anions: From Main Group Chemistry and Catalysis to Energy Storage:

S. P. Fisher; A. W. Tomich; S. O. Lovera; J. F. Kleinsasser; J. Guo; M. J. Asay; H. M. Nelson; V. Lavallo; “Nonclassical Applications of *closo*-Carborane Anions: From Main Group Chemistry and Catalysis to Energy Storage” *Chem. Rev*., **2019**, *ASAP*.

Chapter 2: On the Reactivity of the Carba-*closo*-Dodecaborate Anion with the Trityl Cation:

J. F. Kleinsasser; S.P. Fisher; F.S. Tham; V. Lavallo; “On the Reactivity of the Carba-*closo*-Dodecaborate Anion with the Trityl Cation” *Eur. J. Inorg. Chem*., **2017**, *38*, 4417-4419 **(Invited: Boron Special Issue)**.

Chapter 3: Synthesis of an Anionic Au(I) Hydroamination Precatalyst Supported by Charged Hydrido-carboranyl Phosphine Ligands:

J. F. Kleinsasser, S. E. Lee, C. A. Lugo, V. Tej, S. G. McArthur, V. Lavallo, “Synthesis of an Anionic Au(I) Hydroamination Precatalyst Supported by Charged Hydrido-carboranyl Phosphine Ligands” *Polyhedron*, **2018**, *156*, 245-248 **(Invited)**.

Chapter 5: Ethylene Oligomerization and Polymerization by Palladium(II) Methyl Complexes Supported by Phosphines Bearing a Perchlorinated 10-Vertex *closo*-Carborane Anion Substituent:

J. F. Kleinsasser, E. Reinhart, J. Estrada, Jess, R. Jordan, V. Lavallo, "Ethylene Oligomerization and Polymerization by Palladium(II) Methyl Complexes Supported by

Phosphines Bearing a Perchlorinated 10-Vertex *closo*-Carborane" *Organometallics*, **2018**, *37*, 4773-4783.

Table of Contents

LIST OF FIGURES

LIST OF TABLES

CHAPTER 1: Introduction

The landmark paper by Longuet-Higgins[1] reporting the modern structure of diborane, first synthetized by Alfred Stock[2], as having two bridging hydrides sparked a revolution in borohydride cluster chemistry that has persisted for decades. Though their chemical formulas do not vary much, the molecules themselves have widely diverse properties. These can range from the extremely pyrophoric, such as pentaborane B_5H_9, infamously known as the "green dragon"[3], to the dianionic compounds $[B_{12}H_{12}^{-2}]$ (**1**) and $[B_{10}H_{10}^{-2}]$ (**2**) (Fig. 1), first reported by Hawthorne[4,5], which are considered the most thermally, chemically and electrochemically stable species known to science.[6–8] An important subset of these species are carboranes,[9–17] where one or more of the vertices of the boron cluster have been replaced by a carbon. By replacing a boron atom with carbon, the overall charge of the cluster reduces by 1. This is a product of the extra proton found on the carbon atom and the total number of electrons within the cluster remaining constant per the rules of counting skeletal electron pairs as developed by Wade and Mingos.[18–20] As shown in Figure 1, both **1** and **2** have their isoelectronic partners in the icosahedron, $[HCB_{11}H_{11}]^-$ **3**, and the bicapped square antiprism, $[HCB_9H_9]^-$ **4**, both of which are monoanionic.[21] Compounds **1**-**4** are *closo*-clusters as they have closed polyhedral shapes and closed shell electronic structures.[10]

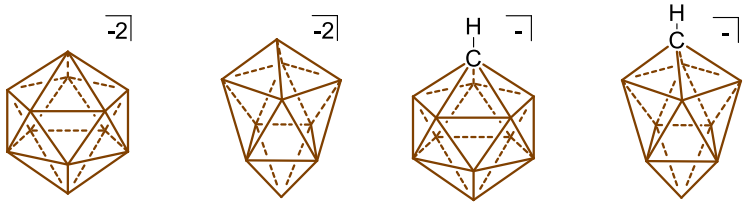

*Figure 1. The most thermodynamically stable closo dianionic borohydride and monoanionic carborane clusters **1-4** (unlabeled vertices = B-H).*

These clusters are considered to be 3D, σ-aromatic compounds whose electrons

are delocalized throughout the cluster. As shown in Figure 2, this 3D delocalization is through the p_x, p_y and sp_z orbitals from each vertex. Moreover, computational studies show that these clusters have equal to or greater aromaticity than benzene and benzene analogues. One such study is the Nucleus Independent Chemical Shift (NICS) which computationally measures the magnetic shielding at the center of the aromatic system. Benzene has a value of -9.7 while **3** has a value of -34, where increasing negative values denotes increasing aromaticity.[17]

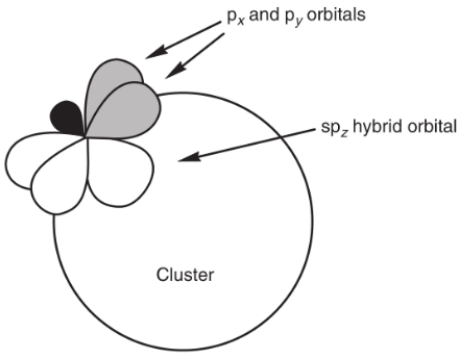

Figure 2. Orientation of p_x, p_y, and sp_z orbitals displaying the orientation of the MO's in carborane clusters.[10]

Carborane anions **3** and **4** are some of the most weakly coordinating species as their charges are delocalized throughout the three dimensional aromatic core.[9,17] Functionalization of these clusters' surfaces with halogens or alkyl groups, proceed through electrophilic aromatic substitution "like" reactions, which renders these species even more weakly coordinating. Indeed, much of the work from Christopher Reed utilized **3**, **4**, and their halogenated derivatives as weakly coordinating anions to study reactive alkyl and silyl cations as well as super acid chemistry.[9,22,23]

An important set of derivatives in carborane anions are the halogenated carborane clusters. Here, halogens replace the B-H bonds for B-X bonds. This has been shown to be highly selective where the antipodal boron is the first substitution site, followed by the *meta* or lower belt, and lastly, the *ortho* or upper belt becomes substituted for halogens.[9,24] This unique and selective substitution provides these clusters with tremendous inertness allowing for the study and isolation of some of the most elusive cationic species.[25–36] This

inertness comes from the electron withdrawing effect that halogens facilitate which further enhances the delocalization of the negative charge within the cluster. Moreover, the halogens blanket the carborane with a protective screen of electron density.

Some lesser explored aspects of carborane chemistry are that of organometallic chemistry and catalysis. Only a small handful groups from around the world have indeed invented unique ways to bind carborane anions to metals, but fewer still have studied the catalytic behavior of these carboranyl metal complexes. In fact, there exists only a single review article in the literature that properly encapsulates the little explored organometallic chemistry and catalysis utilizing carboranes.[37]

This document will focus on the reactivity and organometallic chemistry of carboranes. Specifically, most sections will discuss carboranes used as substituents in phosphine ligand development and their application in catalysis and organometallic chemistry. Phosphine chemistry has a long and vibrant history owing to its ease of synthesis, utility as a ligand, and highly tunable functionality making them a top choice in the organometallic chemist's toolkit. The first anionic carboranyl phosphine was developed by Reed shown in Figure 3.[38] Despite this discovery, he did not pursue any investigation into its use as a ligand. Though there are several published works that have studied carborane anions as ligands,[37] only the Lavallo research group has truly pioneered their use in single cite catalysis. These works will be discussed in the relevant sections below.

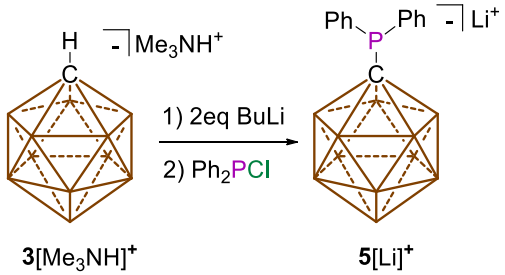

*Figure 3. Reed's synthesis for the first carboranyl phosphine **5**[Li]⁺ in 1993.*

CHAPTER 2: On the Reactivity of the Carba-*closo*-Dodecaborate Anion with the Trityl Cation

Introduction

Carboranes[8–11,13,16,17,39,40] are a class of boron cluster compounds that contain at least one carbon atom in the skeleton. The most thermodynamically and chemically robust carborane clusters are the 12-vertex icosahedral derivatives. Such clusters are neutral if they contain two carbon atoms[11] and monoanionic if they contain one carbon atom.[17] The latter family of charged clusters contain a CB_{11} core and are of particular interest as weakly coordinating anions for highly electrophilic cations,[9,25,26,41–50] substituents in ligand design,[51–60] and components of ionic conducting materials.[61–63] The parent cluster, specifically the carba-*closo*-dodecaborate anion $[HCB_{11}H_{11}]^{-1}$, is the basic building block for functionalized derivatives (Fig. 4). The B-H vertices of this molecule can undergo electrophilic substitution reactions,[17] most commonly with elemental halogens or alkyl electrophiles, that lead to replacement of hydrides with X or R groups, respectively. The substitution occurs selectively, first at the B-H antipodal to carbon because this position is the most electron rich, then at the central and subsequently upper pentagonal belt.

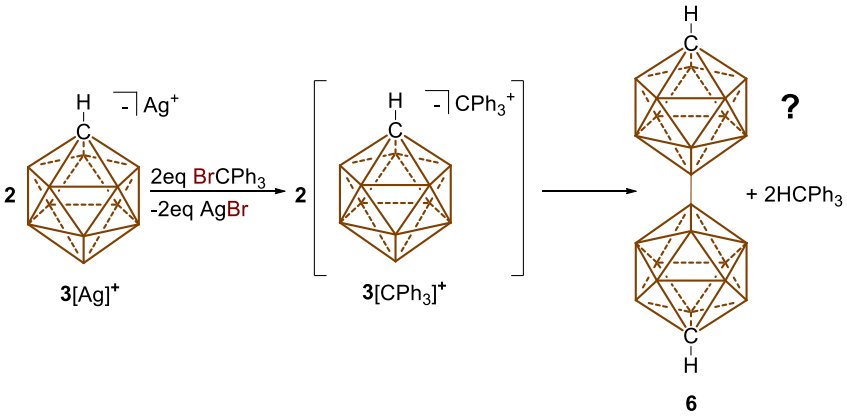

*Figure 4. Reed and coworkers previously discovered an incompatibility between the trityl cation and the carborane anion **3**. Hydride abstraction from the carborane followed by dimerization to produce **6** was the proposed decomposition pathway. Unlabeled vertices = B-H.*

In 1994, elegant and pioneering work by Reed and coworkers[64] showed the synthesis of trityl cations with various polyhalogenated derivitives of **3**. These trityl salts are the basis for the synthesis of Reed's silylium cations and subsequent carborane superacids.[9] Interestingly, they found an incompatibility between the trityl cation and unsubstituted **3**. They reported that when the silver salt of **3**$[Ag]^+$, was reacted with trityl bromide, salt metathesis did occur, but the reaction did not lead to the desired trityl carborane salt **3**$[C(Ph)_3]^+$ (Fig. 4). Instead, a new, unidentified product was observed that retained the local C_{5V} symmetry of the cluster but contained a substituted B-H vertex as indicated by ^{11}B NMR spectroscopy. Based on an early report by Hawthorne[65] on the electrochemical oxidation of the related 10-vertex anion $[HCB_9H_9]^{-1}$ which results in the formation of a carborane B-B dimer, they proposed that perhaps the trityl cation abstracted hydrides from the cluster **3** and a similar dimer **6** formed (Fig. 4). Additionally, under certain reaction conditions, they observed the formation of $HCPh_3$, which is supportive of this reaction pathway. Out of genuine curiosity, we decided to reinvestigate this reaction and unambiguously determine its outcome.

Results and Discussion

In lieu of preparing[17] **3**$[Ag]^+$, which would require an extra synthetic step, we chose to examine the salt metathesis reaction of trityl bromide with the lithium salt **3**$[Li]^+$. As a solvent, we chose fluorobenzene, since both reactants are very soluble in this medium

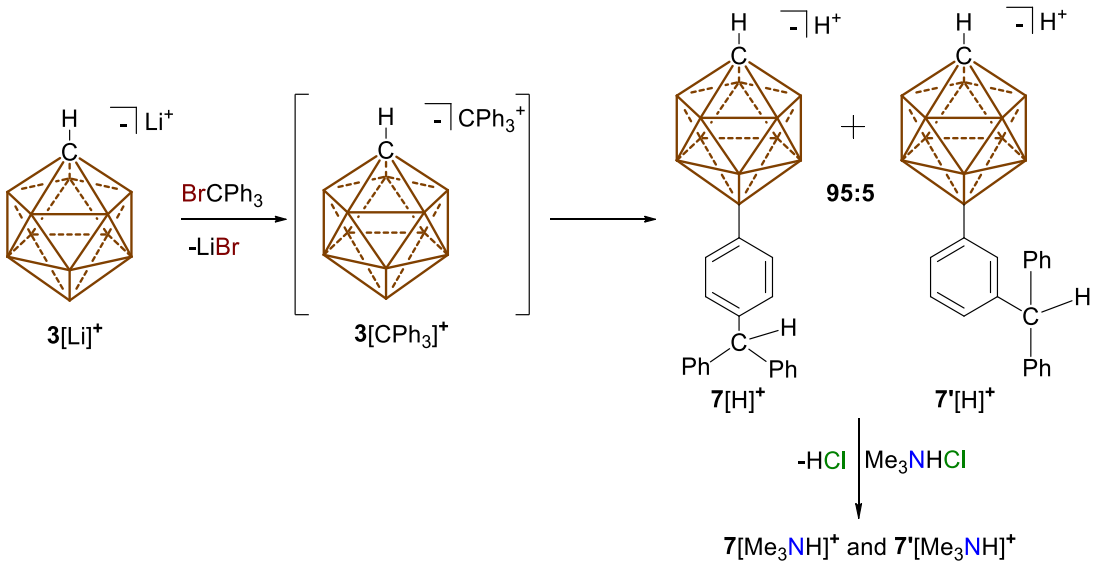

*Figure 5. Reaction of **3**[Li] + with BrC(Ph)$_3$ in F-C$_6$H$_5$ solvent leads to electrophilic arylation of the carborane at the B-vertex antipodal to C. The reaction produces a mixture (95:5) of arylated carboranes **7** and **7'**. Unlabeled vertices = B-H.*

and LiBr is not. Thus, we performed the reaction and as expected saw a rapid precipitation of LiBr (Fig. 5). The reaction was filtered and subsequently concentrated to dryness under high vacuum. The material was then dissolved in H_2O and for convenience Me_3HNCl was added to precipitate any carborane containing salts. After drying the precipitate, it was analyzed by $^{11}B\{^1H\}$ NMR spectroscopy. Similar to what Reed reported,[64] we observed three resonances (7.0, -8.1, -12.1ppm) in a 1:5:5 ratio, respectively. Substitution of the antipodal B-vertex at 7.0ppm was corroborated by ^{11}B NMR spectroscopy, which shows this signal as a singlet.

We next analyzed the residue by ^1H NMR spectroscopy. The proton NMR spectrum shows a large singlet for the $[Me_3NH]^+$ cation's methyl groups at 3.10ppm, a singlet at 5.46 that integrates for 1H relative to $[HNMe_3]^+$, two 2H doublets at 6.82 and 7.33ppm that are coupled (7.9Hz), as well as a 10H multiplet between 7.12-7.29ppm. Importantly, *vide infra*, a trace (< 5%) of a minor compound with distinct ^1H NMR chemical

shifts was observed. An HSQC (^{1}H-^{13}C correlation experiment) shows that the ^{1}H resonance at 5.46ppm correlates with a ^{13}C nucleus at 57.5ppm indicating the formation of a new sp^{3} hybridized carbon center. High resolution mass spectrometry (negative ion mode) showed that the new compound has a mass that corresponds to **7** plus CPh_3, less 1 proton. All of this data is consistent with the formation of the product **7**[Me_3NH]$^{+}$ (Fig. 5). Presumably, the reaction proceeds via initial formation of the trityl cation **3**[$C(Ph)_3$]$^{+}$ as an intermediate, where subsequently the carborane acts as a nucleophile that attacks the *para*-position of the trityl cation. It should be noted that it is well known that bulky nucleophiles attack the para-position of trityl cations if the central carbon is sterically inaccessible. The net reaction is an electrophilic aromatic arylation of the carborane cage to produce the carborane acid **7**[H]$^{+}$, which upon cation exchange is isolated as the trimethylammonium salt **7**[Me_3NH]$^{+}$ (Fig. 4).

A single crystal X-ray diffraction study confirmed the identity of **7**[Me_3NH]$^{+}$ as the arylated carborane, which is substituted at a phenyl *para*-position (Fig. 6, left). While we were unable to obtain very high quality crystals that would provide accurate data for bond length and angle analysis (even utilizing a Cs^{+} counter cation), the connectivity of **7**[Me_3NH]$^{+}$ is unambiguous. In the same mass of crystals we found a small amount of morphologically distinct material.

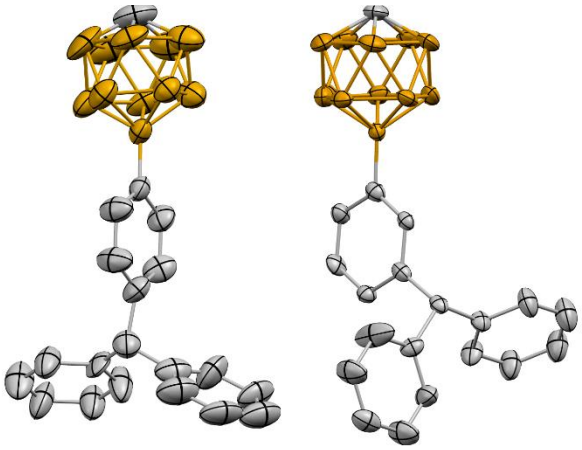

7 **7'**

*Figure 6. Solid state structures of **7**[Me_3NH]$^{+}$, major crystals (left). Note: [Me_3NH]$^{+}$ cation, hydrogens, and disordered positions omitted for clarity. Portion of the lattice from the minor crystal containing cocrystalized **7** and **7'** (right). Note: [Me_3NH]$^{+}$ cation, hydrogens, and isordered population of **7** omitted for clarity. Color code: carbon = grey, boron = brown.*

Although highly disordered over two positions, crystallographic analysis of the material reveals the cocrystalization of two distinct carborane anions, namely the *para*-arylated product **7**[Me_3NH]$^+$ and the *meta*-arylated product 7'[Me_3NH]$^+$, in a 7:3 occupancy ratio in the lattice (Fig. 6, right). We attribute the minor peaks observed in the ^{1}H NMR spectra to that of **7**[Me_3NH]$^+$. Given that we chose different reaction conditions than that reported by Reed and coworkers, we next sought to replicate their exact experimental conditions[64] to unambiguously confirm that the carborane B-B dimer **6** does not form. Thus, **3**[Ag]$^+$ was reacted with trityl bromide in acetonitrile. As reported, an equivalent of AgBr forms, but in our hands we do not observe even a trace of $HCPh_3$. After an analogous workup described above, we isolated a mixture of **7**[Me_3NH]$^+$ and **7'**[Me_3NH]$^+$, but in this case, the ratio of the products was 1:1, *para* to *meta*, respectively.

Conclusion

The communication above unambiguously explains the incompatibility of the carborane anion **3** and the trityl cation. The carborane anion **3** is not susceptible to hydride abstraction by [CPh_3]$^+$, instead it undergoes classical electrophilic substitution chemistry,[17] that shows solvent and countercation dependence on *para* to *meta* selectivity. While we do not fully understand the observed formation of the unusual *meta* product of electrophilic aromatic substitution on a phenyl ring, the result is intriguing and may lead to new approaches to *meta* directed arene functionalization. Furthermore, all previous B-arylations of **3** have been achieved utilizing transition metal coupling[38,66–70] or Li$^+$ initiated sigma bond metathesis.[71] Thus, the observed electrophilic arylation of a B-H vertex of **3** introduces a new paradigm in the chemical elaboration of this anion.

Experimental

General Considerations: All manipulations were carried out using standard Schlenk or glovebox techniques under a dinitrogen or argon atmosphere unless otherwise stated. Fluorobenzene was distilled from a solvent still over P_2O_5 and refluxed for several days. Acetonitrile was distilled from a solvent still over CaH_2 and refluxed for several days. Lithium 1-carba-*closo*-undecaborate **3**$[Li]^+$ was prepared from a modified procedure by Uchiyama and co-workers:[72] **3**$[Me_3NH]^+$ was deprotonated with LiH in acetonitrile. Unless specifically stated, reagents were purchased from commercial vendors and used without further purification. Nuclear magnetic resonance (NMR) spectroscopy was carried out using: Bruker Avance 300MHz, Bruker Avance 600MHz, or Varian Inova 300MHz spectrometers. NMR chemical shifts are reported in parts per million (ppm) with ^1H and ^{13}C chemical shifts referenced to the residual non-deutero solvent. High-resolution mass spectrometry (HRMS) was collected on an Agilent Technologies 6210 (TOF LC/MS) multimode-ESI/APCI with direct injection. IR was taken on a PerkinElmer Spectrum One. Crystallographic data for compounds **7**$[Me_3NH]^+$ and **7'**$[Me_3NH]^+$ are available free of charge from the Cambridge Crystallographic Data Center under reference numbers 1552016 and 1552017, respectively. This structure can be accessed at: http://www.ccdc.cam.ac.uk/Community/Requestastructure/Pages/DataRequest.aspx.

Synthesis of Trityl Carborane, **3**[Me_3NH]$^+$ and **3**[Me_3NH]$^+$:

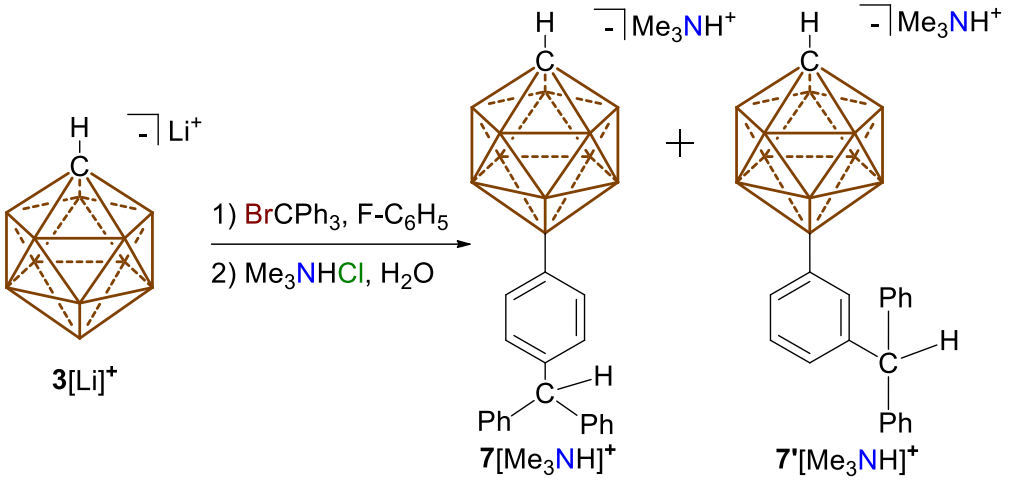

A glass scintillation vial equipped with a stir bar was loaded with **3**[Li]$^+$ (300mg, 955µmol) and dry fluorobenzene (2mL). A separate vial was loaded with a solution of trityl bromide (309mg, 955µmol) dissolved in fluorobenzene (2mL). The solution of trityl bromide was transferred to the solution containing **3**[Li]$^+$. The vial that originally contained the trityl bromide was washed with fluorobenzene (2 x 1mL) and the wash was transferred to the solution of **3**[Li]$^+$ as well. The reaction was stirred for 20 minutes at room temperature. After 20 minutes, the fluorobenzene was concentrated down to a thick oil under vacuum. This oil was subsequently dissolved in 10mL of deionized H_2O. Once fully dissolved, trimethylammonium hydrochloride (100mg, 1.0mmol) was added to the aqueous solution producing an off-white precipitate. The precipitate was then washed with deionized H_2O (3 x 4mL) resulting in products, **7**[Me_3NH]$^+$ and **7'**[Me_3NH]$^+$. Yield: 359mg, 89%. *Note: picks picked are for compound **7** only.* ^{1}H NMR (300MHz, acetone-d_6, 25°C): δ = 7.33 (d, ^{3}*J(H,H)* = 7.9 Hz, 2H), 7.29 - 7.24 (m, 4H), 7.19 - 7.12 (m, 6H), 6.83 (d, ^{3}*J(H,H)* = 7.9 Hz, 2H), 5.46 (s, 1H), 3.10 (s, 9H), 2.23 (s, 1H), 2.60 - 0.88 (bm, 10H, B-H) ppm. ^{1}H{^{11}B} NMR (300MHz, acetone-d_6, 25°C): δ = 7.34 – 7.14 (10H), 6.81 (1H), 6.79 (1H),

5.45 (1H), 3.17 (9H), 2.21 (B-H), 1.79 (B-H), 1.76 (B-H) ppm, 1.72 (B-H) ppm. $^{13}C\{^{1}H\}$ NMR (75MHz, acetone-d_6, 25°C): δ = 145.7, 140.7, 133.6, 130.7, 130.1, 128.9, 128.0, 126.7, 126.3, 57.5, 47.0, 46.0 ppm. $^{11}B\{^{1}H\}$ NMR (96MHz, acetone-d_6, 25°C): δ = 7.0, -8.1, -12.1 ppm. ^{11}B NMR (96MHz, acetone-d_6, 25°C): δ = 7.0, -8.1 ($^{1}J(H,B)$ = 136.3 Hz), -12.1 ($^{1}J(H,B)$ = 149.5 Hz) ppm. IR (Solid, ATR, 25°C): B-H stretch = 2549 and 2512 cm^{-1}. HRMS (negative mode ESI/APCI) $[M]^{-}$ m/z calc'd = 385.3131 : Found = 385.3154.

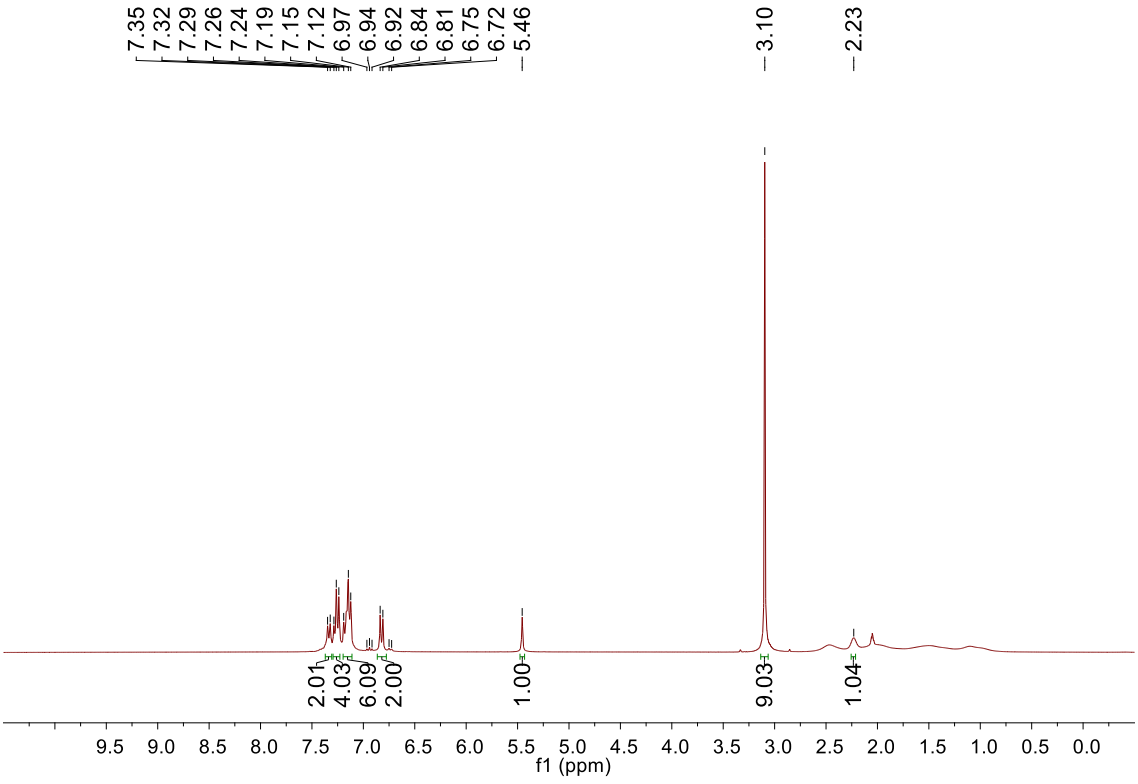

*Figure 7. ^{1}H NMR of **7**$[Me_3NH]^+$ (300MHz, acetone-d_6, 25°C). Note: **7'**$[Me_3NH]^+$ is seen at 6.94 and 6.73 ppm.*

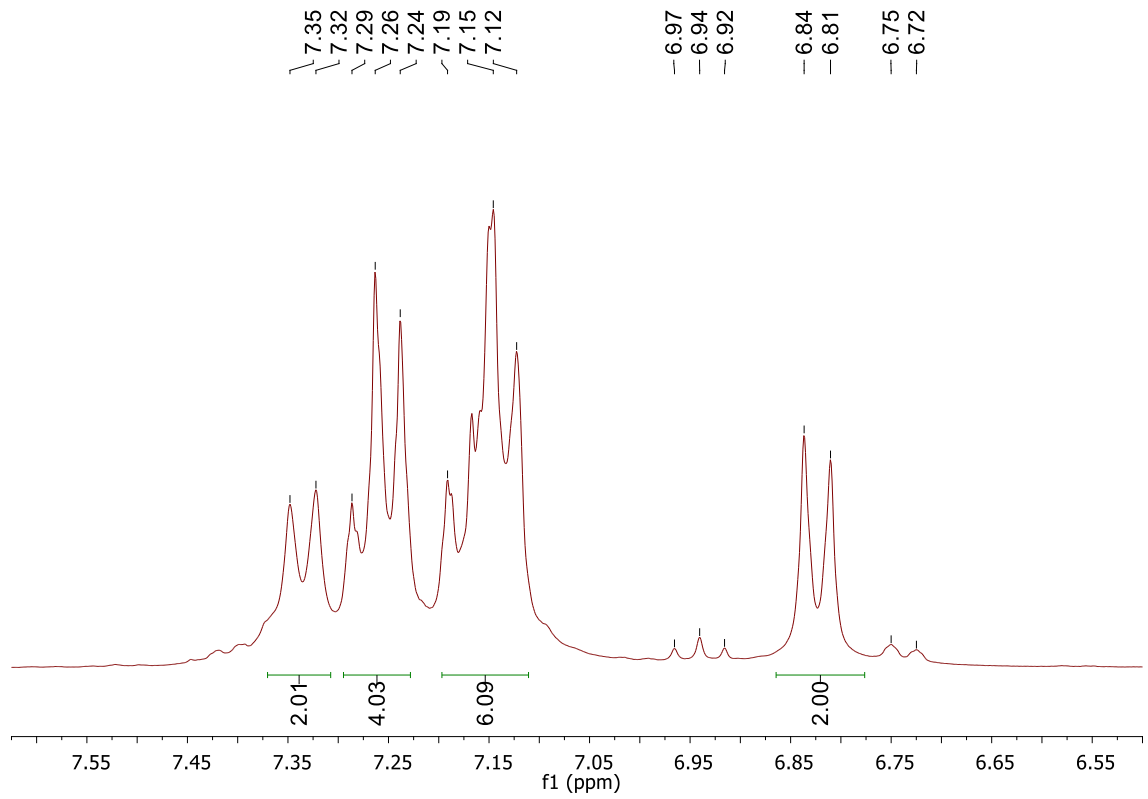

*Figure 8 An expansion of the aromatic region of ^{1}H NMR spectrum of **7**[Me_3NH]$^+$ in acetone-d_6. Note: **7'**[Me_3NH]$^+$ can be seen at 6.94 and 6.74 ppm.*

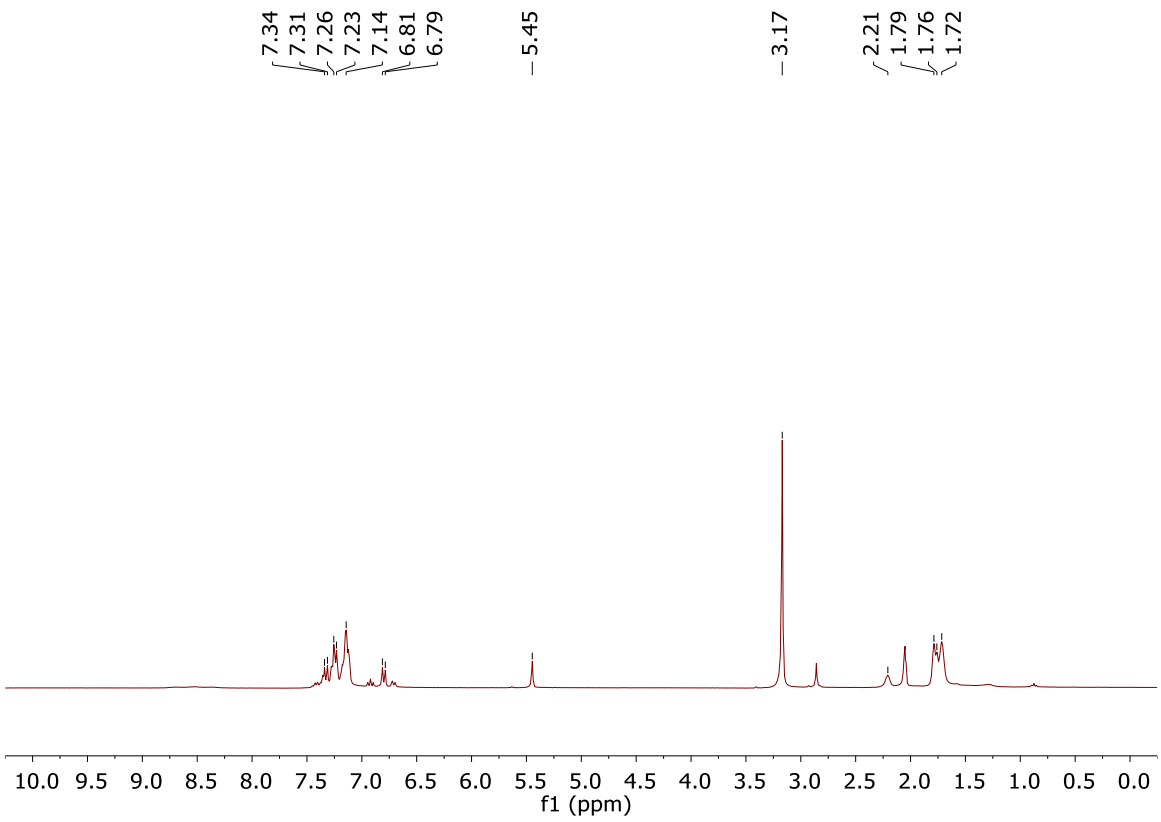

*Figure 9. $^{1}H\{^{11}B\}$ NMR of the mixture containing **7**$[Me_3NH]^+$ in acetone-d_6 (300MHz, acetone-d_6, 25°C).*

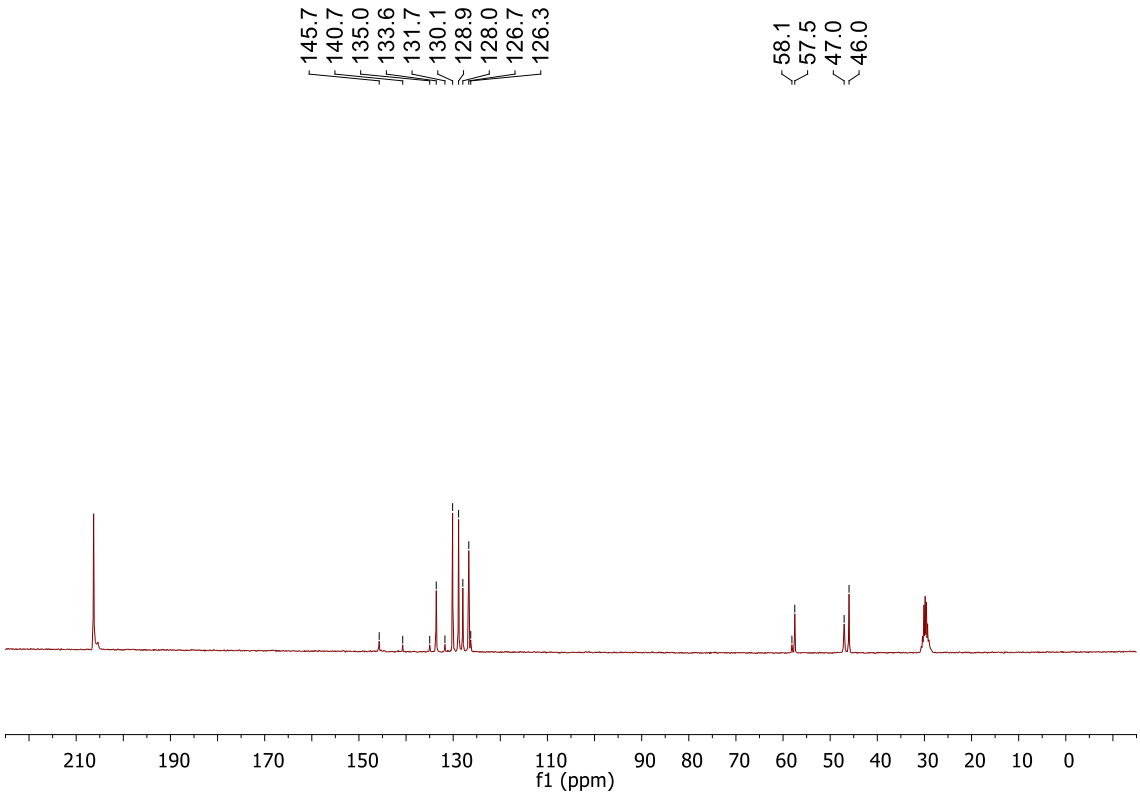

*Figure 10. $^{13}C\{^{1}H\}$ NMR of **7**[Me_3NH]$^+$ (75MHz, acetone-d_6, 25°C). Note: **7'**[Me_3NH]$^+$ is seen at 135.0, 131.7, 126.3, and 58.1 ppm.*

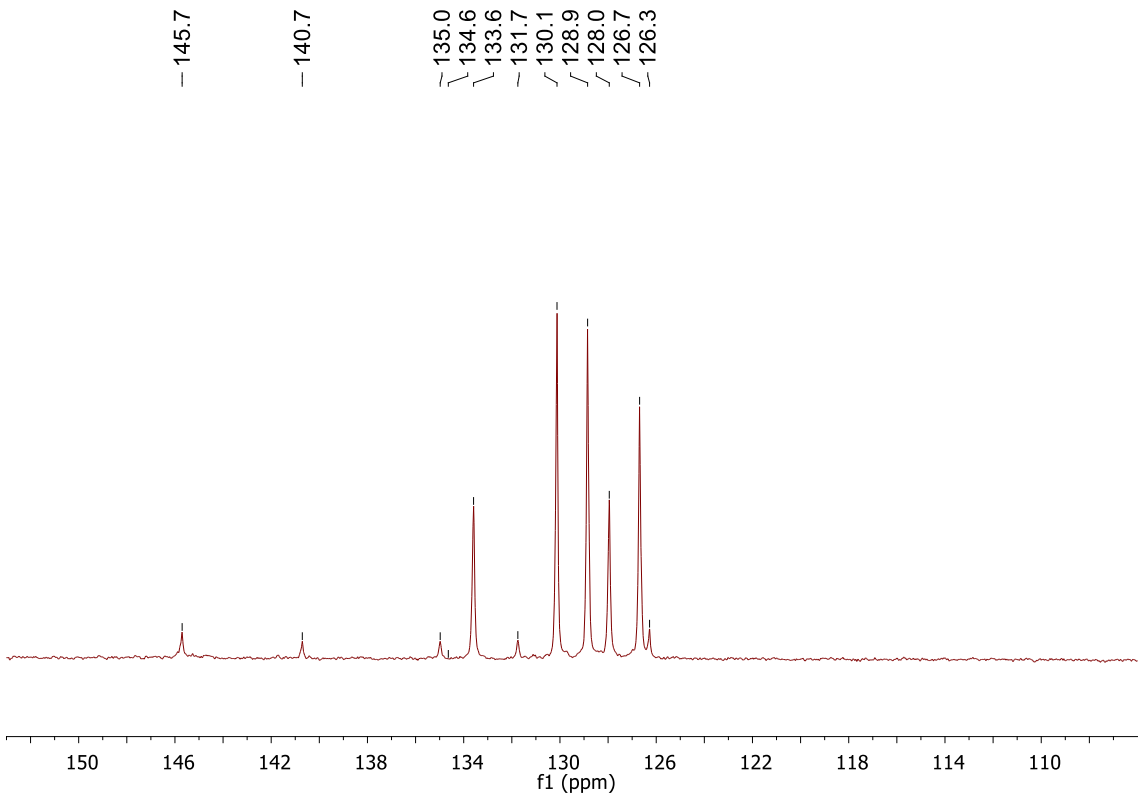

*Figure 11. An expansion of the aromatic region of the $^{13}C\{^{1}H\}$ NMR spectrum of **7**$[Me_3NH]^+$ in acetone-d_6. Note: **7'**$[Me_3NH]^+$ is seen at 135.0, 131.7, 126.3, and 58.1 ppm.*

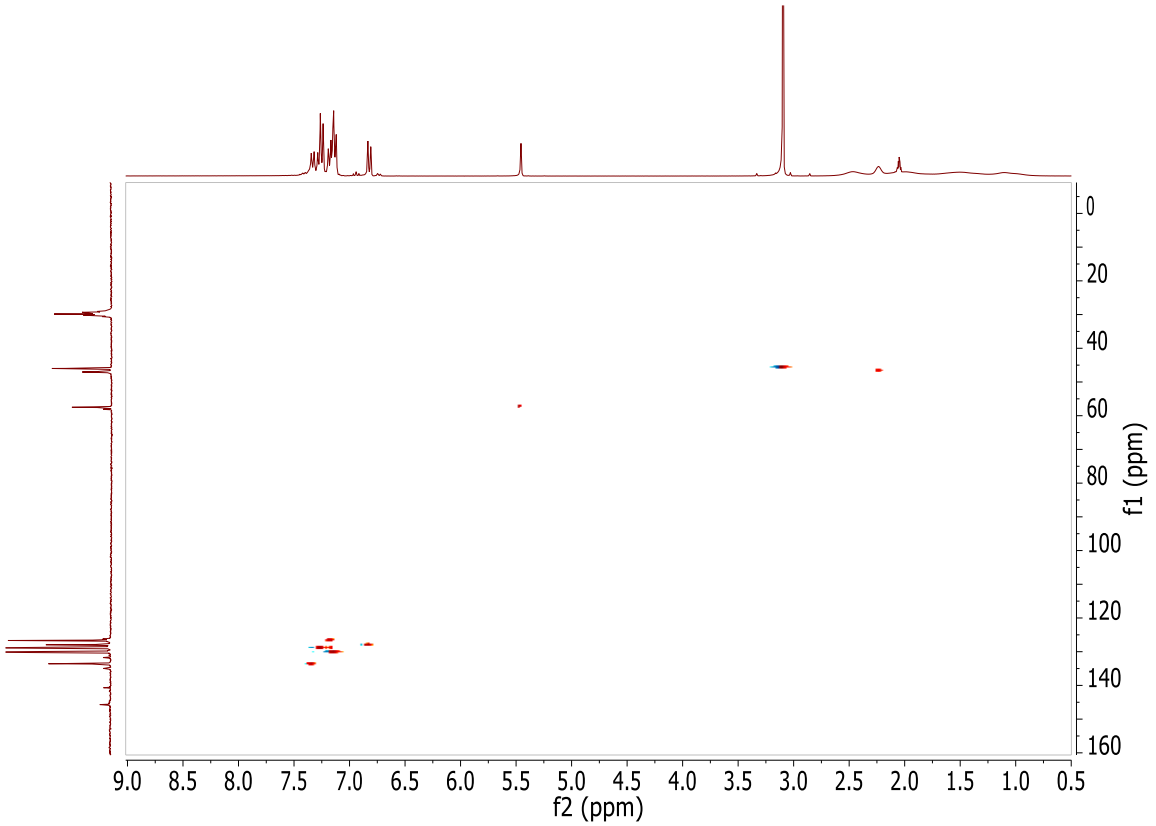

*Figure 12. HSQC NMR spectrum of **7**[Me_3NH]$^+$ in acetone-d_6.*

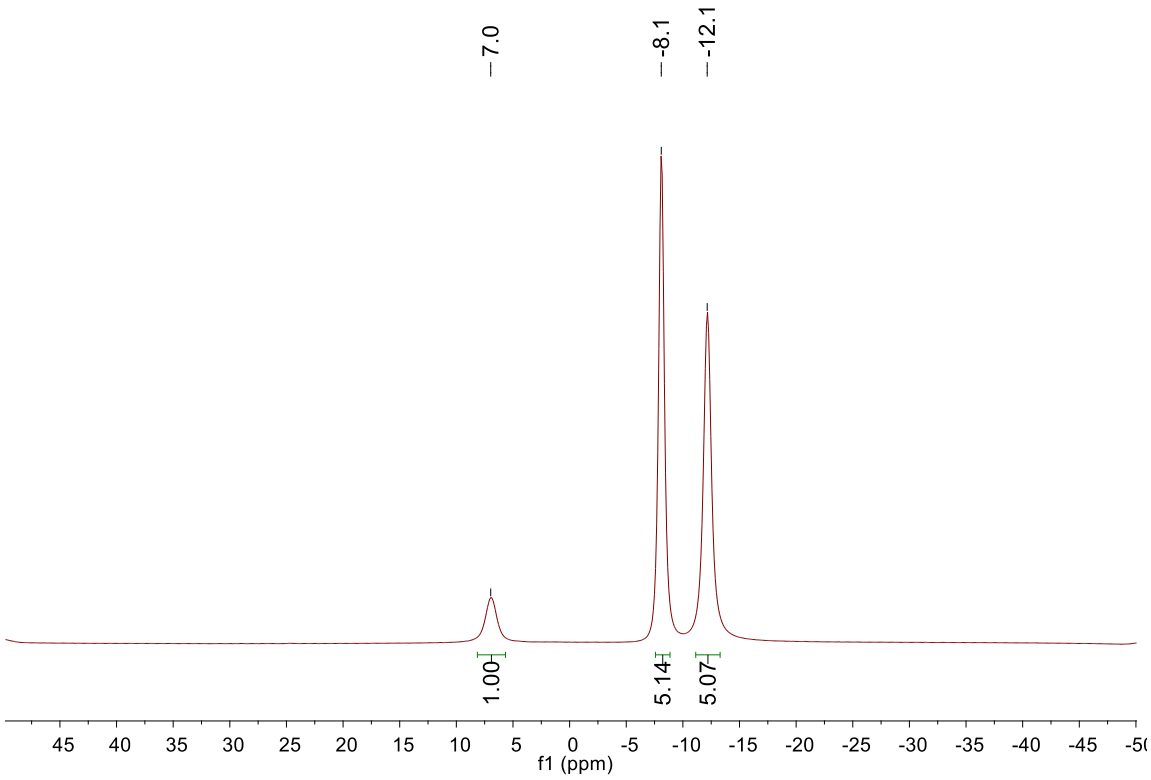

*Figure 13. $^{11}B\{^{1}H\}$ NMR of compound **7**$[Me_3NH]^+$ (96MHz, acetone-d_6, 25°C).*

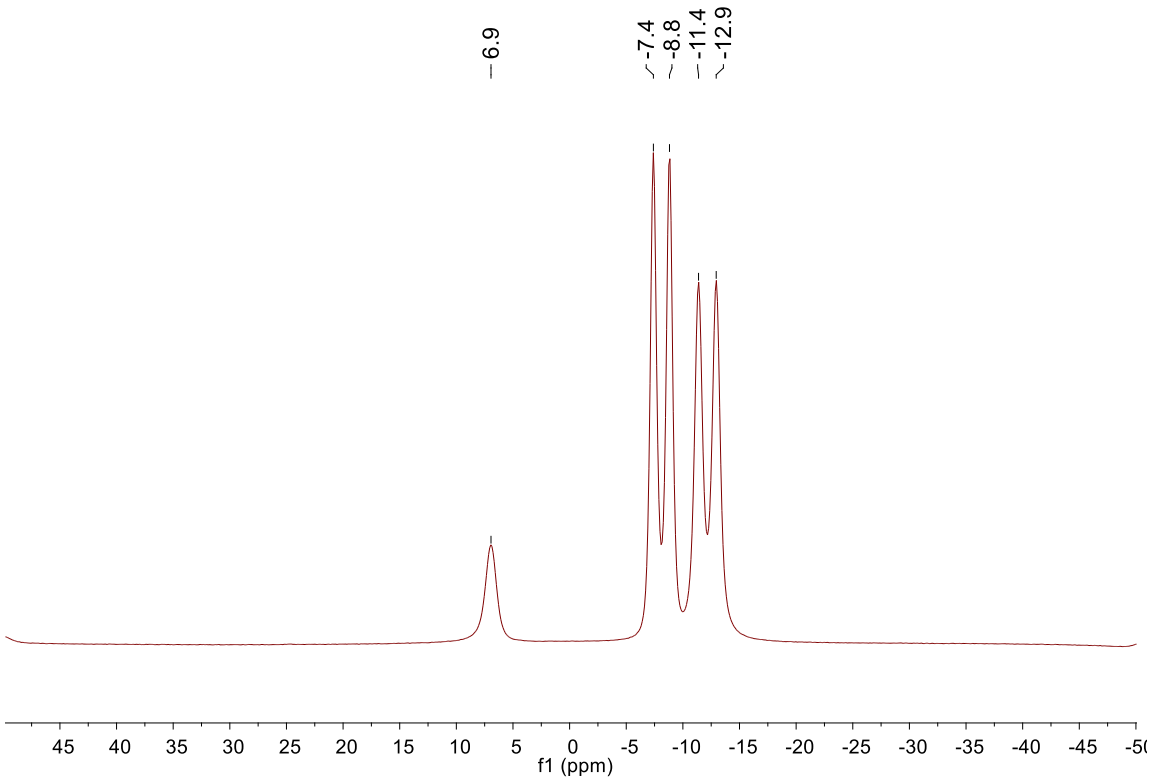

*Figure 14. ^{11}B NMR of compound **7**[Me_3NH]$^+$ (96MHz, acetone-d_6, 25°C).*

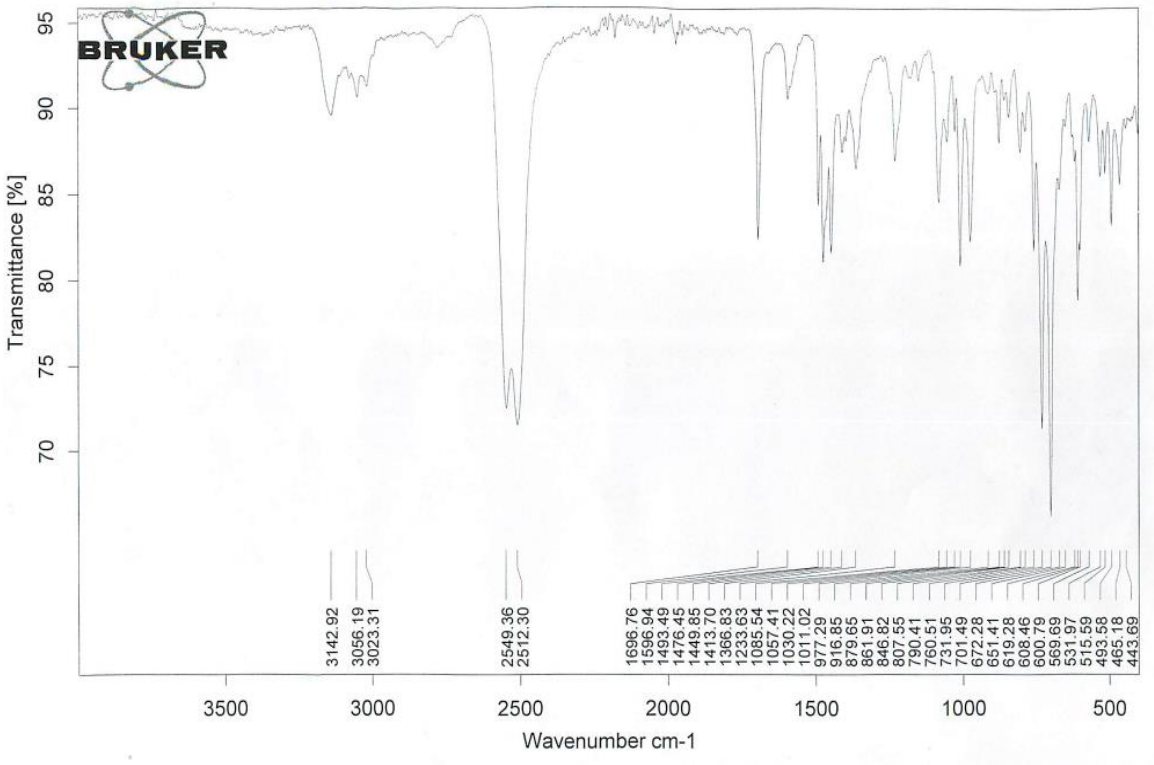

Figure 15. IR spectrum of solid ***7****[Me_3NH]$^+$ .Showing the B-H stretches at 2549 and 2512 cm^{-1}.*

Synthesis of Trityl Carborane, **7**[Me_3NH]$^+$ and **7**[Me_3NH]$^+$ with the **3**[Ag]$^+$ Salt **:**

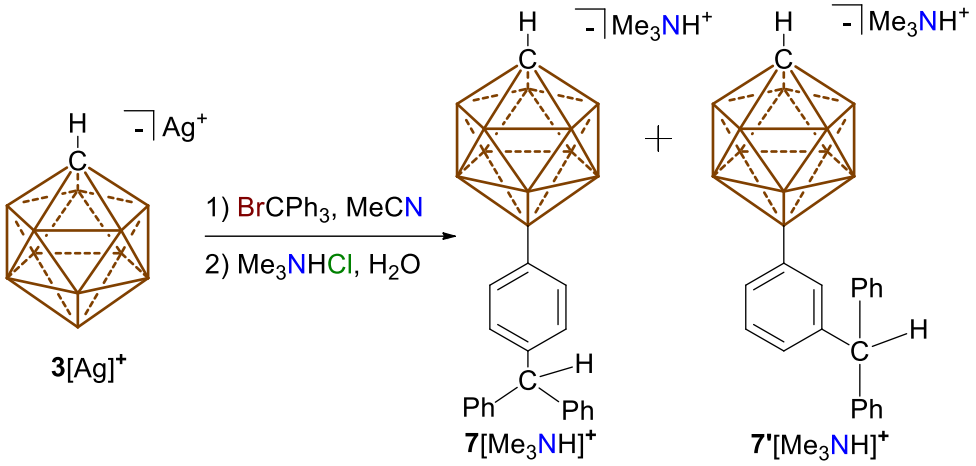

A glass scintillation vial equipped with a stir bar was loaded with **3**[Ag]$^+$ (100mg, 399µmol) and dry acetonitrile (2mL). A separate vial was loaded with a solution of trityl bromide (129mg, 399µmol) dissolved in acetonitrile (2mL). The solution of trityl bromide was transferred to the solution containing **3**[Ag]$^+$.The vial originally containing the trityl bromide solution was washed with acetonitrile (2 x 1 mL) and transferred to the solution of **3**[Ag]$^+$ as well. The reaction was stirred for 20 minutes at room temperature. After 20 minutes, the acetonitrile was concentrated down to a thick oil under vacuum. This oil was subsequently dissolved in 10mL of deionized H_2O. Once fully dissolved, trimethylammonium hydrochloride (40mg, 420µmol) was added to the aqueous solution producing an off-white precipitate. The precipitate was then washed with deionized H_2O (3 x 4mL) resulting in products, **7**[Me_3NH]$^+$ and **7'**[Me_3NH]$^+$ (147 mg, 83% yield). *Note: Peaks picked are for compound* **7'**[Me_3NH]$^+$ *only.* ^{1}H NMR (300MHz, acetone-d_6, 25°C): δ = 7.35 – 7.11 (m, 10H), 6.91 (dd, $^3J(H,H)$ = 7.4 Hz, $^3J(H,H)$ = 7.4 Hz, 1H), 6.70 (d, $^3J(H,H)$ = 7.4 Hz, 1H), 5.45 (s, 1H), 3.21 (s, 9H), 2.20 (s, 1H), 2.60 - 0.78 (bm, 10H, B-H)

ppm. $^{1}H\{^{11}B\}$ NMR (300MHz, acetone-d_6, 25°C): δ = 7.38 – 7.14 (10H), 6.95 (1H), 6.75 (1H), 5.46 (1H), 3.01 (9H), 2.24 (1H), 1.80 (B-H), 1.77 (B-H), 1.74 (B-H) ppm. $^{13}C\{^{1}H\}$ NMR (75MHz, acetone-d_6, 25°C): δ = 145.8, 134.9, 131.7, 129.0, 128.8, 127.9, 127.0, 126.6, 126.2, 58.1, 47.0, 46.1 ppm. $^{11}B\{^{1}H\}$ NMR (96MHz, acetone-d_6, 25°C): δ = 7.0, -8.0, -12.1 ppm *(broad $C_{aromatic}$-B resonance not detected)*. ^{11}B NMR (96MHz, acetone-d_6, 25°C): δ = 7.0, -8.0 ($^{1}J(H,B)$ = 136.3 Hz), -12.1 ($^{1}J(H,B)$ = 149.5 Hz) ppm. IR (Solid, ATR, 25°C): B-H stretch = 2545 cm^{-1}. HRMS (negative mode ESI/APCI) $[M]^{-}$ m/z calc'd = 385.3131 : Found = 385.3147.

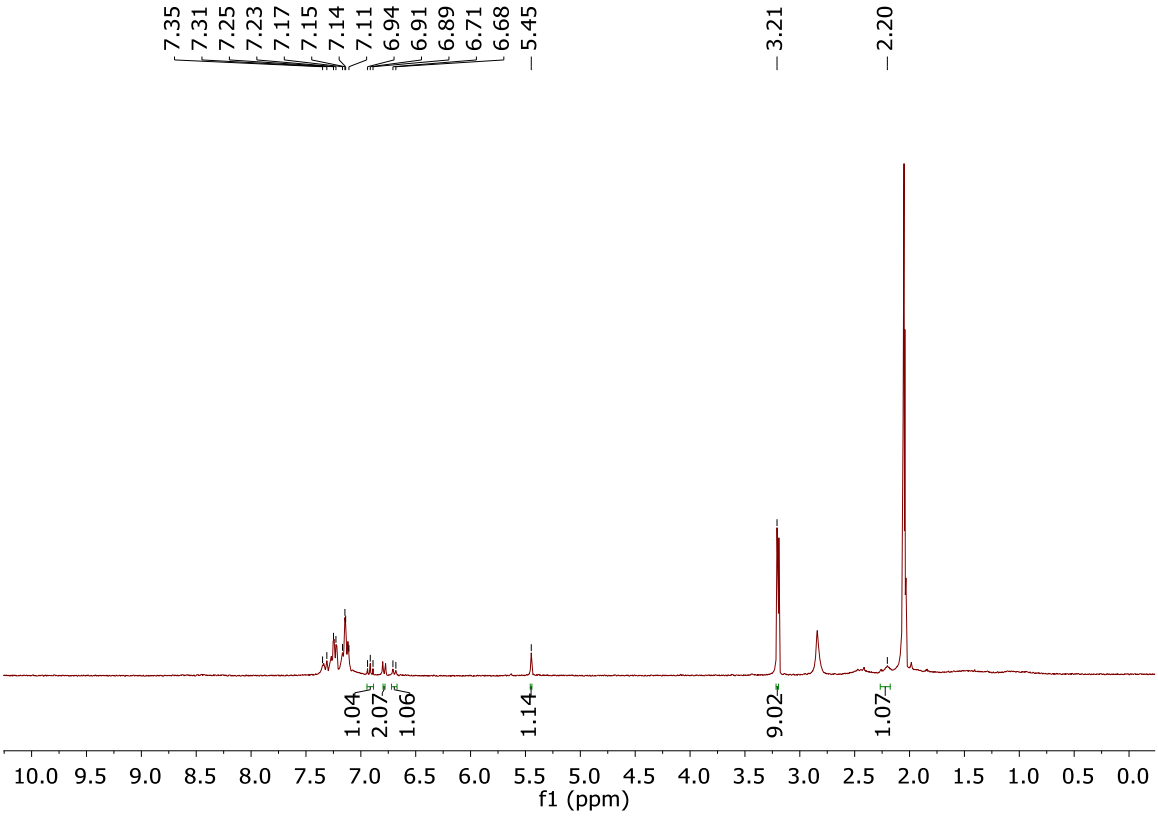

*Figure 16. ^{1}H NMR of the mixture containing **7'**$[Me_3NH]^+$ (300MHz, acetone-d_6, 25°C). Note: Water is seen at 2.84 ppm. Integration of 1.04 to 2.07 shows a 1:1 ratio of **7**$[Me_3NH]^+$ to **7'**$[Me_3NH]^+$, respectively.*

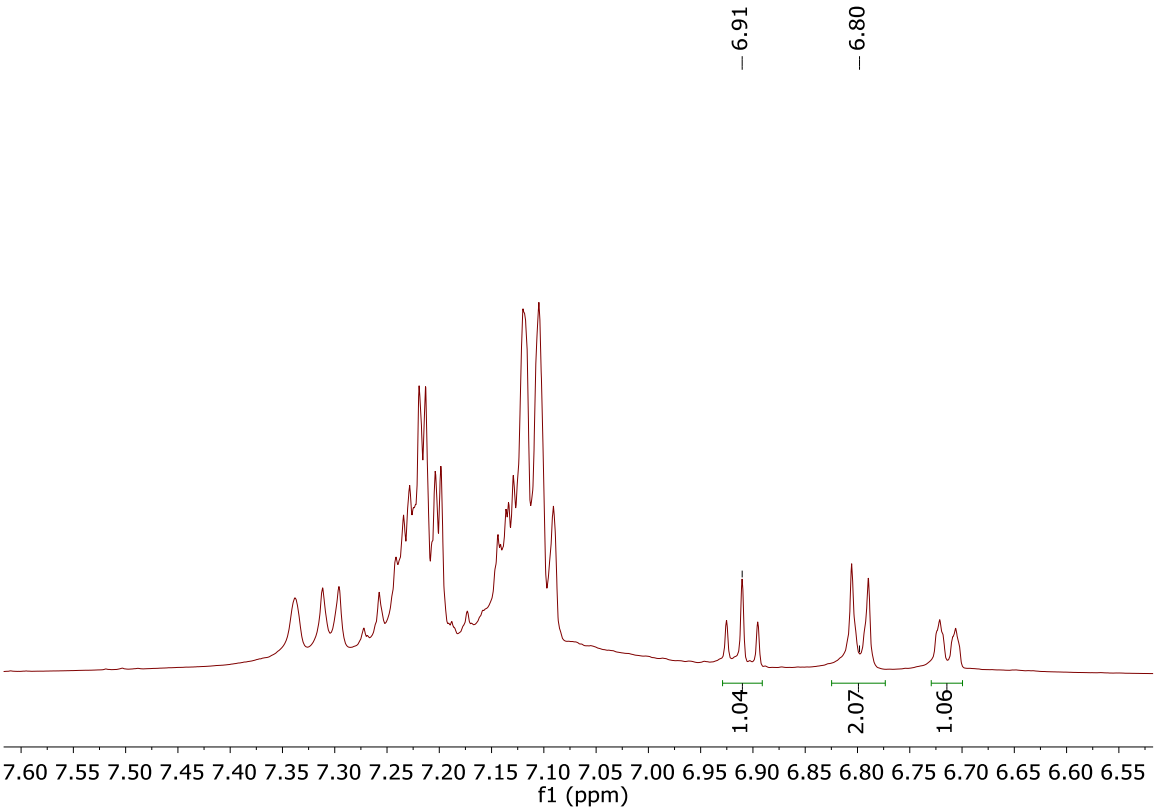

*Figure 17. An expansion of the 1H NMR spectrum of the mixture containing **7'**[Me_3NH]$^+$ in acetone-d_6. Note: Compound **7'**[Me_3NH]$^+$ is seen at 6.91 ppm and **7**[Me_3NH]$^+$ is seen at 6.80 ppm.*

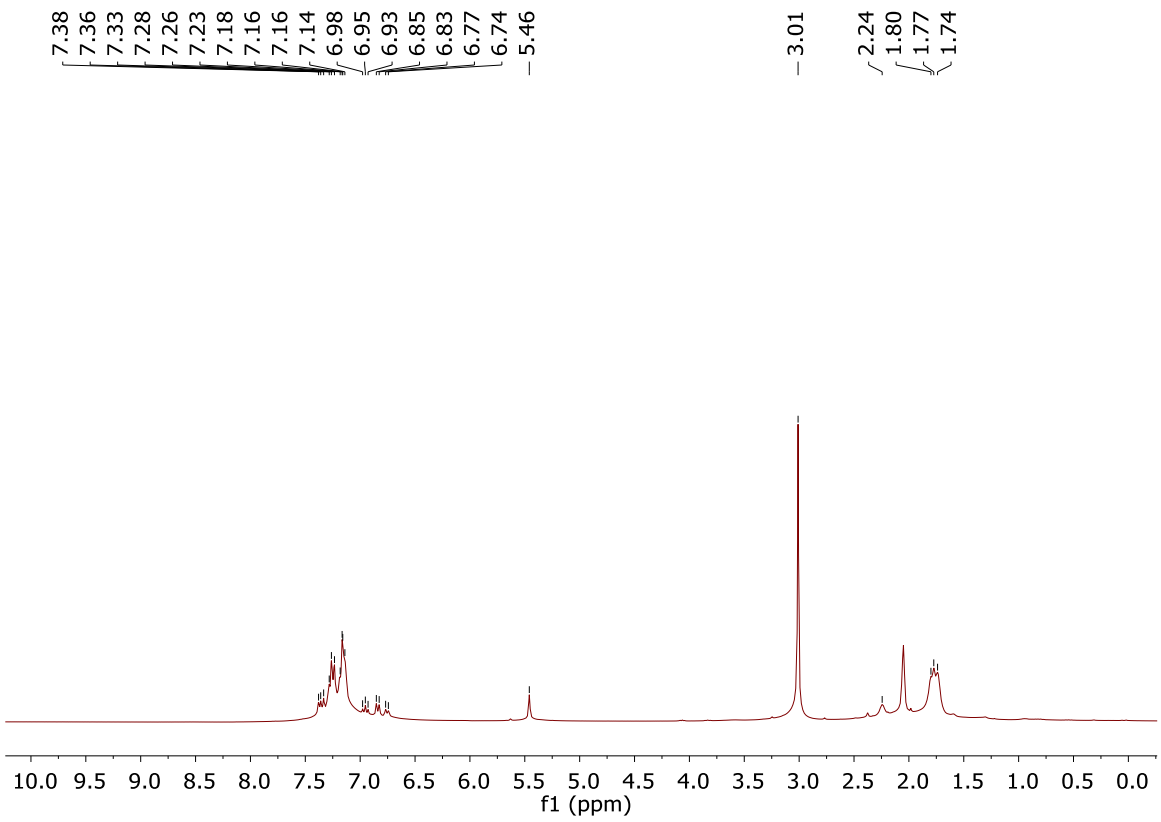

*Figure 18. $^{1}H\{^{11}B\}$ NMR of the mixture containing **7'**$[Me_3NH]^+$ (300MHz, acetone-d_6, 25°C).*

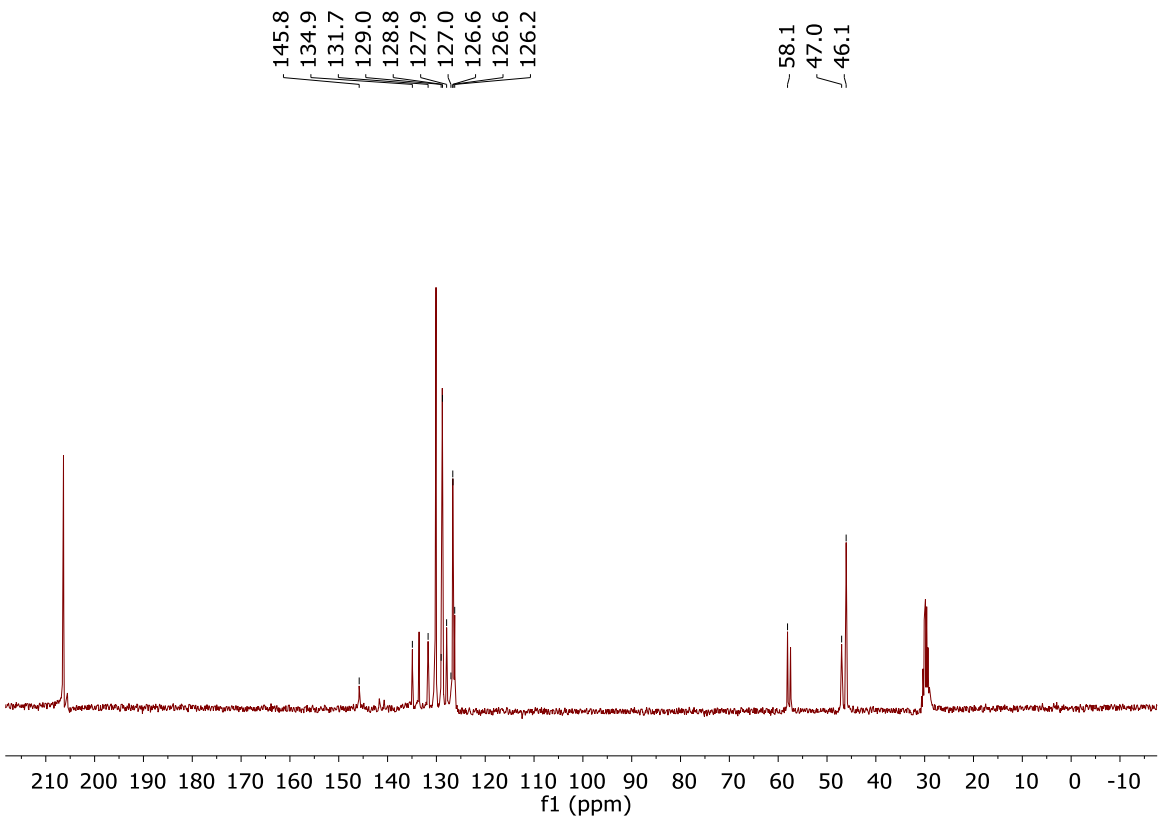

*Figure 19. $^{13}C\{^{1}H\}$ NMR of the mixture containing **7'**[Me_3NH]$^+$ (75MHz, acetone-d_6, 25°C).*

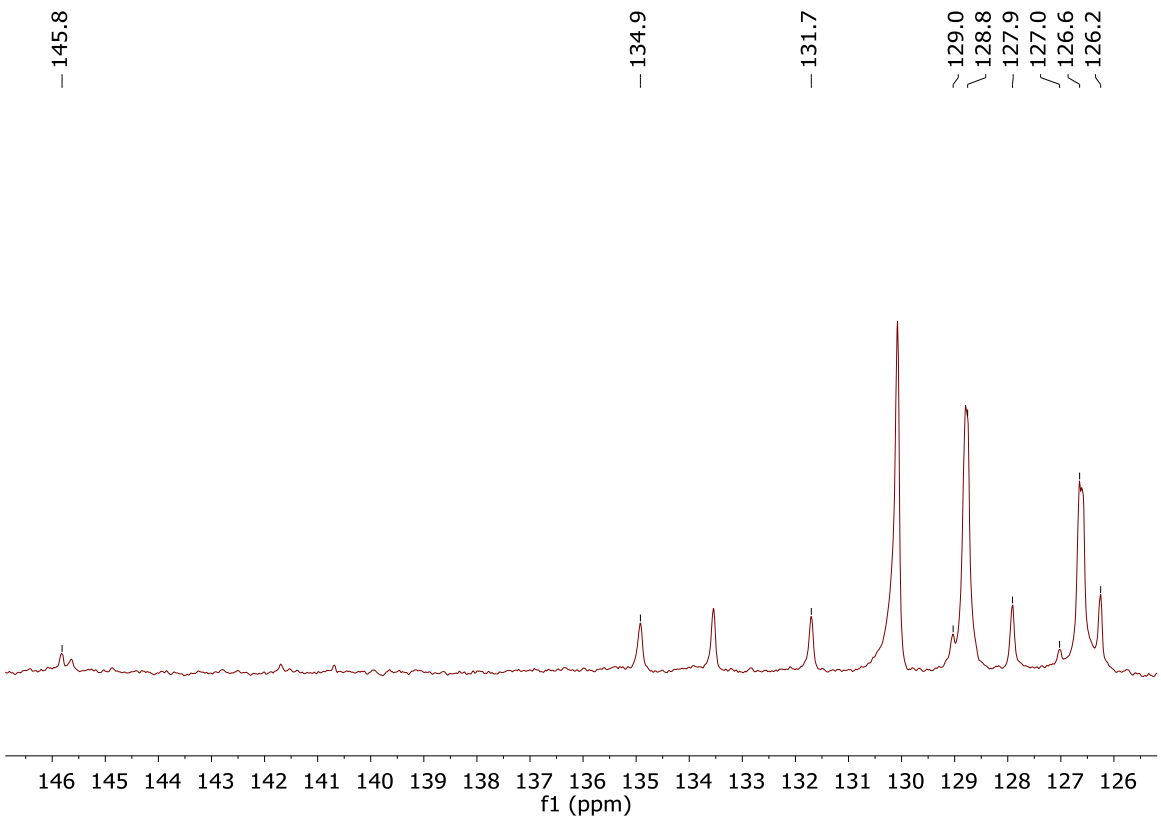

Figure 20. An expansion of $^{13}C\{^{1}H\}$ NMR of the aromatic region of the mixture containing ***7'****$[Me_3NH]^+$.*

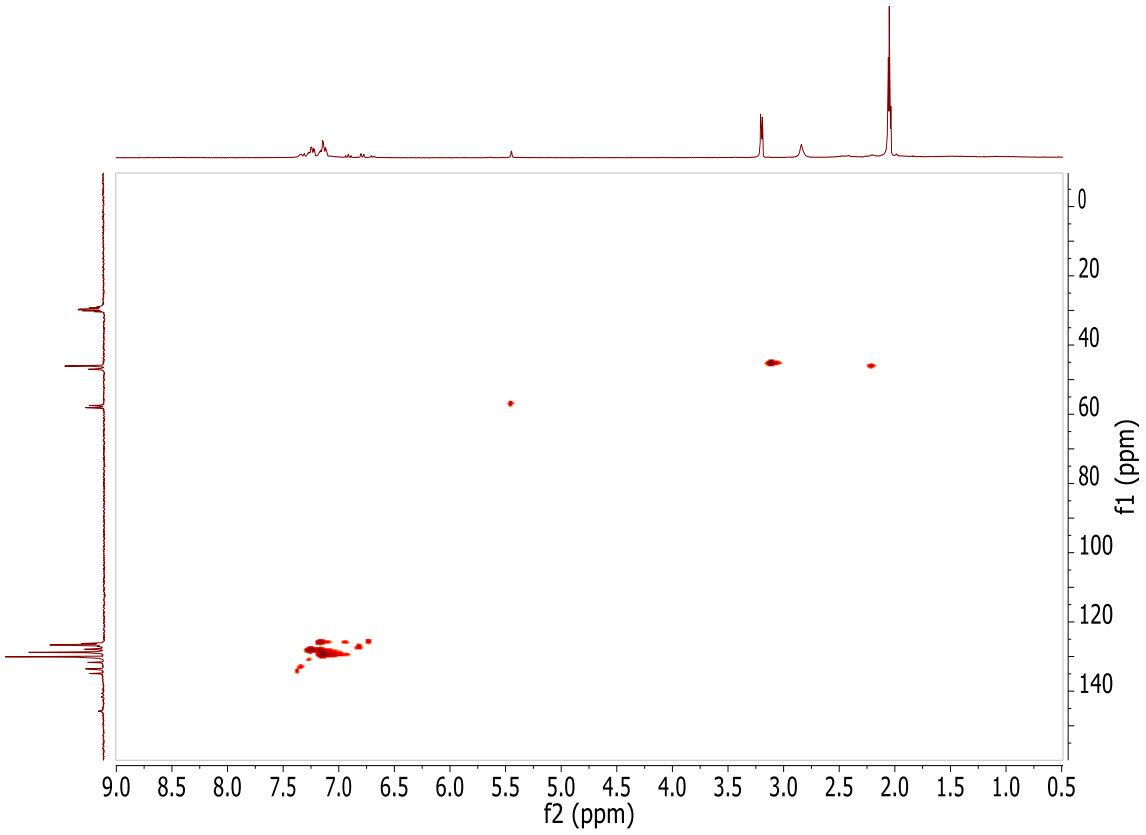

*Figure 21. HSQC NMR spectrum of the mixture containing **7'**[Me_3NH]$^+$ in acetone-d_6.*

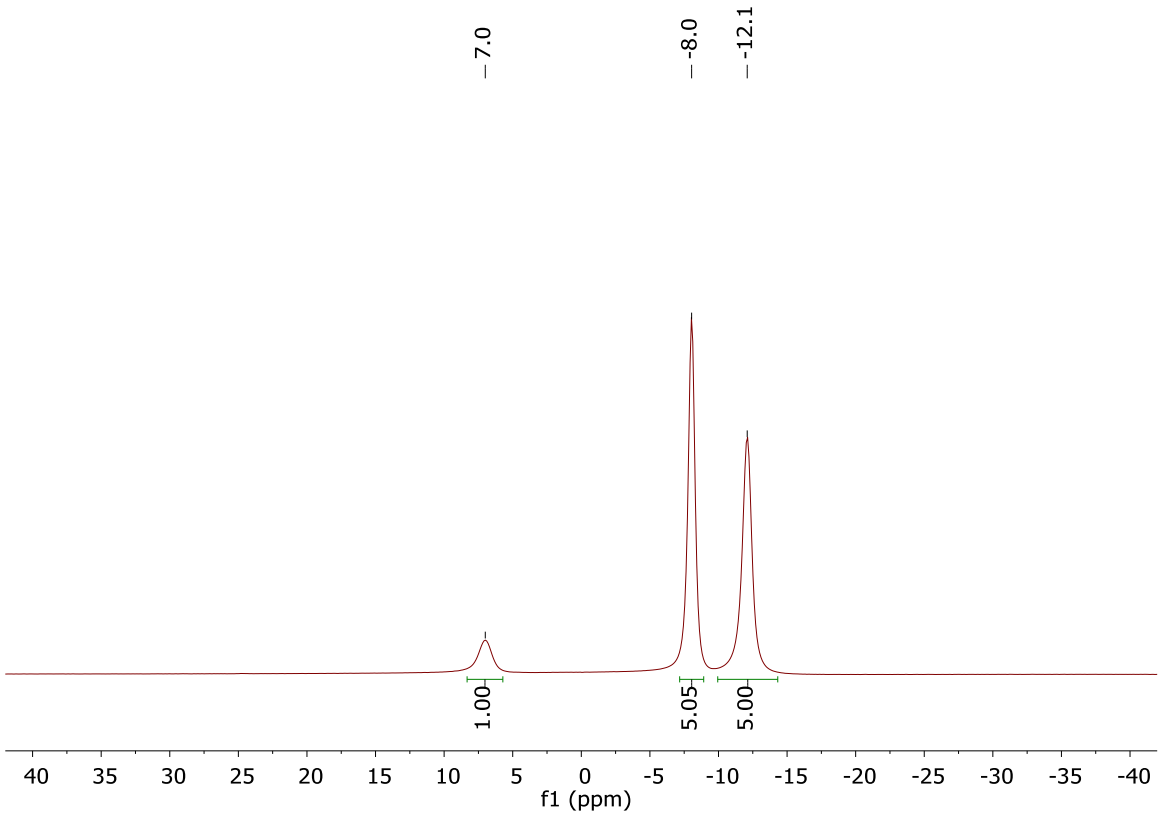

Figure 22. $^{11}B\{^{1}H\}$ NMR of the mixture containing **7**$[Me_3NH]^+$ *and* ***7'****$[Me_3NH]^+$ (96MHz, acetone-d_6, 25°C).*

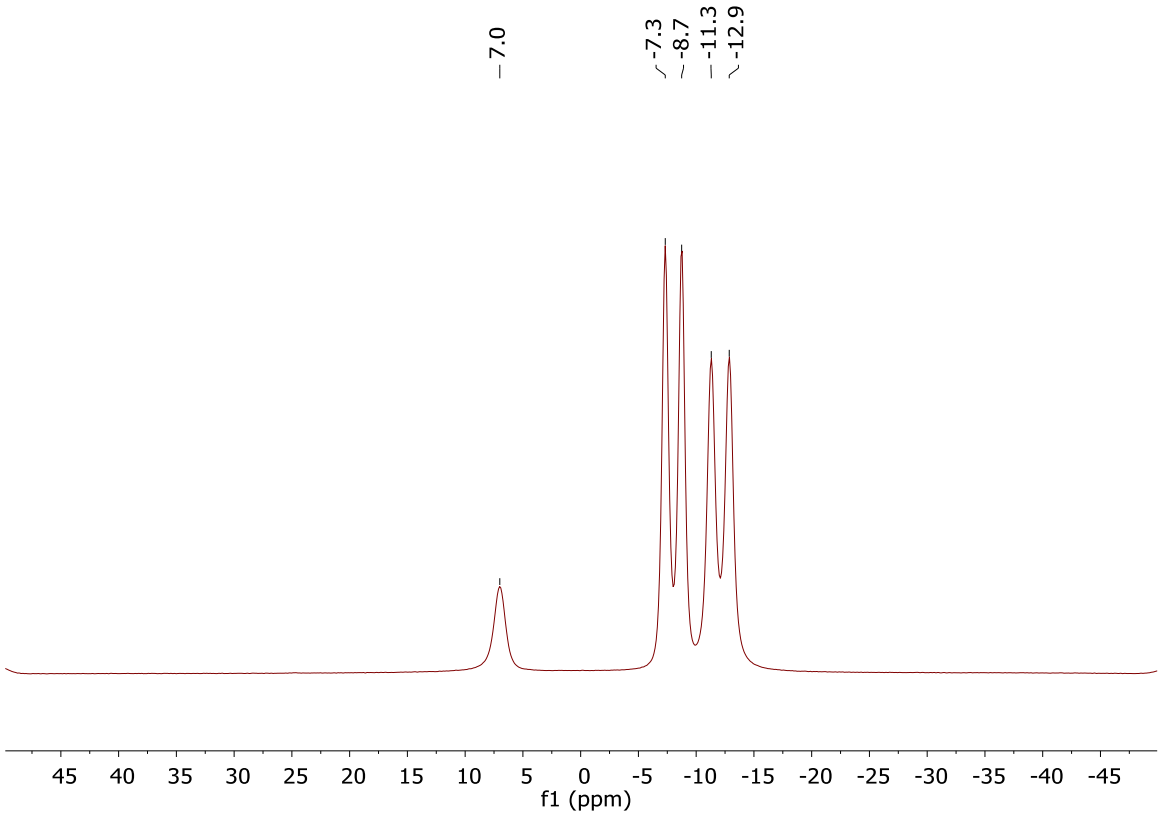

*Figure 23. $^{11}B\{^{1}H\}$ NMR of the mixture containing **7'**$[Me_3NH]^+$ (96MHz, acetone-d_6, 25°C).*

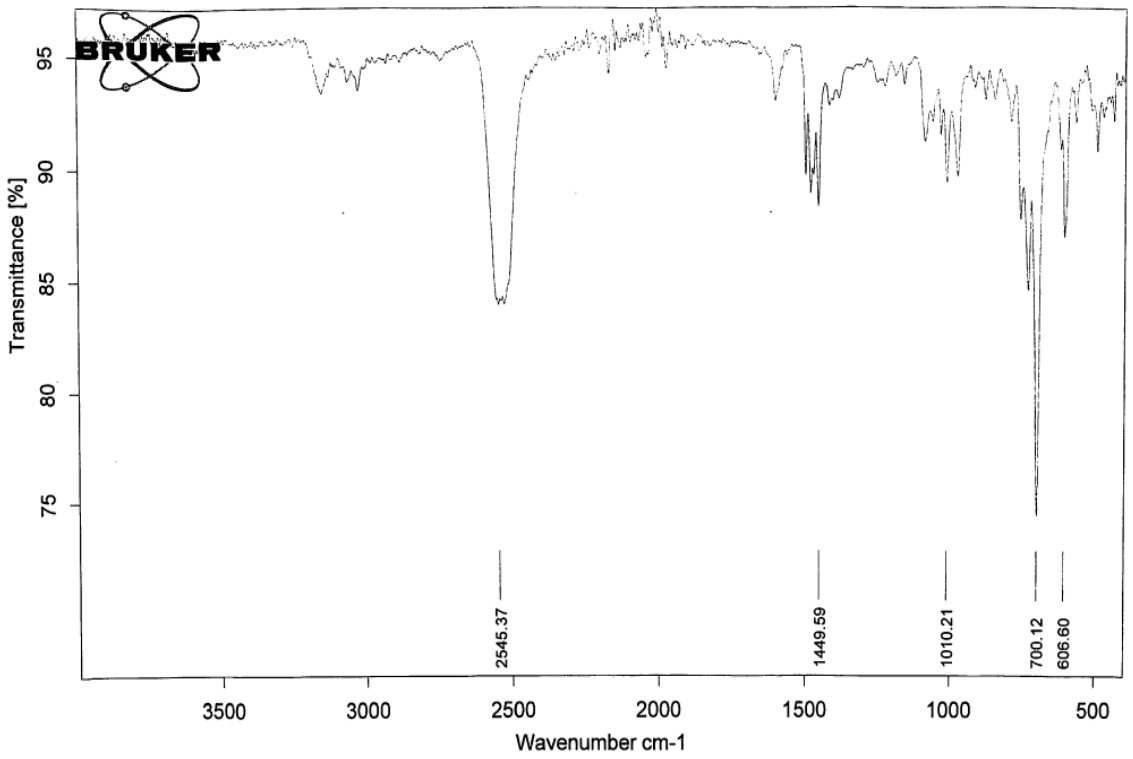

*Figure 24. IR spectrum of the solid mixture **7**[Me_3NH]$^+$ and **7'**[Me_3NH]$^+$. Showing the B-H stretches at 2545 cm^{-1}.*

X-Ray Structure of **7**[Me_3NH]$^+$:

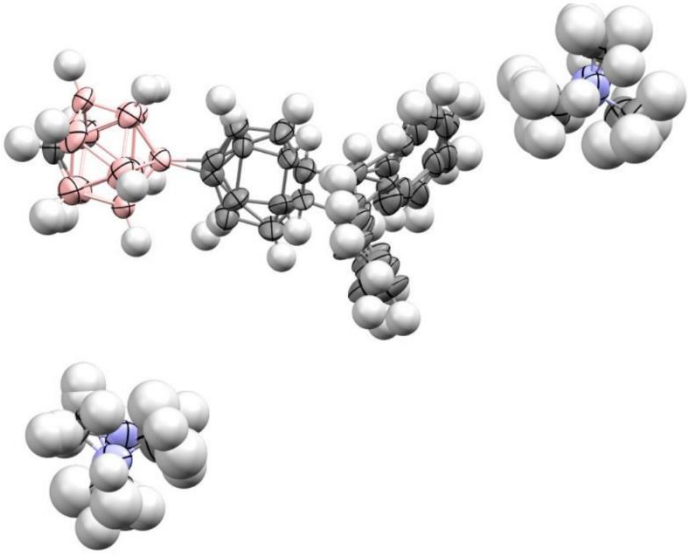

A colorless prism fragment (0.516 x 0.289 x 0.128 mm3) was used for the single crystal x-ray diffraction study of $[CH_{11}B_{11}C_{19}H_{15}]^-.[C_3H_{10}N]^+$(sample vL266JK_0m-5). The crystal was coated with paratone oil and mounted on to a cryo-loop glass fiber. X-ray intensity data were collected at 100(2)K on a Bruker APEX2 (ref. 4) platform-CCD x-ray diffractometer system (fine focus Mo-radiation, λ= 0.71073Å, 50KV/30mA power). The CCD detector was placed at a distance of 5.0600cm from the crystal. A total of 3600 frames were collected for a sphere of reflections (with scan width of 0.30in ω, starting ω and 2θ angles of –30^o, and ϕangles of 0^o, 90^o, 120^o, 180^o, 240^o and 270^o for every 600 frames, 120 sec/frame exposure time). The Bruker Cell_Now program (ref. 5) was used to obtain the two different orientation matrices of the rotational twin components (Twin law is 94orotation about the 0 1 0 real axis). These matrices were imported into the APEX2 program for Bravais lattice determination and initial unit cell refinement. The frames were integrated using the Bruker SAINT software package (ref. 6) and using a narrow-frame

integration algorithm. Based on a monoclinic I-center crystal system, the integrated frames yielded a total of 2350 unique independent reflections [maximum 2θ= 42.520° (0.98 Å resolution), data completeness = 61.8%] and 1839(78.3%) reflections were greater than $2\sigma(I)$. The unit cell parameters were, a= 15.8564(26) Å, b= 10.6647(18) Å, c= 15.8859(26) Å, β= 94.2825(25)o, V = 2678.9(8) Å3, Z = 4, calculated density Dc= 1.104 g/cm3. Absorption corrections were applied

S24(absorption coefficient μ= 0.057 mm-1; max/min transmission = 0.993/0.971) to the raw intensity data using the Bruker TWINABS program (ref. 7). The Bruker SHELXTL software package (ref. 8) was used for phase determination and structure refinement. Using the first twin domain HKL 4 intensity data, the distribution of intensities (E2-1 = 0.734) and systematic absent reflections indicated three possible space groups, I2, I2/m, and Im. The space group I2 (#5) was later determined to be correct. Direct methods of phase determination followed by two Fourier cycles of refinement led to an electron density map from which most of the non-hydrogen atoms were identified in the asymmetry unit of the unit cell. With subsequent isotropic refinement, all of the non-hydrogen atoms were identified. The combined (major and minor components) HKLF 5 intensity dataset was used in the final structure refinement. There were two half disordered-cations of $[C_3H_{10}N]^+$ and one disordered-anion of $[CH_{11}B_{11}C_{19}H_{15}]^-$ present in the asymmetry unit of the unit cell. The two disordered-cations were located at the 2-fold rotation axis parallel to the b-axis, and modeled with 50%/50% site occupancy ratio disorder. The site occupancy ratio of the disordered-anion was 54%/46%. The rotational twin law was 94° rotation about the 0 1 0 real axis. The major/minor twin component ratio was 54%/46%. The alert levels A and B are due to the poor crystal quality with low resolution data diffracting to 0.98 Angstroms at 120 seconds long exposure time. The

disorder of the cation and anion further contributed to the poor resolution data. Attempts to obtain bigger and better quality crystal were unsuccessful. Atomic coordinates, isotropic and anisotropic displacement parameters of all the non-hydrogen atoms were refined by means of a full matrix least-squares procedure on F2. The H-atoms were included in the refinement in calculated positions riding on the atoms to which they were attached, except the H1 atom bonded to C1A was refined with DFIX restraint. The refinement converged at R1 = 0.0722, wR2 = 0.1857, with intensity, I>2σ(I). The largest peak/hole in the final difference map was 0.235/-0.158 e/Å3.Table S1. Crystal data and structure refinement for **3**[$HNMe_3$]$^+$. Identification code vL266JK_0m-5. Empirical formula: $C_{23}H_{36}B_{11}N$. Formula weight 445.44. Temperature 100(2)K. Wavelength 0.71073Å. Crystal system MonoclinicSpace group I 2Unit cell dimensions **a** = 15.856(3)Å α= 90°. **b** = 10.6647(18)Å β= 94.283(3)°. **c** = 15.886(3)Å γ= 90°. Volume: 2678.9(8)Å 3Z4

Density (calculated)1.104 Mg/m3. Absorption coefficient 0.057 mm-1F(000)944. Crystal size 0.516 x 0.289 x 0.128mm^3. Theta range for data collection 1.750 to 21.260°. Index ranges-16<=h<=16, 0<=k<=10, 0<=l<=16. Reflections collected: 7977. Independent reflections: 2350 [R(int) = 0.0357]. Completeness to theta = 25.242° 61.8%. Absorption correction Semi-empirical from equivalents Refinement method Full-matrix least-squares on F2Data / restraints / parameters2350 / 1085 / 414Goodness-of-fit on F21.137Final R indices [I>2σ(I)] R1 = 0.0722, wR2 = 0.1857R indices (all data)R1 = 0.0940, wR2 = 0.1999Absolute structure parameter-9(7)Extinction coefficient n/a Largest diff. peak and hole0.235 and -0.158 e.Å-3.

X-Ray Structure of **7**[Cs]$^+$:

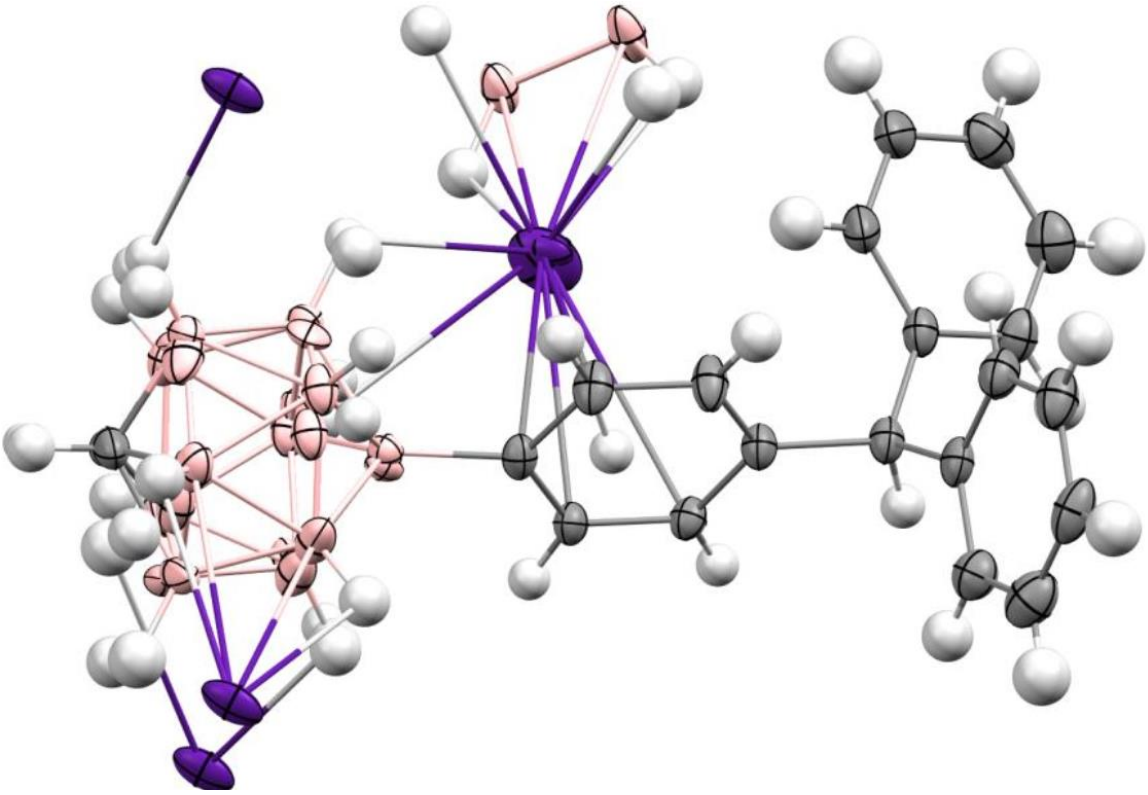

A colorless prism fragment (0.434 x 0.273 x 0.126 mm3) was used for the single crystal x-ray diffraction study of $[Cs]^+[C_{20}H_{26}B_{11}]^-$ (sample vL266JKr2-20_0m). The crystal was coated with paratone oil and mounted on to a cryo-loop glass fiber. X-ray intensity data were collected at 100(2) K on a Bruker APEX2 (ref. 4) platform-CCD x-ray diffractometer system (fine focus Mo-radiation, λ=0.71073 Å, 50KV/30mA power). The CCD detector was placed at a distance of 5.0600 cm from the crystal. A total of 3600 frames were collected for a sphere of reflections (with scan width of 0.30in ω, starting ω and 2θ angles of –30^o, and ϕ angles of 0^o, 90^o, 120^o, 180^o, 240^o, and 270^o for every 600 frames, 20 sec/frame exposure time). The frames were integrated using the Bruker SAINT

software package (ref. 6) and using a narrow-frame integration algorithm. Based on a monoclinic crystal system, the integrated frames yielded a total of 57635 reflections at a maximum 2θangle of 63.056° (0.70Å resolution), of which 7865 were independent reflections (Rint = 0.0234, Rsig = 0.0140, redundancy = 7.3, completeness = 99.0%) and 6993 (88.9%) reflections were greater than 2σ(I). The unit cell parameters were, a= 13.7371(4) Å, b= 10.4955(3) Å, c= 17.4166(5) Å, β= 108.6604(5)°, V =2379.08(12) Å3, Z = 4, calculated density Dc= 1.447 g/cm3. Absorption corrections were applied (absorption coefficient μ= 1.563 mm-1; max/min transmission = 0.827/0.550) to the raw intensity data using the SADABS program (ref. 7). The Bruker SHELXTL software package (ref. 8) was used for phase determination and structure refinement. The distribution of intensities (E2-1 = 0.946) and systematic absent reflections indicated one possible space group, P2(1)/n. The space group P2(1)/n (#14) was later determined to be correct. Direct methods of

S27phase determination followed by two Fourier cycles of refinement led to an electron density map from which most of the non-hydrogen atoms were identified in the asymmetric unit of the unit cell. With subsequent isotropic refinement, all of the non-hydrogen atoms were identified. There was one disordered cation of $[Cs]^+$ and one disordered anion of $[C_{20}H_{26}B_{11}]^-$ present in the asymmetric unit of the unit cell. The Cs and $CH_{11}B_{11}^-$ group were modeled with disordered (disordered site occupancy ratio was 79%/21%). The molecule is a polymeric structure. The cation-anion polymeric chains form a plane along the b-axis and the n-glide direction. The B level alert is probably due to the disorder of the Cs and $CH_{11}B11^-$ group. Atomic coordinates, isotropic and anisotropic displacement parameters of all the non-hydrogen atoms were refined by means of a full matrix least-squares procedure on F2. The H-atoms were included in the refinement in

calculated positions riding on the atoms to which they were attached, except H1, H1D, H3A, H4A, H6A and H7A bonded to C1, C1D, C3, C4, C6, and C7, respectively were refined with DFIX restraints. The refinement converged at R1 = 0.0315, wR2 = 0.0708, with intensity I>2σ(I). The largest peak/hole in the final difference map was 0.999/-0.490 e/Å3.Table S2. Crystal data and structure refinement for **7**[Cs]$^{+}$. Identification code vL266JKr2-20_0mEmpirical formula $C_{20}H_{26}B_{11}Cs$ Formula weight: 518.23 Temperature: 100(2)K. Wavelength: 0.71073Å. Crystal system: Monoclinic Space group P 21/n. Unit cell dimensions: **a** = 13.7371(4) Å α= 90°. **b** = 10.4955(3) Å β= 108.6604(5)°. **c** = 17.4166(5) Å. γ = 90°. Volume: 2379.08(12)Å. 3Z4 Density (calculated): 1.447 Mg/m^3. Absorption coefficient: 1.563 mm^{-1}. F(000)1024 Crystal size: 0.434 x 0.273 x 0.126 mm^3. Theta range for data collection: 1.654 to 31.528°. Index ranges: -20<=h<=19, -15<=k<=15, -25<=l<=25 Reflections collected: 57635. Independent reflections: 7865 [R(int) = 0.0234]. Completeness to theta = 25.242°. 100.0% Absorption correction. Semi-empirical from equivalents. Refinement method. Full-matrix least-squares on F2Data / restraints / parameters 7865 / 329 / 413. Goodness-of-fit on F21.140. Final R indices [I>2sigma(I)]R1 = 0.0315, wR2 = 0.0708R indices (all data). R1 = 0.0372, wR2 = 0.0732. Extinction coefficient: n/a .Largest diff. peak and hole: 0.999 and -0.490 e.Å^{-3}.

X-Ray Structure of **7'**[Me_3NH]$^+$:

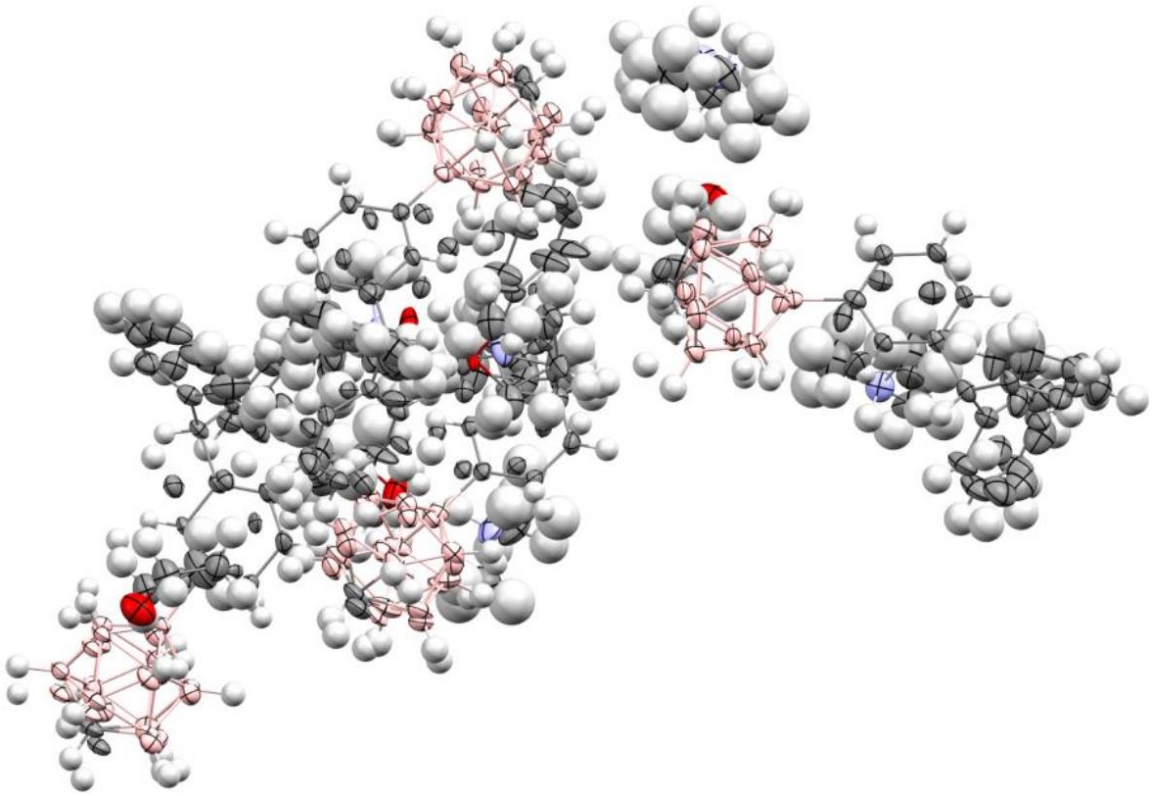

A colorless prism fragment (0.542 x 0.303 x 0.123 mm3) was used for the single crystal x-ray diffraction study of $[C_3H_{10}N]^+.[C_{20}H_{26}B_{11}]^-.C_4H_8O$ (sample vL266JKr_0m). The crystal was coated with paratone oil and mounted on to a cryo-loop glass fiber. X-ray intensity data were collected at 100(2)K on a Bruker APEX2 (ref. 4) platform-CCD x-ray diffractometer system (fine focus Mo-radiation, λ= 0.71073Å, 50KV/30mA power). The CCD detector was placed at a distance of 5.0600 cm from the crystal. A total of 3600 frames were collected for a sphere of reflections (with scan width of 0.30in ω, starting ω and 2θ angles of –30^o, and ϕ angles of 0^o, 90^o,120^o, 180^o, 240^o, and 270^o for every 600 frames, 80 sec/frame exposure time). The frames were integrated using the Bruker SAINT

software package (ref. 6) and using a narrow-frame integration algorithm. Based on a monoclinic crystal system, the integrated frames yielded a total of 136026 reflections at a maximum 2θangle of 58.260º(0.73 Å resolution), of which 32906 were independent reflections (Rint= 0.0447, Rsig= 0.0353, redundancy = 4.1, completeness = 99.9%) and 26149 (79.5%) reflections were greaterthan 2σ(I). The unit cell parameters were, **a**= 8.5424(3) Å, **b**= 21.3147(7) Å, **c**= 33.6589(11) Å, β= 90.2206(6)o, V =6128.5(4) Å3, Z = 8, calculated density Dc= 1.122 g/cm3. Absorption corrections were applied (absorption coefficient μ= 0.060 mm-1; max/min transmission = 0.993/0.968) to the raw intensity data using the SADABS program (ref. 7). The Bruker SHELXTL software package (ref. 8) was used for phase determination and structure refinement. The distribution of intensities (E2-1 = 0.741) and systematic absent reflections indicated two possible space groups, Pc and P2/c. The space group Pc (#7) was later determined to be correct. Direct methods of phase determination followed by two Fourier cycles of refinement led to an electron density map from which most of the non-hydrogen atoms were identified in the asymmetric unit of the unit cell. With subsequent isotropic refinement, all of the non-hydrogen atoms were identified. There were four cations of $[C_3H_{10}N]^+$, four meta/para disordered-anions of $[C_{20}H_{26}B_{11}]^-$, and four solvent molecules of THF (where one of the four THF was modeled with 50%/50% site occupancy disorder) present in the asymmetric unit of the unit cell. The four meta/para anion-disordered site occupancy ratios were 83%/17%, 81%/19%, 73%/27%, and 61%/39%. The two cation-disordered site occupancy ratios were 73%/27% and 50%/50%. There was space group ambiguity between Orthorhombic Pca2(1) and monoclinic Pc. The final structure refinement was based on the monoclinic Pc space group. The structure was refined as a pseudo-merohedral twin (twin law 1 0 0, 0 -1 0, 0 0 -1) and the major/minor component twin ratio was 76%/24%. Using Pca2(1) space group,

data reduction and refinement gave a much higher Rint= 0.0829, Rsig= 0.0285 and R1 = 0.0768 at 0.81 Angstroms resolution, respectively in comparision to Pc space group (Rint= 0.0447, Rsig= 0.0353, R1 = 0.0768 at 0.73 Angstroms resolution). The B level Alert of the C-C bond precession is probably due to the cations, THF, and the four whole molecule-anion meta/para disorders where restraints were used to allow the refinement to converge. The hydrogen bond angles and distances of the anions-THF are given in Table 7. Atomic coordinates, isotropic and anisotropic displacement parameters of all the non-hydrogen atoms were refined by means of a full matrix least-squares procedure on F2. The H-atoms were included in the refinement in calculated positions riding on the atoms to which they were attached, except the H1A, H1B, H1C, H1D, H1E, HIF, HIG and H1H atoms bonded to C1A, C1B, C1C, C1D, C1E, C1F, C1G and C1H, respectively were refined with DFIX restraints. The refinement converged at R1 = 0.0768, wR2 = 0.2054, with intensity I>2σ(I). The largest peak/hole in the final difference map was 0.724/-0.543e/Å3.Table S3.Table 1. Crystal data and structure refinement for 3'[HNMe3]+.Identification code vL266JKr_0mEmpirical formula C27 H44 B11 N OFormula weight 517.54Temperature 100(2) KWavelength 0.71073 ÅCrystal system MonoclinicSpace group P cUnit cell dimensions: **a** = 8.5424(3)Å. α= 90°. **b** = 21.3147(7)Å. β= 90.2206(6)°. **c** = 33.6589(11)Å. γ = 90°. Volume: 6128.5(4)Å^3. Z8 Density (calculated): 1.122 Mg/m^3. Absorption coefficient: 0.060mm^{-1}. F(000)2208 Crystal size: 0.542 x 0.303 x 0.123 mm^3. Theta range for data collection: 1.542 to 29.130°. Index ranges-11<=h<=11, -29<=k<=29, -46<=l<=46. Reflections collected: 136026. Independent reflections: 32906 [R(int) = 0.0447]. Completeness to theta = 25.242°. 100.0% Absorption correction Semi-empirical from equivalents. Refinement method Full-matrix least-squares on F2Data / restraints / parameters 32906 / 7534 / 2333. Goodness-of-fit on F21.013. Final R indices

[I>2sigma(I)]R1 = 0.0768, wR2 = 0.2054R indices (all data)R1 = 0.0976, wR2 = 0.2262. Absolute structure parameter-0.1(3). Extinction coefficient: n/a. Largest diff. peak and hole 0.724 and -0.543 e.Å-.

CHAPTER 3: Synthesis of an Anionic Au^{I} Hydroamination Precatalyst Supported by Charged Hydrido-carboranyl Phosphine Ligands

Introduction

Neutral phosphine ligands are ubiquitous ancillary ligands in homogenous catalysis. Such species are typically appended with alkyl or aryl groups, to manipulate the steric environment and electronic properties of the metal center. Neutral *closo*-carborane clusters,[11,73,74] specifically $H_2C_2B_{10}H_{10}$ congeners, are alternative R-groups,[15,16] which have been heavily investigated over the last 60 years. However, despite these efforts, little progress has been made in developing competitive or superior catalysts, compared to classical systems supported by ligands with hydrocarbon R- groups. This fact is perhaps partially explained by the tendency of such clusters to undergo catalyst deactivation by cage degradation,[16] B-H cyclometallation reactions,[14] or other degradation pathways.[75,76] In contrast to neutral $H_2C_2B_{10}H_{10}$ clusters, their anionic analogue $[HCB_{11}H_{11}]^{-1}$ and its derivatives,[17] are not susceptible to chemical cage degradation[9] and are more resistant to cyclometallation.[55] Several years ago, we began implementing a variety of ligands functionalized with such *closo*-carborane anions, including phosphine[52,54,55,58,77,78]

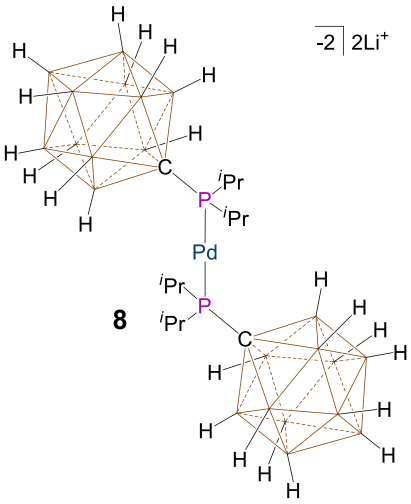

8

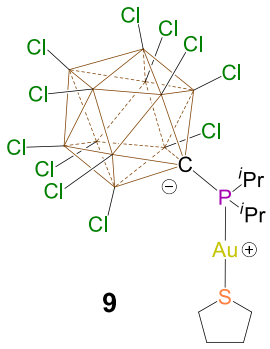

9

*Figure 25. Dianionic Pd^{0} complex **8** is the most active isolable compound for the oxidative addition of arylchlorides. Zwitterionic Au^{I} complex **9** is the most active catalyst for the hydroamination of alkynes.*

and N-heterocyclic carbenes.[51,79] So far, we have found two examples of phosphine supported systems that display remarkable reactivity **8**[52] and catalytic activity **9**,[58] respectively (Fig. 25). Compound **8** is a dianionic Pd^0 species that undergoes the oxidative addition of certain chloroarenes in less than 10 minutes at ambient temperature. No other isolable Pd^0 species has been reported to undergo such rapid oxidative addition reactions. The extreme reactivity of **8** was found both experimentally and computationally to be the result of electrostatic effects of coordinating two charged phosphine ligands to Pd^0. Electrostatic repulsion between the ligands results in facile ligand dissociation of one phosphine, allowing immediate access to a highly reactive, mono phosphine ligated Pd^0. Compound **9** is a zwitterionic Au^I species, which functions as a single component Au^I catalyst that does not need an activator, such as Ag^+ or acid. This catalyst displays the highest activity yet reported for the hydroamination of amines with alkynes.[80,81] Turn over numbers (TONs) of around 100,000 in a 24 hour period were observed for some substrates. The high activity of **9** is thought to result from the size of the ligand, which prevents double phosphine substitution, but more importantly the electrostatic stabilization of the Au^I cation by field effects of the proximal carborane anion (see Fig. 25.). Here, we report our efforts to synthesize a linear monoanionic dicoordinate Au^I complex analogous to **8** (Fig. 26). The rational for this approach was that if facile ligand dissociation, similar to **8**, was observed when two charged phosphine ligands were attached to Au^I, we might be able to achieve an even more active

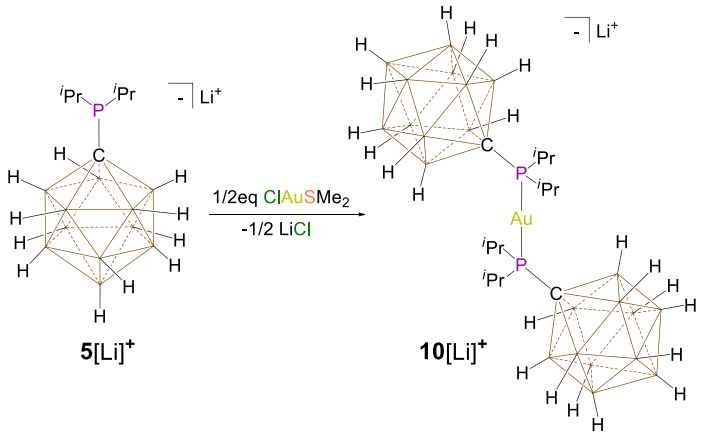

*Figure 26. Synthesis of anionic Au^I complex **10***

system than **9**.

Results and Discussion

Given our success at preparing the diphosphine substituted Pd^0 species **8**[52] we imagined it should certainly be possible to form a similar compound with Au^I, as gold is a larger atom. Thus, we reacted two equivalents of ligand **5** with $ClAuSMe_2$ in methylene chloride solvent, and a white precipitate of LiCl immediately formed. After filtration and concentration of the supernatant, the residue was analyzed by mass spectrometry (negative-ion mode), which showed a molecular ion peak corresponding to the formation of a gold complex bearing two carboranyl phosphines.

Analysis of the ^1H NMR spectrum of the residue in CD_2Cl_2 reveals the existence of THF, which suggests the presence of a lithium cation coordinated by THF, consistent with the formation of the anionic complex **10**. Integration of the THF peaks shows that there are three THF molecules coordinated to the Li cation. Additionally, we see the signature isopropyl multiplets at 2.56ppm and 1.50 through 1.35ppm, indicating the presence of the carboranyl phosphine. One resonance is present in the $^{31}P\{^1H\}$ NMR at 83.6ppm, indicating a single phosphorus product. Analyzing the $^{11}B\{^1H\}$ NMR presents three peaks at -2.9, -11.7, and -12.9ppm, respectively, in a 1:5:5

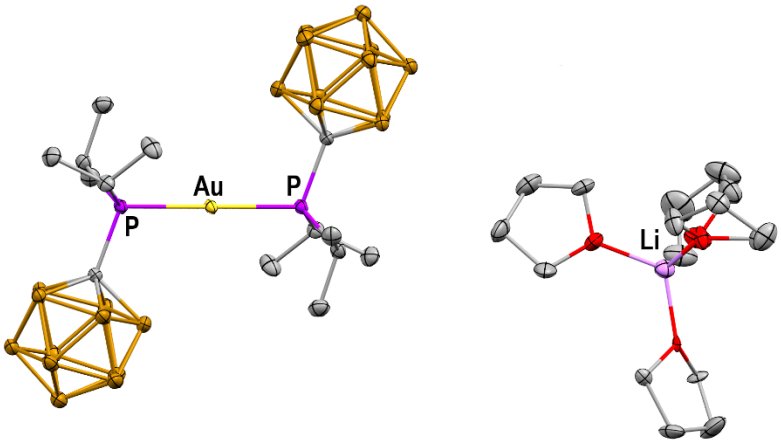

*Figure 27 Solid-state structure of **10**. Thermal ellipsoids drawn at the 50% probability level and hydrogen atoms omitted for clarity. Note: THF molecules coordinated to Li^+ disordered over two positions. Color code: grey = carbon, brown = boron, violet = phosphorus, yellow = gold, red = oxygen, pink = lithium. (Color online.)*

ratio showing that the local C_{5v} symmetry of the cluster is preserved.

A single crystal X-ray diffraction study unambiguously confirmed the structure of **10**. In the solid-state, **10** displays the expected perfectly linear geometry (P–Au–P angle = 180°) of a symmetrical dicoordinate Au^{I} complex, as well as a single lithium counter cation coordinated by THF (Fig. 27). The P–Au–P bond lengths are 2.3079(5) and 2.3099(2)Å, close to both the reported P–Au bond length for the neutral *ortho*-dicarba-*closo*-decaborane-substituted phosphine–AuCl complex (2.232(3)Å)[82] and the anionic carborane substituted phosphine-AuCl in 2 (2.2477(12)Å).[58] The closest B–H distance to the Au^{I} center is 3.001(5)Å, which is outside of the range for covalent Au–H interactions,

Table 1. Hydroamination of alkynes with primary amines in the presence of catalyst **10**.

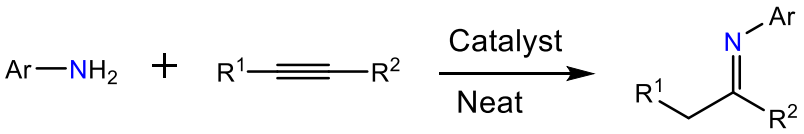

Entry	Ar	R^1	R^2	Catalyst Loading [%]	T [°C]	Yield [%][a,b]	TON [24h]
1	Ph	H	Ph	1.0	80	90	90
2	Ph	H	Ph	0.5	80	86	172
3	Ph	H	Ph	0.1	80	77 (74)	765
4	Mes	H	Ph	0.1	80	71	710
5	Dipp	H	Ph	1.0	80	80 (74)	80
6	Ph	H	4-FC_6H_4	1.0	80	90(86)	90
7	Mes	H	4-FC_6H_5	1.0	80	90	90
8	Dipp	H	4-FC_6H_6	1.0	80	87 (83)	85
9	Ph	H	4-$MeOC_6H_4$	0.1	80	92	920
10	Mes	H	4-$MeOC_6H_4$	0.1	80	95(92)	950
11	Dipp	H	4-$MeOC_6H_4$	0.1	80	78	780
12	Ph	H	*n*-C_4H_9	1.0	80	65	65
13	Mes	H	*n*-C_4H_9	1.0	80	55	55
14	Dipp	H	*n*-C_4H_9	1.0	80	50	50

[a]The yield was determined by NMR spectroscopy by the direct integration of the peak for the amine starting material with respect to the peak for the imine product. [b]The yield of the isolated product is given in parentheses. Dipp = 2,6-diisopropylphenyl, Mes = mesityl (2,4,6,-trimethylphenyl).

demonstrating that the carborane anion substituent does not interact strongly with the cationic Au center.

We next investigated the catalytic activity of complex **10** towards the hydroamination of alkynes with primary amines (Table 1) and compared its behavior to the previously reported catalyst **9**[58] (Fig. 25). Unlike **9**, complex **10** did not produce any hydroamination products with any of the chosen substrates at ambient temperature, run under neat conditions. In fact, reasonable rates of conversion were not observed until 80^{o}C. Our initial test substrates, aniline and phenylacetylene, were reacted with a 1.0% catalyst loading, producing the corresponding imine in 90% yield (TON = 90) after 24 hours (Table 1, entry 1). Dropping the catalyst loading to 0.5 and 0.1mol% respectively, resulted in reasonable but lower yields (86%: TON = 177; 77%: TON = 765; respectively) (Table 1, entries 2 and 3). Comparatively, **9** catalyzes this reaction with a 0.1mol% loading at ambient temperature in one hour to produce the product in >95% yield (TON >950). Furthermore, catalyst **9** achieves an identical yield even with 0.01mol% loading but at only slightly elevated temperatures (50^{o}C). Complex **10** shows similar performance with the larger mesityl amine (71%; TON = 710), but the very sterically demanding 2,6-diisoppropylamine required the utilization of higher catalyst loading (1.0mol%) to achieve any appreciable conversion (Table 1, entries 4 and 5, respectively). On the other hand, complex **9** catalyzes these reactions at 50^{o}C with 0.001% loading to achieve maximum turnovers of 67,000 and 85,000, respectively.

In contrast to **10**, catalyst **9** displays a clear trend in improved yields with bulkier amines for all substrates tested, which was rationalized by sterically related amine substrate and imine product coordination inhibition. Catalyst **10** mediated the hydroamination of the electron poor alkyne *para*-fluorophenylacetylene with all three

sterically differentiated amines providing the imine products in 85–90% yields (Table 1, entries 6–8). However, appreciable conversions were not observed below 1.0mol% catalyst loading. In contrast, the zwitterionic catalyst **9** mediates these reactions at 50^{o}C with 0.001mol% loading and achieves TONs between 54,000–92,000. Complex **10** is highly active for the hydroamination of the electron rich alkyne, *para*-methoxyphenylacetylene, producing the imine products in 78–92% yield at 0.1mol% loading (Table 1, entries 9–11). However, complex **9** is again far more active for these reactions, achieving 90,000–95,000 turnovers for the same amines at 0.001mol% loading. Complex **10** was less active for the hydroamination of the alkyl substituted alkyne, 1-hexyne, affording the ensuing imines in 50–65% yields at 1.0mol% loading (Table1, entries 12–14). Comparatively, catalyst **9** is an order of magnitude more active for the same substrates at the same temperature. Additionally, we attempted to react an internal alkyne, biphenylacetylene, but the resulting TONs were less than 5% after 24 hours which were not included in the table. Catalyst **9** on the other hand, could achieve yields between 67% and 89%, depending on the amine, at 80^{o}C with 0.1mol% loading.

The difference in reactivity between **9** and **10** can likely be explained, in part, by the fact that in contrast to our initial hypothesis, repulsive electrostatic effects in this system are not strong enough to induce facile phosphine dissociation, as they are in the analogous Pd^{0} species. Since Au^{I} is formally positively charged, in contrast to Pd^{0}, some of the electrostatic repulsion between the anionic carborane substituents is negated, rendering phosphine ligand dissociation less favorable. Indeed, we monitored by $^{31}P\{^{1}H\}$ NMR the hydroamination reaction of aniline and phenylacetylene at both 1.0% and 0.1% catalyst loading and saw no change in the ^{31}P at ambient temperature, confirming that the phosphines of **10** are not labile without external heating. In addition, at completion of the

heated reactions with **10**, we visually notice the formation of colored Au nanoparticles and metal plating on the reaction vessels, whereas with complex **9**, we see no such visual cues of decomposition. This observation is in line with the far greater chemical stability of the perchlorinated carborane present in **9**. Lastly, although not quantified but empirically noted based on the difference of C-H acidities of the $[HCB_{11}H_{11}]^{-1}$ and $[HCB_{11}Cl_{11}]^{-1}$ anions,[83] the perchlorinated carboranyl substituent should be a far stronger electron withdrawing group compared to its hydridic congener, thus rendering this phosphine a weaker donor and the Au a stronger π-acid towards alkynes.

Conclusion

An anionic gold complex **10** bearing two charged hydrido carboranyl phosphine ligands is reported and fully characterized. In contrast to the previously reported mono-phosphine ligated zwitterionic Au^{I} species **9**, supported by a phosphine with a perchlorinated carborane anion substituent, **10** is much less catalytically active for the hydroamination of alkynes. The difference in reactivity can likely be explained by the overall superior stability and π-acidity of **9**, and also the reluctance of one of the phosphines in **10** to dissociate. Given these results, subsequent investigations into such systems will focus on monophosphine ligated zwitterionic species with enhanced π-acidity.

Experimental

General Considerations: Unless otherwise stated, all manipulations were carried out using standard Schlenk or glovebox techniques (O_2, H_2O < 1ppm) under a dinitrogen or argon atmosphere. Solvents were dried on K or CaH_2 and distilled under argon before use. Ligand $[Li(THF)_3]^{+}[P(C_3H_7)_2CB_{11}H_{11}]^{-}$ was prepared according to literature.[77] The

amines were dried over CaH_2 and distilled before use. The alkynes were dried over molecular sieves and used without further purification. All other reagents were purchased from commercial vendors and used without further purification. Known catalytically produced imines from Table 1 were identified by comparison to their reported spectroscopic data for ^{1}H NMR and ^{13}C NMR. NMR spectra were recorded at room temperature on Bruker Avance 300MHz, Bruker Avance 400MHz, or Bruker Avance 600MHz spectrometers. NMR chemical shifts are reported in parts per million (ppm). ^{1}H NMR and ^{13}C NMR chemical shifts were referenced to residual protio solvent. ^{11}B NMR chemical shifts were externally referenced to BF_3OEt_2. ^{31}P NMR chemical shifts were externally referenced to 80% H_3PO_4 in H_2O. The mass spectra were collected on an Agilent LCTOF Multimode-ESI/APCI with direct injection. Crystallographic data for compound **10** is available free of charge from the Cambridge Crystallographic Data Center under reference number 1850911. This structure can be accessed at: http://www.ccdc.cam.ac.uk/Community/Requestastructure/Pages/DataRequest.aspx.

Synthesis of Complex **10**:

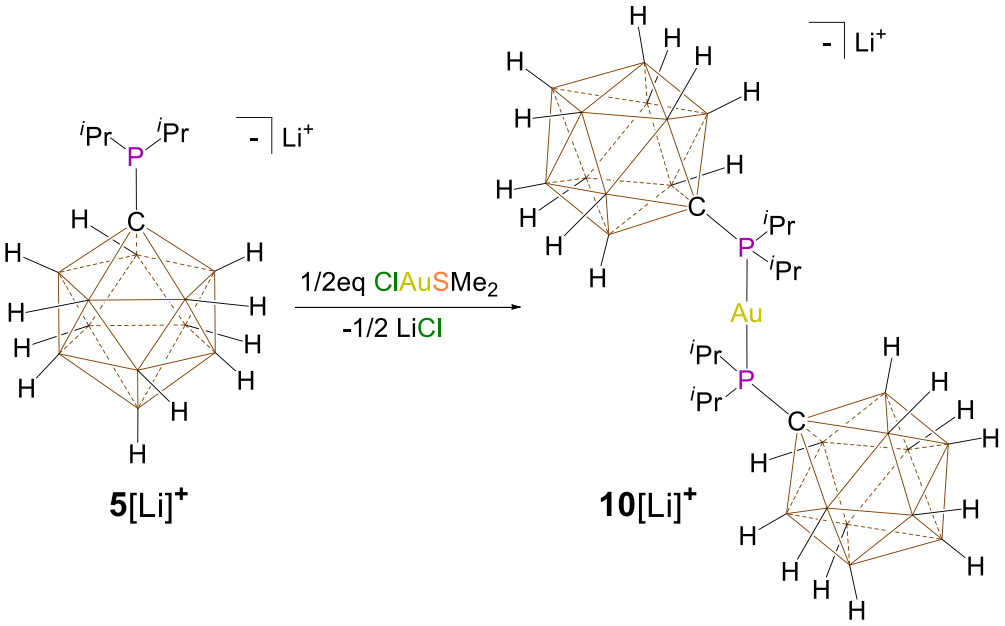

In a vial equipped with a stir bar, **5** (757mg, 1.57mmol) and $ClAuSMe_2$ (231mg, 0.785mmol) were added and subsequently dissolved in 10mL of methylene chloride. The mixture was stirred and a white precipitate rapidly formed. After one hour the mixture was filtered through a glass pipette plugged with glass wool to remove LiCl. The solvent was removed under vacuum and remaining solid was washed with pentane. The compound was dried under vacuum overnight to afford the purified product (total yield = 701.0mg, 1.35mmol, 86.1%). Crystals suitable for an X-ray diffraction study were obtained by layering a CH_2Cl_2 solution of **10** with pentane. m.p. = 110°C (dec.); ^{1}H NMR (300MHz, CD_2Cl_2, 25°C): $\delta = 3.82$ (m, 12H, THF), $\delta = 2.56$ (d-sep, $J^3(H,H) = 7.2$ Hz, $J^2(H,P) = 4.0$ Hz 1H, CH), $\delta = 1.99$ (m, 12H, THF), $\delta = 1.47$ (m, 6H, CH_3), $\delta = 1.37$ (m, 6H, CH_3); $^{1}H\{^{11}B\}$ NMR (300MHz, CD_2Cl_2, 25°C): $\delta = 2.13$ (br-s, 5H, BH), $\delta = 1.91$ (br-s, 1H, BH), $\delta = 1.70$ (br-s, 5H, BH); $^{31}P\{^{1}Hdec\}$ NMR (162MHz, THF-d_8, 25°C): $\delta = 83.6$; $^{13}C\{^{1}H\}$ NMR (101MHz, CD_2Cl_2, 25°C): $\delta = 69.0, 28.8, 25.8, 22.6, 19.2$; ^{11}B NMR (96MHz, CD_2Cl_2, 25°C): $\delta = -2.9$

(d J^1(B,H) = 120 Hz), −11.7(d J^1(B,H) = 120 Hz), −12.9(d J^1(B,H) = 120 Hz); HRMS: (Multimode-ESI/APCI) [M]- m/z calc'd for $H_{34}B_{11}C_{11}PAu$: 715.5239 g/mol; found: 715.5432 g/mol.

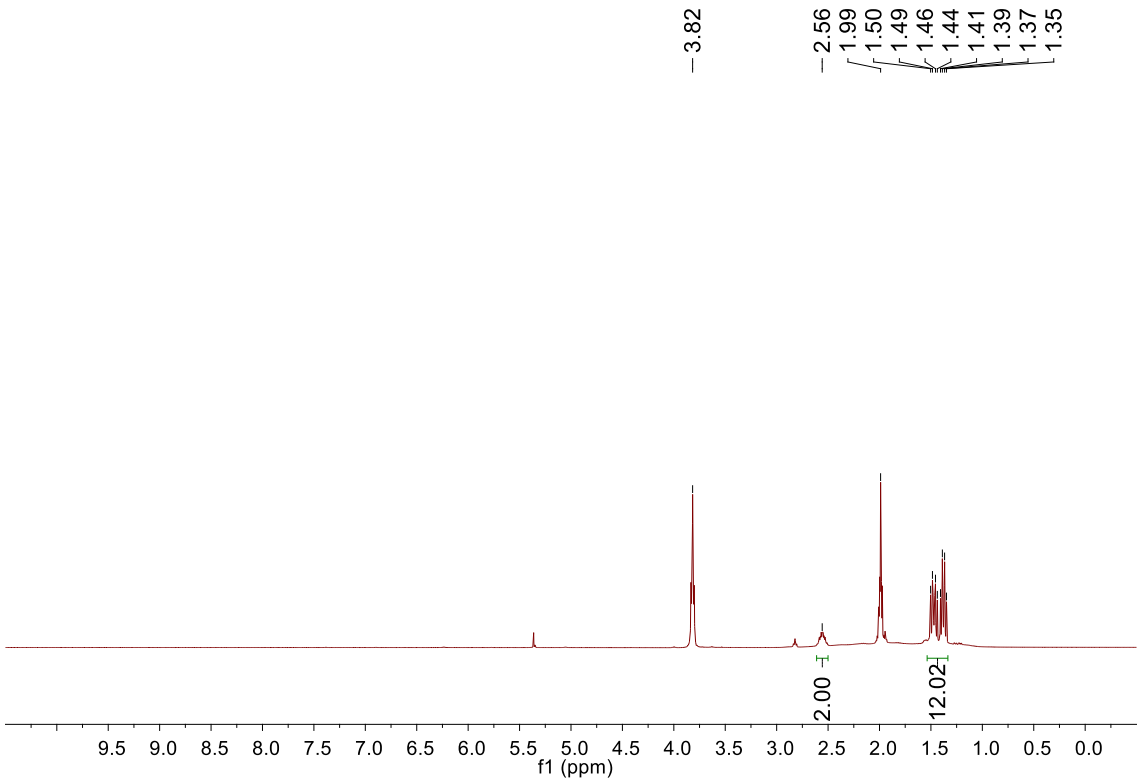

*Figure 28. ^{1}H NMR of **10** (300MHz, CD_2Cl_2, ^{11}B coupled, 25°C).*

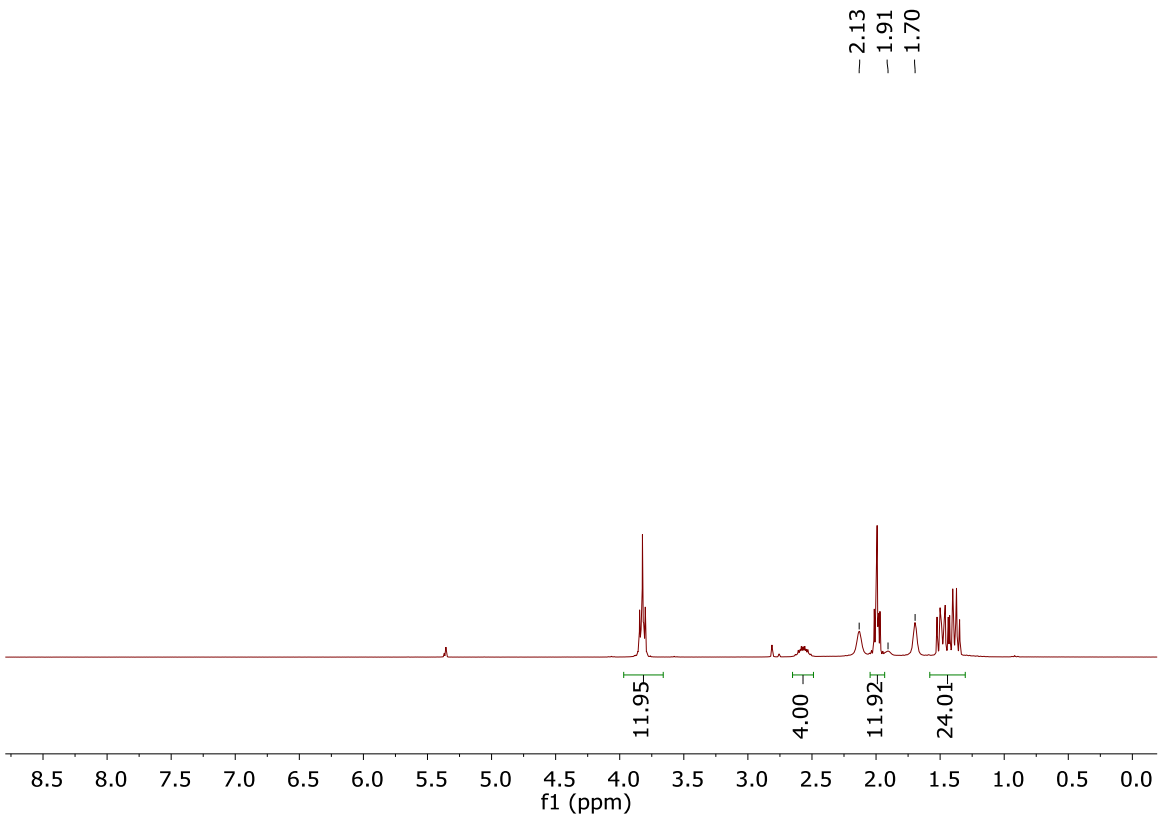

*Figure 29. $^{1}H\{^{11}B\}$ NMR of **10** (300MHz, CD_2Cl_2, 25°C).*

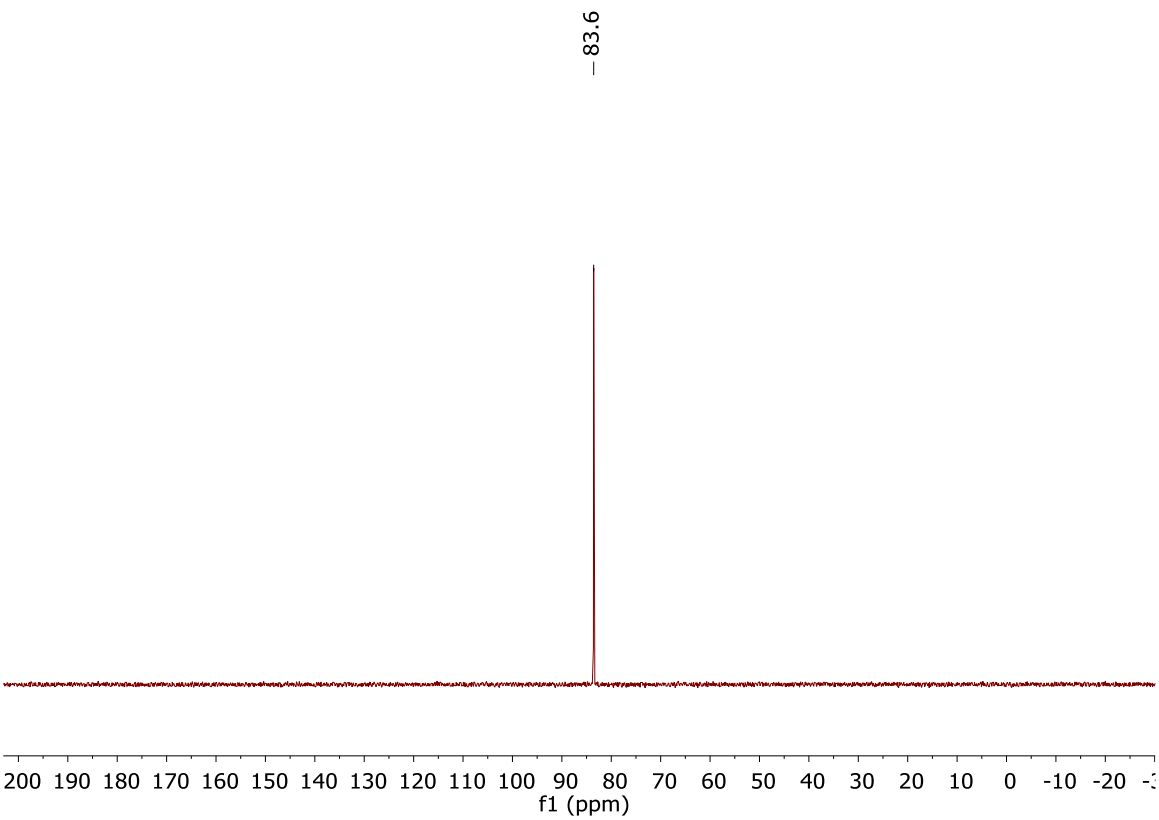

*Figure 30. $^{31}P\{^{1}H\}$ NMR of **10** (162MHz, CD_2Cl_2, 25°C).*

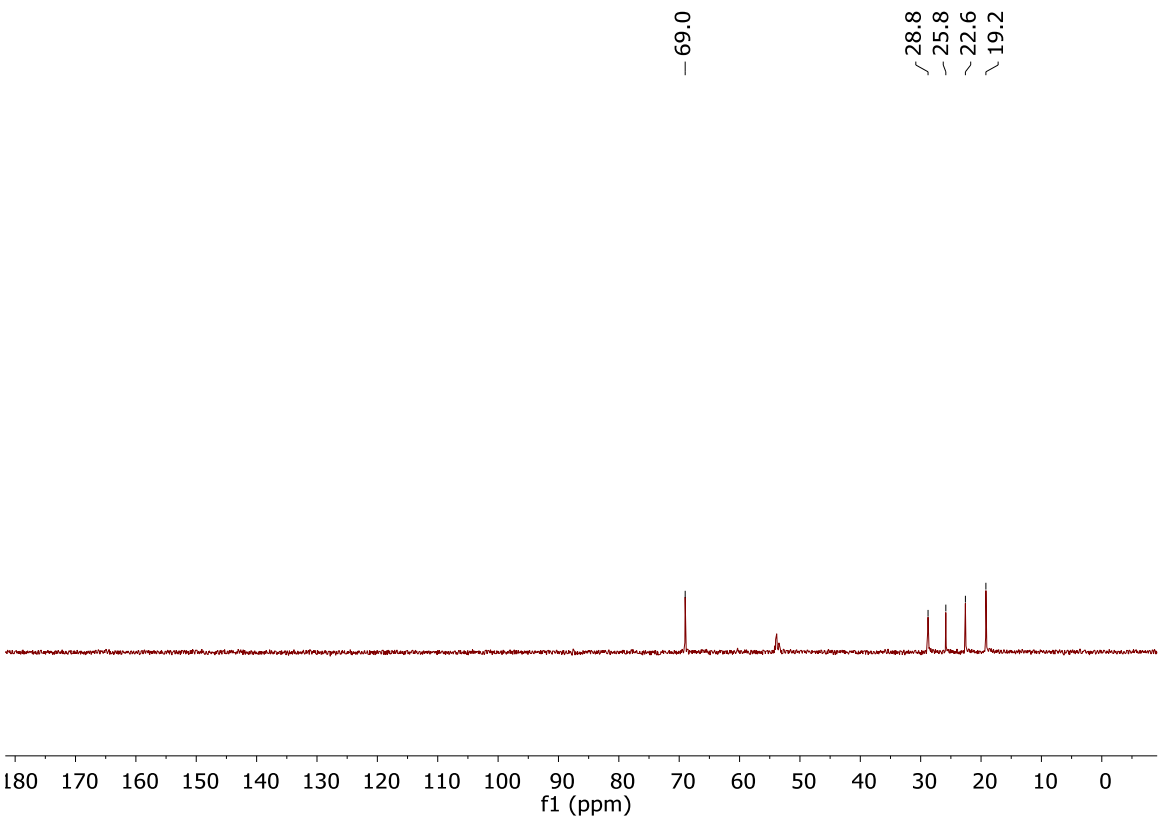

*Figure 31. ^{13}C NMR of **10** (101MHz, CD_2Cl_2, 25°C).*

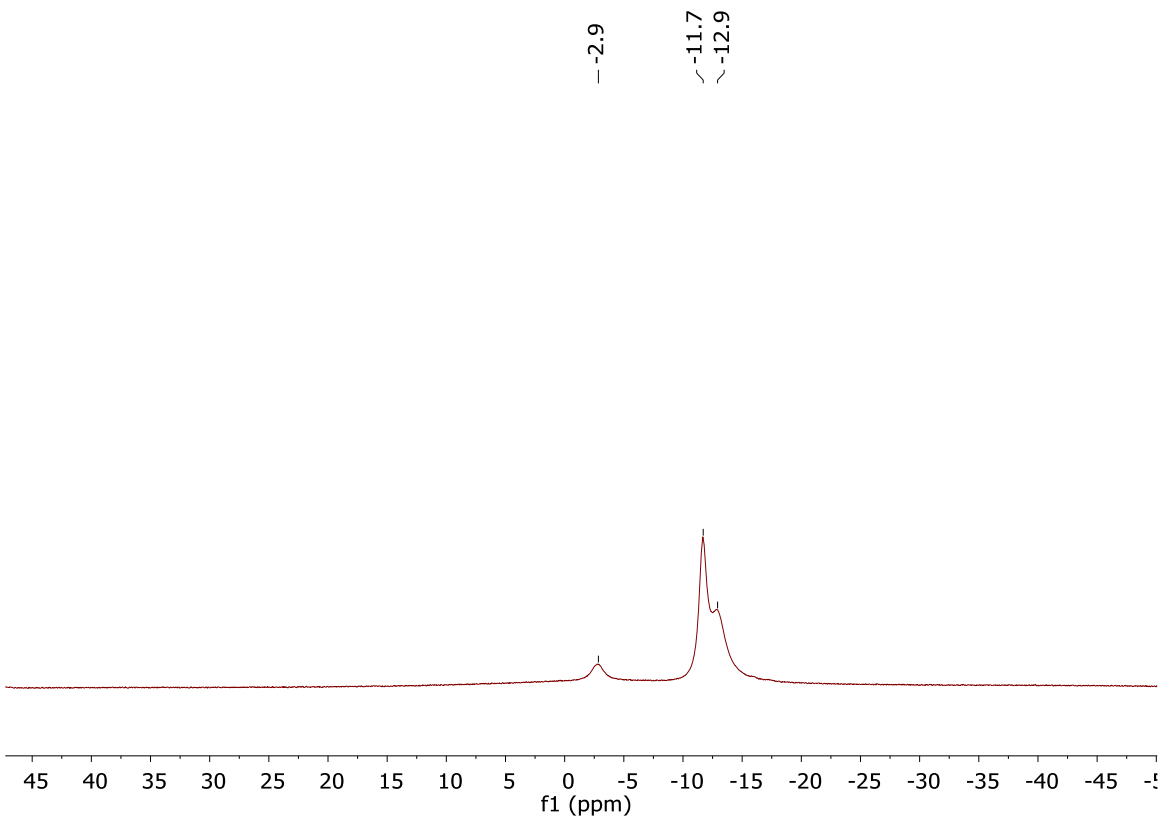

*Figure 32. $^{11}B\{^{1}H\}$ NMR of **10** (96MHz, CD_2Cl_2, 25°C).*

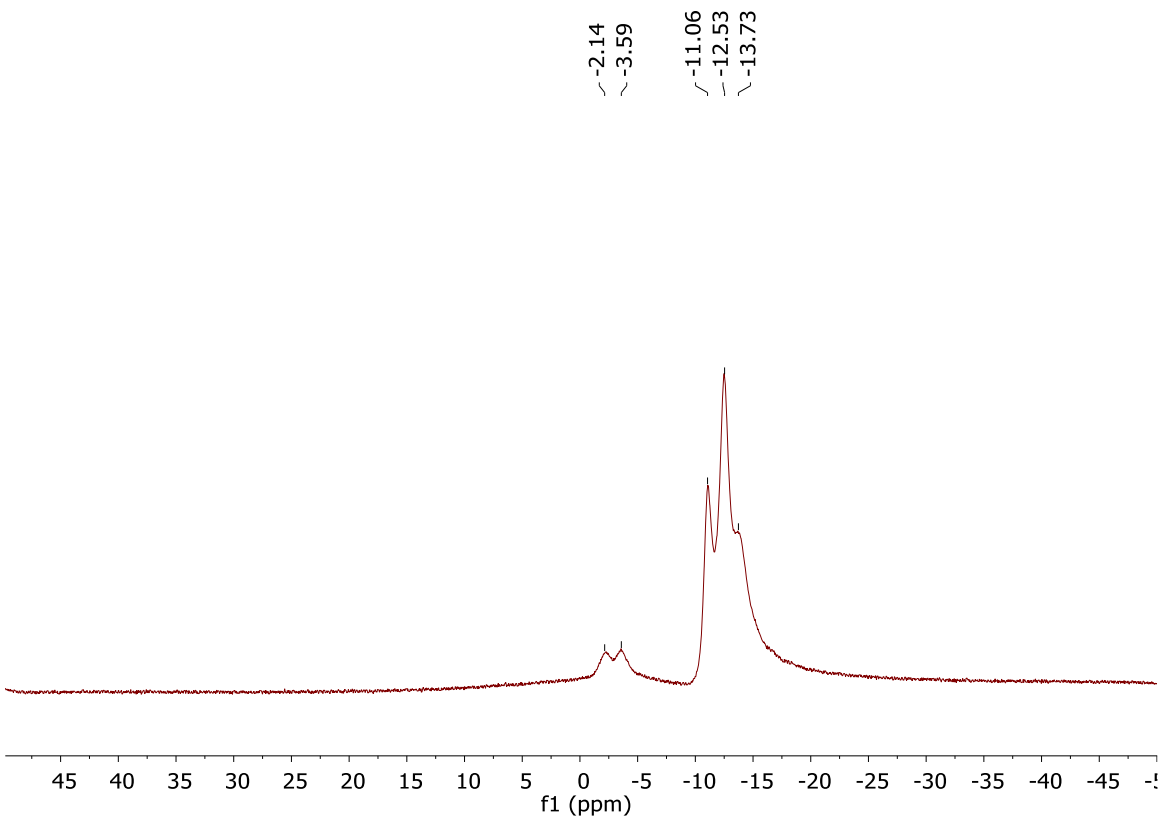

*Figure 33. ^{11}B NMR of **10** (96MHz, CD_2Cl_2, 25°C).*

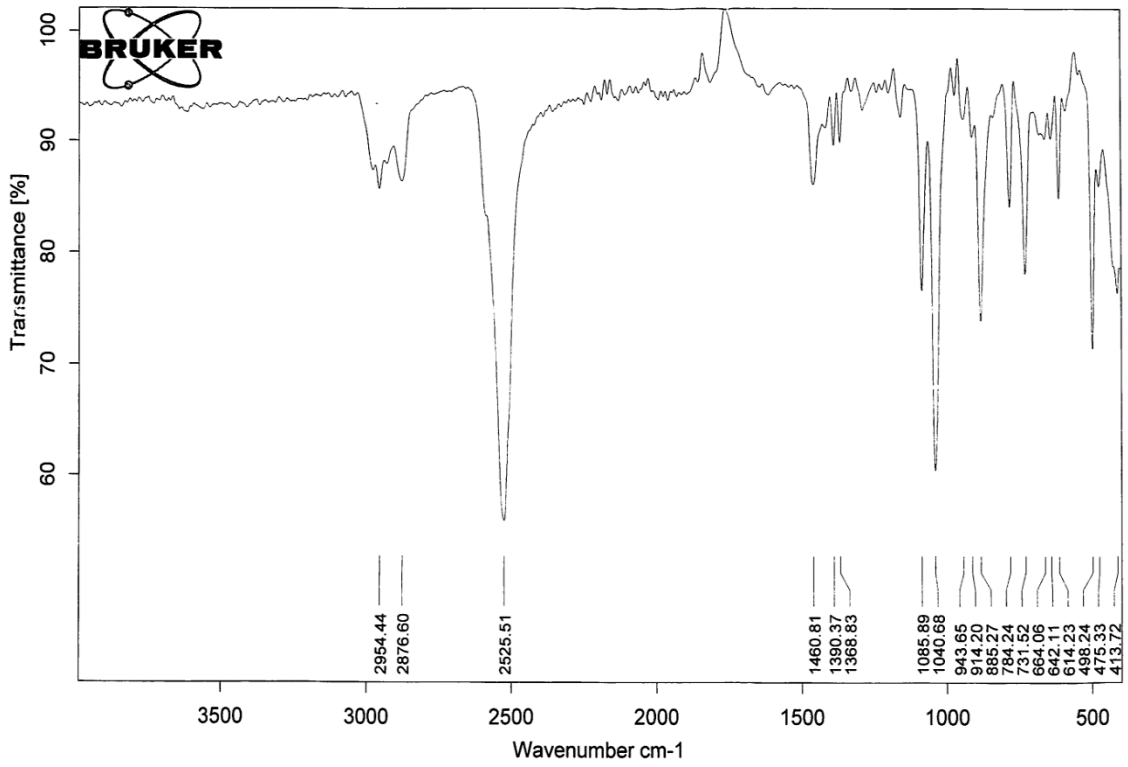

*Figure 34. IR spectrum of **10**. Showing the B-H stretches at 2525 cm^{-1}.*

General procedure for catalysis. A standard solution of catalyst **10** was prepared in CH_2Cl_2 and the desired amount of standard solution was immediately transferred via micropipette to screw capped (PTFE) vials. The CH_2Cl_2 was allowed to evaporate from the open vial in a heating block (50°C, 10min), and a stir bar was added. The neat amines and alkynes were then transferred via micropipette (or added directly if solid) to the screw capped vials, sealed and heated to the indicated temperature and stirred for the allotted times (Table 1, Main Text). Yields were calculated by integration of the ^1H NMR, via direct comparison of the imine formed to the amine consumed. The validity of this approach was confirmed by obtaining isolated yields of several compounds (entries **3**, **5**, **6**, **8**, and **10**). In these cases, the products were isolated by dissolving the catalytic mixture in pentane,

followed by filtration, and subsequent crystallization (entries **3**, **6**, **8**) of the solution at -25°C or by column chromatography (entry **5**) using pentane as eluent. Entries **4**[84], **7**[58], **9**[85], **11**[58], **12**[86], **13**[87], **14**[87] have been previously characterized.

Entry 3: (E)-N-(1-phenylethylidene)-aniline

^{1}H NMR (400MHz, $CDCl_3$, 25°C): δ= 7.98 (m, 2H, Ar), 7.50-7.43 (m, 3H, Ar), 7.38-7.33 (2H m), 7.12-7.06 (m, 1H Ar), 6.84-6.78 (m, 2H, Ar), 2.24 (s, 3H). ^{13}C NMR (100MHz, $CDCl_3$, 25°C): δ= 165.7, 152.1, 139.8, 130.8, 129.3, 128.7, 127.6, 123.6, 119.8, 17.7 ppm.

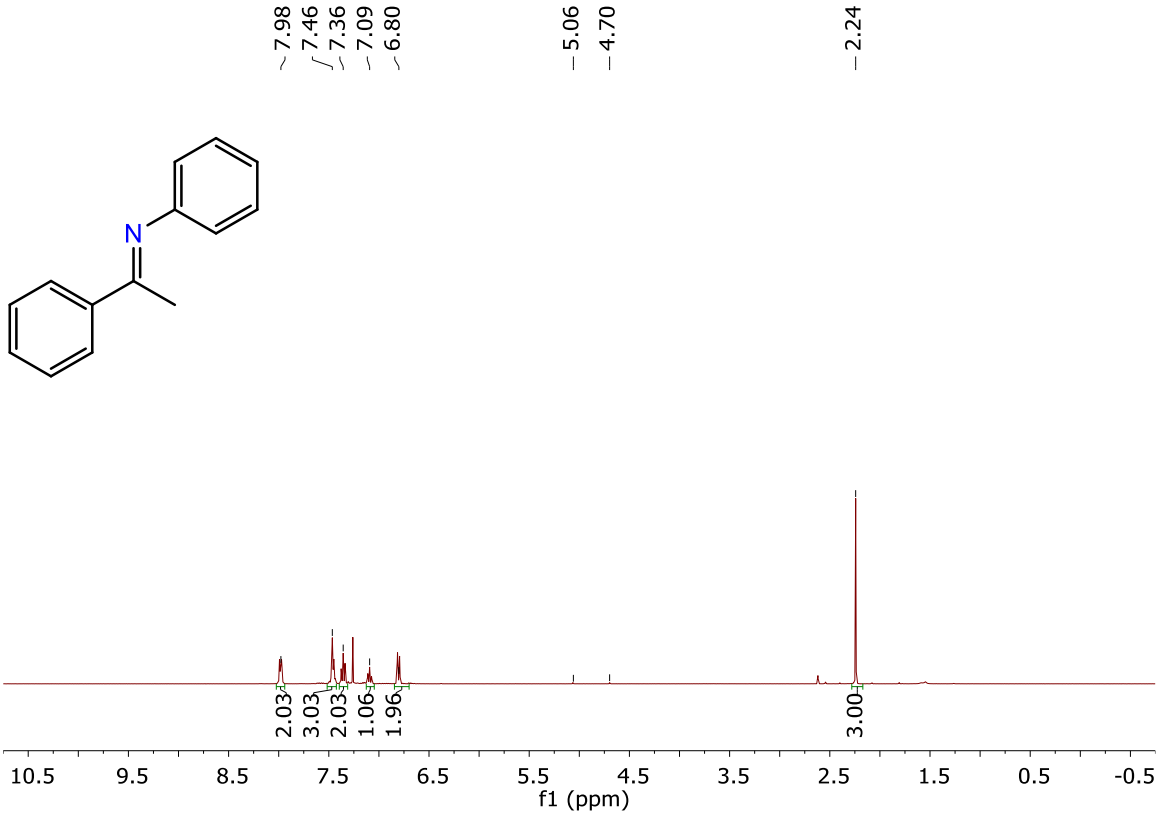

*Figure 35. ^{1}H NMR of **Entry 3** (400MHz, $CDCl_3$, 25°C).*

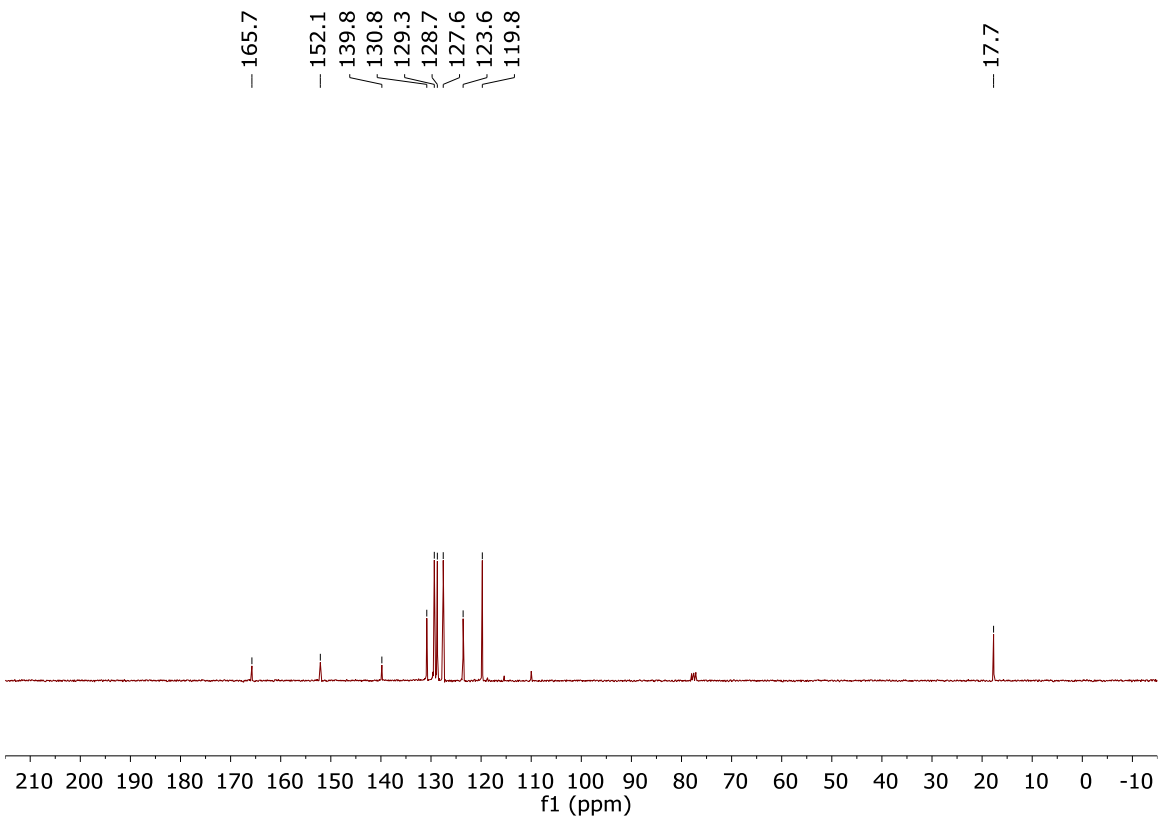

*Figure 36. ^{13}C NMR of **Entry 3** (101MHz, $CDCl_3$, 25°C).*

Entry 5: (E)-N-(1-phenylethylidene)-2,6-diisopropylaniline

^{1}H NMR (400MHz, $CDCl_3$, 25°C): δ= 8.10-8.02 (m, 2H, Ar), 7.54-7.47 (m, 3H, Ar), 7.19-7.15 (m, 2H, Ar), 7.13-7.07 (m, 1H Ar), 2.82-2.72 (m, 2H), 2.12 (s, 3H), 1.19-1.13 (m, 12H).

^{13}C NMR (100MHz, $CDCl_3$, 25°C): δ= 164.7, 146.7, 139.1, 136.0, 130.3, 128.4, 127.1, 123.2, 122.9, 28.2, 23.2, 22.9, 18.1 ppm.

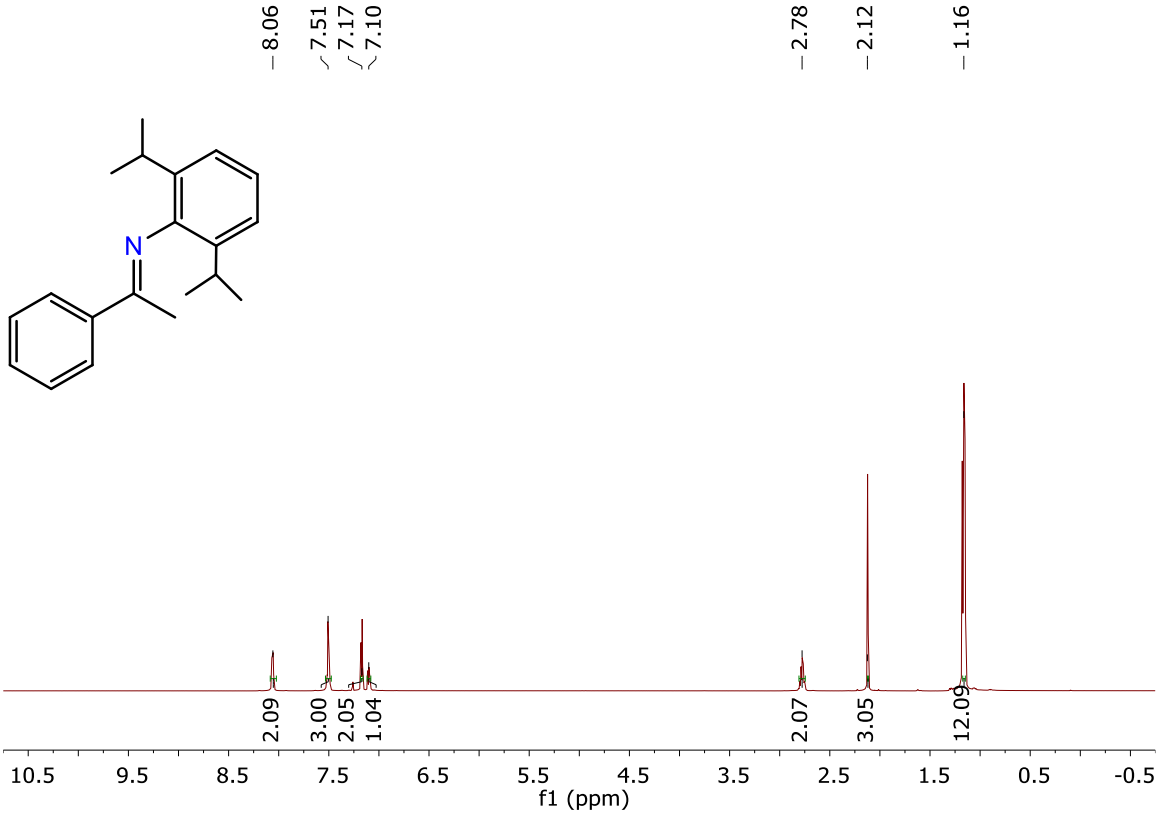

*Figure 37. ^{1}H NMR of **Entry 5** (400MHz, $CDCl_3$, 25°C).*

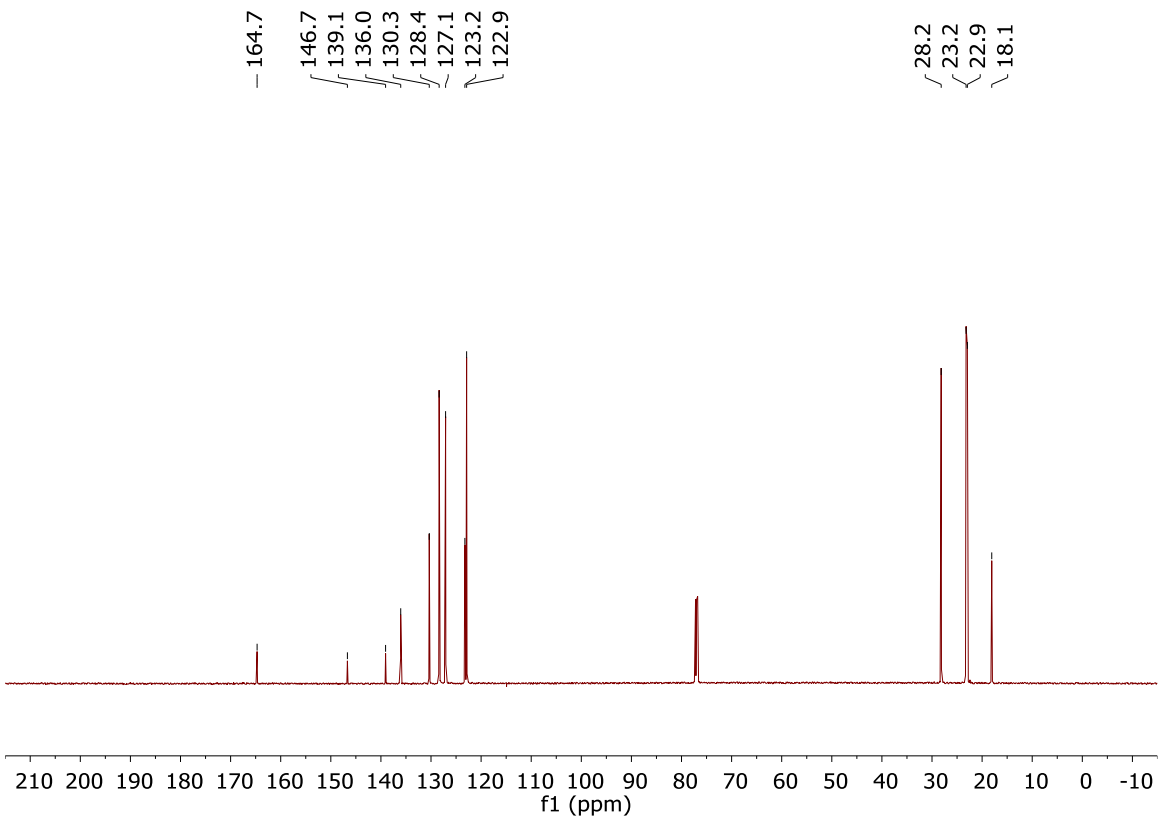

*Figure 38. ^{13}C NMR of **Entry 5** (101MHz, $CDCl_3$, 25°C).*

Entry 6: (E)-N-(1-(4-fluorophenyl)ethylidene)-aniline

^{1}H NMR (400MHz, $CDCl_3$, 25°C): δ= 8.09-8.00 (m, 2H, Ar), 7.46-7.38 (m, 2H, Ar), 7.21-7.13 (m, 3H, Ar), 6.82-6.76 (m, 2H Ar), 2.26 (s, 3H). ^{13}C NMR (100MHz, $CDCl_3$, 25°C): δ= 165.6, 164.1, 163.1, 151.6, 135.7, 129.4, 129.3, 129.1, 123.4, 119.5, 115.4, 115.2, 28.2, 17.3 ppm. ^{19}F NMR (376MHz, $CDCl_3$, 25°C): δ= -111.5 ppm.

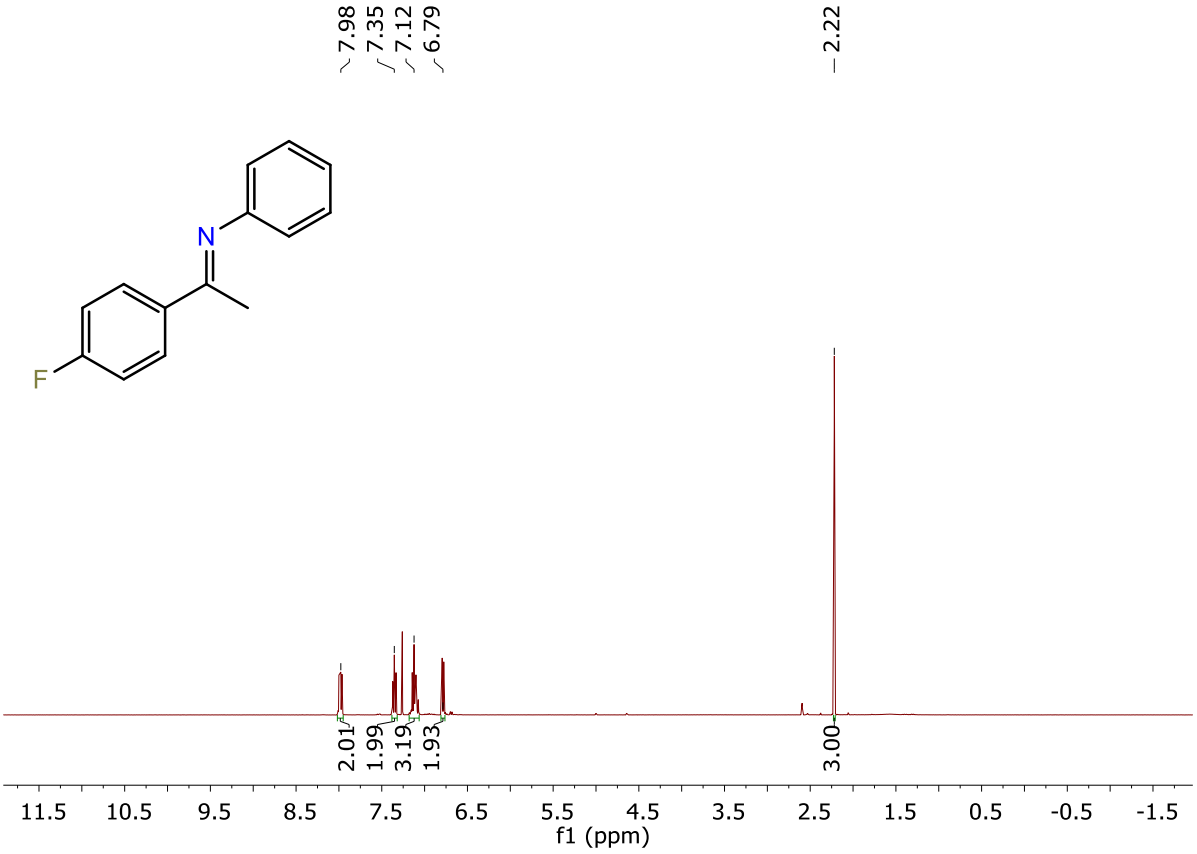

*Figure 39. ^{1}H NMR of **Entry 6** (400MHz, $CDCl_3$, 25°C).*

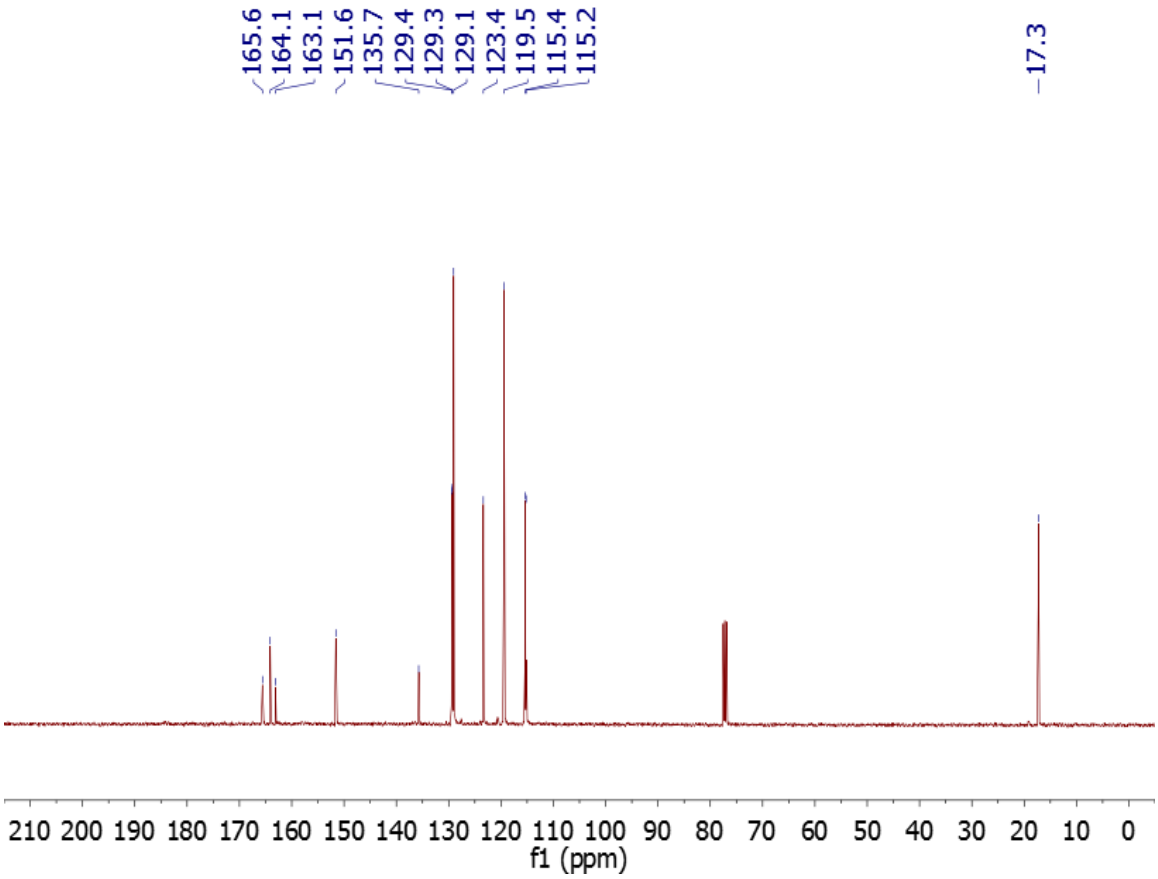

*Figure 40. ^{13}C NMR of **Entry 6** (100MHz, $CDCl_3$, 25°C).*

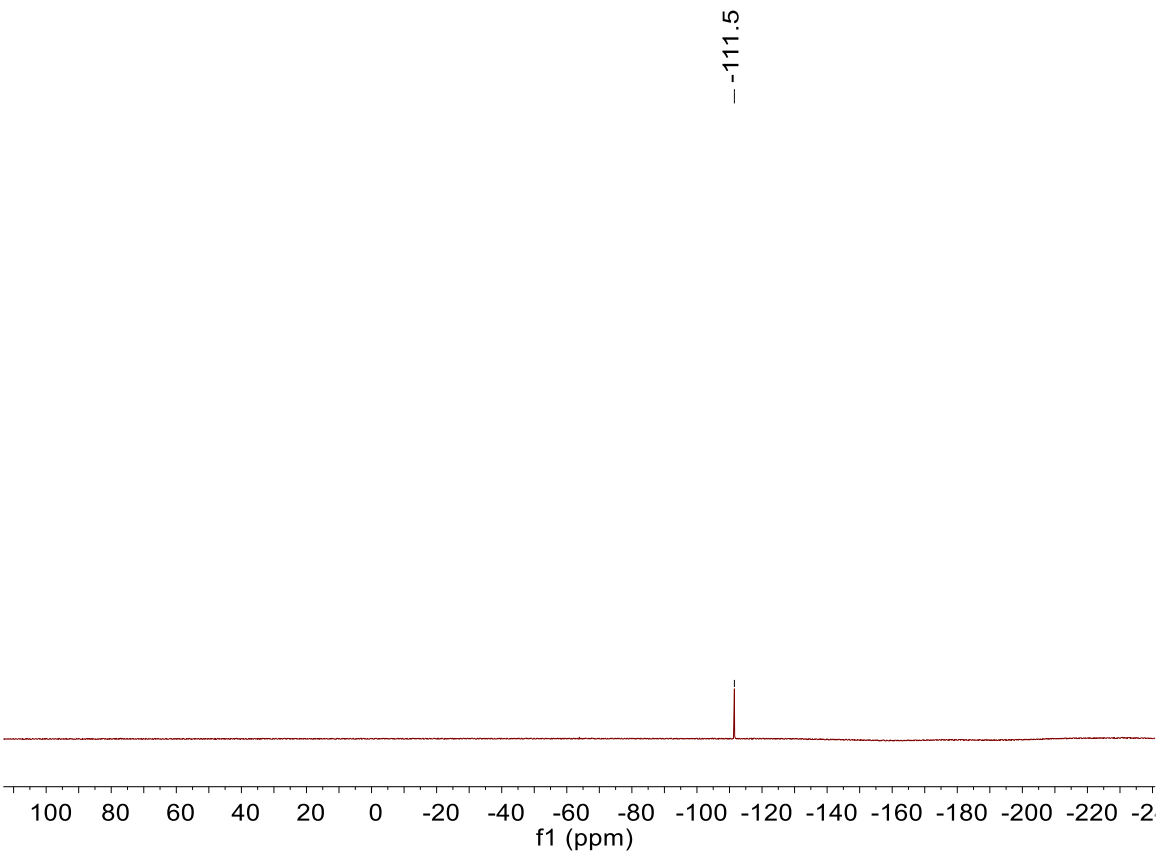

*Figure 41. ^{19}F NMR of **Entry 6** (376MHz, $CDCl_3$, 25°C).*

Entry 8: (E)-N-(1-(4-fluorophenyl)ethylidene)-2,6-diisopropylaniline

^{1}H NMR (400MHz, $CDCl_3$, 25°C): δ= 8.15-8.09 (m, 2H, Ar), 7.38-7.15 (m, 5H, Ar), 2.94-2.79 (m, 2H), 2.18 (s, 3H), 1.34-1.19 (s, 12H). ^{13}C NMR (100MHz, $CDCl_3$, 25°C): δ= 165.6, 163.5, 163.1, 146.6, 136.1, 135.3, 129.2, 123.5, 123.0, 115.5, 28.3, 23.3, 23.0, 18.0 ppm. ^{19}F NMR (376MHz, $CDCl_3$, 25°C): δ= -118.7 ppm.

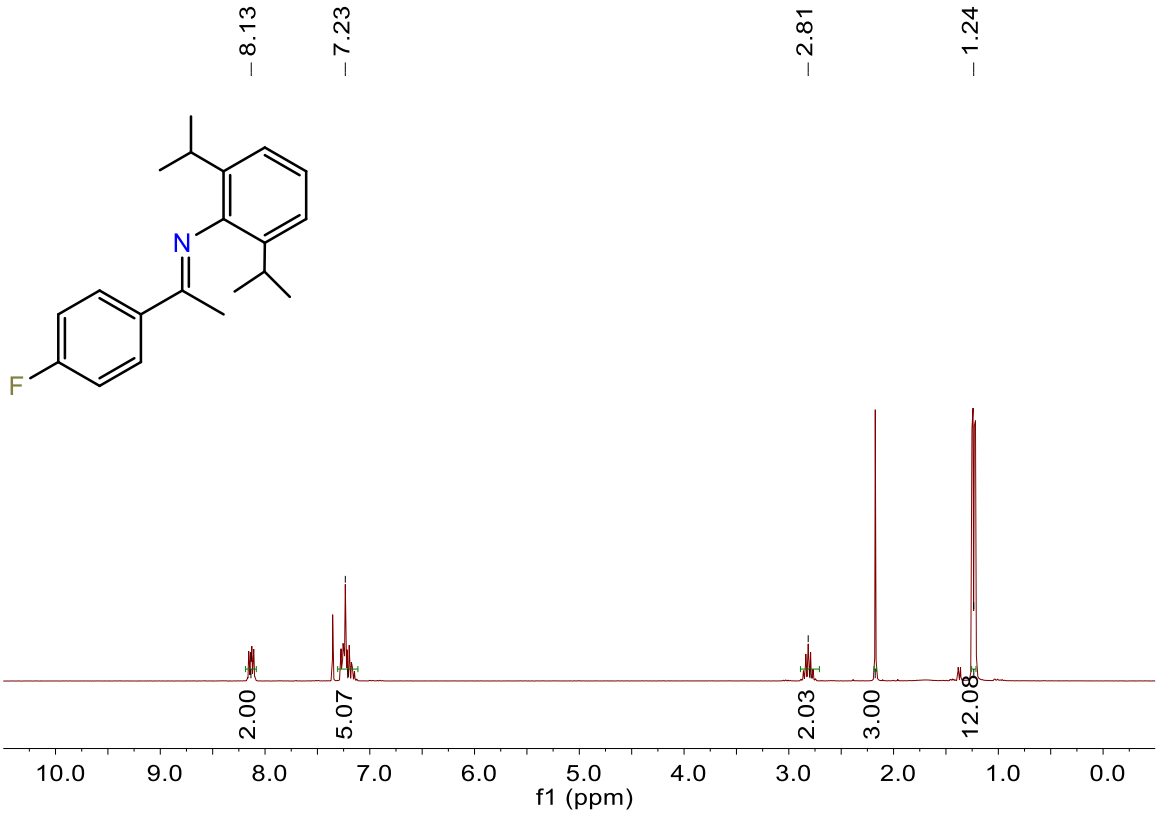

*Figure 42. ^{1}H NMR of **Entry 8** (400MHz, $CDCl_3$, 25°C).*

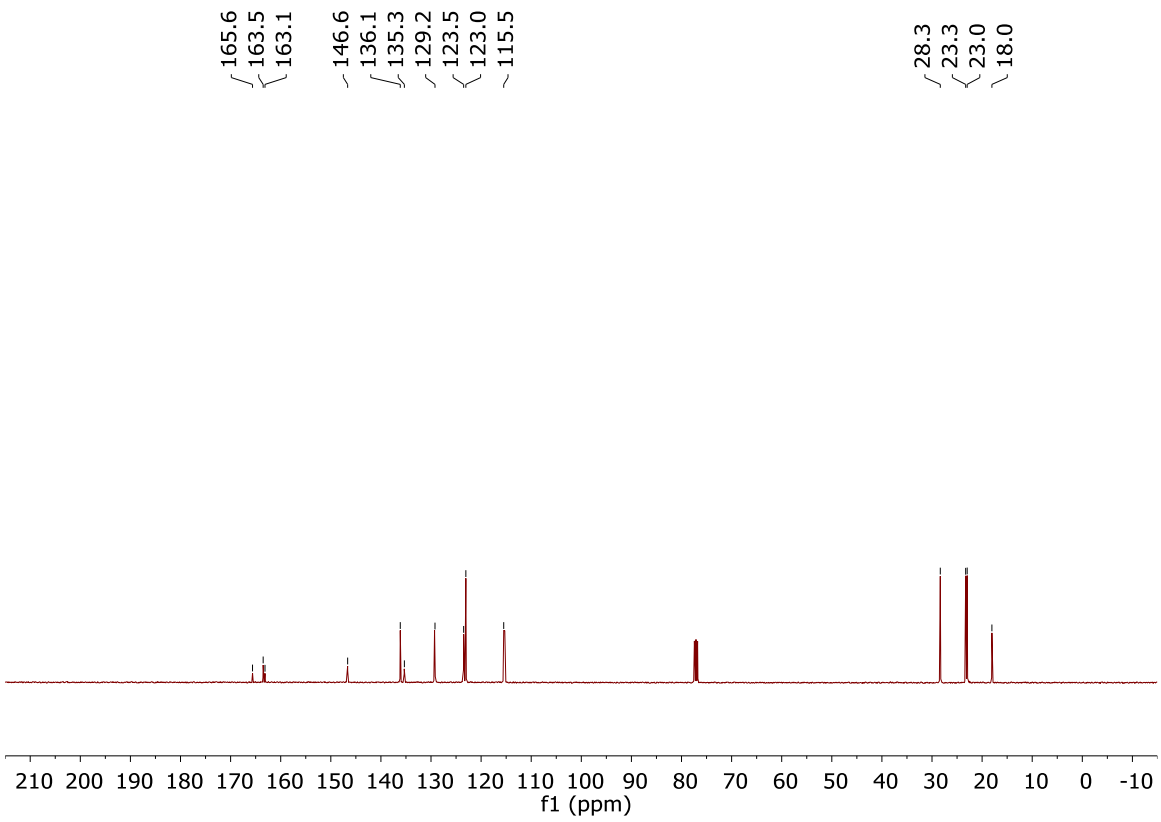

*Figure 43. ^{13}C NMR of **Entry 8** (101MHz, $CDCl_3$, 25°C).*

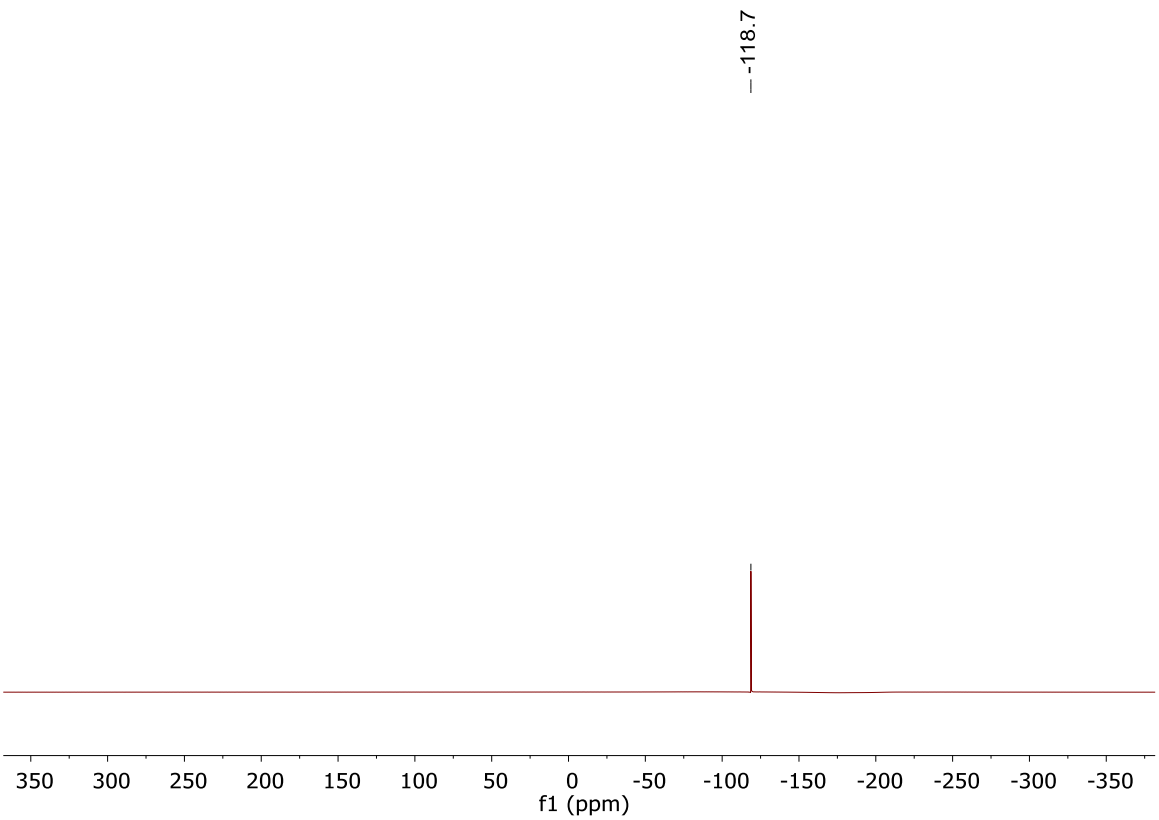

*Figure 44. ^{19}F NMR of **Entry 8** (396MHz, $CDCl_3$, 25°C).*

Entry 10: (E)-N-(1-(4-methoxyphenyl)ethylidene)-2,4,6-trimethylaniline

^{1}H NMR (400MHz, $CDCl_3$, 25°C): δ= 8.09-7.95 (m, 2H, Ar), 7.01-6.95 (m, 2H, Ar), 6.92-6.83 (m, 2H, Ar), 3.88 (s, 3H), 2.29 (s, 3H), 2.03 (s, 3H), 1.99 (s, 6H). ^{13}C NMR (100MHz, $CDCl_3$, 25°C): δ= 164.5, 161.5, 146.6, 132.0, 131.7, 128.7, 128.5, 125.8, 113.6, 55.4, 20.8, 18.0, 17.2 ppm.

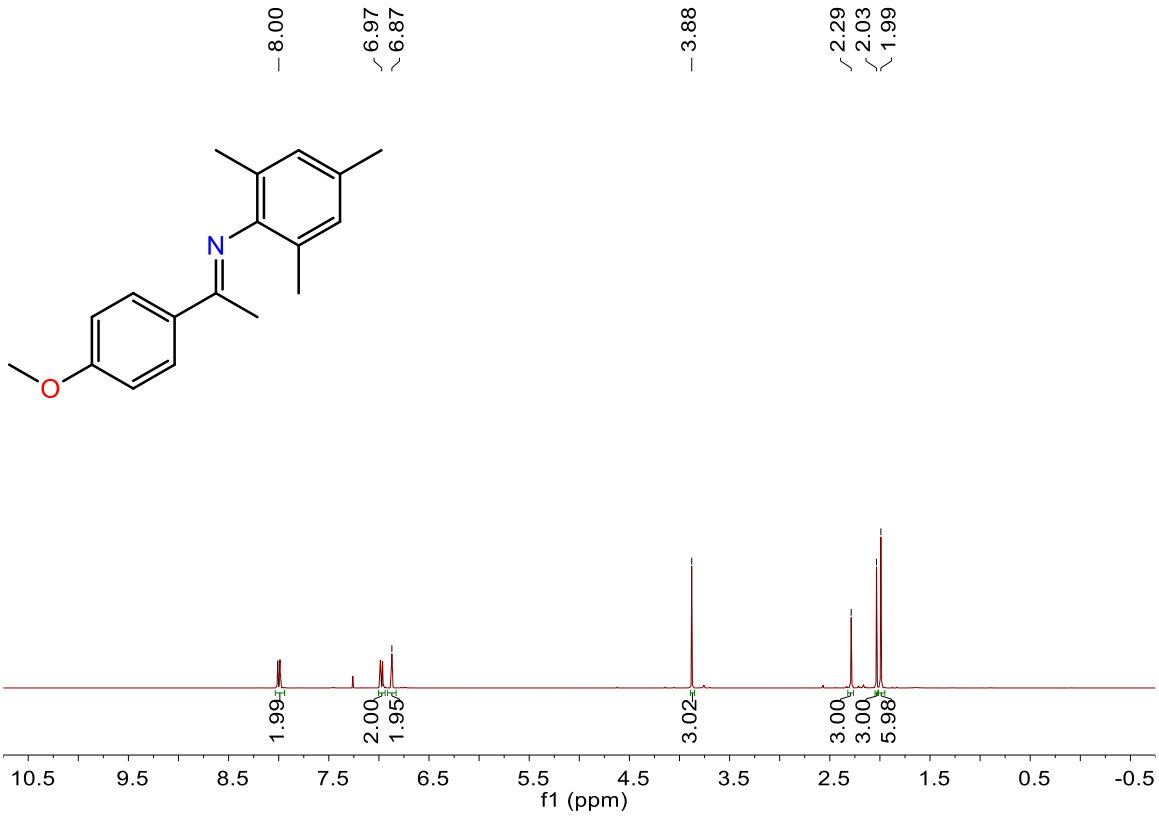

*Figure 45. ^{1}H NMR of **Entry 10** (400MHz, $CDCl_3$, 25°C).*

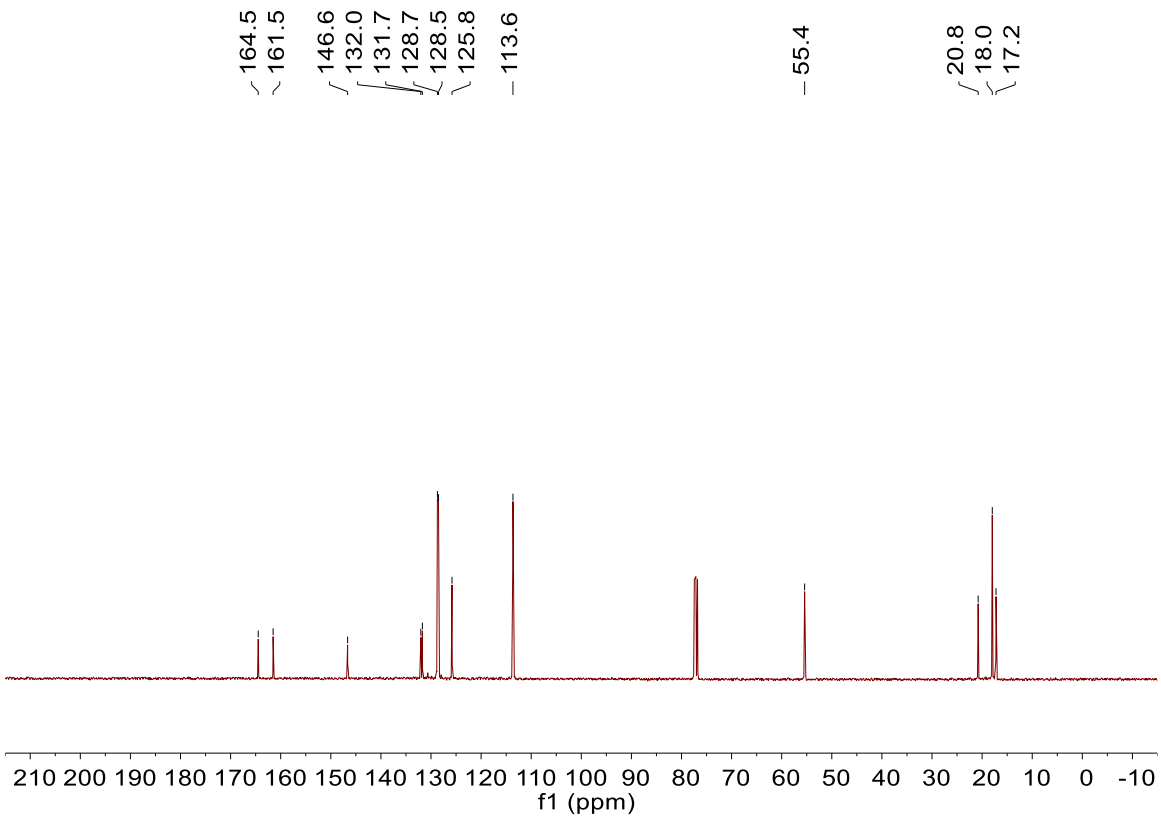

*Figure 46. ^{13}C NMR of **Entry 10** (101MHz, $CDCl_3$, 25°C).*

X-Ray Crystal Data for Compound **10**:

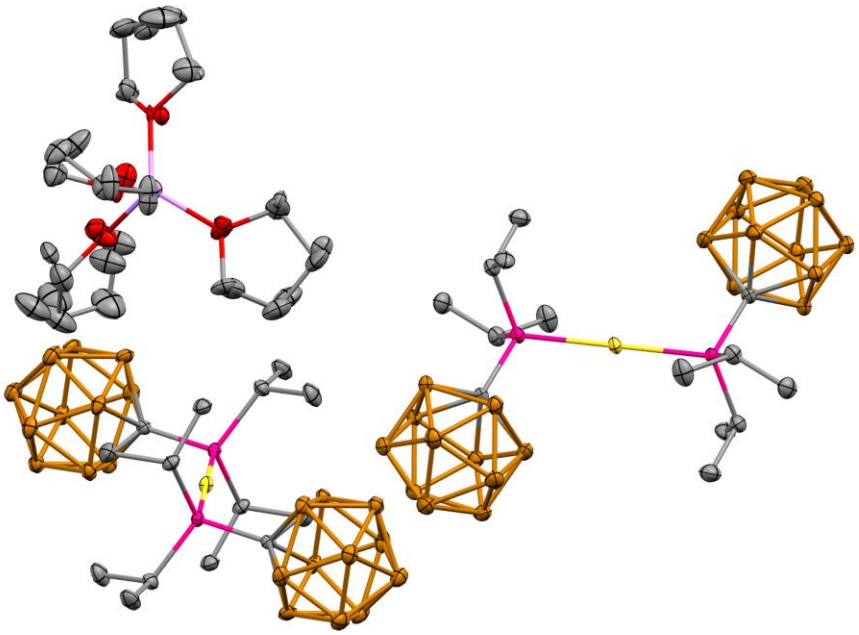

A colorless prism fragment (0.406 x 0.249 x 0.237 mm^3) was used for the single crystal x-ray diffraction study of $[C_{14}H_{50}B_{22}P_2Au]^-.[Li[C_4H_8O]_4]^+$. The crystal was coated with paraffin oil and mounted on to a cryo-loop glass fiber. X-ray intensity data were collected at 100(2) K on a Bruker APEX2[88] platform-CCD x-ray diffractometer system (fine focus Mo-radiation, λ = 0.71073 Å, 50KV/30mA power). The CCD detector was placed at a distance of 5.0600 cm from the crystal.

A total of 3600 frames were collected for a sphere of reflections (with scan width of 0.3° in ω, starting ω and 2σ angles of –30°, and Φ angles of 0°, 90°, 120°, 180°, 240° and 270° for every 600 frames, 10 sec/frame exposure time). The frames were integrated using the Bruker SAINT software package[89] and using a narrow-frame integration algorithm. Based on a monoclinic crystal system, the integrated frames yielded a total of 120686 reflections at a maximum 2σ angle of 61.016° (0.70 Å resolution), of which 15411

were independent reflections (R_{int} = 0.0316, R_{sig} = 0.0179, redundancy = 7.8, completeness = 100%) and 11376 (73.8%) reflections were greater than 2σ(I). The unit cell parameters were, **a** = 8.3143(6) Å, **b** = 24.9319(18) Å, **c** = 24.3529(17) Å, **σ** = 90.8613(11)°**,** V = 5047.6(6) Å^3, Z = 4, calculated density D_c = 1.330 g/cm^3. Absorption corrections were applied (absorption coefficient μ = 3.011 mm$^{-1;}$ max/min transmission = 0.536/0.374) to the raw intensity data using the SADABS program.[90]

The Bruker SHELXTL software package[91] was used for phase determination and structure refinement. The distribution of intensities (E^2-1 = 1.367) and systematic absent reflections indicated one possible space group, P2(1)/c. The space group P2(1)/c (#14) was later determined to be correct. Direct methods of phase determination followed by two Fourier cycles of refinement led to an electron density map from which most of the non-hydrogen atoms were identified in the asymmetric unit of the unit cell. With subsequent isotropic refinement, all of the non-hydrogen atoms were identified. There was one disordered cation of $[Li[C_4H_8O]_4]^+$ (the four disordered THF site occupancy ratios were 79%/21%, 69%/31%, 57%/43% and 51%/49%) and two half-anions of $[C_{14}H_{50}B_{22}P_2Au]^-$ present in the asymmetric unit of the unit cell. Both the anions were located at the inversion centers.

Atomic coordinates, isotropic and anisotropic displacement parameters of all the non-hydrogen atoms were refined by means of a full matrix least-squares procedure on F^2. The H-atoms were included in the refinement in calculated positions riding on the atoms to which they were attached. The refinement converged at R1 = 0.0297, wR2 = 0.0575, with intensity I>2σ (I). The largest peak/hole in the final difference map was 2.537/-0.887 e/Å^3. The high difference electron density peak/hole near the two Au-atoms are

probably due to absorption corrections and Fourier truncation errors.

Table 1. Crystal data and structure refinement for Compound **10**.

Identification code	vL321JK_0m	
Empirical formula	C30 H82 Au B22 Li O4 P2	
Formula weight	1010.62	
Temperature	100(2) K	
Wavelength	0.71073 Å	
Crystal system	Monoclinic	
Space group	P 21/c	
Unit cell dimensions	a = 8.3143(6) Å	α= 90°.
	b = 24.9319(18) Å	β= 90.8613(11)°.
	c = 24.3529(17) Å	γ= 90°.
Volume	5047.6(6) $Å^3$	
Z	4	
Density (calculated)	1.330 Mg/m^3	
Absorption coefficient	3.011 mm^{-1}	
F(000)	2064	
Crystal size	0.406 x 0.249 x 0.237 mm^3	
Theta range for data collection	1.634 to 30.508°.	
Index ranges	-11<=h<=11, -35<=k<=35, -34<=l<=34	
Reflections collected	120686	
Independent reflections	15411 [R(int) = 0.0316]	
Completeness to theta = 25.242°	100.0 %	

Absorption correction	Semi-empirical from equivalents
Refinement method	Full-matrix least-squares on F^2
Data / restraints / parameters	15411 / 754 / 718
Goodness-of-fit on F^2	1.184
Final R indices [I>2sigma(I)]	R1 = 0.0297, wR2 = 0.0575
R indices (all data)	R1 = 0.0445, wR2 = 0.0622
Extinction coefficient	n/a
Largest diff. peak and hole	2.537 and -0.887 e.$Å^{-3}$

Table 2. Atomic coordinates (x 10^4) and equivalent isotropic displacement parameters ($Å^2$x 10^3)

for Compound **10**. U(eq) is defined as one third of the trace of the orthogonalized U^{ij} tensor.

CHAPTER 4: A Study of a Series of Zwitterionic Ruthenium Complexes Bearing Perchlorinated *closo*-Carboranyl Phosphine Ligands

Introduction

Olefin metathesis was first developed in the 1960's by the Phillips Petroleum Company whose method was termed the *Triolefin Process*.[92] This process utilized tungsten oxide supported on silica to generate ethylene and 2-butenes from propylene.[92] This process evolved dramatically as a result of the work from Robert Grubbs, Yves Chauvin, and Richard Shrock with the development of metal-carbon double bonds, or carbenes, whose collective work won them a Nobel Prize in Chemistry in 2005. Specifically, the Grubbs group designed a Ru alkylidene catalyst supported by phosphine ligands which was able to catalyze various metathesis reactions with a robust functional group tolerance.[93,94]

In ruthenium catalyzed olefin metathesis, it is essential for high reaction turnover that the starting ruthenium complex to undergo a ligand substitution reaction where a coordinated phosphine disassociates followed by olefin substrate association to the new vacant cite to generate the active species.[95] Moreover, this substitution reaction was found to be a crucial step preceding the rate limiting formation of the metalocycle.[96,97] It was found that by having an electron donating phosphine, the ligand *trans* to that phosphine will more readily substitute for substrate.[97] Furthermore, in this same report, Grubbs *et. al*. uncovered that the more electron withdrawing Cl atom covalently bound to Ru was dramatically more activating than I, resulting from the stronger electronegativity from Cl. The conclusions made, therefore, were that the design of a competent Ru metathesis catalyst should include both electron deficiency and be coordinated with a strong donor

phosphine.

With these principles in mind, we postulated that ligating an anionic carboranyl phosphine with a lithium counter cation will not only bind to the Ru, but also undergo salt metathesis at the Ru center losing LiCl and giving a highly electron deficient, cationic Ru metal center. Indeed, this strategy had been utilized successfully with the perchlorinated carba-*closo*-dodecaborate phosphine in the gold catalyzed hydroamination of alkynes.[58] In this report, complexation of the carboranyl ligand produces a formally cationic metal center which enhances the metal's π-acidity, favoring substrate binding. Additionally, by utilizing a carboranyl phosphine whose strong *trans* effect should enhance ligand substitution for olefin substrate.[98]

Results and Discussion

In pursuit of a ruthenium carboranyl phosphine complex, **11**$[Li]^+$ can be made via a series of procedures developed by Ringstrand, Brellochs, Xie, and Lavallo.[99–102] Several modifications to these procedures have been made by our lab which are discussed in detail in the *Experimental* section. Though **4** is already a weakly coordinating anion, it can be advantageous to enhance this weakly coordinating property by substituting the B-H bonds with halogens, namely, Cl. This can be achieved using rather hazardous chemicals and conditions. Iodine monochloride in triflic acid are heated along with **4**$[Cs]^+$ to 200°C in an acid digestion vessel for several days.[101] Then, this product can be converted into ligand **11**$[Li]^+$ using the procedure developed by Reed, as shown in Figure 3.

With ligand **11**$[Li]^+$ in hand, it was possible to achieve the desired ruthenium complex through salt metathesis of **11**$[Li]^+$ and a ruthenium starting material. We first attempted to complex **11** to η^6-benzeneruthenium(II) dichloride dimer and precipitate LiCl

directly. However, this route was unsuccessful showing no reactivity. Therefore, we attempted to use an already cationic Ru starting material, $[(\eta^6\text{-}C_6H_6)Ru(CH_3CN)_2Cl]^+[BF_4]^-$ which can be synthesized from a known procedure.[103] Gratuitously, mixing $[(\eta^6\text{-}C_6H_6)Ru(CH_3CN)_2Cl]^+[BF_4]^-$ with **11**$[Li]^+$ in fluorobenzene at room temperature for 30 minutes produces complex **12**, as shown in Figure 58. Upon reaction, the yellow starting material turns to a deep red slurry which is filtered and washed with diethyl ether to remove $[Li]^+[BF_4]^-$. The resulting red powder is then extracted with copious amounts of dichloromethane to yield spectroscopically pure product **12**. It is noteworthy that **12** is only slightly soluble in dichloromethane and is completely soluble in THF. However, it slowly decomposes into a mixture of products immediately upon dissolution in THF. Interestingly, **12** reverts back to **11** with $[(\eta^6\text{-}C_6H_6)Ru(CH_3CN)_2Cl]^+$ as the counter cation when in acetonitrile. **12** is not soluble in any other solvent.

Nuclear magnetic resonance studies confirm the structure of **12**. Taken in dichloromethane-d_2, the coordinated benzene is seen at 6.13ppm, far upfield from free benzene, suggesting strong π-back donation from the ruthenium center. Additionally, the methyne multiplet from the isopropyl groups on the phosphine appears at 4.05ppm. The corresponding methyl groups appear as four sets of doublets, with two pairs partially overlapping, seen farther upfield ranging from 2.07-1.50ppm. Both of these resonances differ dramatically from free ligand. Furthermore, no acetonitrile from the starting ruthenium complex is observed which suggests that **11** has fully decoordinated

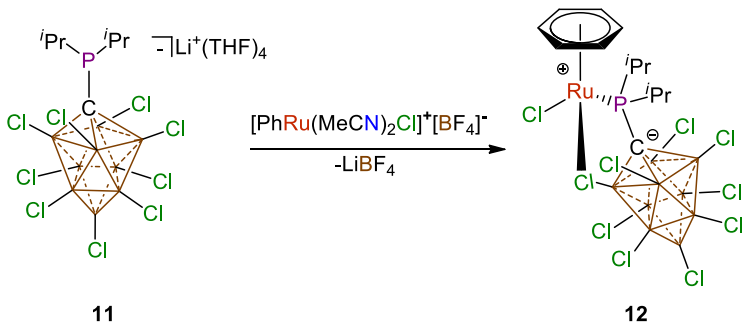

*Figure 47. Synthesis of complex **12**.*

those ligands and taken their place. The $^{31}P\{^{1}H\}$ NMR also shows a dramatic change. Free **11** in dichloromethane-d_2 has a singlet resonance at 45.6ppm while **12** is far downfield at 96.2ppm. In the $^{11}B\{^{1}H\}$ NMR, it can be seen that the local C_{4v} symmetry of the boron cluster is no longer observed where the antipodal peak lies at 24.0ppm and the remaining peaks ranging from -0.9 to -8.1ppm. This is quite unlike many other similar carboranyl phosphine complexes.[54,58,102] The data suggest two possible phenomena: 1) that the cluster has been chemically altered such that the symmetry is now changed or 2) that one of the chlorine atoms from the cluster is strongly ligated to the Ru center inhibiting free rotation about the P-C bond which is observed on the NMR timescale at room temperature. To test which phenomenon is occurring, a ^{11}B-^{11}B COSY experiment was carried out. Here, we see correlation peaks from the antipodal boron with all the remaining peaks meaning all boron atoms are connected in one species (Fig 56, *Experimental*). This data demonstrates that the cluster integrity still holds, proving that the loss of the C_{4v} is a result of the strong ligation from the B-Cl to the Ru center. Next, we became interested in probing the strength of this cluster Cl-Ru interaction. To do so, VT NMR was used to observe the change in cluster symmetry by increasing the temperature in an attempt to break that Ru-$Cl_{cluster}$ interaction. Due to the low boiling point of dichloromethane, dichloroethane was used in this experiment. Strangely enough, the symmetry of the boron cluster was never restored. In fact, complex decomposition was observed by the emergence of free ligand appearing upon heating to 80^{o}C which persisted even when cooled to room temperature. This suggests an extremely strong Ru-$Cl_{cluster}$ interaction.

Next, we sought to study this complex by X-ray diffraction. A single crystal was grown from slow diffusion of pentane into a solution of dichloromethane containing **12**. The structure can be seen in Figure 48 which unambiguously confirms **12** in a "piano stool" geometry. Additionally, this proves that the cluster had not undergone cyclometallation of a B-Cl vertex. At the Ru center, a benzene ring is coordinated in a η^6 fashion with average C-Ru bond lengths at 2.203Å which is slightly longer than the bond length in the cationic Ru starting material (2.178Å).[103] This is a result of the ligated phosphine producing a *trans* influence which, in turn, elongates the Ru-benzene ligand bond. The Ru-P distance is 2.4073(5)Å which is within the typical range for Ru-P distances. The Ru-Cl(1) bond is 2.3794(5)Å; also not atypical. The Ru-Cl(2) distance is 2.4631(5)Å which is substantially longer than the covalent Ru-Cl bond length, unsurprisingly. This interaction between Cl(2) and Ru elongates the B-Cl bond slightly (1.788(2)Å) from the average B-Cl length of 1.768Å. The Ru-P-C-B-Cl chelate forms a planar envelope conformation.

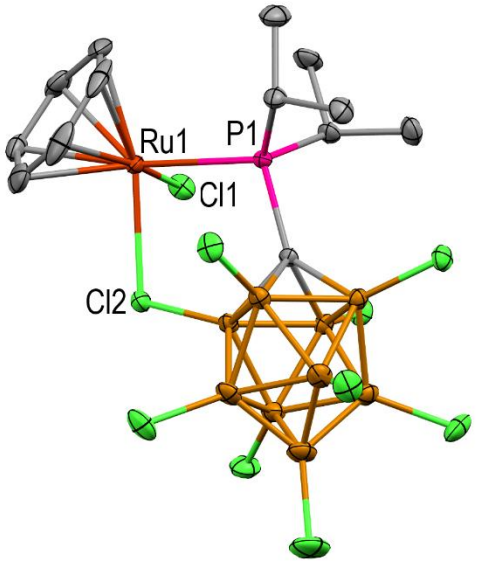

*Figure 48. Crystal structure of **12**.*

Next, we were interested in the reactivity of **12**, specifically towards reagents that might produce alkylidenes, vinylidenes, and allenylidenes with the hope of generating a catalyst capable of performing metathesis. To this end, our first reagent was the commercially available ethyl diazoacetate. Upon reaction of **12** with ethyl diazoacetate at room temperature in dichloromethane, rapid evolution of N_2 gas is observed. Inspection of the ^{1}H NMR shows mixtures of diethyl fumarate and diethyl maleate, as well as some

complex decomposition. $^{31}P\{^{1}H\}$ and $^{11}B\{^{1}H\}$ NMR also show a mixture of unreacted **12** and free ligand **11**$[Li]^+$. Several other diazo reagents were tested yielding only their dimerized organic products. Phenyldiazomethane, diphenyldiazomethane, trimethylsilyldiazomethane, and 2-diazo-1,1,1-trifluoroethane were all used with no success. Several alkynes were also probed with the intention of generating vinylidenes. Phenylacetylene was first attempted with simply no reaction taking place. In the hopes of having a more electron rich alkyne promoting the desired reaction, 4-methoxyphenyl acetylene was also mixed with **12**. While some reactivity was observed, this reactivity only produced small amounts of decomposition. 4-fluorophenyl acetylene was also used with no desirable effect. Since the previous three alkynes used require a hydride migration to form the desired vinylidene[104], silyl functionalities were also attempted with no success. Unfettered with the stubbornness of **12**'s ability to form the desired carbenes, allenylidenes were thought to be good candidates for forming Ru-C double bonds. Work by Dixneuf showed that several complexes similar to **12** showed success in forming Ru allenylidenes.[105–111] Reacting **12** with a series of propargyl alcohols to generate that allenylidene proved to be futile. No reaction took place across all alcohols attempted (2-methyl-3-butyn-2-ol, 1,1-diphenyl-2-propyn-1-ol, and 2-propyn-1-ol).

In an interesting discovery, if **11**$[Li]^+$ is left to react with $[(\eta^6\text{-}C_6H_6)Ru(CH_3CN)_2Cl]^+[BF_4]^-$ over a 24 hour period in the presence of a drop of acetonitrile, a new complex is formed **13**, shown in Figure 49. Under these conditions, the coordinated benzene

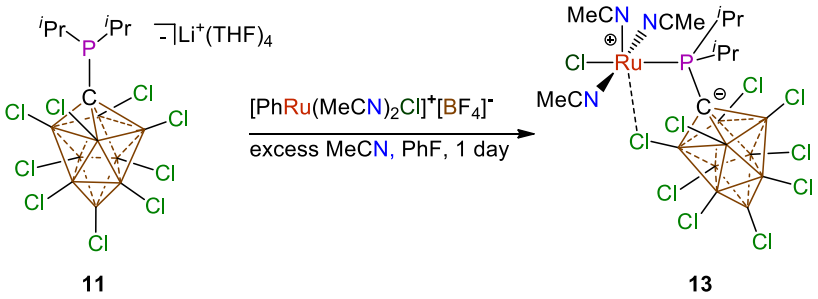

*Figure 49. Synthesis of complex **13**.*

becomes displaced by acetonitrile. This reaction is evidenced by a color change to a light orange slurry. This is substantially different from the formation of **12** which produces a dark red slurry. **13** proved to be even less soluble than **12** showing to be soluble in only acetonitrile and DMSO. However, unlike in **12**, the carboranyl ligand is not decoordinated by acetonitrile in **13**.

Multinuclear NMR studies of **13** were carried out. In the ^{1}H NMR in acetonitrile-d_3, the ^{i}Pr groups can be easily seen as the methyne multiplet at 3.63ppm. This is an upfield shift from complex **12**. The methyl groups appear as two sets of doublets of doublets ranging from 1.67-1.1.37ppm. This range is shortened from the methyl group doublets in **12**. Furthermore, the coordinated benzene peak is now gone. In the $^{11}B\{^{1}H\}$ NMR, again, we see destruction of the C_{4v} symmetry within the boron cluster. Though the $^{11}B\{^{1}H\}$ NMR spectrum for **13** closely resembles that of **12**, close inspection shows that they are indeed different. The most downfield singlet is around 23.3ppm. The remaining resonances in the spectrum lie within the range of 0.3 to -7.2ppm, which again, is similar to complex **12**. The $^{3}1P\{^{1}H\}$ NMR shows an even further downfield singlet at 117.0ppm.

Single crystal X-ray diffraction studies were carried out on **13**. The structure can be seen in Figure 50, *vida infra*. Here, we can unambiguously see that the cluster remains intact. The Ru-Cl(2) is a strong interaction that can be observed at room temperature in the NMR timeframe, as in **12**. The Ru center has its ligands arranged in an octahedral geometry with the three acetonitrile ligands having an average Ru-N distance of 2.009Å. An

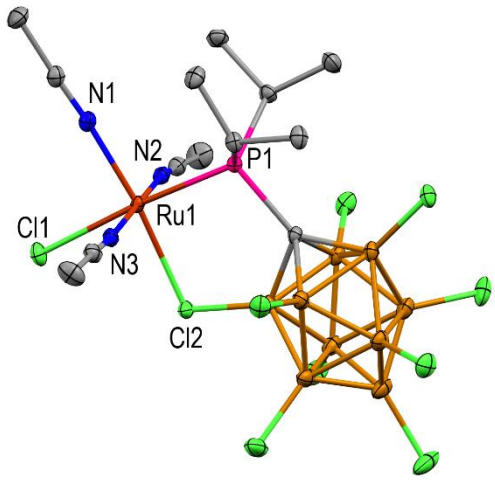

*Figure 50. Crystal structure of Complex **13**.*

interesting observation is that the Ru-Cl(2) distance (2.403Å) is indeed shorter than the covalent Ru-Cl(1) distance (2.450Å). This is probably a result of the increased electrophilicity at Ru with the exchange of the benzene ligand, a worse π-acceptor, than the three acetonitrile ligands. This effect contracts the Ru-Cl(2) bond. The elongation of the Ru-Cl(1) bond is also a result of the strong *trans* influence from the phosphine. This strong Ru-Cl(2) interaction elongates the B-Cl bond to 1.792Å as compared to the B-Cl average (1.772Å). Lastly, the Ru-P bond distance is 2.306Å which is slightly shorter than in **12**. The Ru-P-C-B-Cl chelate forms a planar envelope conformation. No reactivity was investigated with this complex.

With the significant problems of solubility associated with complexes **12** and **13**, it was thought that perhaps by having larger aliphatic substituents on the phosphorus atom, this might enhance solubility of the resulting complex. Thus, complex **15** was produced with the same procedure as in complex **12** using cyclohexyl groups, as shown in Figure 51. As in the synthesis of **12**, by simple mixing of **15** and $[(\eta^6\text{-}C_6H_6)Ru(CH_3CN)_2Cl]^+[BF_4]^-$ in fluorobenzene produces a dark red slurry within thirty minutes at room temperature. Filtration and several washes of diethyl ether, followed by an extraction with copious amounts of dichloromethane, produce clean **15**. Unfortunately, it was obvious from the beginning of the extraction step that **15** proved to be just as insoluble as the previous Ru complexes and thus no reactivity was investigated.

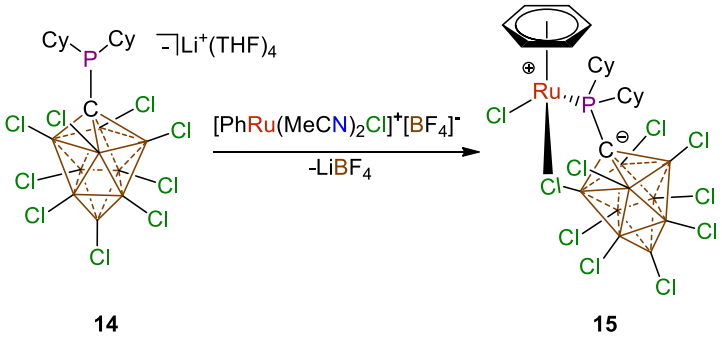

*Figure 51. Synthesis of Complex **15** from Ligand **14**.*

With **15** in hand, multinuclear NMR studies were carried out. In the ^1H NMR, the

cyclohexyl groups can be clearly seen evidenced by several multiplets at 3.60ppm, 2.74ppm, and a range from 2.19-1.15ppm. Furthermore, the ligated η^6-benzene falls at 6.05ppm, slightly more upfield from **12**. In the $^{11}B\{^1H\}$ NMR, again, we see disruption of the C_{4v} of the cluster, likely a result of the strong Ru-Cl interactions similar to what was discussed previously. The most downfield peak lies at 24.2ppm and the remaining cluster of peaks are within the range -0.9 through -8.1ppm. Lastly, the $^{31}P\{^1H\}$ NMR shows a dramatic shift downfield to 90.4ppm when compared to free ligand **14** at 30.0ppm.

Next, a single crystal was grown for X-ray diffraction analysis. The structure can be seen in Figure 63, *vida infra*. It can be seen that as in **12** and **13**, complex **15** retains its cluster constitution, despite the loss of its local C_{4v} symmetry seen in the $^{11}B\{^1H\}$ NMR. The Ru-Cl(2) distance is 2.4471(8)Å which is slightly longer than the covalent Ru-Cl(1) (2.3764(8)Å). This interaction elongates the B-Cl bond to 1.789(3)Å which is only slightly longer than the average of the uncoordinated B-Cl of 1.761Å. This elongation is comparable to compounds **12** and **13**. The Ru-P distance is 2.4211(8)Å which is typical for Ru-P bond distances. The benzene distance is measured as the average of the Ru-C bonds which equates to 2.192(3)Å which is slightly shorter than compound **12**, but still comparable. The Ru-P-C-B-Cl chelate forms a slightly puckered envelope conformation which is different from the planar **12** and **13** conformations. As a result of solubility issues relating to complex **15**, no reactivity was investigated with this complex.

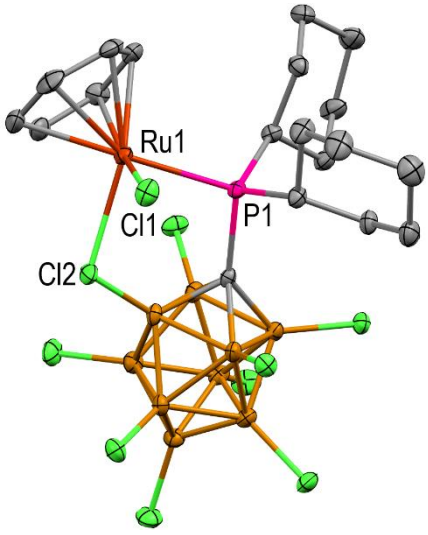

*Figure 52. Crystal structure of Complex **15**.*

Conclusion

Here, we have synthesized three, new zwitterionic Ru complexes and studied their properties. Compound **12** was unable to produce any alkylidene, vinylidene, or allenylidene. All three structures showed a noticeable *trans* influence resulting from the ligated phosphine and all had cationic metal centers, as intended. Disappointingly, the solubility remained a significant problem across all three complexes that we were unable to resolve. Despite these disappointments, we have learned the ease with which carboranyl ligands are able to form unique complexes with transition metals.

Experimental

General Considerations: Unless otherwise stated, all manipulations were carried out using standard Schlenk or glovebox techniques (O_2, H_2O < 1ppm) under a dinitrogen or argon atmosphere. Solvents were dried on elemental K or CaH_2 and distilled under argon before use. $[(\eta^6\text{-}C_6H_6)Ru(CH_3CN)_2Cl]^+[BF_4]^-$ was prepared according to the literature procedure.[112] NMR spectra were recorded at room temperature on Bruker Avance 300MHz, Bruker Avance 400MHz, or Bruker Avance 600MHz spectrometers. NMR chemical shifts are reported in parts per million (ppm). ^1H NMR and ^{13}C NMR chemical shifts were referenced to residual protio solvent. ^{11}B NMR chemical shifts were externally referenced to BF_3OEt_2. ^{31}P NMR chemical shifts were externally referenced to 80% H_3PO_4 in H_2O. The mass spectrometry data was collected on an Agilent LCTOF Multimode-ESI/APCI with direct injection. Crystallographic data for compounds **12**, **13**, and **15** are available free of charge from the Cambridge Crystallographic Data Center under reference number 1908384, 1908385, and 1908386, respectively. These structures can be accessed at: http://www.ccdc.cam.ac.uk/Community/Requestastructure/Pages/DataRequest.aspx.

Modified Synthesis of **4**:

$B_{10}H_{14}$ (8.0g, 65.5mmol) was placed in a 1L round bottom flask and hexanes (20mL) was added to the round bottom with a stirbar. The flask was placed in an ice bath. A prechilled aqueous solution of NaOH (10% w/w, 240mL) was then added. An addition funnel was fitted to the top of the round bottom flask and an aqueous formaldehyde solution (10.0g, 37%, w/w, stabilized with methanol), was added to the funnel. Water (10mL) was then added to the formaldehyde solution and the additional funnel was set to add to the NaOH solution dropwise over a period of 1 hour. After all formaldehyde was added, the ice bath was refreshed and the reaction was set to stir overnight, warming to ambient temperature.

Subsequently, the hexane layer was removed via seperatory funnel. Extractions with diethyl ether (100mL x3) were performed and ether layers combined and placed in a 2L round bottom flask equipped with a stir bar and was cooled to 0°C in an ice bath. A prechilled aqueous solution of KOH (1M, 600mL) was added. The ether was then removed in vacuo. Once all ether was evaporated, I_2 (20g x3 every 30min, 210mmol) was added. The ice bath was refreshed and the reaction was allowed to stir overnight and warm to room temperature. Next, the pale yellow solution was gravimetrically filtered and then Et_4NCl (15g, 90mmol) was added. The precipitate was filtered and washed with copious amounts of water. The filtered precipitate was allowed to dry overnight on the filter paper.

Next, the precipitate was added to a 500mL round bottom flask equipped with a stir bar. An aqueous HCl solution (10% w/w of 37% HCl, 200mL) was added, followed by diethyl ether (100mL). The reaction was stirred vigorously until all solids had dissolved. The ether layer was separated via seperatory funnel and the aqueous solution was

washed with more diethyl ether. All organic layers were combined and placed into a 1L round bottom flask equipped with a stir bar. Water (300mL) was then added to the ether. The liquid mixture was then placed under vacuum to remove the ether layer. Once all ether was removed, the aqueous solution was heated to reflux for 24 hours. Once the time had elapsed, the reaction was gravimetrically filtered while hot. CsCl (15g, 90mmol) was then added to the solution and $[Cs]^+[HCB_9H_9]^-$ was recrystallized from this solution and filtered. Yield: 10.2g, 40.4mmol, 62%.

Synthesis for compound **12**:

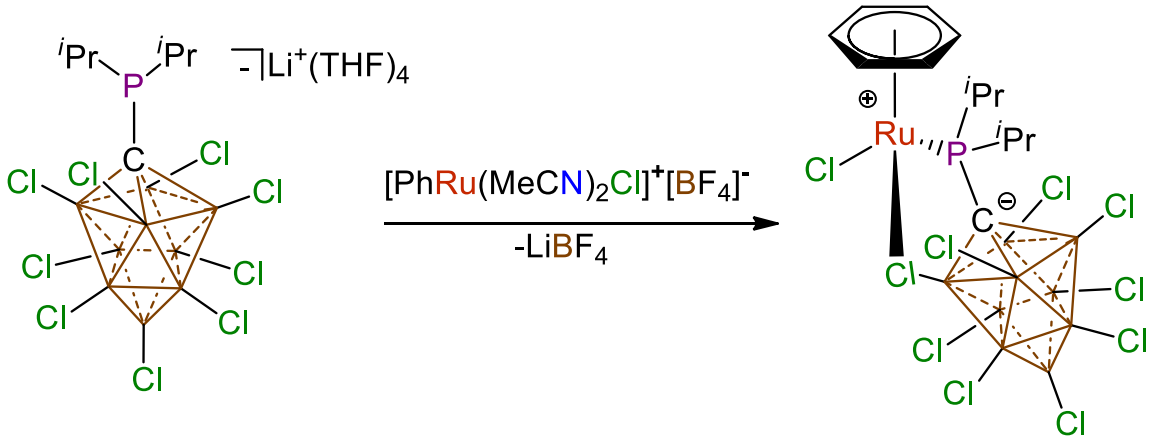

11 (300mg, 357μmol) was added to a 20mL scintillation vial equipped with a stir bar. Fluorobenzene (3mL) was then added. $[(\eta^6\text{-}C_6H_6)Ru(CH_3CN)_2Cl]^+[BF_4]^-$ (136mg, 357μmol) was added to a 20mL scintillation vial and Fluorobenzene (1mL) was added. The Ru slurry was then added to the solution of **11** and the reaction was allowed to stir for 30 minutes at room temperature. After 30 minutes, the reaction was passed through a Hirsch funnel fitted with a glass microfiber filter. The resulting solid was then washed with copious amounts of fluorobenzene, followed by diethyl ether washes. The washings were discarded and the red solid was dissolved through the filter paper with copious amounts

of DCM. The solvent was then removed in vacuo giving pure **24**. Yield: 227mg, 88%. ^{1}H NMR (400MHz, CD_2Cl_2, 23°C): δ 6.13 (s, 6H), 4.05 (m, 2H), 2.07-2.02 (dd, 3H, $^{3}J_{H-H}$ = 7.4Hz, $^{4}J_{P-H}$ = 14.6Hz), 1.89-1.80 (m, 6H), 1.57-1.50 (dd, 3H, $^{3}J_{H-H}$ = 6.3Hz, $^{4}J_{P-H}$ = 20.6Hz). $^{11}B\{^{1}H\}$ NMR (96MHz, CD_2Cl_2, 23°C): δ 24.0 (1B). -0.9, -1.7, -3.7, -8.1 (9B). $^{31}P\{^{1}H\}$ NMR (162MHz, CD_2Cl_2, 23°C): δ 96.2.

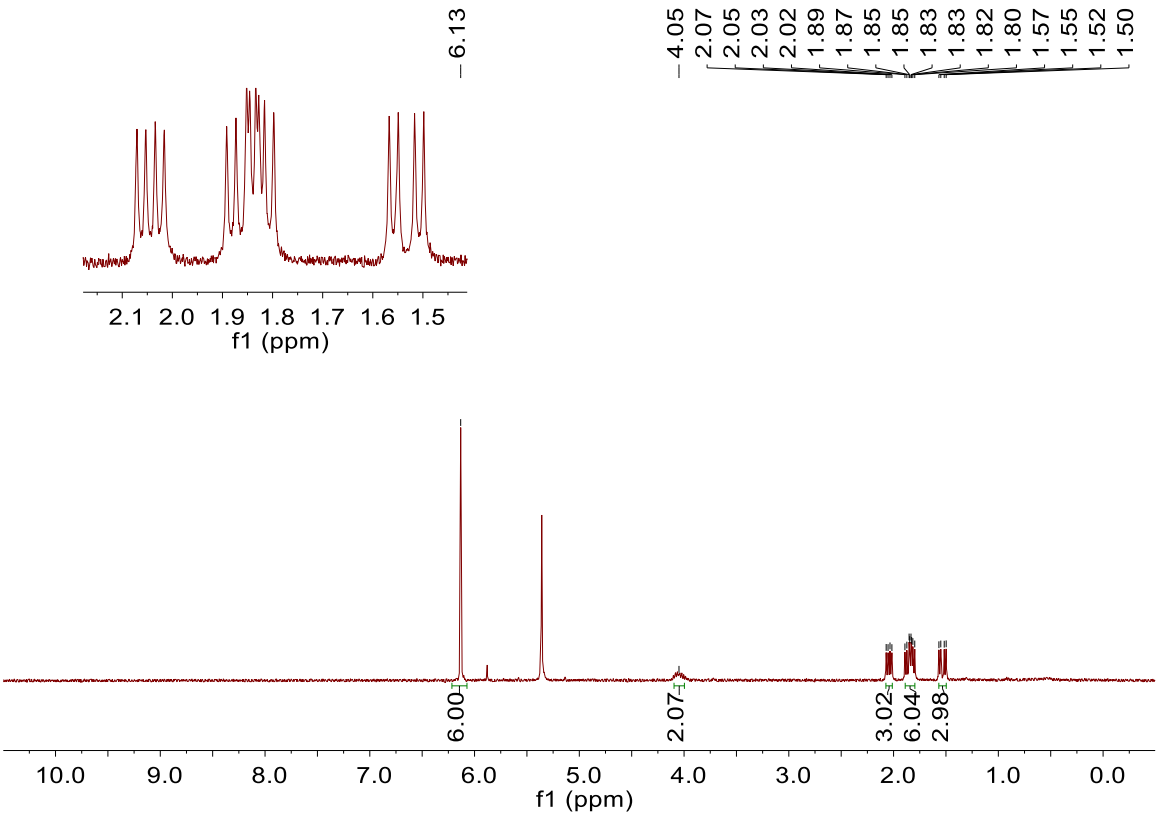

*Figure 53. ^{1}H NMR of **12** (400MHz, CD_2Cl_2, 23°C).*

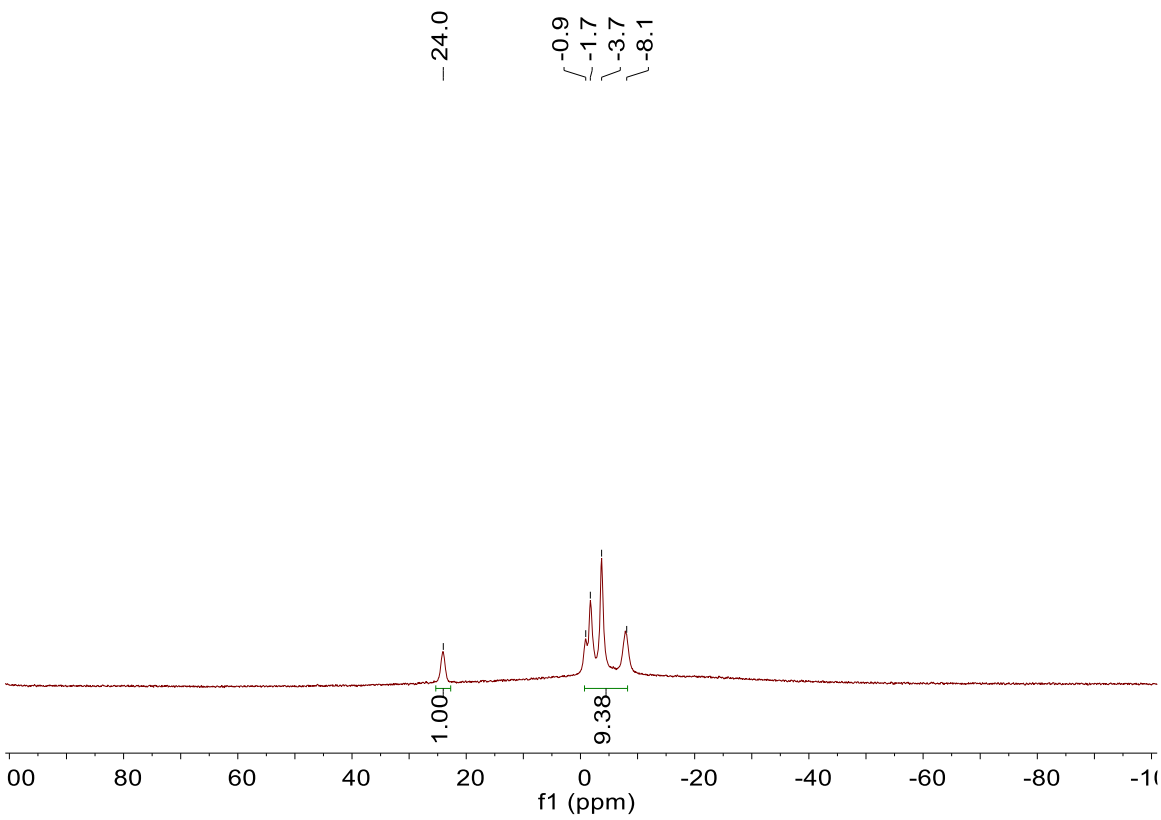

*Figure 54. $^{11}B\{^{1}H\}$ NMR of **12** (96MHz, CD_2Cl_2, 23°C).*

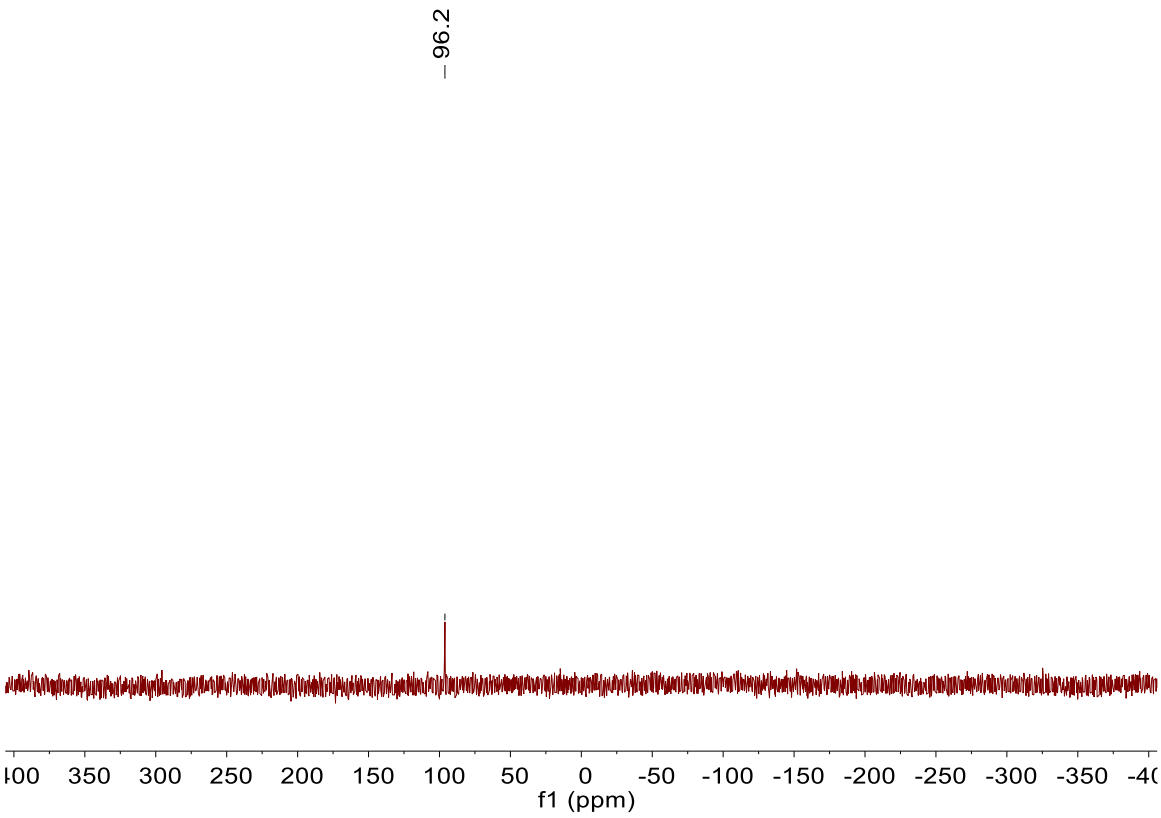

*Figure 55. $^{31}P\{^{1}H\}$ NMR of **12** (162MHz, CD_2Cl_2, 23°C).*

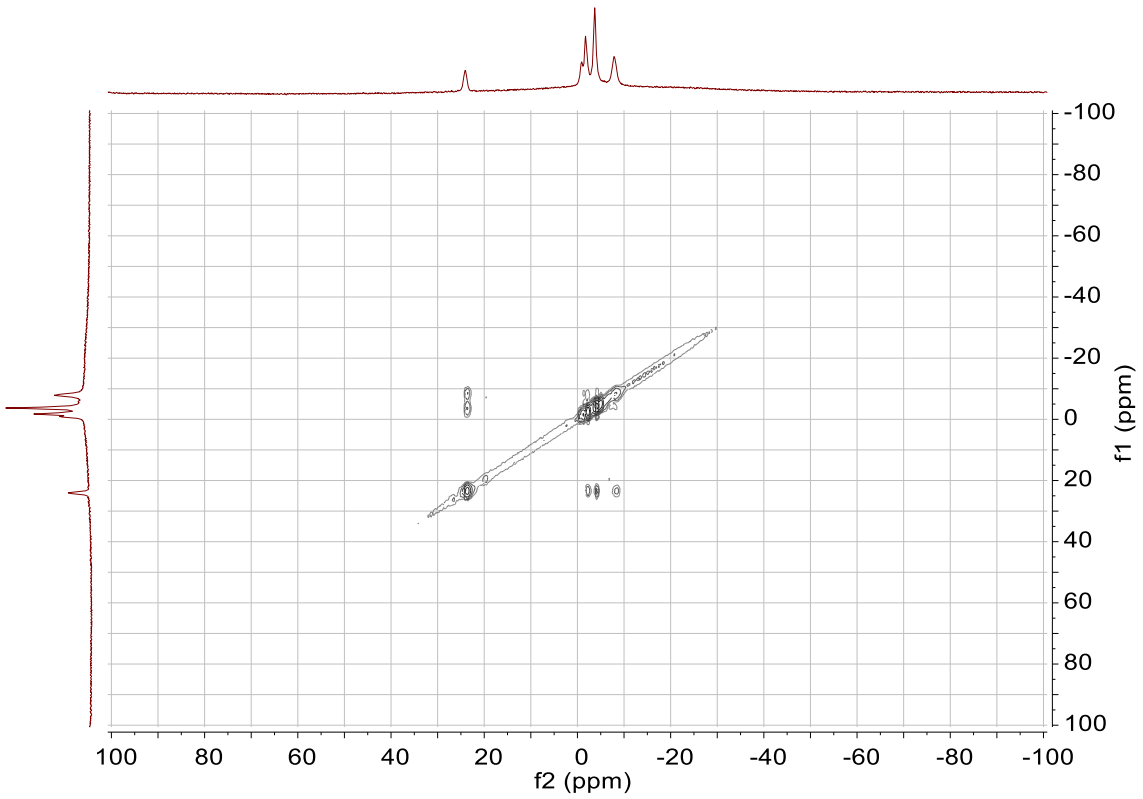

*Figure 56. $^{11}B\{^1H\}$-$^{11}B\{^1H\}$ COSY NMR of **12** (96MHz, CD_2Cl_2, 23°C).*

Synthesis for compound **13**:

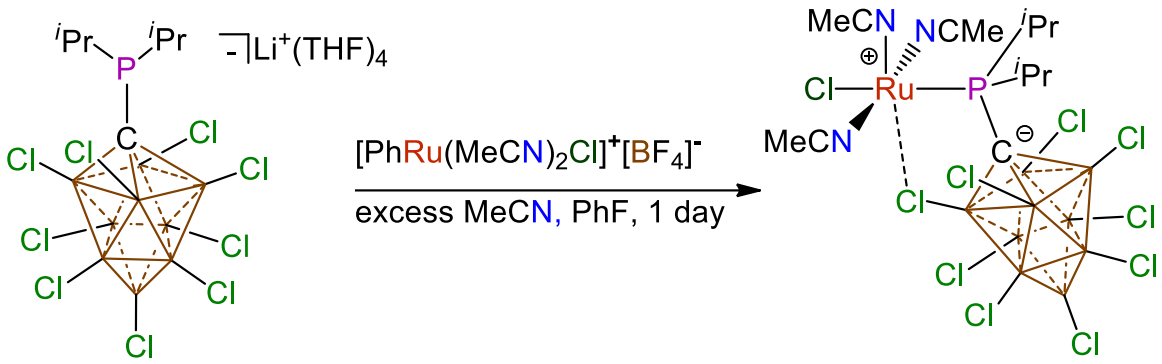

11 **13**

11 (300mg, 357µmol) was added to a 20mL scintillation vial equipped with a stir bar. Fluorobenzene (3mL) was then added. $[(\eta^6\text{-}C_6H_6)Ru(CH_3CN)_2Cl]^+[BF_4]^-$ (124mg, 357µmol) was added to a 20mL scintillation vial and Fluorobenzene (1mL) was added.

The Ru slurry was then added to the solution of **11**. One drop of acetonitrile was then added to the reaction mixture. The reaction was allowed to stir for 24 hours at room temperature. After 24 hours, the reaction was passed through a Hirsch funnel fitted with a glass microfiber filter. The resulting solid was then washed with copious amounts of fluorobenzene, followed by diethyl ether washes. The washings were discarded and the red solid was dissolved through the filter paper with acetonitrile. The solvent was then removed in vacuo giving pure **13**. Yield: 261mg, 91% yield. ^{1}H NMR (600MHz, CD_3CN, 23°C): δ 3.36 (m, 2H), 2.22 (s, 8H), 1.67-1.55 (dd, 6H, $^{3}J_{H-H}$ = 7.0Hz, $^{4}J_{P-H}$ = 13.1Hz), 1.52-1.37 (dd, 6H, $^{3}J_{H-H}$ = 7.0Hz, $^{4}J_{P-H}$ = 13.1Hz). $^{11}B\{^{1}H\}$ NMR (128MHz, CD_3CN, 23°C): δ 23.3, 0.3, -2.5, -3.4, -7.2. $^{31}P\{^{1}H\}$ NMR (162MHz, CD_3CN, 23°C): δ 117.0.

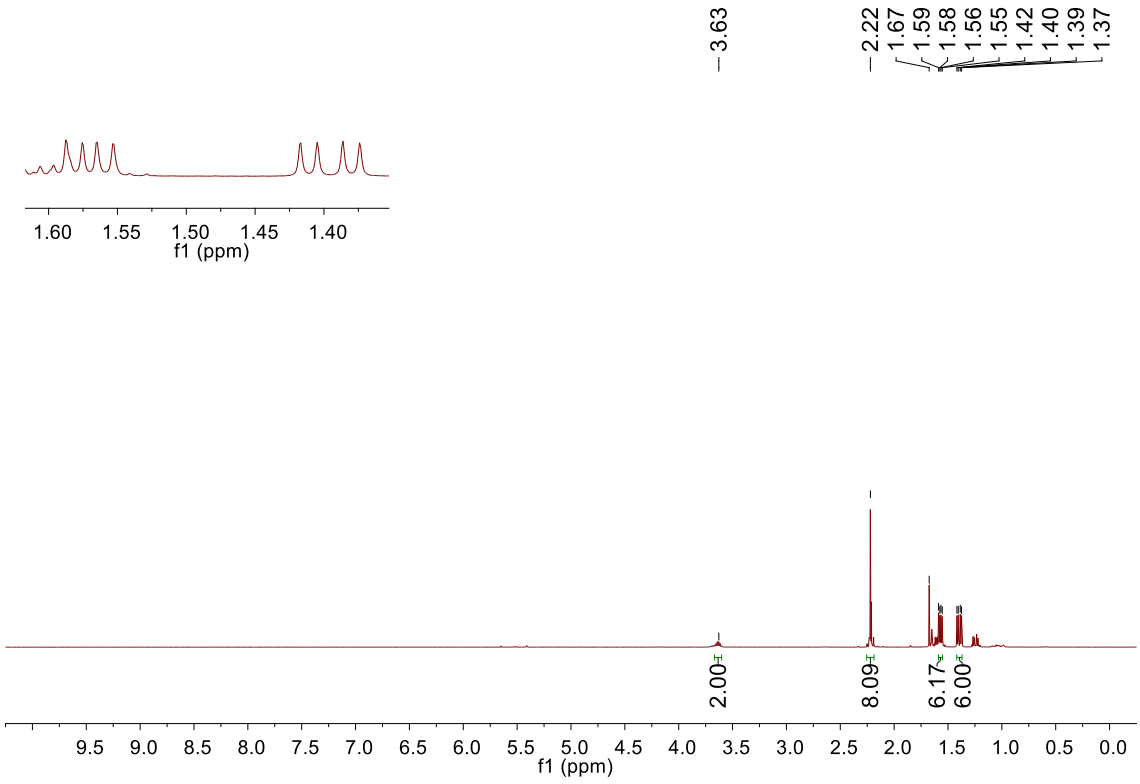

*Figure 57. ^{1}H NMR of **13** (600MHz, CD_3CN, 23°C).*

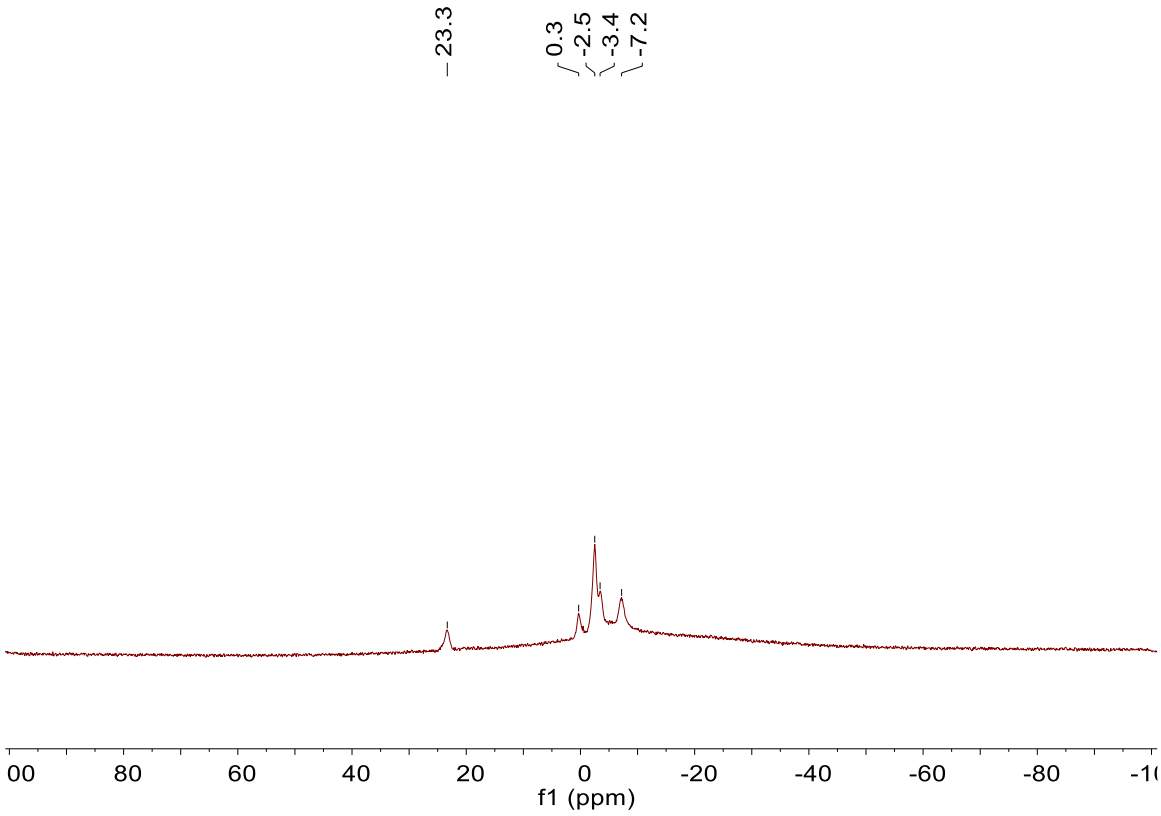

*Figure 58. $^{11}B\{^{1}H\}$ NMR of **13** (128MHz, CD_3CN, 23°C).*

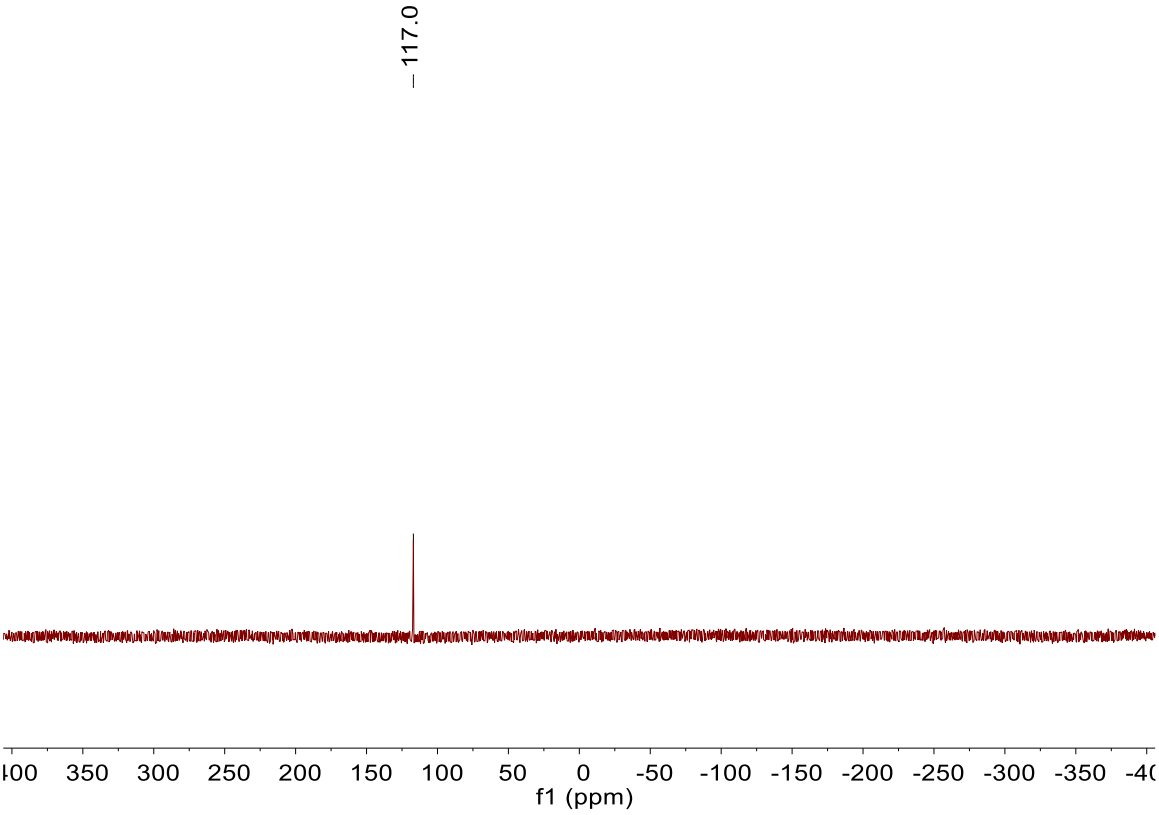

*Figure 59. $^{31}P\{^{1}H\}$ NMR of **13** (CD_3CN, 23°).*

Synthesis for compound **14**:

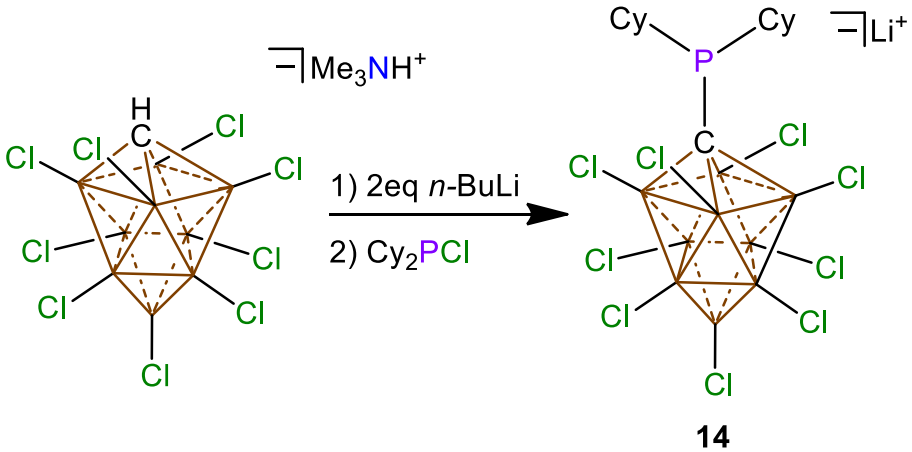

14

$[Me_3NH]^+[HCB_9Cl9]^-$ (500mg, 1.02mmol) was dissolved in THF (3mL) in a 20mL

scintillation vial equipped with a stir bar. *n*-BuLi (2.1 equiv, 2.0M in hexanes) was added, and the mixture was stirred for 30min. This mixture was added to pentane (15mL) that was being stirred, and a white solid precipitated. The solid was collected by filtration, washed twice with pentane, and dried under vacuum. The resulting white powder was dissolved in THF (3mL), Cy_2PCl (262mg, 1.12mmol) added, and the mixture stirred for 1h. The volatiles were removed under vacuum. The resulting oil was washed with pentane, taken up in PhF, and the insoluble LiCl removed by filtration. The filtrate was evaporated to dryness to yield **14** as a white solid. Yield: 961mg, 0.95mmol, 93%. ^{1}H NMR (600MHz, CD_2Cl_2, 23°C): δ 3.80, (m, 8H, THF), 2.67, (m, 2H), 2.22, 2.16 (m, 4H), 1.96 (m, 8H, THF), 1.77, 1.71 (m, 2H), 1.42 (m, 6H), 1.30 (m, 4H). $^{13}C\{^{1}H\}$ NMR (151MHz, CD_2Cl_2, 23°C): δ 68.8, 34.1 (d, $^{1}J_{P\text{-}C}$ = 23.9Hz), 32.2 ($^{2}J_{P\text{-}C}$ = 19.5Hz), 30.8, 27.7 ($^{2}J_{P\text{-}C}$ = 14.2Hz), 26.7, 26.4, 25.6. $^{11}B\{^{1}H\}$ NMR (192MHz, CD_2Cl_2, 23°C): δ 19.5 (1B), -4.6, 6.2 (9B). $^{31}P\{^{1}H\}$ NMR (162MHz, CD_2Cl_2, 23°C): δ 35.6.

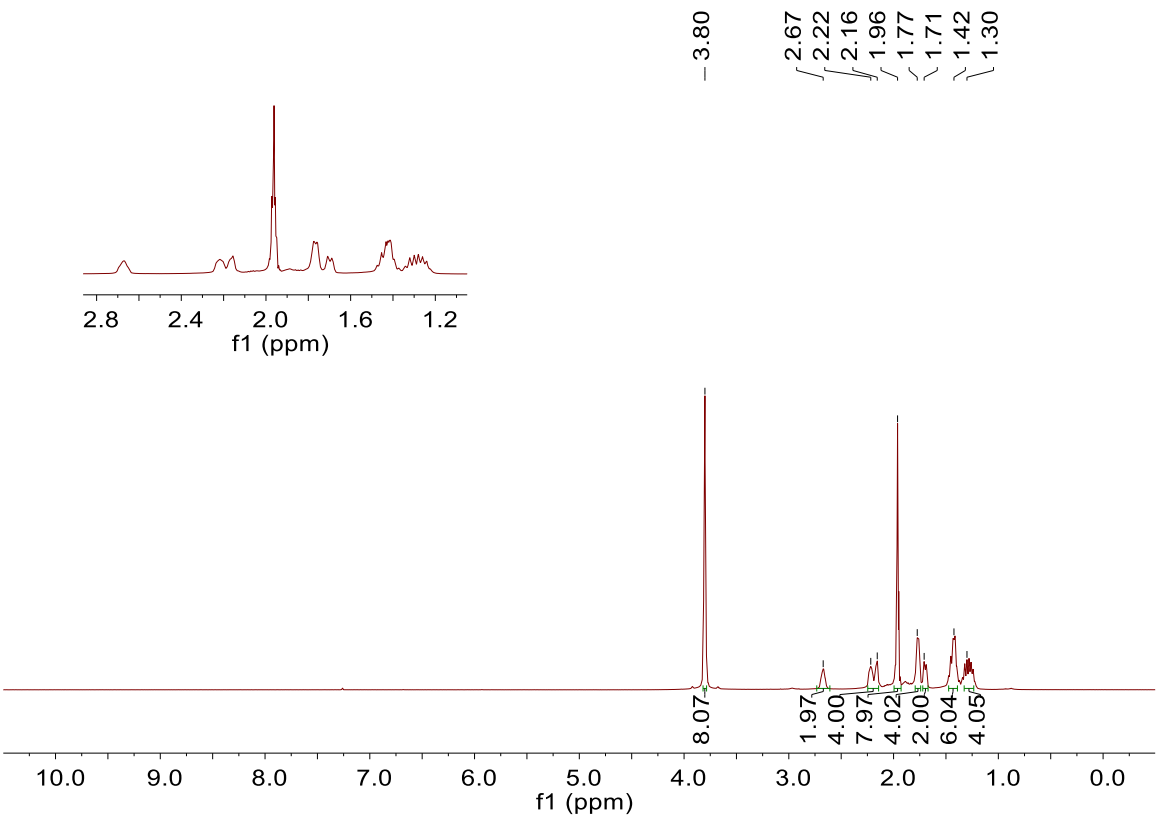

Figure 60. ^{1}H NMR of **14** (600MHz, CD_2Cl_2, 23°C).

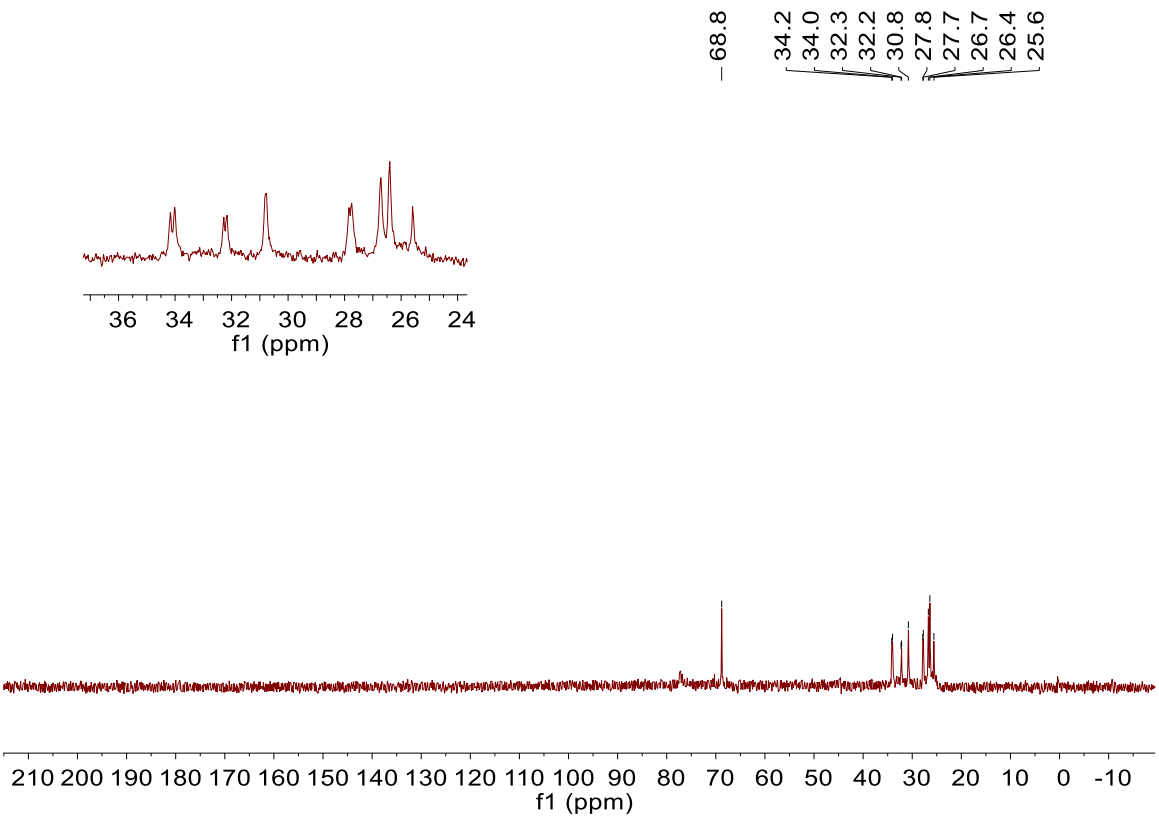

*Figure 61. $^{13}C\{^{1}H\}$ NMR of **14** (151MHz, CD_2Cl_2, 23°C).*

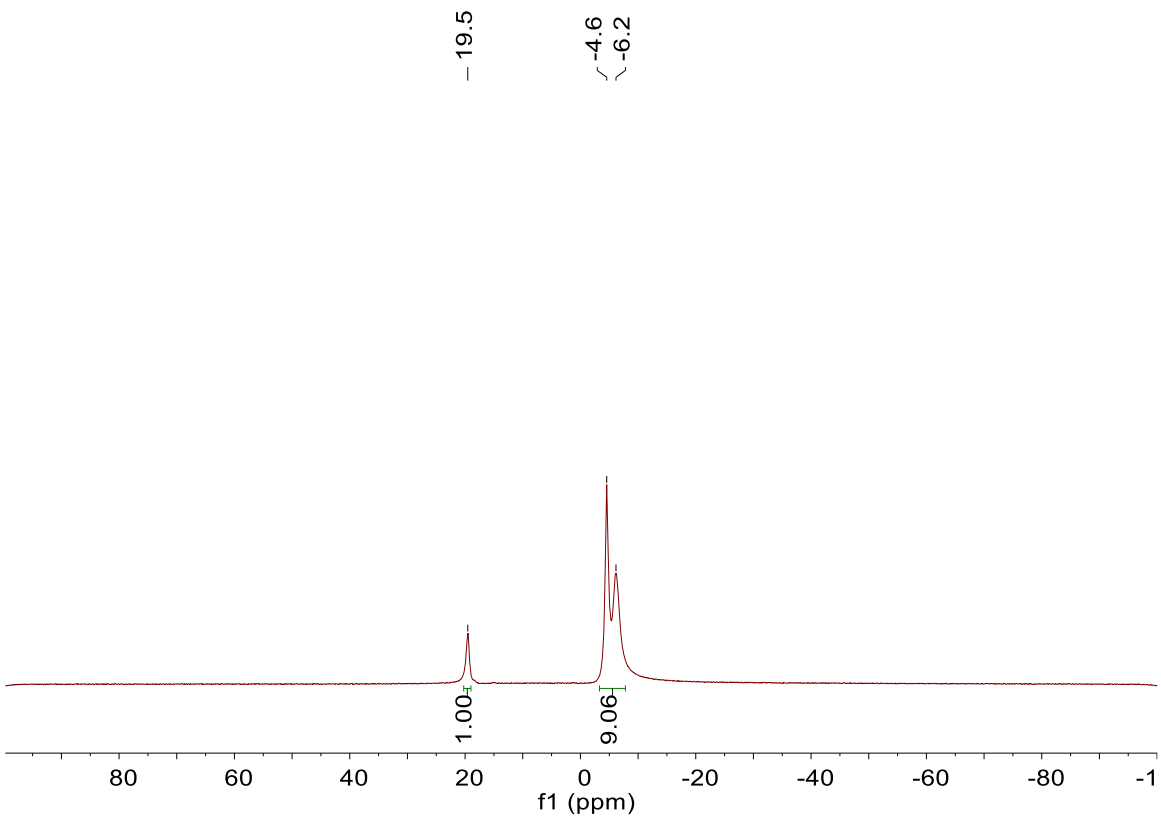

*Figure 62. $^{11}B\{^{1}H\}$ NMR of **14** (192MHz, CD_2Cl_2, 23°C).*

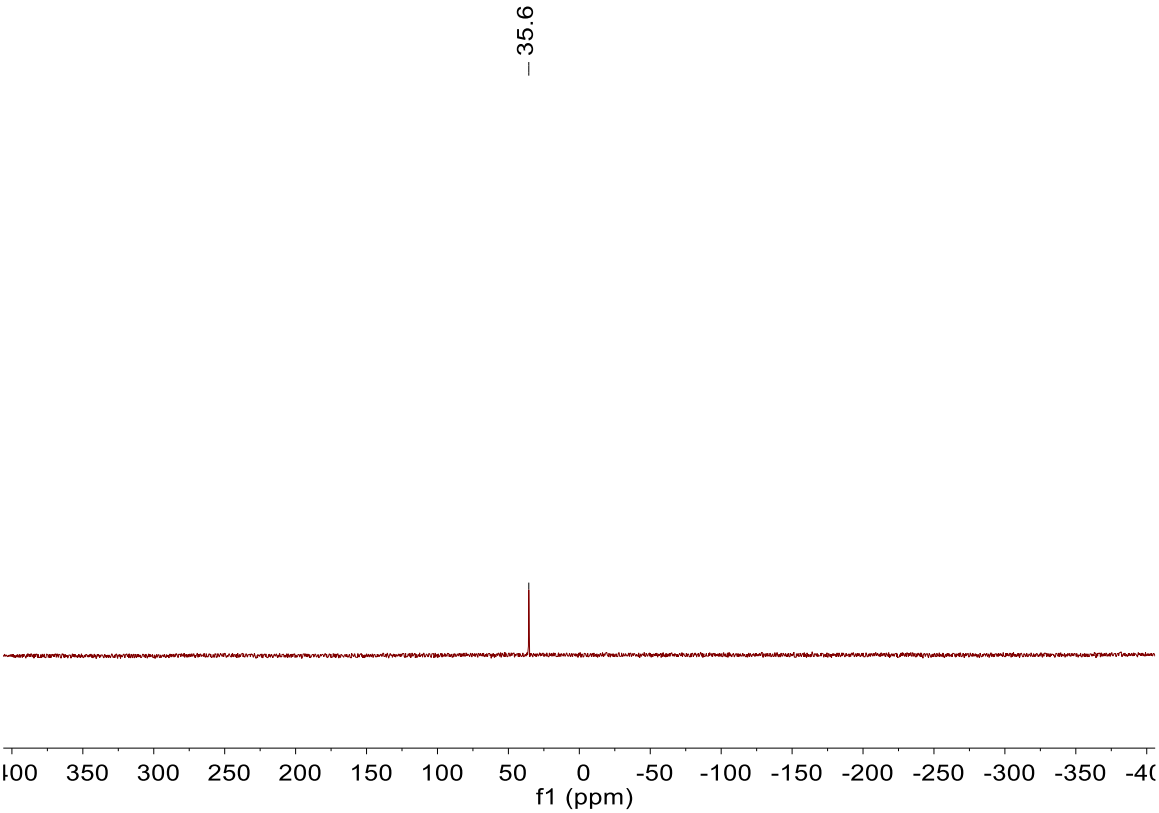

*Figure 63. $^{31}P\{^{1}H\}$ NMR of **14** (162MHz, CD_2Cl_2, 23°C).*

Synthesis for compound **15**:

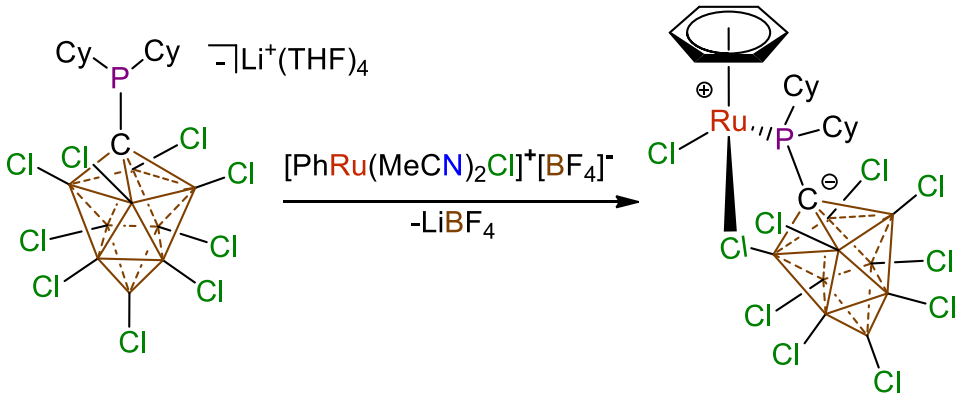

14 **15**

14 (300mg, 325µmol) was added to a 20mL scintillation vial equipped with a stir bar. Fluorobenzene (3mL) was then added. $[(\eta^6\text{-}C_6H_6)Ru(CH_3CN)_2Cl]^+[BF_4]^-$ (124mg,

325μmol) was added to a 20mL scintillation vial and Fluorobenzene (1mL) was added. The Ru slurry was then added to the solution of **14** and the reaction was allowed to stir for 30 minutes at room temperature. After 30 minutes, the reaction was passed through a Hirsch funnel fitted with a glass microfiber filter. The resulting solid was then washed with copious amounts of Fluorobenzene, followed by diethyl ether washes. The washings were discarded and the red solid was dissolved through the filter paper with copious amounts of DCM. The solvent was then removed in vacuo giving pure **15**. Yield: 232mg, 276μmol 85%. ^{1}H NMR (300MHz, CD_2Cl_2, 23°C): δ 6.05 (s, 6H), 3.60 (m, 2H), 2.74 (m, 2H), 2.19 (m, 2H), 2.07, (m, 2H), 1.82 (m, 6H), 1.54-1.32 (m, 8H). $^{11}B\{^{1}H\}$ NMR (192MHz, CD_2Cl_2, 23°C): 24.2, -0.9, -1.9, -3.6, -8.1. $^{31}P\{^{1}H\}$ NMR (162MHz, CD_2Cl_2, 23°C): δ 89.4.

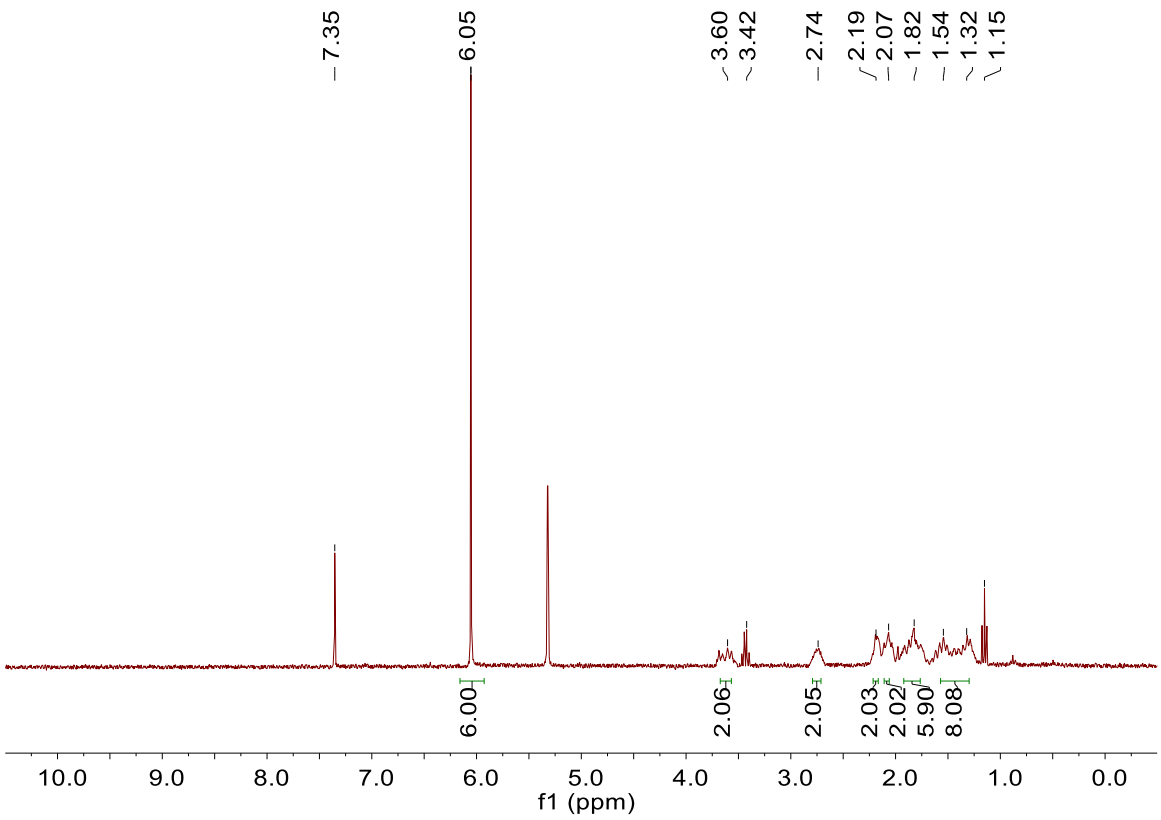

*Figure 64. ^{1}H NMR of **15** (300MHz, CD_2Cl_2, 23°C). Note: Benzene and diethyl ether impurities are seen at 7.35 and 3.42, 1.15ppm, respectively.*

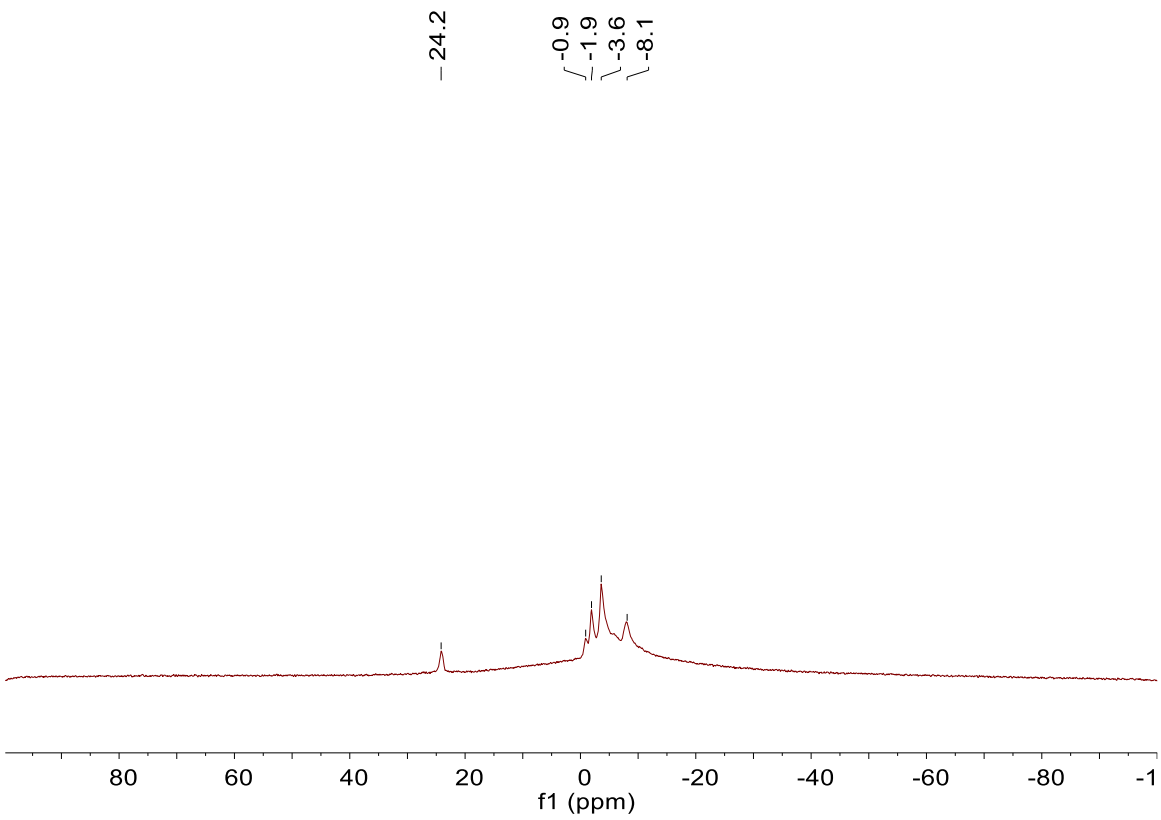

*Figure 65. $^{11}B\{^{1}H\}$ NMR of **15** (196MHz, CD_2Cl_2, 23°C).*

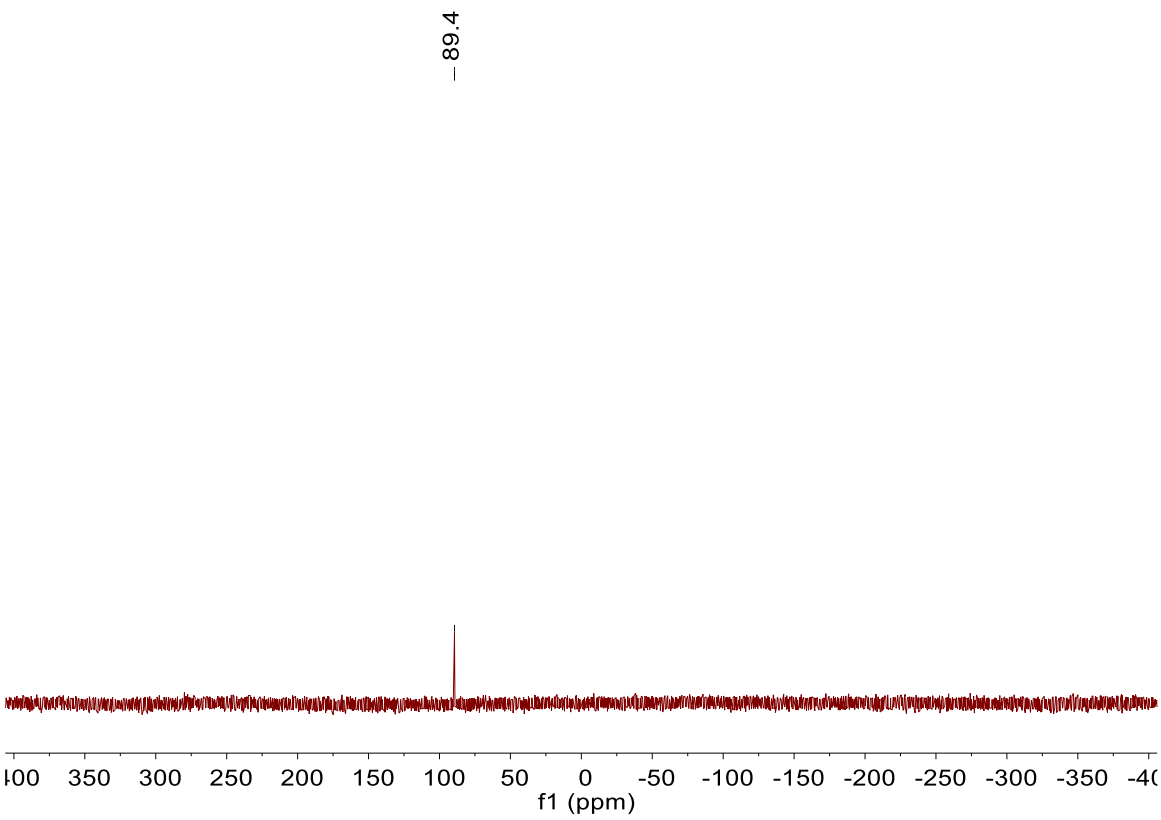

*Figure 66. $^{31}P\{^{1}H\}$ NMR of **15** (162MHz, CD_2Cl_2, 23°C).*

X-Ray Structure of (η^6-C_6H_6)(κ^2-P,Cl-$P_2CB_9Cl_9$)RuCl (**12**):

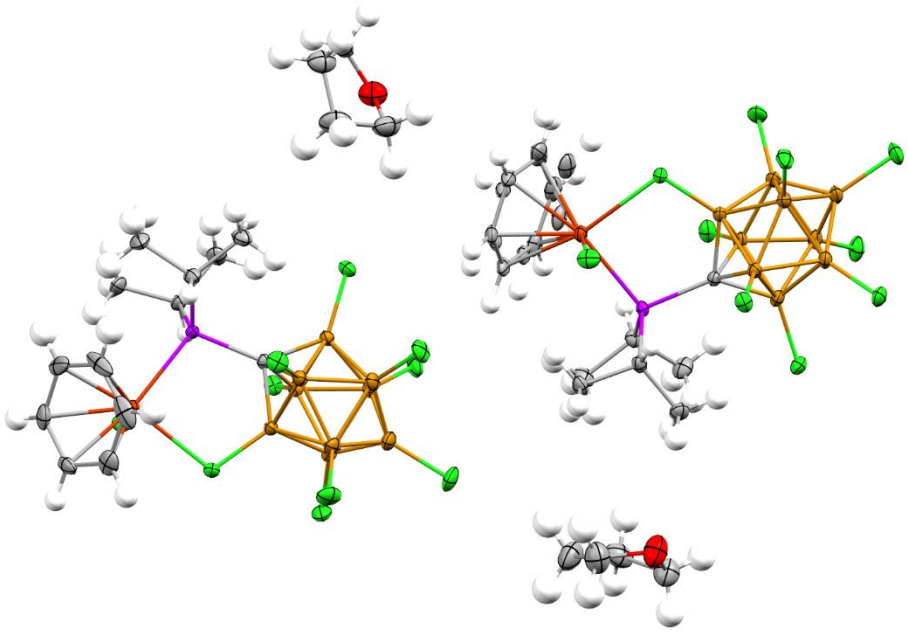

X-Ray Structure Determination

A red prism fragment (0.425 x 0.315 x 0.087 mm^3) was used for the single crystal x-ray diffraction study of $C_{13}H_{20}B_9Cl_{10}PRu.C_4H_8O$ (sample vL306JKr_0m). The crystal was coated with paratone oil and mounted on to a cryo-loop glass fiber. X-ray intensity data were collected at 100(2) K on a Bruker APEX2 (**ref. 1**) platform-CCD x-ray diffractometer system (fine focus Mo-radiation, Φ = 0.71073 Å, 50KV/30mA power). The CCD detector was placed at a distance of 5.0600 cm from the crystal.

A total of 5400 frames were collected for a sphere of reflections (with scan width of 0.3° in ω starting ω and 2θ angles of –30°, and θ angles of 0°, 45°, 90°, 120°, 135°, 180°, 225°, 240°, and 270° for every 600 frames, 10 sec/frame exposure time). The frames were integrated using the Bruker SAINT software package (**ref. 2**) and using a narrow-frame integration algorithm. Based on a triclinic crystal system, the integrated frames

yielded a total of 100601 reflections at a maximum 2θ angle of 56.564° (0.75 Å resolution), of which 15920 were independent reflections (R_{int} = 0.0272, R_{sig} = 0.0175, redundancy = 6.3, completeness = 99.9%) and 14393 (90.4%) reflections were greater than 2θ(I). The unit cell parameters were, **a** = 9.8700(3) Å, **b** = 17.5026(5) Å, **c** = 18.9830(6) Å, **α** = 92.4996(5) **β** = 94.6971(5)°, **γ** = 100.1995(5), V = 3211.01(17) Å^3, Z = 4, calculated density D_c = 1.721 g/cm^3. Absorption corrections were applied (absorption coefficient μ = 1.387 mm^{-1}; max/min transmission = 0.889/0.590) to the raw intensity data using the SADABS program (**ref. 3**).

The Bruker SHELXTL software package (**ref. 4**) was used for phase determination and structure refinement. The distribution of intensities (E^2-1 = 0.939) and no systematic absent reflections indicated two possible space groups, P-1 and P1. The space group P-1 (#2) was later determined to be correct. Direct methods of phase determination followed by two Fourier cycles of refinement led to an electron density map from which most of the non-hydrogen atoms were identified in the asymmetric unit of the unit cell. With subsequent isotropic refinement, all of the non-hydrogen atoms were identified. There were molecules of $C_{13}H_{20}B_9Cl_{10}PRu$ and two solvent molecules of THF present in the asymmetric unit of the unit cell. The benzene coordinated to the Ru2-atom was modeled with disorder (benzene disordered site occupancy ratio was 81%/19%).

Atomic coordinates, isotropic and anisotropic displacement parameters of all the non-hydrogen atoms were refined by means of a full matrix least-squares procedure on F^2. The H-atoms were included in the refinement in calculated positions riding on the atoms to which they were attached. The refinement converged at R1 = 0.0270, wR2 = 0.0650, with intensity I>2θ (I). The largest peak/hole in the final difference map was 1.212/-1.052 e/Å^3.

X-Ray Structure of (κ^2-P,Cl-$P_2CB_9Cl_9$)RuCl($NCCH_3$)$_3$ (13):

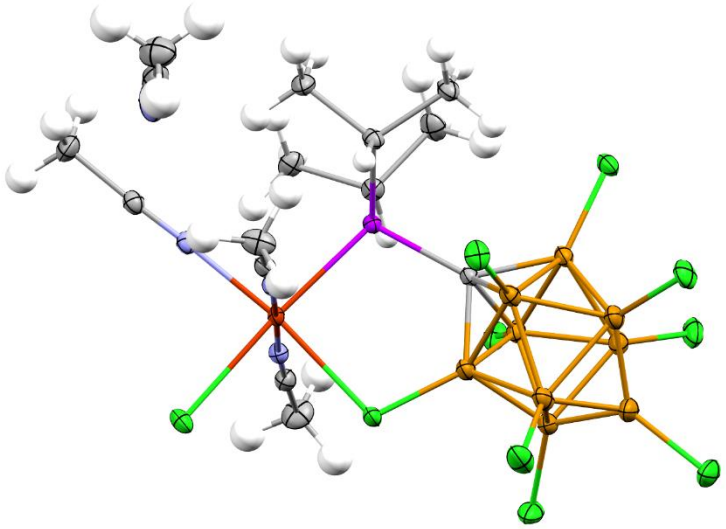

X-Ray Structure Determination

A yellow fragment of a prism (0.328 x 0.285 x 0.223 mm^3) was used for the single crystal x-ray diffraction study of $CB_9Cl_9PC_6H_{14}[CH_3CN]_3ClRu.CH_3CN$ (sample vL210JK_0m). The crystal was coated with paratone oil and mounted on to a cryo-loop glass fiber. X-ray intensity data were collected at 100(2) K on a Bruker APEX2 (**ref. 1**) platform-CCD x-ray diffractometer system (fine focus Mo-radiation, Φ = 0.71073 Å, 50KV/30mA power). The CCD detector was placed at a distance of 5.0600 cm from the crystal.

A total of 2400 frames were collected for a hemisphere of reflections (with scan width of 0.3° in ω, starting ω and 2θ angles at –30°, and θ angles of 0°, 90°, 180°, and 270° for every 600 frames, 10 sec/frame exposure time). The frames were integrated using the Bruker SAINT software package (**ref. 2**) and using a narrow-frame integration

algorithm. Based on an orthorhombic crystal system, the integrated frames yielded a total of 102778 reflections at a maximum 2θ angle of 61.016º (0.70 Å resolution), of which 10189 were independent reflections (R_{int} = 0.0385, R_{sig} = 0.0189, redundancy = 10.1, completeness = 100%) and 8875 (87.1%) reflections were greater than 2□(I). The unit cell parameters were, **a** = 14.2022(5) Å, **b** = 16.2883(6) Å, **c** = 28.8733(11) Å, **α** = **β** = **γ** = 90º**,** V = 6679.3(4) Å^3, Z = 8, calculated density D_c = 1.683 g/cm^3. Absorption corrections were applied (absorption coefficient μ = 1.336 mm^{-1}; max/min transmission = 0.755/0.668) to the raw intensity data using the SADABS program (**ref. 3**).

The Bruker SHELXTL software package (**ref. 4**) was used for phase determination and structure refinement. The distribution of intensities (E^2-1 = 0.995) and systematic absent reflections indicated one possible space group, Pbca. The space group Pbca (#61) was later determined to be correct. Direct methods of phase determination followed by two Fourier cycles of refinement led to an electron density map from which most of the non-hydrogen atoms were identified in the asymmetric unit of the unit cell. With subsequent isotropic refinement, all of the non-hydrogen atoms were identified. There was one molecule of $CB_9Cl_9PC_6H_{14}[CH_3CN]_3ClRu$ and one solvent molecule of CH_3CN present in the asymmetric unit of the unit cell.

Atomic coordinates, isotropic and anisotropic displacement parameters of all the non-hydrogen atoms were refined by means of a full matrix least-squares procedure on F^2. The H-atoms were included in the refinement in calculated positions riding on the atoms to which they were attached. The refinement converged at R1 = 0.0224, wR2 = 0.0502, with intensity, I>2θ(I). The largest peak/hole in the final difference map was 0.704/-0.633 e/Å^3.

X-Ray Structure of (η^6-C_6H_6)(κ^2-P,Cl-$P_2CB_9Cl_9$)RuCl (**15**):

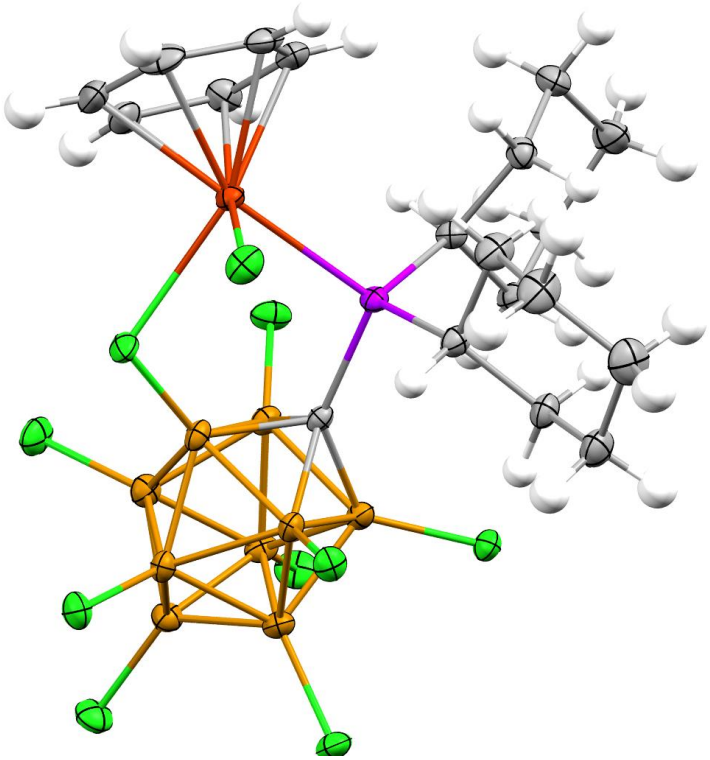

Diffraction data were collected on a Bruker-AXS Apex II diffractometer with an Apex II CCD detector using Mo K_α radiation (λ = 0.71073 Å) from a fine-focus sealed tube source. Data were collected at 100 K by performing 0.5° φ- and ω-scans, integrated using SAINT[1], and absorption corrected using SADABS[2]. The structure was solved by direct methods using SHELXT[3] and refined against F^2 on all data by full-matrix least squares with SHELXL-2018/3[4] following established refinement strategies[5]. All non-hydrogen atoms were refined anisotropically. All hydrogen atoms were included into the model at geometrically calculated positions and refined using a riding model. The isotropic displacement parameters of all hydrogen atoms were fixed to 1.2 times the *U* value of the

atoms they are linked to (1.5 times for methyl groups). Crystal and data quality details, as well as a summary of the residual refinement values, are listed in the accompanying table.

Compound **vl341jk** crystallizes in the orthorhombic centrosymmetric space group *Pbca* with one molecule of **vl341jk.**

CHAPTER 5: Ethylene Oligomerization and Polymerization by Palladium^{II} Methyl Complexes Supported by Phosphines Bearing a Perchlorinated 10-Vertex *closo*-Carborane Anion Substituent

Introduction

Square planar Pd^{II} alkyl complexes that contain unsymmetrical chelating phosphine-arenesulfonate ligands (**A**, Fig. 67) have been studied extensively because of their ability to polymerize ethylene to linear polyethylene and copolymerize ethylene with polar monomers.[113–115] However, the performance of these catalysts is generally inferior compared to that of other classes of olefin polymerization catalysts, which has motivated studies of related catalysts with other unsymmetrical ligands.[116–124] One interesting analog of **A**, studied independently by the Jordan and Piers groups, is zwitterionic phosphine-trifluoroborate system **B**, in which the sulfonate unit of **A** is replaced by a weakly coordinating trifluoroborate group.[121,125] In the presence of $[H(OEt_2)_2]^+[B(3,5\text{-}(CF_3)_2\text{-}C_6H_3)_4]^-$ to sequester the collidine ligand as $[collidinium]^+[B(3,5\text{-}CF_3)_2\text{-}C_6H_3)_4]^-$, **B** (L = collidine) catalytically dimerizes ethylene to butene with a turnover frequency (TOF) of 385 t.o./h at 23°C (CD_2Cl_2 solvent, 150 psi ethylene). Under these conditions, the catalyst resting state is the (κ^2-P,F-*o*-$PPh_2C_6H_4BF_3$)PdEt(η^2-$H_2C{=}CH_2$) complex and the primary product 1-butene

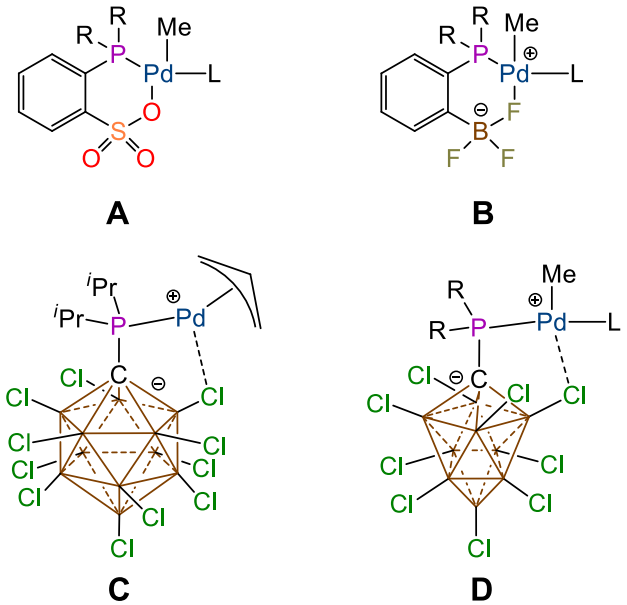

Figure 67. Pd^{II} Alkyl Complexes with Unsymmetrical Chelating Ligands.

is isomerized to *cis*- and *trans*-2-butene. Carborane clusters offer interesting possibilities as frameworks or components for ligands for organometallic catalysts due to their structural rigidity, steric and electronic tunability,[51,77,126–128] and synthetic availability.[10,11,15–17,58,73,74,129–142] In particular, halogenated *closo*-carborane anions are exceptionally stable[22,30] and may engage in weak dative BX → M interactions that may influence catalyst performance.[10]

Lavallo and co-workers recently reported the synthesis and characterization of zwitterionic ($P^iPr_2CB_{11}Cl_{11}$)Pd(allyl) (**C**, Fig. 67), bearing a diisopropyl phosphine ligand with a 12- vertex perchloro-*closo*-carborane anion substituent.[54] In the solid-state, the $[P^iPr_2CB_{11}Cl_{11}]^-$ ligand in **C** is bound in an κ^2-P,Cl mode; thus, **C** may be viewed as a structural analogue of **B.** Complex **C** reacts with norbornene to give organic-soluble polynorbornene but does not react with ethylene.

Here, we describe the synthesis and reactivity with ethylene of ($PR_2CB_9Cl_9$)PdMe(THF) complexes of type **D**, which contain phosphino-perchlorocarba-*closo*-decaborate ligands (Fig. 67). On the basis of studies of the parent $[P^iPr_2CB_9H_9]^-$ and $[P^iPr_2CB_{11}H_{11}]^-$ ligands, a $[PR_2CB_9Cl_9]^-$ ligand is expected to be a stronger donor and to exhibit a slightly smaller cone angle compared to an analogous $[PR_2CB_{11}Cl_{11}]^-$ ligand.[77] The objective of the present work was to explore how these differences influence the reactivity of complexes of type **D** with ethylene. The steric and electronic properties of the phosphine-arenesulfonate ligands in **A** strongly influence the ethylene polymerization performance.[143] We report the synthesis of a new family of $[PR_2CB_9Cl_9]^-$ ligands (**11**, R = ^{i}Pr; **16**, R = Ph; **17**, R = *o*-MeO-Ph; **18**, R = *o*-MeS-Ph) and the corresponding zwitterionic ($PR_2CB_9Cl_9$)PdMe(THF) complexes (**22**-**25**). Complexes **22** and **23**, which contain

diisopropyl- and diphenyl-phosphino units, respectively, are structurally analogous to **B**, with the $[PR_2CB_9Cl_9]^-$ ligands bound to Pd in a κ^2-P,Cl mode. In contrast, **24** and **25**, which contain a di-*o*-anisolyl, and di-*o*-thioanisolyl phosphine units, adopt κ^2-P,O and κ^3-P,S,S bonding modes in which one *o*-anisolyl methoxy (**24**) and both *o*-thioanisolyl (**25**) groups are bound to Pd at the ether and thioether functionalities, respectively.

Results and Discussion

$[PR_2CB_9Cl_9]^-$ ligands **11** and **16−18** were synthesized as the $Li(THF)_x$ salts (x = 2−4) following the procedure developed earlier for the 12-vertex analogue $[Li(THF)_3]^+[P^iPr_2CB_{11}Cl_{11}]^-$ (Fig . 67).[54,58] C-Lithiation of $[HCB_9Cl_9]^-$ followed by addition of the appropriate R_2PCl electrophile affords [**11**, **16−18**]$^-$[$Li(THF)_x$]$^+$ in >90% yield. The reaction of [**11**, **16−18**]$^-$[$Li(THF)_x$]$^+$ with (COD)PdMeCl yields the chloro-bridged dinuclear complexes $[Li(THF)_3]^+[\{(PR_2CB_9Cl_9)PdMe\}_2(\mu\text{-}Cl)]^-$ **19**-**21**. Reaction of **19**-**21** with 0.5 equivalent of $AgBF_4$ yields corresponding $(PR_2CB_9Cl_9)PdMe(THF)$ complexes **22**-**24** in >80% yield. However, complex **25** is produced directly from the reaction of **18** with (COD)PdMeCl. X-ray quality crystals of chloro-bridged dinuclear complex **20** were grown from THF/pentane. Crystallization of **21** from CH_3CN/PhF gave X-ray quality crystals of the corresponding CH_3CN adduct $(P^iPr_2CB_9Cl_9)PdMe(CH_3CN)\cdot(PhF)_{0.35}$ (**21**−$CH_3CN\cdot(PhF)_{0.35}$).

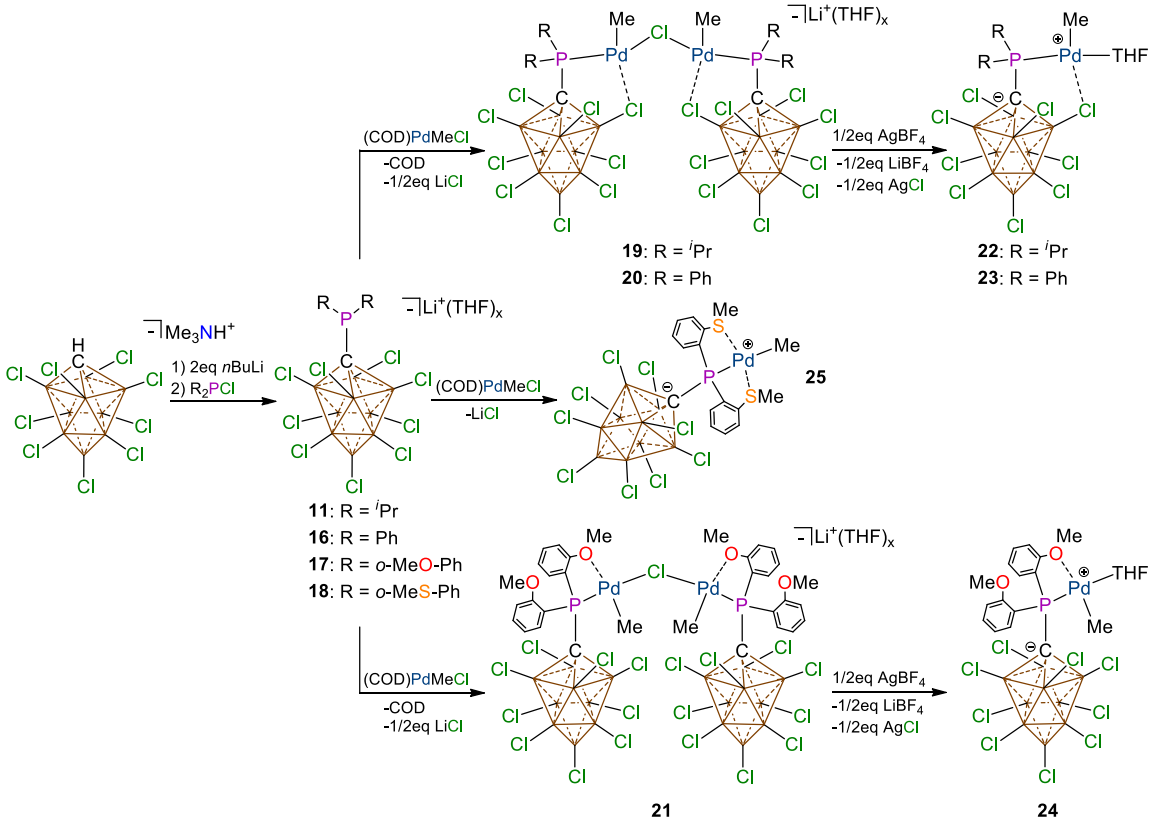

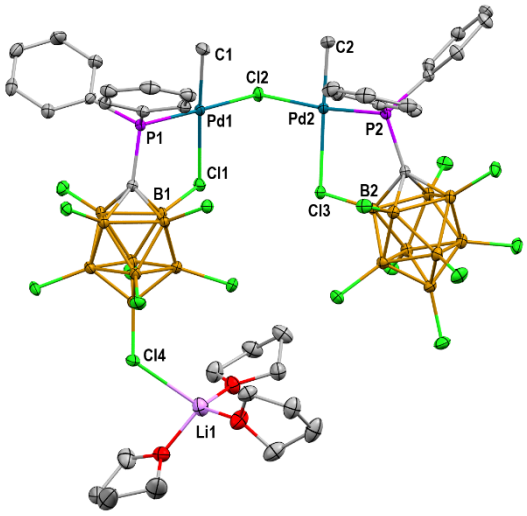

*Figure 68. Solid-state structure of **20**: H atoms are omitted. Thermal ellipsoids are drawn at the 50% probability level. Key bond lengths (Å): Li1−Cl4 2.575(4) Pd1−C1 2.024(2), Pd1−P1 2.2255(6), Pd1−Cl1 2.4950(5), Pd1−Cl2 2.3847(6), B1−Cl1 1.790(2), Pd2−C2 2.024(2), Pd2−P2 2.2137(8), Pd2−Cl3 2.5600(5), Pd2−Cl2 2.3963(8), B2−Cl3 1.789(2). Key bond angles: C1−Pd1−P2 89.62(6)°, C1−Pd1−Cl2 84.70(2)°, P1−Pd1−Cl1 9.62(6)°, Cl2−Pd1−Cl 84.70(2)°, Pd1−Cl2−Pd2 103.34(2) °. Color code: C, gray; B, brown; Cl, green; P, violent; Pd, light blue; O, red; Li, pink.*

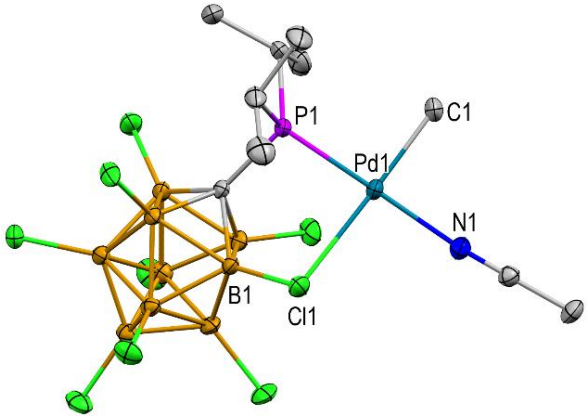

*Figure 69. Solid-state structure of **22**. H atoms and PhF molecules are omitted and only one orientation of the disordered ^{i}Pr unit is shown. Thermal ellipsoids are drawn at the 50% probability level. Key bond lengths (Å): Pd1−C1 2.029(3), Pd1−P1 2.2329(6), Pd1−N1 2.088(2), Pd1−Cl1 2.5876(7), B1−Cl1 1.795(2). Key bond angles: C1−Pd1−P1 91.79(8)°, C1−Pd1−N1B 88.4(1)°, P1−Pd1−Cl1 87.36(2)°, N1−Pd1−Cl 92.78(6)°. Color code: C, gray; B, brown; Cl, green; P, violet; Pd, light blue; O, red; N, blue.*

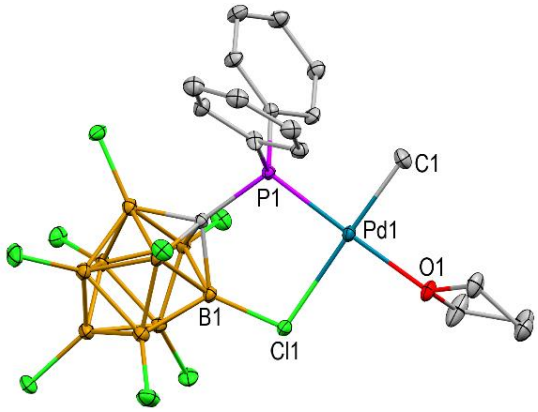

*Figure 71. Solid-state structure of **23**. H atoms are omitted. One orientation is shown. Thermal ellipsoids are drawn at the 50% probability level. Key bond lengths (Å): Pd1−C1 2.021(2), Pd1−O1 2.1362(15), Pd1−P1 2.2070(7), Pd1−Cl1 2.5135(6), B2−Cl1 1.800(2). Key bond angles: C1−Pd1−O1 90.05(8)°, C1−Pd1−P1 88.18(7)°, O1−Pd1−Cl1 88.71(5)°, Cl1−Pd1−P1 93.20(2)°. Color code: C, gray; B, brown; Cl, green; P, violet; Pd, light blue; O, red.*

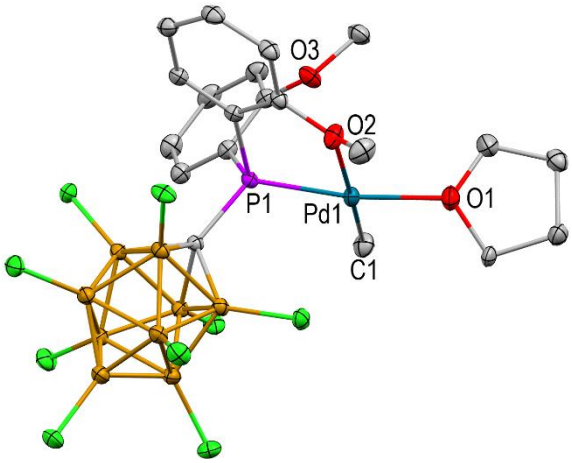

*Figure 72. Solid-state structure of **24**. H atoms and CH_2Cl_2 and pentane solvent molecules are omitted. Thermal ellipsoids are drawn at the 50% probability level. Only one orientation of the disordered THF ligand is shown. Bond lengths (Å): Pd1−O1 2.127(1), Pd1−C1 2.019(1), Pd1−P1 2.1855(7), Pd1−O2 2.225(1). Key bond angles: O1−Pd1−C1 92.75(5)°, O1−Pd1−O2 89.98(4)°, C1−Pd1−P1 94.33(4)°, P1−Pd1−O1 82.53(3)°. Color code: C, gray; B, brown; Cl, green; P, violet; Pd, light blue; O, red.*

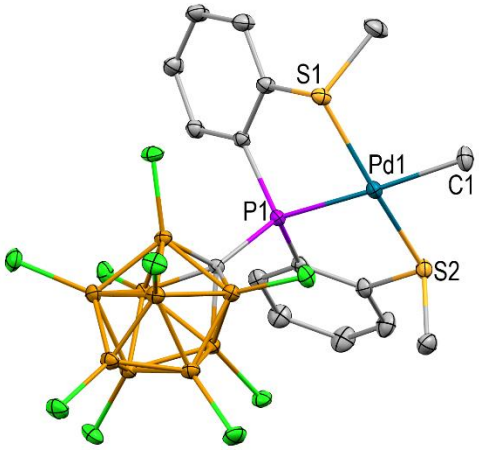

*Figure 70. Solid-state structure of **25**. H atoms, THF and pentane solvent molecules are omitted. Thermal ellipsoids are drawn at the 50% probability level. Only one orientation of the disordered THF ligand is shown. Bond lengths (Å): Pd1−C1 2.081(6), Pd1−S1 2.2806(3) Pd1−S2 2.3010(3), Pd1−P1 2.2794(3). Key bond angles: S1−Pd1−P1 85.540(11)°, P1−Pd1−S2 88.938(11)°, C1−Pd1−S2 89.3(2)°, S1−Pd1−C1 94.4(2) °. Color code: C, gray; B, brown; Cl, green; P, violet; Pd, light blue; S, orange.*

X-ray quality crystals of **23** were grown from PhF/hexanes. X-ray structural analyses of **20**, **22**−CH_3CN, and **23** (Fig. 69-71) show that the $[PR_2CB_9Cl_9]^-$ ligands are bound in a κ^2-P,Cl mode in these complexes. The B−Cl bond lengths for the bound B−Cl units **20**: 1.790(2) Å, **22**−CH_3CN: 1.795(2) Å; **23**: .800(2) Å) are ca. 0.03Å longer than average lengths of the terminal B−Cl bonds in the *ortho* layer of the carboranyl unit **20**: 1.761(1)Å, **22**−CH_3CN: 1.768(1)Å; **23**: 1.764(4)Å), similar to what is observed for **C**.[54] The 5-membered Pd−P−C−B−Cl chelate ring adopts an envelope conformation in **23** and a planar conformation in **20** and **23**. The Pd−Me group is *cis* to the phosphine in all three complexes as expected due to the stronger *trans* influence of the phosphine versus the weakly coordinating B−Cl unit. In the solid-state structure of **20**, the positively charged $[Li(THF)_3]^+$ unit is in close contact with the sterically accessible P-Cl of one of the $[CB_9Cl_9]^-$ units, indicative of negative charge density located on the cluster.

X-ray quality crystals of **24**·$(CH_2Cl_2)_2(pentane)_{1.5}$ were grown from CH_2Cl_2/pentane. In contrast to the κ^2-P,Cl bonding mode observed for the $[PR_2CB_9Cl_9]^-$ ligands in **20**, **22**−CH_3CN, and **23**, X-ray analysis shows that the $[P(o\text{-MeO-Ph})_2CB_9Cl_9]^-$ ligand in **24** is bound in a κ^2-P,O mode through one of the *o*-anisolyl methoxy groups (Fig. 72). The difference in structure between **23** and **24** may be driven by steric effects. Analysis of a space-filling model of **22** (Fig. 100, *Experimental*) reveals that the PPh_2 rings are pinned by the bulky perchlorocarboranyl unit in sterically crowded positions that would be inaccessible for the larger P(*o*-MeO−Ph)$_2$ groups of **24** (Fig. 106, *Experimental*). Additionally, the ether functionality in **24** is a stronger donor compared to the weakly coordinating B−Cl moiety of the $[CB_9Cl_9]^-$ unit. The Pd−P−C−C−O chelate ring in **24** adopts an envelope conformation. The non-Pd-bound MeO- group is positioned above the

Pd square plane and is in close contact with the Pd center (Pd−O3 = 3.063Å; sum of O and Pd van der Waals radii = 3.15Å).

X-ray quality crystals of **25** were grown from layering THF and benzene. In further contrast from **22**-**24**, where the phosphorous is *cis* to the Pd-methyl group, **25** chelated in a k^3-P,S,S configuration to the Pd center forcing a *trans* relationship between the phosphorous and Pd-methyl (Fig. 73). Both 5-membered Pd−P−C-C−S chelate rings adopt an envelope conformation. Additionally, the *trans* influence from the phosphorous onto the Pd-methyl group elongates that bond substantially to 2.081(6)Å, relative to the average Pd-methyl bond lengths for **22**-**24** (2.023(1)Å). Furthermore, each methyl group from the thioether point in opposite directions, relative to the planes of the chelate rings.

The $^{11}B\{^1H\}$ NMR spectra of **20** and **22**-**25** contain three resonances in a 1:4:4 intensity ratio, indicative of effective local C_{4v} symmetry of the $[CB_9Cl_9]^-$ cluster. This is consistent with the $[CB_9Cl_9]^-$ unit rotating rapidly around the C−P bond with concomitant exchange of the Pd-bound and non-Pd-bound B−Cl units on the *ortho*-ring of the carborane clusters in these compounds, as observed previously for **C**.[54]

The low-temperature (−60°C ^1H NMR and $^{13}C\{^1H\}$ NMR spectra in CD_2Cl_2 of **24** contain two sets of *o*-anisolyl resonances (Fig. 73). The difference in the chemical shifts of the MeO- resonances (^1H: Δδ = 0.32; ^{13}C: Δδ(13 C) = 3.7) is close to the coordination shift for the THF α-H resonances (^1H: δ − δ_{free} = 0.47;^{13}C: δ_{bound} − δ_{free} = 4.6), which is consistent with the coordination of one MeO- group to Pd, observed in the solid-state structure. The ^1H NMR and $^{13}C\{^1H\}$ spectra of **24** in CD_2Cl_2 at room temperature contain one set of *o*-anisolyl resonances, indicating that the *o*-anisolyl groups exchange rapidly on the NMR time scale at this temperature (Fig. 74). The barrier to anisolyl group

exchange, $\Delta G^{\ddagger}$ = 12.3kcal/mol, was determined from the coalescence of the MeO- ^{1}H NMR resonances ($T_{coalescence}$ = −5°C, 500MHz). The $^{11}B\{^{1}H\}$ NMR spectrum of **24** is similar to those of **20**, **22**, **23**, and **25** indicating that the $[CB_9Cl_9]^-$ unit rotates rapidly around the C−P bond, regardless of the phosphine−carborane bonding mode, κ^2-P,Cl or κ^2 P,O.

The ^{1}H and $^{31}P\{^{1}H\}$ NMR spectra of **21** at −60°C in CD_2Cl_2 show that this species exists as a 1.6/1 mixture of two isomers, each of which exhibits two sets of anisolyl resonances in the ^{1}H spectrum. The isomers are assigned as diastereomers that differ in the relative configuration of the phosphorus atoms, which are stereogenic centers due to the κ^2-P,O bonding mode of the [P(*o*-MeO−Ph)$_2$CB$_9$Cl$_9$]$^-$ ligand. In contrast, only one species is observed at room temperature and −60°C in the ^{1}H and $^{31}P\{^{1}H\}$ NMR spectra of κ^2-P,Cl-**20**. The difference in the ^{1}H chemical shifts for the Pd-bound and non-Pd-bound MeO- groups of **21** ($\Delta\delta_{major\text{-}isomer}$ = 0.52, $\Delta\delta_{minor\text{-}isomer}$ = 0.80) are similar to that for **24**. Isomer exchange is fast on the NMR time scale at 23°C due to fast exchange of the Pd-bound and non-Pd-bound methoxy groups.

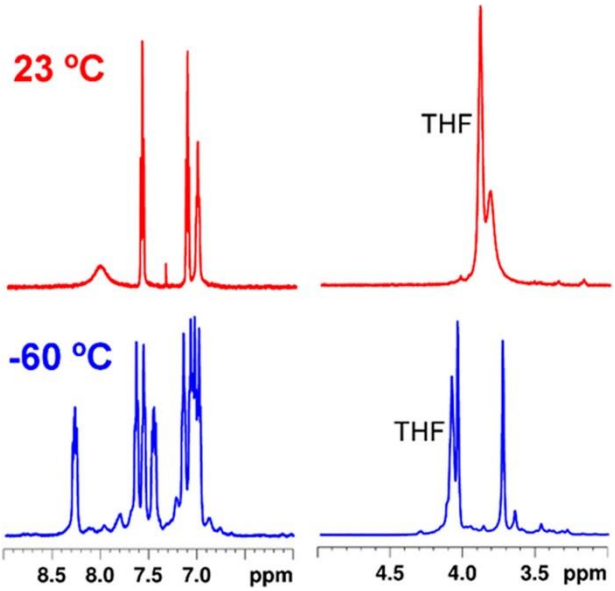

*Figure 73. ^{1}H NMR spectra of **24** at 23°C (top) and −60°C (bottom) illustrating the exchange of the anisolyl rings. The aromatic and MeO- regions of the spectra are shown. The MeO- resonances appear at δ 4.05 and 3.73 at −60°C and are coalesced at 23°C (CD_2Cl_2).*

We next sought to investigate how complexes **22**-**25** react with ethylene. Complexes **22** and **23** oligomerize ethylene to a Schulz−Flory distribution of C_4−C_{10} olefins at 23°C and 2atm ethylene pressure in mixed toluene/fluorobenzene solvent (Table 2). GC-MS analysis of the oligomers shows that **22** produces predominately α-olefins, while **23** produces an approximately 1/1 mixture of α-olefins and internal olefins. Catalyst **22** is 5 times more active than **23**. In both cases, the catalytic activity and molecular weight distribution of the oligomers (as assessed by the Schulz−Flory propagation probability α, Fig. 123 and 124, *Experimental*)[144] are independent of ethylene pressure and are unaffected by the addition of $B(C_6F_5)_3$.

Table 2. Ethylene Oligomerization Data for Catalysts **22** and **23**[a]

Entry[b]	cat.	P (atm)	Ethylene Consumed (mg)[d]	activity (Kg mol_{Pd}^{-1} h^{-1})	TOF (h^{-1})	α[e]	% α-olefin[f]
1	**22**[c]	2	420	210	7500	0.15	85
2	**22**[c]	6	470	240	8400	0.16	91
3[g]	**22**[c]	6	450	220	8000	0.17	83
4	**23**[h]	2	450	45	1600	0.22	47
5	**23**[h]	6	513	51	1800	0.17	46
6[g]	**23**[h]	6	540	54	1900	0.16	48

[a]Conditions: 49mL of toluene, 1mL of fluorobenzene, 23°C, 2h. [b]Average of two identical runs. [c]1μmol of Pd. [d]Determined by mass flow.[e]Schulz−Flory propagation probability. [f]Percentage of olefins that are α-olefins, determined by GC-MS. [g]1eq of $B(C_6F_5)_3$ added. [h]5μmol of Pd.

Table 3. Ethylene Polymerization Data for Catalyst **24**[a]

Entry[b]	P (atm)	yield (mg)	activity (Kg mol_{Pd}^{-1} h^{-1})	TOF (h^{-1})	M_n (Da)[c]	Đ[d]	Branches/1000 C[c]	Tm (˚C)[g]
1	2	103	10.3	370	1080	1.6	14	82.5, 92.3, 104.5
2[e]	2	345	34.5	1240	720	1.4	15	73.2, 89.2, 97.4
3	6	135	13.5	480	950	1.6	12	77.9, 87.0, 103.0
4[f]	6	132	13.2	470	980	1.6	13	76.6, 86.6, 102.6
5	54	100	10	360	810	1.5	14	71.0, 101.5

[a]Conditions: 49mL of toluene, 1mL of fluorobenzene, 23°C, 2h, 5μmol of Pd. [b]Average of two identical runs. [c]Determined by ^1H NMR. [d]Determined by GPC. [e]50°C. [f]1 equiv of $B(C_6F_5)_3$ added. [g]Determined by DSC.

Complex **24** reacts with ethylene at 23°C and 2atm ethylene pressure to produce polyethylene (PE) wax with a narrow molecular weight distribution characteristic of a single-site catalyst (Table 3). At 50°C, the activity is increased by a factor of 4, while the M_n value of the product is decreased by a factor of 3. As observed for **22** and **23**, the catalyst activity and M_n of the polymer are independent of ethylene pressure (up to 54atm) and are unaffected by the presence of $B(C_6F_5)_3$. The observation that the ethylene oligomerization/polymerization activity of **22**-**24** is independent of ethylene pressure and unaffected by the presence of $B(C_6F_5)_3$ suggests that the resting state for these catalysts is the corresponding $(PR_2CB_9Cl_9)PdR'(\eta^2\text{-}H_2C{=}CH_2)$ ethylene complex (R′ = growing chain). The observation that the molecular weight of the oligomer/polymer product is independent of ethylene pressure is consistent with an associative chain transfer mechanism, which is typical for square planar ethylene polymerization catalysts.[145] Complex **25** was completely unreactive toward ethylene under all conditions. This is a result of the unique binding mode of ligand **18** that forces the *trans* P-Pd-CH_3 confirmation.

The PE formed by **24** was characterized by ^1H and $^{13}C\{^1H\}$ NMR. Peak assignments were made based on literature data and 2D NMR experiments (see the Experimental section).[146–155] The PE produced by **24** at 23°C contains one olefin unit per chain, of which >95% are internal olefins. The internal olefins comprise primarily 2-olefins (42%), followed by 3-olefins (21%), 4-olefins (10%) and 5+-olefins (27%), with 70% of the total olefins in the *trans* configuration. The PE produced at 50°C contains 90% internal olefins (Table 3, entry 2) in a 1/1 *cis/trans* ratio. The PEs produced at both 23 and 50°C contain ca. 13 branches per 1000 C (i.e., ca. one branch per chain) as determined by ^1H NMR. $^{13}C\{^1H\}$ NMR analysis shows that methyl, ethyl and *sec*-butyl branches are present in a 3/1/1 ratio. The PE microstructure is independent of ethylene pressure and is

unaffected by the presence of $B(C_6F_5)_3$. DSC analysis shows that the PE produced by **24** melts over abroad temperature range (Fig. 134, *Experimental*) with apparent T_m value of ca. 80, 90, and 103°C (Table 3). Similar results have been observed for other low-molecular-weight PE waxes.[156–159] For example, saturated linear Fischer−Tropsch waxes, such as SasolWax H1 (M_n = 800, Đ = 1.4, 1.6 branches/1000 C), exhibit multiple melt transitions in DSC that are very similar to those observed for the PE formed by **20**.[102] This behavior has been ascribed to the melting of crystallites consisting mainly of short chains at lower temperature and the progressive melting of crystallites composed primarily of longer and longer chains as the temperature is raised.[156,160–162] Generation of a $(PR_2CB_9Cl_9)PdMe(\eta^2\text{-}H_2C{=}CH_2)$.

The reaction of **24** with ethylene was studied by NMR at low temperature in order to probe ethylene binding and monitor the chain growth process. The reaction of **24** with excess ethylene at −78°C in CD_2Cl_2 generates the ethylene adduct (κ^2-P,O-(*o*-MeO-Ph)$_2CB_9Cl_9$)PdMe($H_2C{=}CH_2$) (**26**, Fig. 75). The bound ethylene in **26** gives rise to an AA′BB′ pattern at δ5.42 and 5.30 in the ^1H NMR spectrum and a singlet at δ101.5 in the $^{13}C\{^1H\}$ NMR spectrum at −78°C, consistent with rapid rotation of the bound ethylene around the Pd−ethylene centroid bond.[163] The ^1H and $^{13}C\{^1H\}$ spectra of **26** at −78°C

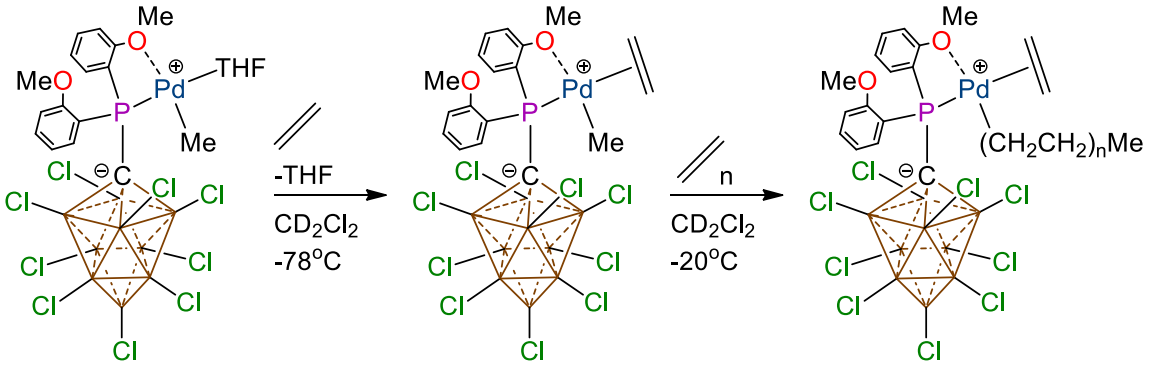

24 **26** **27**

*Figure 74. Generation of ethylene complex **26** and subsequent reaction with ethylene to generate **27**.*

contain two MeO- resonances, the chemical shift differences of which are similar to those observed for **24** and consistent with a κ^2-P,O bonding mode for the phosphine−carborane ligand. The Pd−Me group gives rise to a doublet in the ^{1}H NMR spectrum with a small J^3_{PH} value (3Hz) and a singlet in the $^{13}C\{^1H\}$ spectrum, indicating that the Me group is *cis* to the phosphine. The ^{1}H−^{1}H NOESY spectrum of **26** (−78°C) contains strong correlations between the bound ethylene resonance and the Pd−Me resonance and one MeO- resonance (δ4.03, Pd- bound), as well as a weak correlation with the other MeO- resonance at (δ3.71, non-Pd-bound) (Fig. 115, *Experimental*). The bound ethylene ^{1}H NMR resonances are coalesced with the free ethylene resonance at −30°C. The MeO- ^{1}H NMR resonances are coalesced at −20°C, indicating that **26** undergoes an anisolyl group exchange process, as observed for **24**. Complex **26** undergoes repetitive ethylene insertion at −20°C to generate a mixture of (κ^2-P,O-P(*o*-MeO−Ph)$_2$CB$_9$Cl$_9$)-PdR′(η^2-$H_2C{=}CH_2$) alkyl species (**27**, R′ = growing chain). β-H elimination and olefin formation do not occur at this temperature; therefore, the polymerization is living. The chain growth process was monitored by ^{1}H NMR. As 1 molecule of THF is released per equivalent of **24** in the formation of **26**, the total concentration of Pd species during chain growth is [Pd] total = [**26**] + [**27**] = [THF]. Therefore, the average number of ethylene units inserted per Pd−R′ chain,

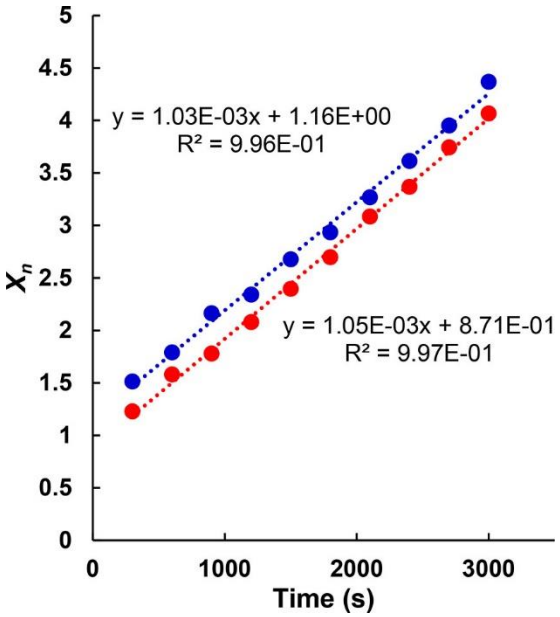

*Figure 75. Representative plots of X_n versus time for the reaction of in situ-generated **26** with ethylene at −20°C. Blue data and curve: $[Pd]_{total}$ = 9.3mM, $[ethylene]_{initial}$ = 0.15M (16 equiv). Red data and curve: $[Pd]_{total}$ = 9.1mM, $[ethylene]_{initial}$ = 0.32M (35 equiv). The two curves do not overlap because the extent of chain growth at the beginning of data collection was different for the two runs. This difference affects the y intercept but not the slope of the line.*

X_n, is equal to the ratio (total integral of the Pd−R′ resonances)/(integral of the THF β-H resonance). Plots of X_n versus time are linear with a slope that is independent of ethylene concentration (Fig. 76), indicating that the growth rate is zero-order in ethylene, which is consistent with the polymerization results. The composite insertion rate constant (for Pd−Me and Pd−R′), *k* insertion (eq1), was determined to be $1.05(6)\times10^{-3}s^{-1}$ (−20°C), which corresponds to an apparent insertion barrier $\Delta G^{\ddagger}$ insertion of 18.1(1)kcal/mol.

Conclusion

In conclusion, we have described the synthesis and characterization of **22**-**25**, which contain phosphino-perchlorocarba-*closo*-decaborate ligands. Compounds **22** and **23**, which contain κ^2-P,Cl-$[PR_2CB_9Cl_9]^-$ ligands, oligomerize ethylene to C_4−C_{10} olefins, while **24**, which contains a κ^2-P,O-$[P(o\text{-MeO-Ph})_2CB_9Cl_9]^-$ ligand, polymerizes ethylene to PE wax. These results contrast with the lack of reactivity with ethylene observed for $[PR_2CB_{11}Cl_{11}]^-$ complex **C**.[54] Though complex **25** was unreactive towards ethylene, it showed an interesting binding mode with the κ^3-P,S,S-$[P(o\text{-MeS-Ph})_2CB_9Cl_9]^-$ ligand. Catalyst **22**, which contains a strong donor P^iPr_2 unit, is significantly more active than **23** or **24**, which contain $P(aryl)_2$ units. A similar trend was observed for analogous phosphine-arenesulfonate palladium alkyl catalysts **A**.[143] It is notable that **23** is ca. 4 times more reactive than trifluoroborate analogue **B**/$[H(OEt_2)_2]^+[B(3,5\text{-}(CF_3)_2C_6H_3)_4]^-$, as assessed by the TOFs for ethylene oligomerization/dimerization.[121,125] As the catalyst resting state in both cases is the corresponding PdR(η^2-$H_2C{=}CH_2$) species, this reactivity trend is due to a difference in the ethylene insertion rate. The steric bulk of the perchlorocarborane backbone may contribute to the enhanced reactivity of **23**. The combination of the low molecular weight, low branch density, predominance of short branches, and

preponderance of internal olefins in the polyethylene formed by **24** indicates that the secondary alkyl−metal species formed by chain walking undergo preferential chain transfer rather than chain growth.

Experimental

General Considerations. All manipulations were carried out using standard Schlenk or glovebox techniques under a nitrogen or argon atmosphere at room temperature unless otherwise stated. Fluorobenzene was dried over and distilled from P_2O_5 or CaH_2. THF was dried and distilled from K metal. CH_2Cl_2, pentane, and toluene were purified by passage through BASF R3−11 oxygen scavenger and activated alumina. CD_2Cl_2 was dried over P_2O_5 or 3Å molecular sieves and degassed. CD_2Cl_2 and CD_3CN were dried over 3Å molecular sieves and degassed. Unless specifically stated, reagents were purchased from commercial vendors and used without further purification. (*o*-SMe-Ph)$_2$PCl was synthesized from literature procedure.[164] NMR spectra were recorded using Bruker Avance 300MHz, Avance 400MHz, Avance 500MHz, or Avance 600MHz instruments or a Varian Inova 300MHz spectrometer. ^{1}H and ^{13}C{^{1}H} NMR chemical shifts are reported relative to $SiMe_4$ and are internally referenced to the residual solvent resonance. ^{31}P{^{1}H} NMR chemical shifts are externally referenced to H_3PO_4. ^{11}B{^{1}H} NMR chemical shifts were externally referenced to BF_3Et_2O and the baseline of the spectra corrected using a multipoint spline. For all compounds, the carboranyl carbon resonance was not observed in ^{13}C{^{1}H} NMR spectra. NMR assignments for **11**-**25** were made based on peak multiplicities and integrations. NMR assignments for **24** and **26** were made using 2D NMR experiments. High-resolution mass spectrometry (HRMS) was performed on an Agilent Technologies 6210 (TOFLC/MS) ESI/APCI instrument. $[Me_3NH]^+[HCB_9Cl_9]^-$ was synthesized according to literature procedures.[165] (COD)PdMeCl was synthesized

according to literature procedures.[166] The purity of all isolated compounds was established by multinuclear NMR and high-resolution mass spectrometry. Crystallographic data for compounds **20** and **22**-**25** are available free of charge from the Cambridge Crystallographic Data Center under reference numbers 1871350, 1867545−1867547, and 1908800, respectively. This structure can be accessed at: http://www.ccdc.cam.ac.uk/Community/Requestastructure/Pages/DataRequest.aspx.

Synthesis for $[Li(THF)_3]^+[P^iPr_2CB_9Cl9]^-$ (**11**):

$[Me_3NH]^+[HCB_9Cl9]^-$ (0.500g, 1.02mmol) was dissolved in THF (3mL) in a 20mL scintillation vial equipped with a stir bar. *n*-BuLi (2.1 equiv, 2.0M in hexanes) was added, and the mixture was stirred for 30min. This mixture was added to pentane (15mL) that was being stirred, and a white solid precipitated. The solid was collected by filtration, washed twice with pentane, and dried under vacuum. The resulting white powder was dissolved in THF (3mL), $^iPr_2PCl$ (171mg, 1.12mmol) added, and the mixture stirred for 1h. The volatiles were removed under vacuum. The resulting oil was washed with pentane, taken up in PhF, and the insoluble LiCl removed by filtration. The filtrate was evaporated to dryness to yield **11** as a white solid. Yield: 720mg, 92%. ^{1}H NMR (400MHz, CD_2Cl_2, 23°C): δ 3.82 (m, 12H, THF), 2.98 (d of septets, $^3J_{H-H}$ = 7.2Hz; $^2J_{P-H}$ = 1.5Hz, 2H), −CH$(CH_3)_2$), 1.99 (m, 12H, THF), 1.34 (two overlapping dds, $^3J_{P-H}$ = 19.6Hz, $^3J_{P-H}$ = 11.2Hz, $^3J_{H-H}$ = 7.4Hz, $^3J_{H-H}$ = 6.9 Hz, 12H, −CH$(CH_3)_2$). $^{13}C\{^1H\}$ NMR (101 MHz, CD_2Cl_2, 23°C): δ 70.1 (THF), 26.9 (THF), 25.6 (d, $^2J_{P-C}$ = 36Hz, −CH$(CH_3)_2$), 23.2 (d, $^2J_{P-C}$ = 26Hz, −CH$(CH_3)_2$), 22.2 (d,$^1J_{P-C}$ = 12Hz, −CH$(CH_3)_2$). $^{11}B\{^1H\}$ NMR (96MHz, CD_2Cl_2, 23°C): δ 27.2 (1B), −3.0 (4B),−5.6 (4B). $^{31}P\{^1H\}$ NMR (162MHz, CD_2Cl_2, 23°C): δ 45.2. ESI/APCI HRMS (m/z): [M] − calculated for $C_7H_{14}B_9PCl_9$: 544.9044. Found: 544.9044. Mp:

100.0−106.7°C.

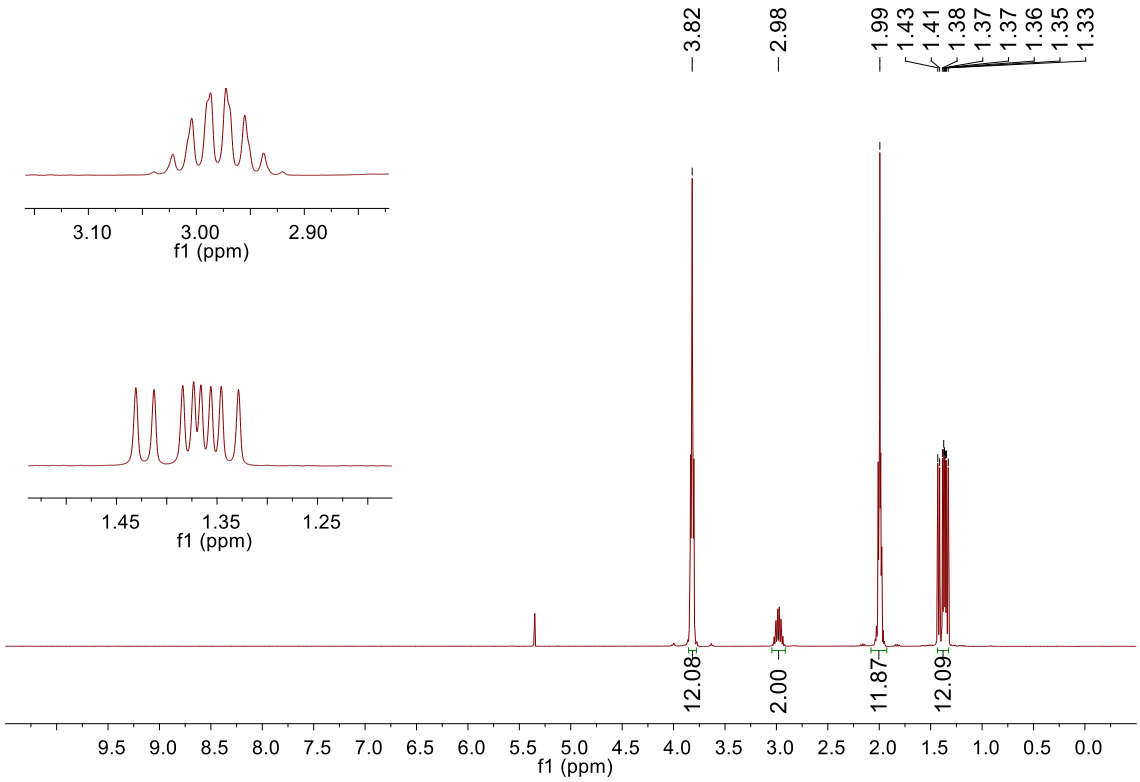

*Figure 76. ^{1}H NMR of **11** (400MHz, CD_2Cl_2, 23°C).*

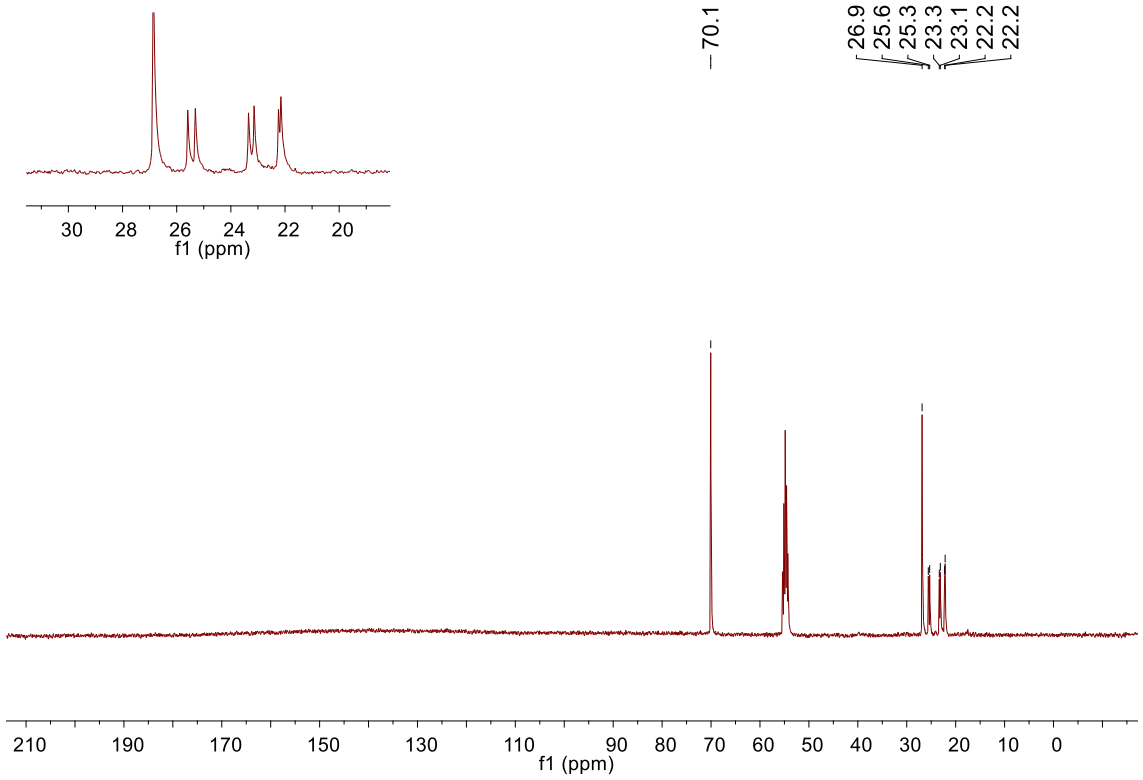

*Figure 77. $^{13}C\{^{1}H\}$ NMR of **11** (101MHz, CD_2Cl_2, 23°C).*

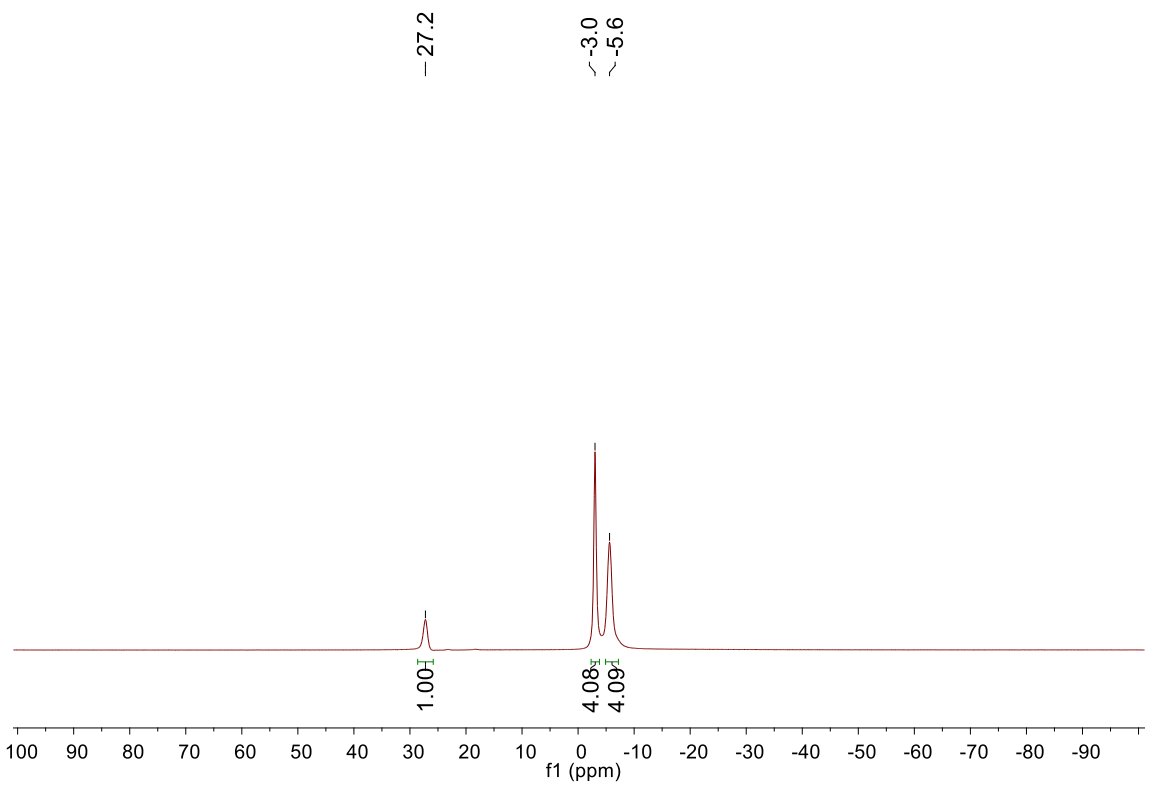

*Figure 78. $^{11}B\{^{1}H\}$ NMR of **11** (96MHz, CD_2Cl_2, 23°C).*

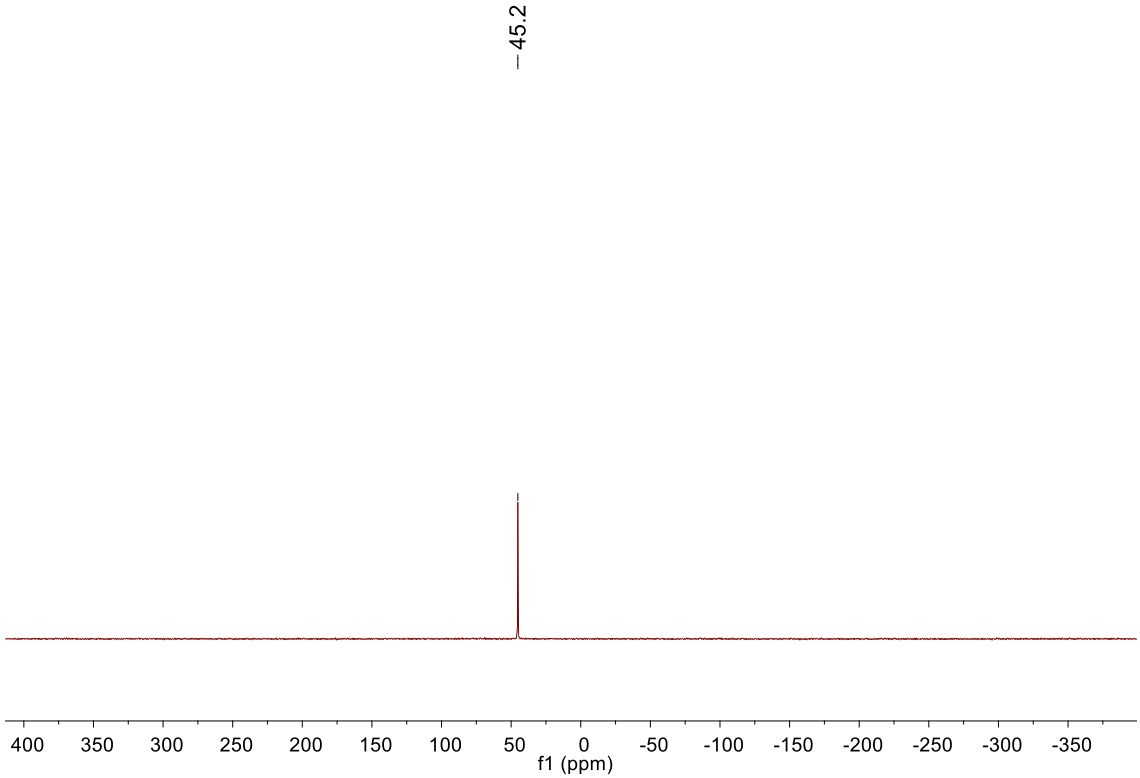

*Figure 79. $^{31}P\{^{1}H\}$ NMR of **11** (162MHz, CD_2Cl_2, 23°C).*

Synthesis for $[Li(THF)_4]^+[PPh_2CB_9Cl_9]^-$ (**16**):

16 was prepared from $[Me_3NH]^+[HCB_9Cl9]^-$ (0.500g, 1.02mmol), *n*-BuLi (2.1 equiv, 2.0 M in hexanes), and Ph 2 PCl (247 mg, 1.12 mmol) using the procedure described above for **11**. Yield: white solid, 880 mg, 95%. ^{1}H NMR (300MHz, CD_2Cl_2, 23°C): δ 8.07 (m, 4H, Ar), 7.37 (m, 6H, Ar), 3.78 (m, 16H, THF), 1.95 (m, 16H,THF). $^{13}C\{^1H\}$ NMR (101MHz, CD_2Cl_2, 23°C): δ 137.5 (d, $^2J_{P-C}$ = 29Hz, *o*-Ph), 133.1 (d,$^1J_{P-C}$= 16Hz, *ispo*-Ph), 130.1 (*p*-Ph), 128.0 (d,$^3J_{P-C}$ = 10Hz, *m*-Ph), 69.1 (THF), 25.9 (THF). $^{11}B\{^1H\}$ NMR (96MHz, CD_2Cl_2, 23°C): δ 20.6 (1B), −4.2 (4B), −6.2 (4B). $^{31}P\{^1H\}$ NMR (162MHz, CD_2Cl_2, 23°C): δ 11.5. ESI/APCI HRMS (m/z): [M] − calculated for $C_{13}H_{10}B_9PCl_9$: 612.8744. Found: 612.8714. Mp: 143.2−145.5°C.

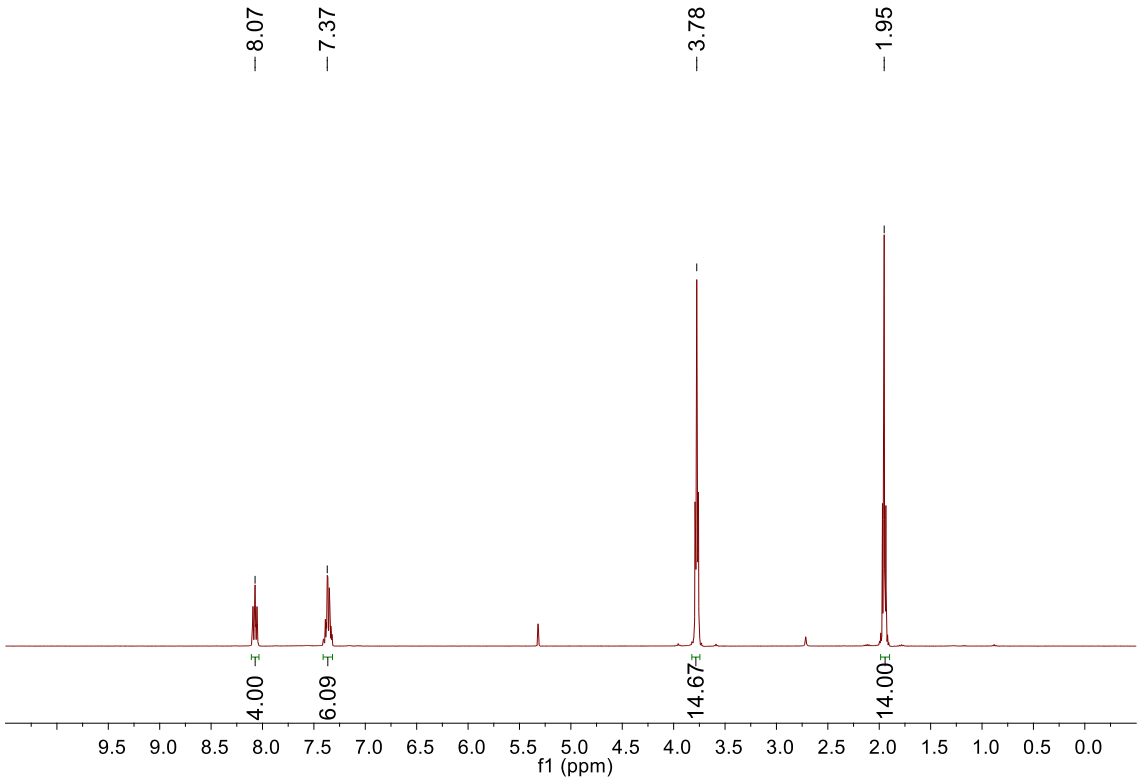

*Figure 80. ^{1}H NMR of **16** (400MHz, CD_2Cl_2, 23°C).*

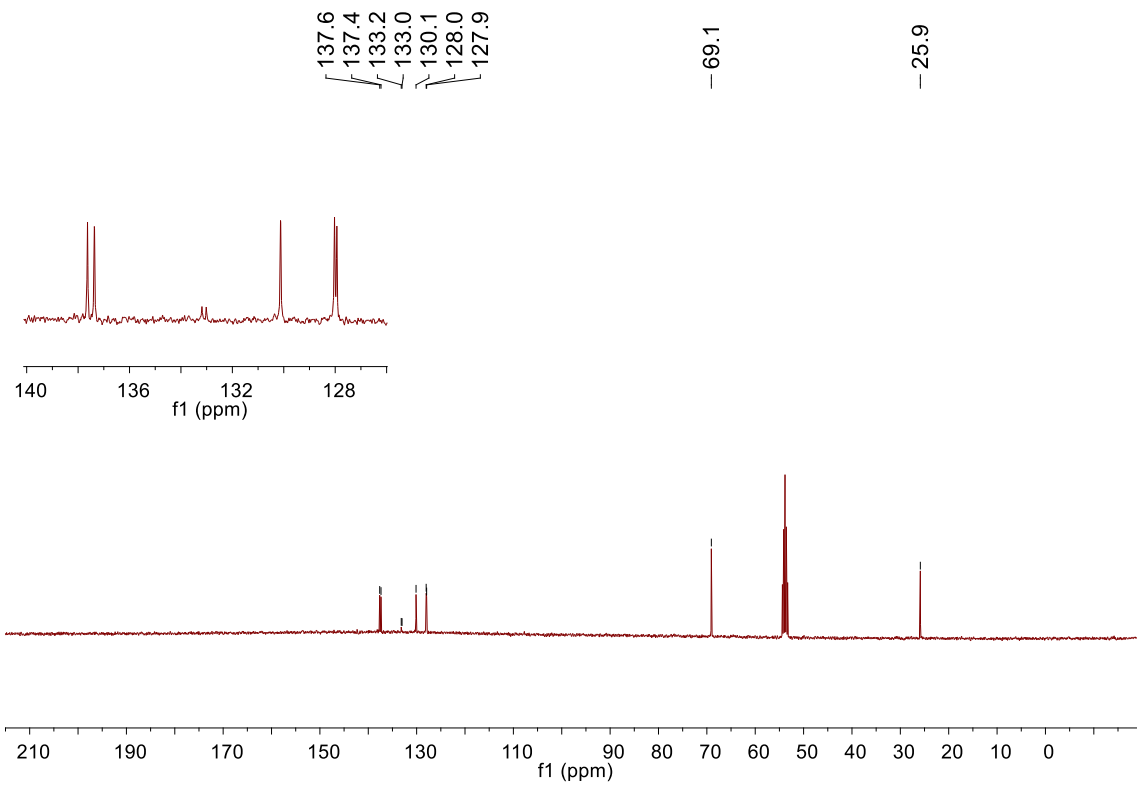

*Figure 81. $^{13}C\{^{1}H\}$ NMR of **16** (101MHz, CD_2Cl_2, 23°C).*

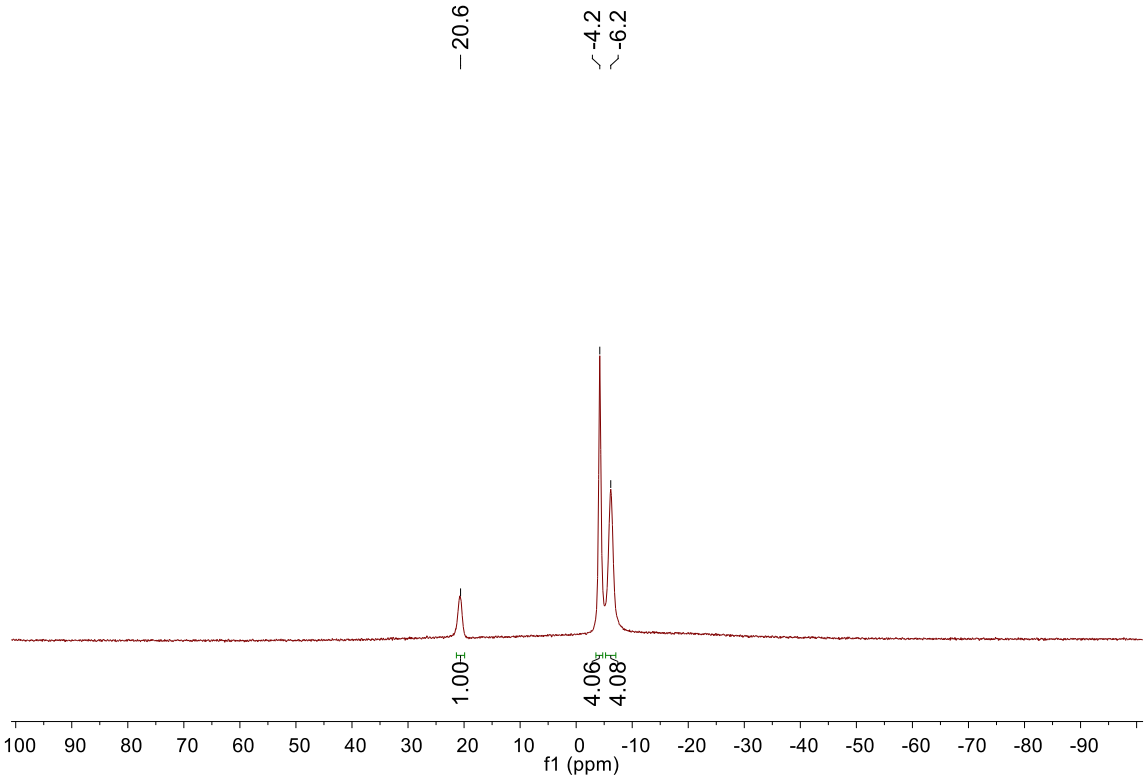

*Figure 82. $^{11}B\{^{1}H\}$ NMR of **16** (96MHz, CD_2Cl_2, 23°C).*

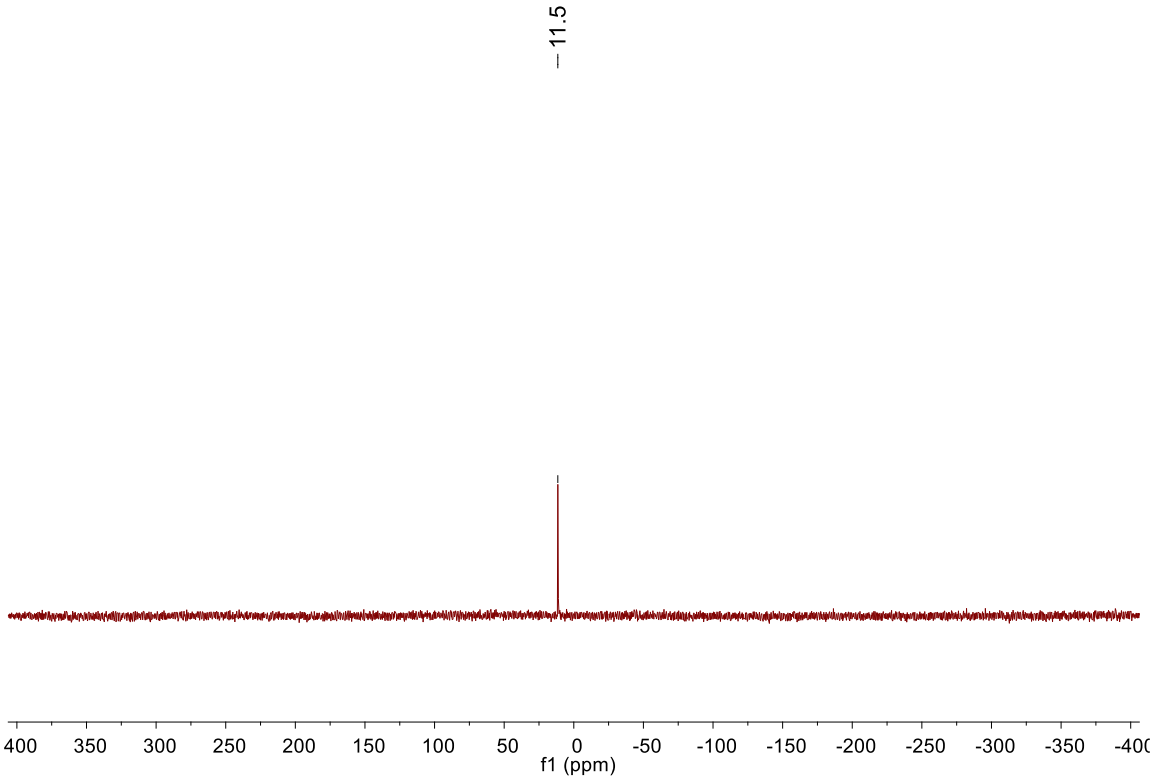

*Figure 83. $^{31}P\{^{1}H\}$ NMR of **16** (162MHz, CD_2Cl_2, 23°C).*

Synthesis for $[Li(THF)_2]^+[P(o\text{-}OMe\text{-}Ph)_2CB_9Cl_9]^-$ (**17**):

17 was prepared from $[Me_3NH]^+[HCB_9Cl_9]^-$ (0.500g, 1.02mmol), *n*-BuLi (2.1 equiv, 2.0 M in hexanes), and $(o\text{-}OMe\text{-}Ph)_2PCl$ (315mg,1.12 mmol) using the procedure described above for **11**. Yield: white solid, 760 mg, 90%.^{1}H NMR (400MHz, CD_3CN, 23°C): δ 7.93 (m, 2H, Ar), 7.36 (m, 2H, Ar), 6.90 (m, 4H, Ar), 3.69 (s,6H, −OCH_3), 3.65 (m, 8H, THF), 1.81 (m, 8H, THF). $^{13}C\{^1H\}$ NMR (101MHz, CD_3CN, 23°C): δ 163.0 (d, $^2J_{P\text{-}C}$ = 22Hz, C−OCH_3), 137.7 (Ar), 131.9 (Ar), 123.2 (d, $^1J_{P\text{-}C}$ = 29Hz, C_{ipso}-P), 120.5(Ar), 111.9 (Ar), 68.3 (THF), 56.4 (−OCH_3), 26.2 (THF). $^{11}B\{^1H\}$ NMR (96MHz, CD_3CN, 23°C): δ 20.3 (1B), −4.4 (4B), −6.3 (4B). $^{31}P\{^1H\}$ NMR (162MHz, CD_3CN, 23°C): δ −9.8. ESI/APCIHRMS (m/z): [M] − calculated for $C_{15}H_{14}B_9O_2PCl_9$: 672.9211 .Found: 672.9199. Mp: 240.1−243.3°C

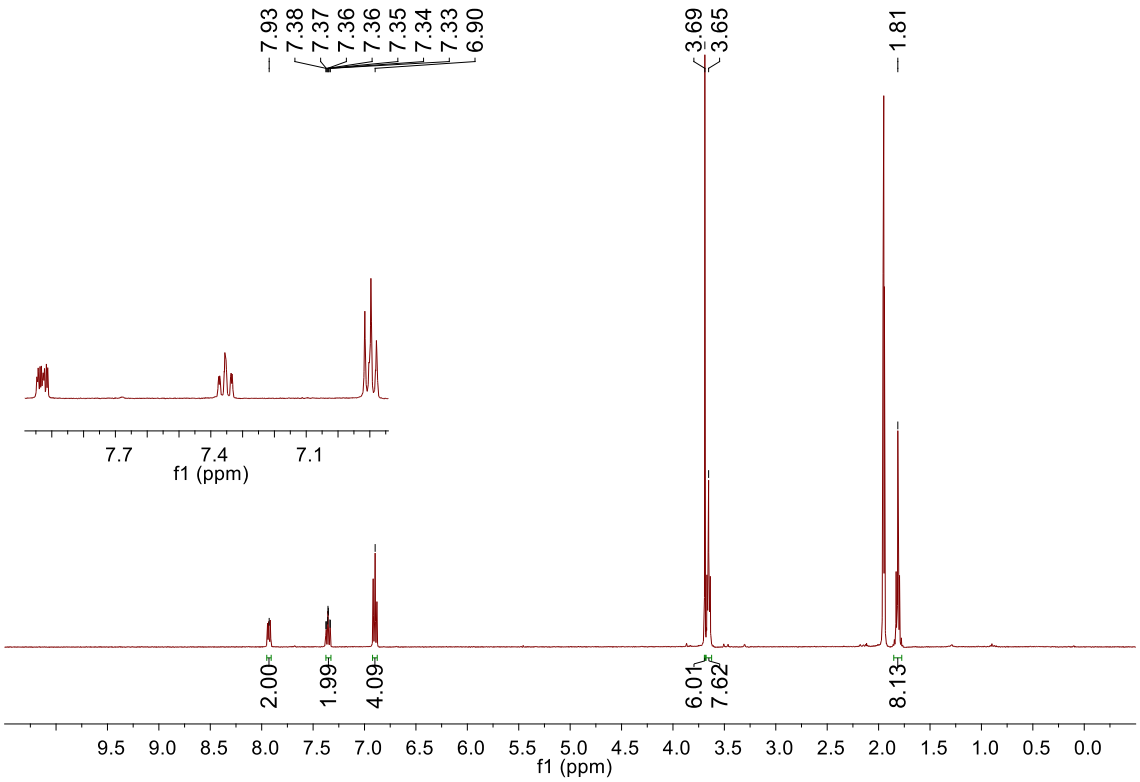

*Figure 84. ^{1}H NMR of **17** (400MHz, CD_2Cl_2, 23°C).*

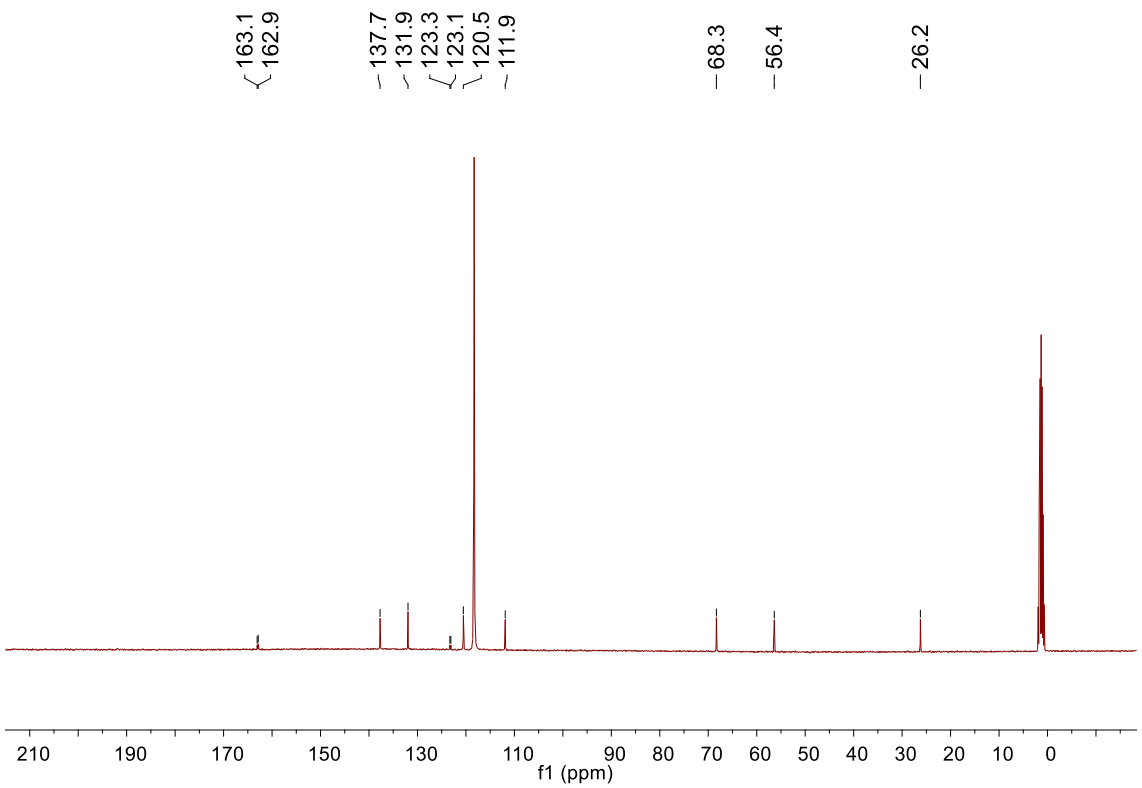

*Figure 85. $^{13}C\{^{1}H\}$ NMR of **17** (101MHz, CD_2Cl_2, 23°C).*

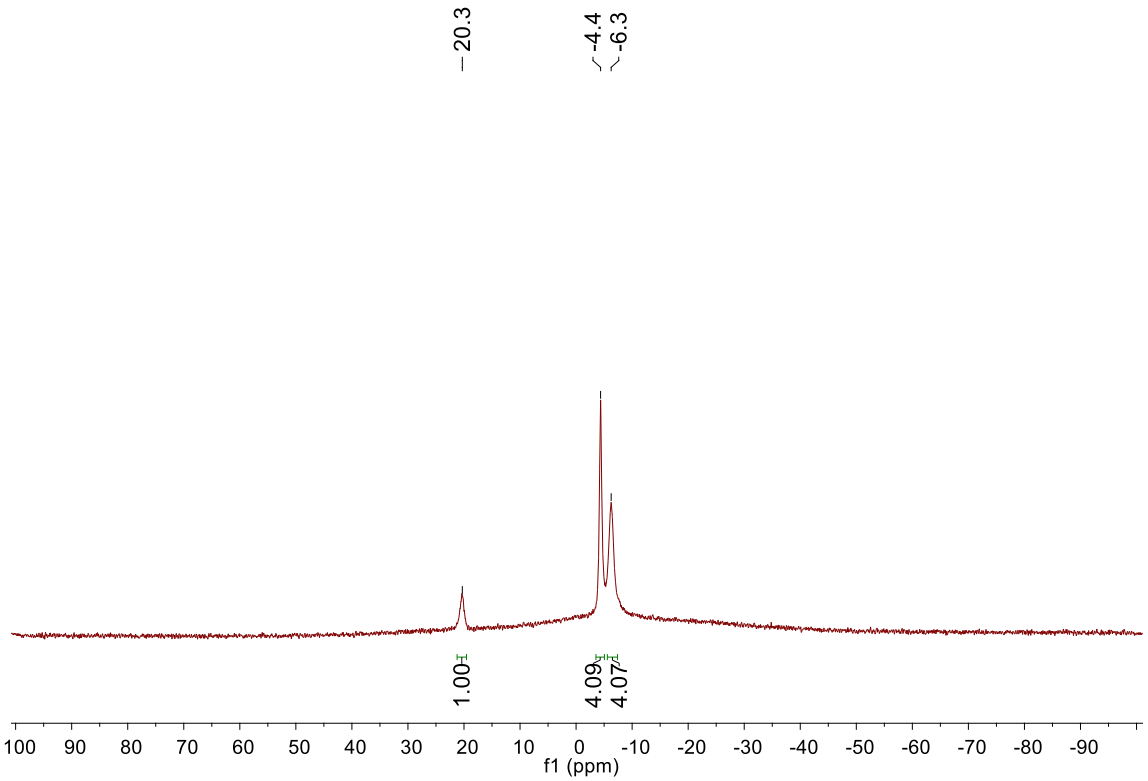

*Figure 86. $^{11}B\{^{1}H\}$ NMR of **17** (96MHz, CD_2Cl_2, 23°C).*

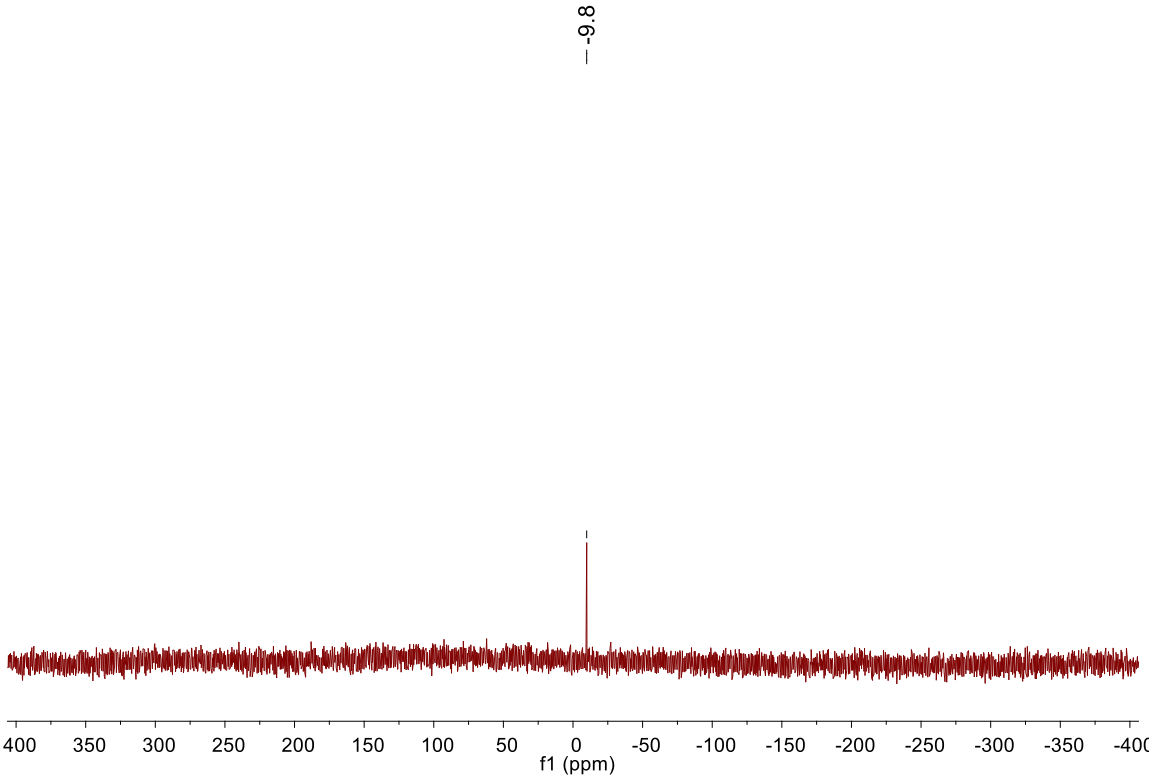

*Figure 87. $^{31}P\{^{1}H\}$ NMR of **17** (162MHz, CD_2Cl_2, 23°C).*

Synthesis for $[Li(THF)_2]^+[P(o\text{-}SMe\text{-}Ph)_2CB_9Cl_9]^-$ (**18**):

18 was prepared from $[Me_3NH]^+[HCB_9Cl_9]^-$ (0.500g, 1.02mmol), *n*-BuLi (2.1 equiv, 2.0 M in hexanes), and $(o\text{-}SMe\text{-}Ph)_2PCl$ (315mg,1.12 mmol) using the procedure described above for **11**. Yield: white solid, 760 mg, 90%.^{1}H NMR (400MHz, CD_2CCl_2, 23°C): δ 8.25 (m, 2H, Ar), 7.36 (td, 2H, ^3J = 7.4Hz, ^1J = 2.2Hz, Ar), 7.28 (td, 4H, ^3J = 7.3Hz, ^1J = 2.1Hz, Ar), 7.20 (td, 4H, ^3J = 7.6hz, ^1J = 2.2Hz, Ar), 3.77 (m, 14H, THF), 2.43 (s, 6H, $-SCH_3$), 1.93 (m, 14H, THF). $^{13}C\{^1H\}$ NMR (101MHz, CD_2CCl_2, 23°C): δ 146.2 (d, $^1J_{P\text{-}C}$ = 34Hz, C_{ipso}-P), 137.7 (Ar), 133.2 (d, $^2J_{P\text{-}C}$ = 14Hz, C-SCH_3), 130.5 (Ar), 127.0 (d, $^2J_{P\text{-}C}$ = 7Hz) 124.6 (Ar), 69.0 (THF), 25.9 (THF), 17.8 ($-SCH_3$). $^{11}B\{^1H\}$ NMR (96MHz, CD_2CCl_2N, 23°C): δ 21.5 (1B), −4.1 (4B), −6.1 (4B). $^{31}P\{^1H\}$ NMR (162MHz, CD_2CCl_2, 23°C): δ −8.4. ESI/APCIHRMS (m/z): [M] − calculated for $C_{15}H_{14}B_9S_2PCl_9$: 843.7443 .Found: 843.7427. Mp: 223.3−228.1°C

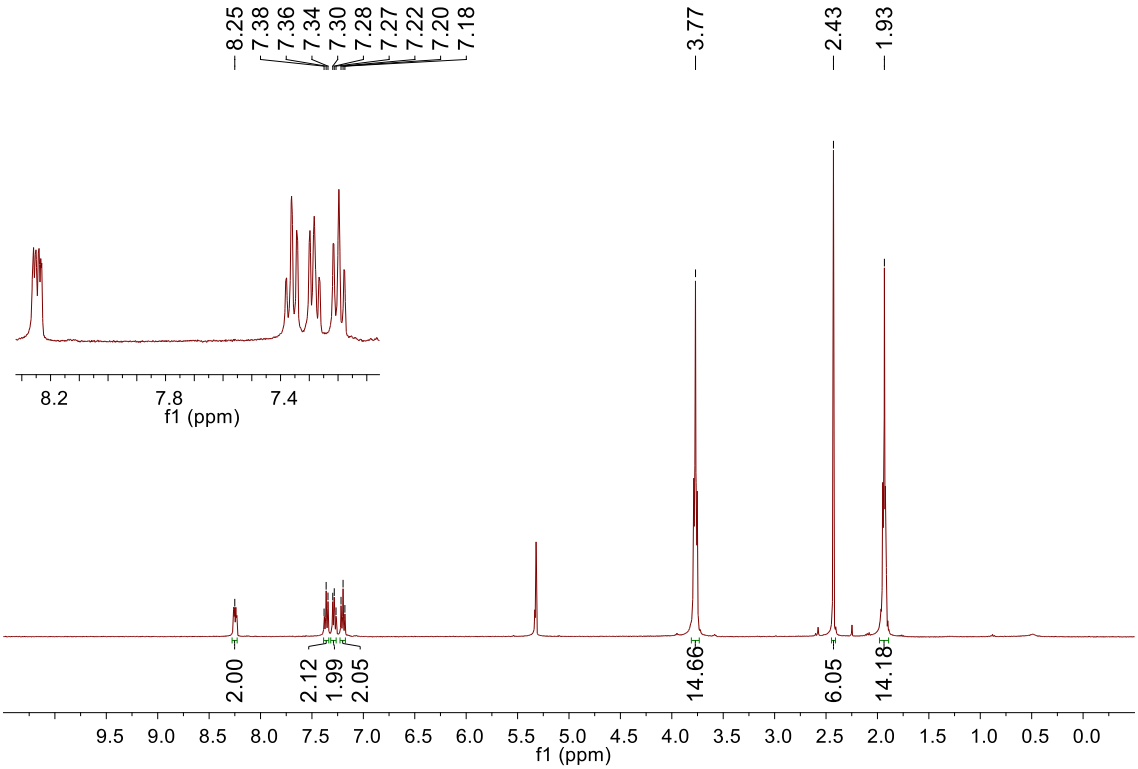

*Figure 88. ^{1}H NMR of **18** (400MHz, CD_2Cl_2, 23°C).*

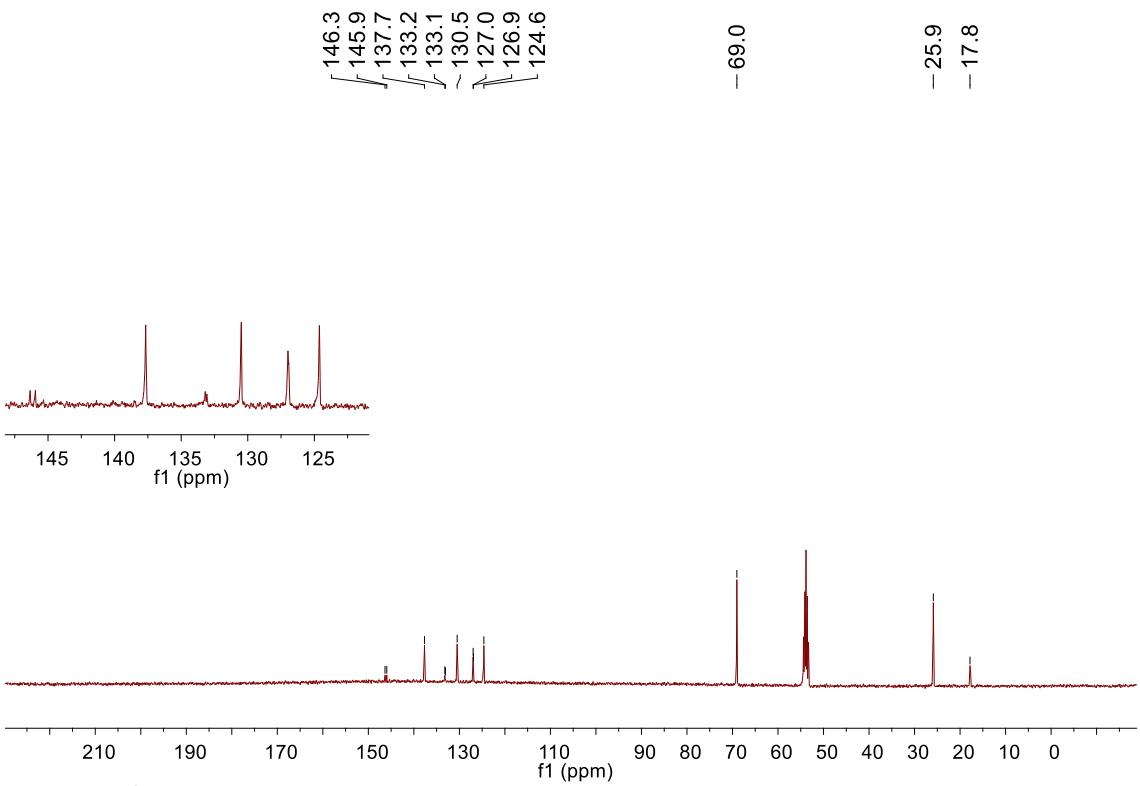

*Figure 89. $^{13}C\{^{1}H\}$ NMR of **18** (101MHz, CD_2Cl_2, 23°C).*

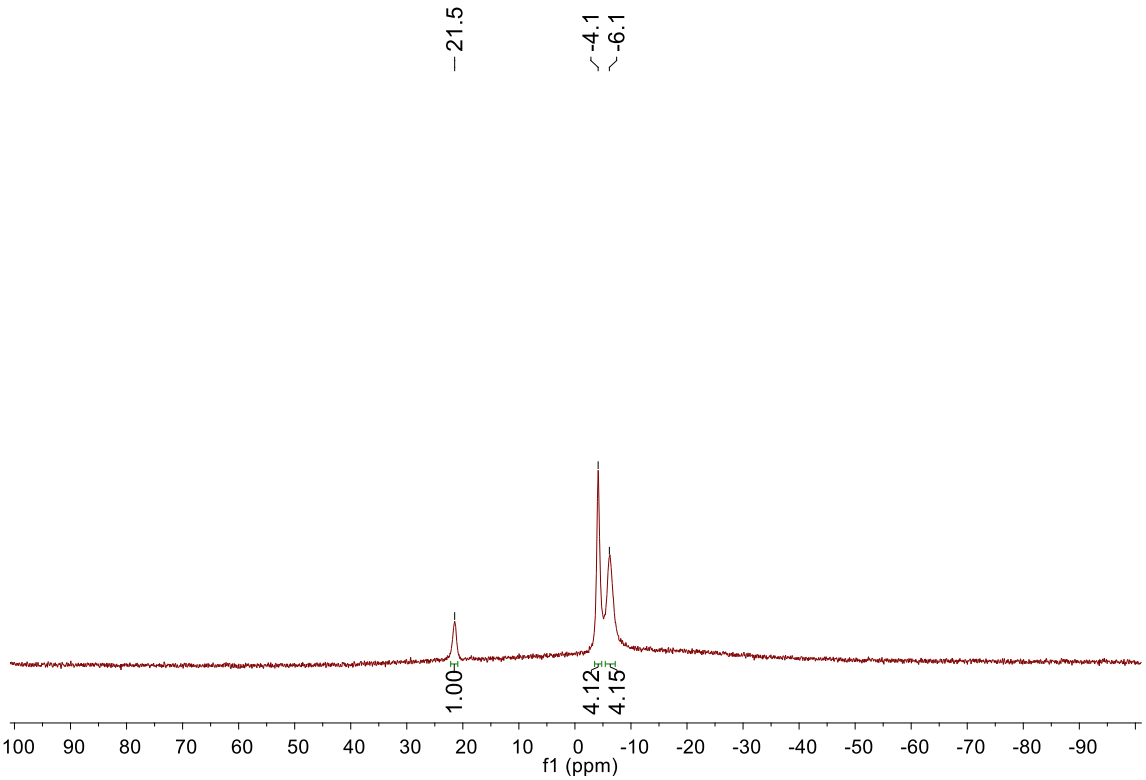

*Figure 90. $^{11}B\{^{1}H\}$ NMR of **18** (96MHz, CD_2Cl_2, 23°C).*

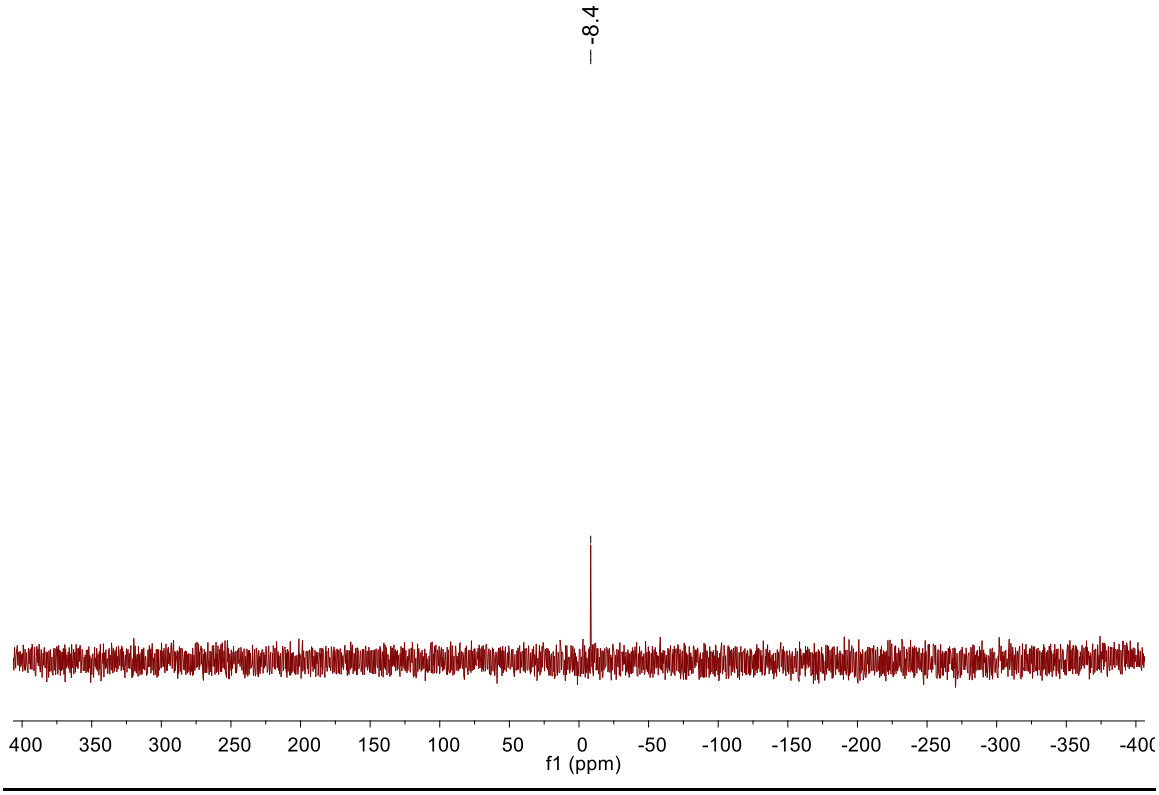

*Figure 91. $^{31}P\{^{1}H\}$ NMR of **18** (162MHz, CD_2Cl_2, 23°C).*

Synthesis for κ^2-P,Cl-P^{i}Pr$_2$CB$_9$Cl$_9$)PdMe(THF) (**22**).

11 (100mg, 0.12mmol) and PhF (1mL) were added to a 20mL scintillation vial equipped with a stir bar. (COD)PdMeCl (31.5 mg, 0.120 mmol) was separately dissolved in PhF (1mL) in a second vial. The (COD)PdMeCl solution was slowly added to the solution of **11**. The second vial was washed with PhF (1mL), and the washing was added to the solution of **11**. The mixture was stirred for 30min and concentrated under vacuum. Pentane was added, and the resulting light brown precipitate was allowed to settle. The pentane supernatant was decanted off, and the precipitate was washed twice with pentane and dried under vacuum to yield **19** as a brown solid. ^{1}H NMR (500MHz, CD_2Cl_2, 23°C): δ 3.07 (m, 12H, THF), 3.27 (m, 4H,−CH(CH$_3$)$_2$), 1.98 (m, 12H, THF), 1.73 (dd, $^3J_{H-H}$ = 7.2Hz, $^2J_{P-H}$ = 19.0Hz), 12H, −CH(CH$_3$)$_2$), 1.01 (overlapping dd and s, $^3J_{H-H}$ = 7.0Hz, $^2J_{P-H}$ = 17.5Hz, 18H, Pd−CH$_3$ and −CH(CH$_3$)$_2$). ^{13}C{^{1}H} NMR (126MHz, CD_2Cl_2, 23°C) δ 68.9 (THF), 27.0 ($^1J_{P-C}$ = 20Hz, −CH(CH$_3$)$_2$), 6.4 (THF), 23.0 (−CH(CH$_3$)$_2$), 19.9 (−CH(CH$_3$)$_2$), 0.3 (Pd−CH$_3$). ^{11}B{^{1}H} NMR (96MHz, CD_3CN, 23°C): δ 24.0 (1B), −3.1 (4B), −5.6 (4B). ^{31}P{^{1}H} NMR (202MHz, CD_2Cl_2, 23°C): δ 76.6. Mp: 92.1−97.5°C (dec). Without further purification, **19** was dissolved in PhF (1mL), and $AgBF_4$ (11.0mg, 0.0600mmol) was added. The mixture was stirred for 4h and filtered, and the collected solid was washed with CH_2Cl_2 (3 × 15mL). The solvent was removed from the filtrate and washed under vacuum to afford **22** as a brown powder that contained a small amount of residual PhF. 81% pure by ^{31}P{^{1}H}NMR. Yield 77mg, 87%. ^{1}H NMR (300MHz, CD_2Cl_2, 23°C): δ3.97 (m, 4H, THF), 3.27 (m, 2H, −CH(CH$_3$)$_2$), 1.98 (m, 4H, THF),1.73 (dd, $^3J_{H-H}$ = 7.1Hz, $^2J_{P-H}$ = 20.6Hz, 6H, −CH(CH$_3$)$_2$), 1.52 (dd, $^3J_{H-H}$ = 7.3Hz, $^2J_{P-H}$ = 20.1Hz, 6H, −CH(CH$_3$)$_2$), 1.43 (s, 3H, Pd−CH$_3$). ^{13}C{^{1}H} NMR (101MHz, CD_2Cl_2, 23°C): δ 72.9 (THF), 27.2 (d, $^1J_{P-C}$ = 24Hz, −CH(CH$_3$)$_2$), 25.6 (THF), 23.3 (br s, −CH(CH$_3$)$_2$), 20.0 (−CH(CH$_3$)$_2$), 1.2 (Pd−Me). ^{11}B{^{1}H}

NMR (96MHz, CD_2Cl_2, 23°C): δ 24.2 (1B), −3.4 (4B), −6.0 (4B). $^{31}P\{^1H\}$ NMR (162MHz, CD_2Cl_2, 23°C): δ 77.4. ESI/APCI HRMS (m/z): [M − THF+ CH_3CN] − calculated for $C_{10}H_{20}B_9NPCl_9$ Pd: 701.8363. Found: 701.8352. Mp: 109.3−117.1 °C (dec).

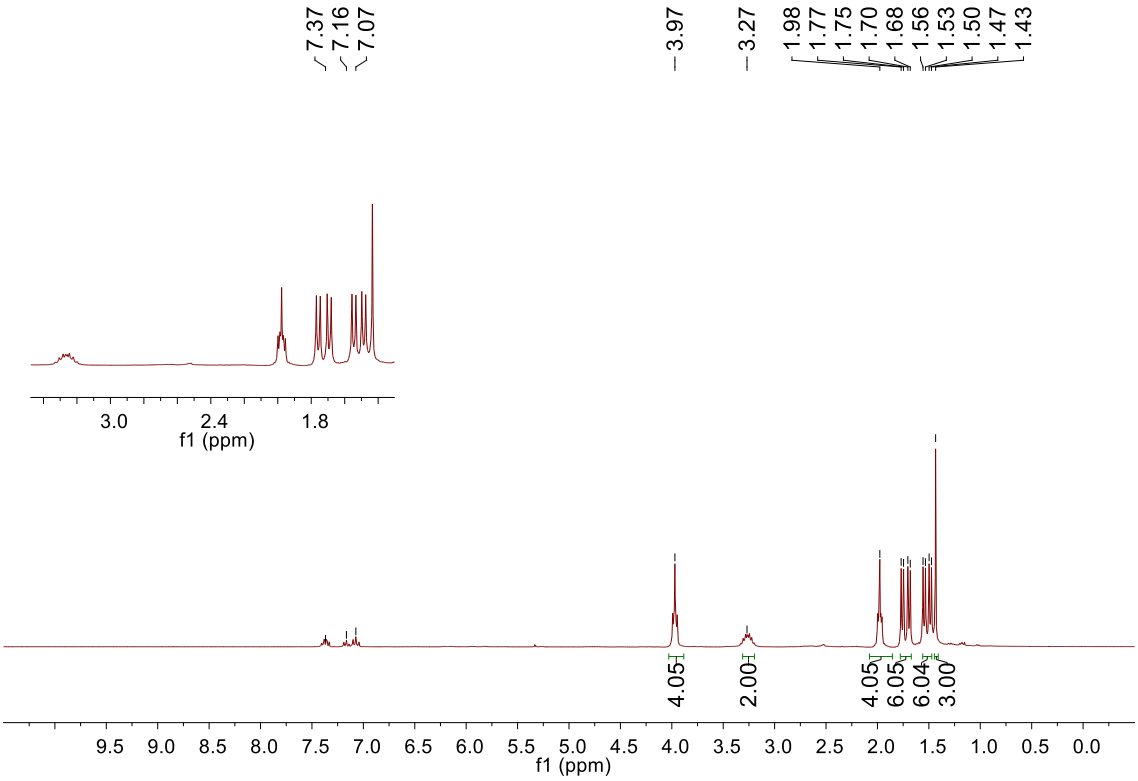

*Figure 92. ^1H NMR of **22** (300MHz, CD_2Cl_2, 23°C). Note: Fluorobenzene impurity is seen at 7.37, 7.16, and 7.07.*

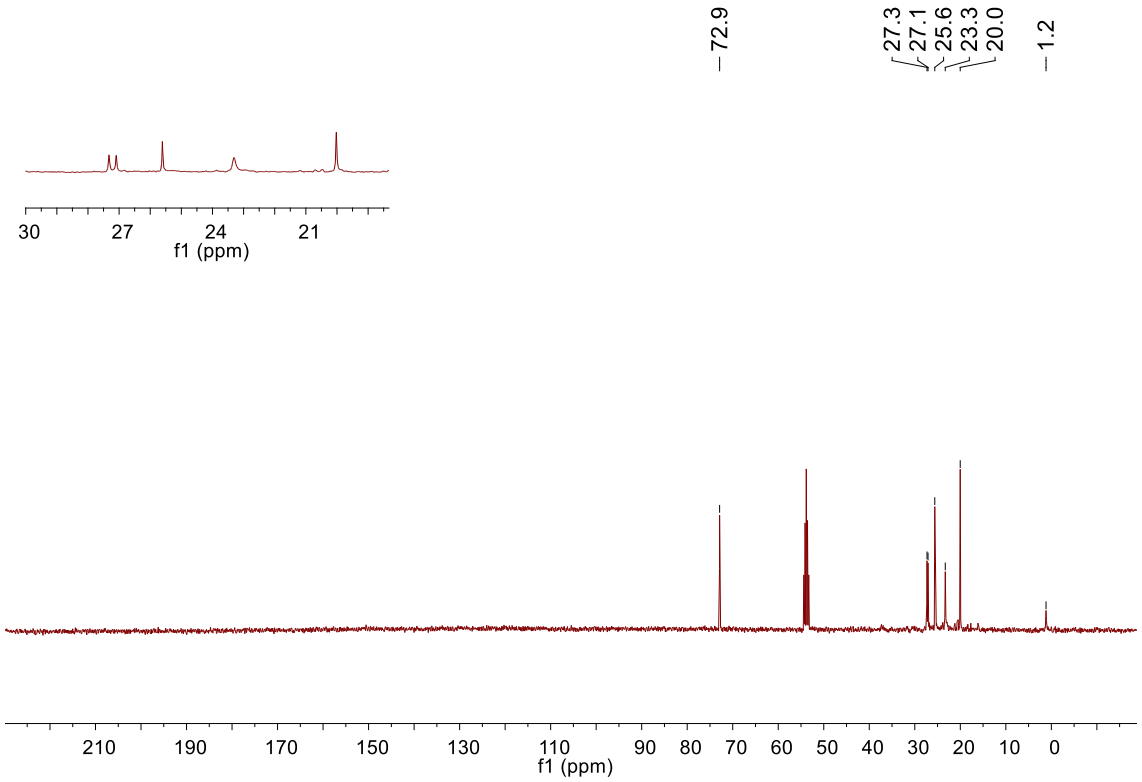

*Figure 93. $^{13}C\{^{1}H\}$ NMR of **22** (162MHz, CD_2Cl_2, 23°C).*

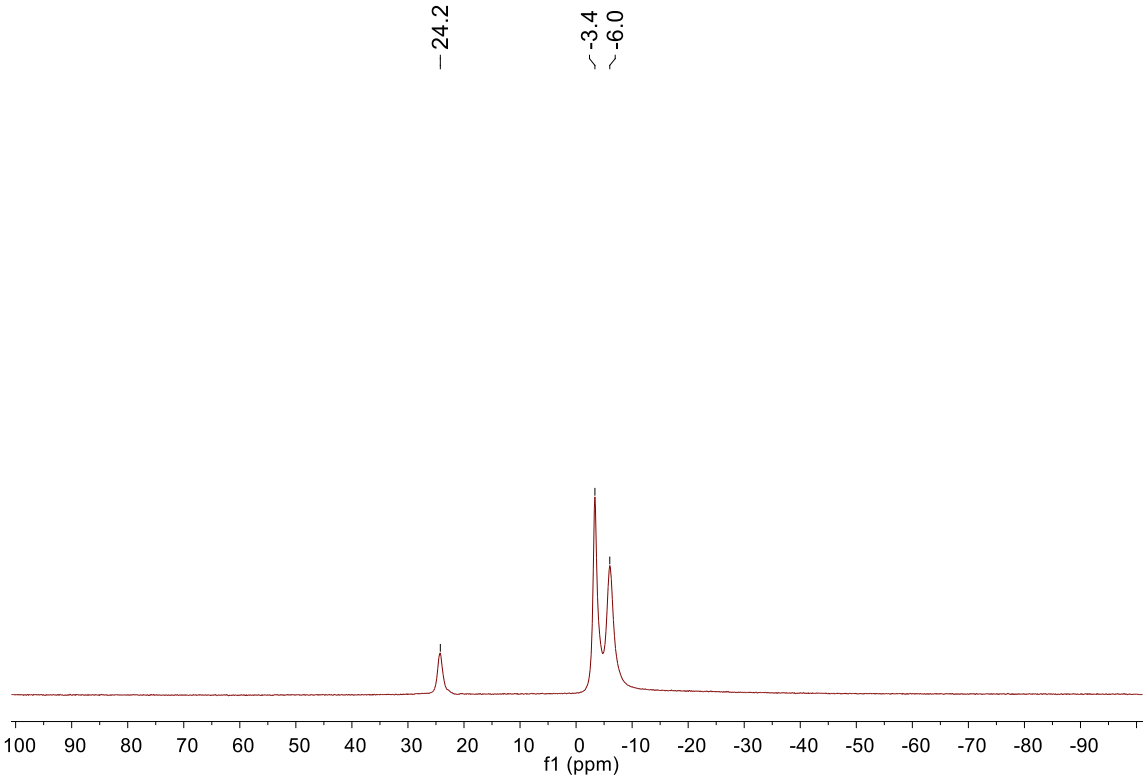

*Figure 94. $^{11}B\{^{1}H\}$ NMR of **22** (162MHz, CD_2Cl_2, 23°C).*

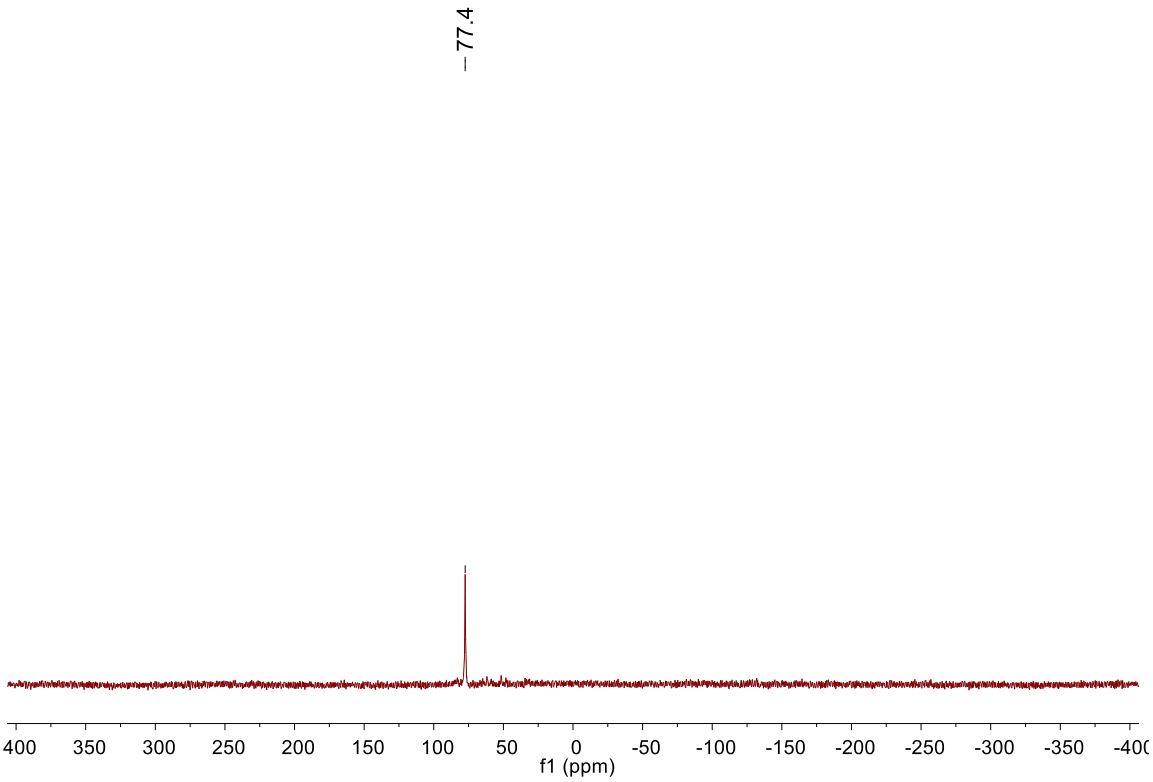

*Figure 95. $^{31}P\{^{1}H\}$ NMR of **22** (162MHz, CD_2Cl_2, 23°C).*

Synthesis for (κ^2-P,Cl-$PPh_2CB_9Cl_9$)PdMe(THF) (**23**):

20 was generated as tan powder from **16** (100mg, 0.110mmol) and(COD)PdMeCl (28.9mg, 0.110mmol) using the procedure for **19**. ^{1}H NMR (400MHz, CD_2Cl_2, 23°C): δ 8.53 (dd, $^2J_{P-H}$ = 12.5Hz, $^3J_{H-H}$ = 8.5Hz, 8H, *o*-Ph), 7.60 (m, 12H, *m*-Ph and *p*-Ph), 3.78 (m, 12H, THF), 1.95 (m, 12H, THF), 1.38 (s, 6H, Pd−CH_3). $^{13}C\{^1H\}$ NMR: δ 138.5 (d, $^2J_{P-C}$ = 16Hz, *o*-Ph), 133.3 (d, $^4J_{P-C}$ = 2Hz, *p*-Ph), 128.8 (d, $^3J_{P-C}$ = 12Hz, *m*-Ph), 124.2 (d, $^1J_{P-C}$ = 55Hz, *ipso*-Ph), 69.2 (THF), 25.9 (THF), 12.6 (Pd−CH_3). $^{11}B\{^1H\}$ NMR (124MHz, CD_2Cl_2, 23°C): δ 23.4 (1B), −3.16 (4B), −5.79 (4B). $^{31}P\{^1H\}$ NMR (162MHz, CD_2Cl_2, 23°C): δ 56.6. Low-temperature NMR data: ^{1}H NMR (500MHz, CD_2Cl_2, −60°C): δ 8.48(dd, $^2J_{P-H}$ = 12.5Hz, $^3J_{H-H}$ = 8.5Hz, 8H, *o*-Ar), 7.59 (m, 12H, *m*-Ar and *p*-Ar), 3.66 (m, 16H, THF), 1.84 (m, 16H, THF), 1.30 (s, 6H, Pd−CH_3). $^{31}P\{^1H\}$ NMR (162MHz, CD_2Cl_2, −60°C): δ 57.8. Mp: 91.4−104.7°C (dec). Without further purification, **20** was reacted with $AgBF_4$ (10.7mg, 0.06mmol) using the procedure described above for **22** to yield **23** as a light brown powder. Yield: 78mg, 88%. ^{1}H NMR (300MHz, CD_2Cl_2, 23°C): δ 8.45 (dd, $^2J_{P-H}$ = 12.5Hz, $^3J_{H-H}$ = 8.5Hz, 4H, *o*-Ph), 7.67 (m, 6H, *m*-Ph and *p*-Ph), 3.92 (m, 4H, THF), 1.97 (m, 4H, THF), 1.21 (s, 3H, Pd−CH_3). $^{13}C\{^1H\}$ NMR (101MHz, CD_2Cl_2, 23°C): δ 138.5 (d, $^2J_{P-C}$ = 14Hz, *o*-Ph), 134.4 (*p*-Ph),128.8 (d, $^3J_{P-C}$ = 13Hz, *m*-Ph), 124.2 (d, $^1J_{P-C}$= 59Hz, *ipso*-Ph), 69.2 (THF), 25.9 (THF), 12.6 (Pd−CH_3). $^{11}B\{^1H\}$ NMR (96MHz, CD_2Cl_2, 23°C): δ 24.2 (1B), −3.3 (4B), −5.9 (4B). $^{31}P\{^1H\}$ NMR (162MHz, CD_2Cl_2, 23°C): δ 56.6. ESI/APCI HRMS (m/z): [M −THF + CH_3CN] − calculated for $C_{16}H_{16}B_9NPCl_9Pd$: 779.8360. Found: 779.8365. Mp: 150.4−159.7 °C (dec).

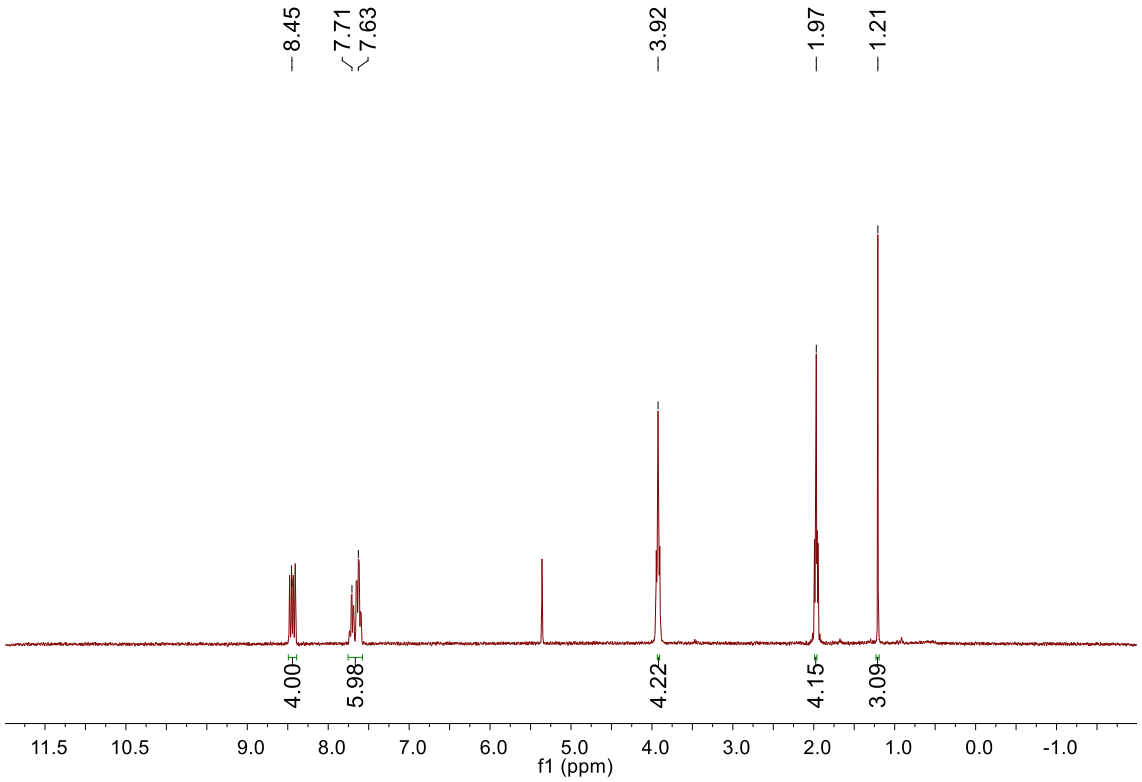

*Figure 96. ^{1}H NMR of **23** (300MHz, CD_2Cl_2, 23°C).*

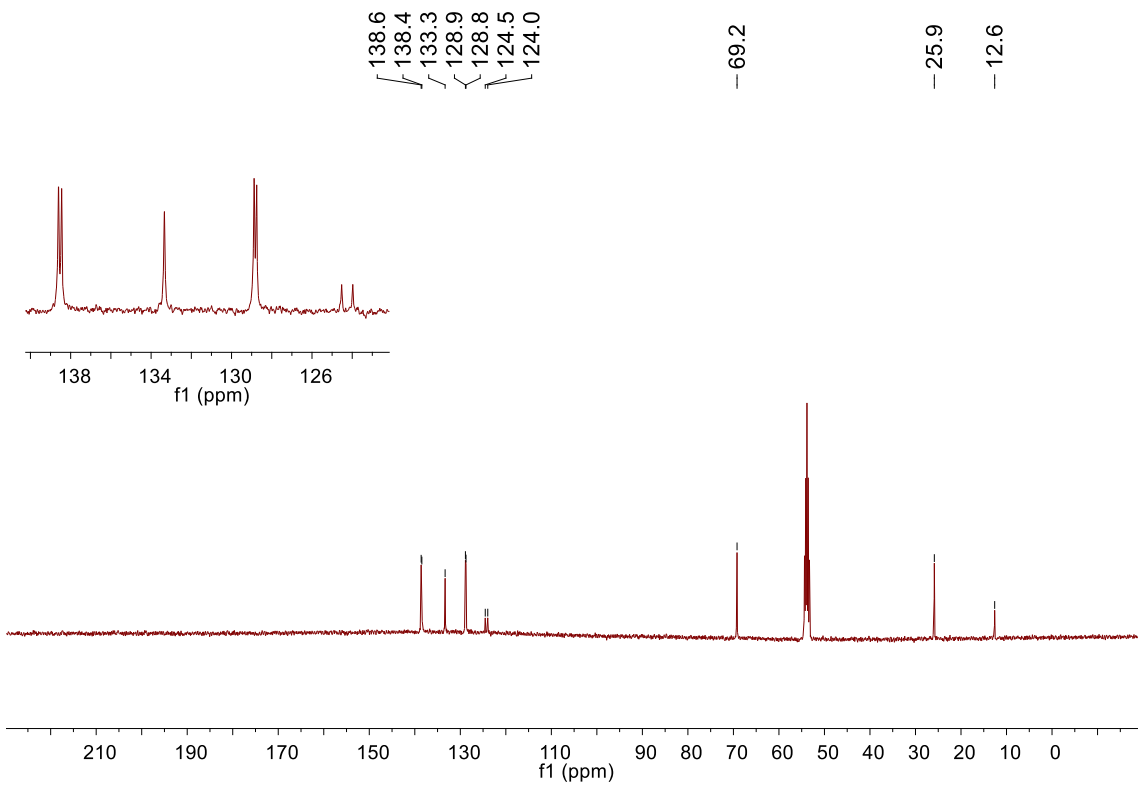

*Figure 97. $^{13}C\{^{1}H\}$ NMR of **23** (101MHz, CD_2Cl_2, 23°C).*

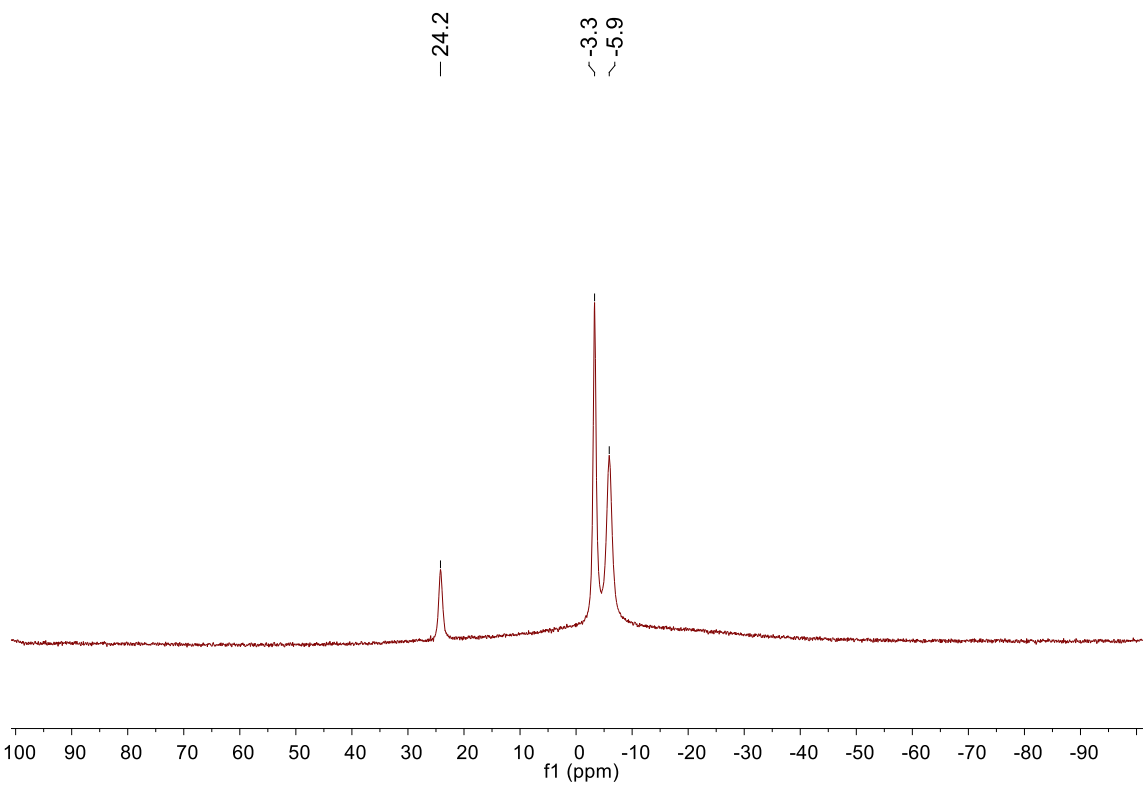

*Figure 98. $^{11}B\{^{1}H\}$ NMR of **23** (128MHz, CD_2Cl_2, 23°C).*

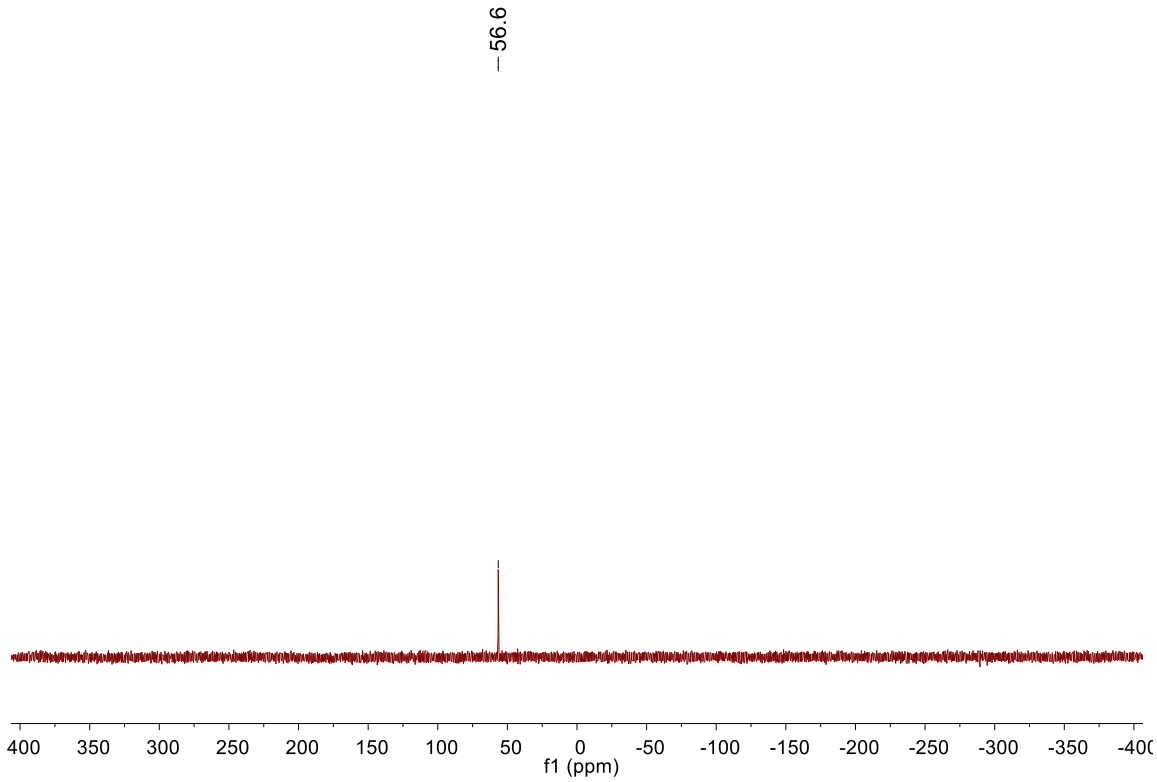

*Figure 99. $^{31}P\{^{1}H\}$ NMR of **23** (162MHz, CD_2Cl_2, 23°C).*

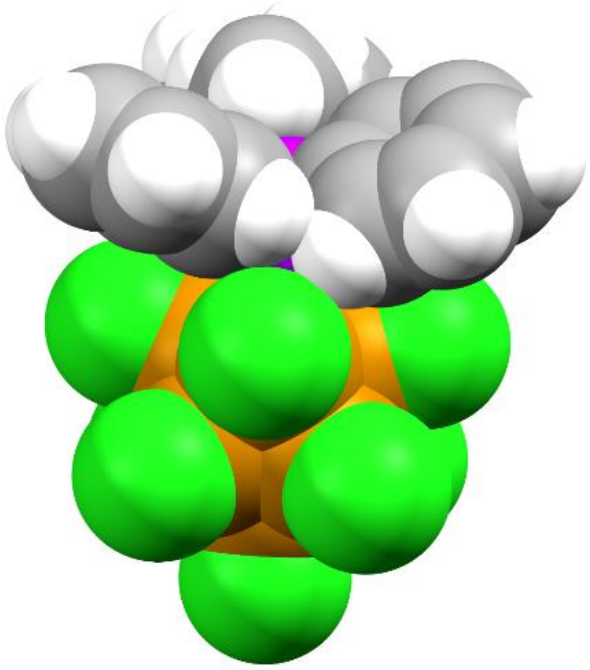

*Figure 100. View of the space-filling model of **23** looking down the P-Pd bond.*

Synthesis for (κ^2 -P,O-P(*o*-OMe-Ph)$_2$CB$_9$Cl$_9$)PdMe(THF) (**24**):

21 was generated as a tan powder from **14** (100mg, 0.10mmol) and (COD)PdMeCl (27.3mg, 0.100mmol) using the procedure for **19**. 94% pure by inverse-gated $^{31}P\{^1H\}$ NMR. ^1H NMR (500MHz, CD_2Cl_2, 23°C): δ 8.00 (br s, Ar, 3H, integration is lower than expected due to broadness), 7.54 (t, J = 7.7Hz, 4H, Ar), 7.06 (t, J = 7.5Hz, 4H, Ar), 6.99 (t, J = 7.1Hz, 4H, Ar), 3.76 (overlapping m and br s, 24 H, −OCH_3 and THF), 1.94 (m, 12 H, THF), 1.13 (s, 6H, Pd−CH_3). $^{13}C\{^1H\}$ NMR (126MHz, CD_2Cl_2, 23°C): δ 161.6 (br s, Ar), 136.1 (br s, Ar) 134.2 (Ar), 121.5 (br s, Ar), 112.6 (Ar), 69.0 (THF), 58.3 (br s, −OCH_3), 56.1 (br s, −OCH_3), 25.9 (THF), 0.7 (br s, Pd−CH_3). $^{11}B\{^1H\}$ NMR (96MHz, CD_2Cl_2, 23°C): δ 24.2 (1B), −3.5 (4B), −6.0 (4B). Inverse-gated $^{31}P\{^1H\}$ NMR (162MHz,CD_2Cl_2, 23°C): δ 21.2. Low-temperature NMR data: Major isomer (62%) ^1H NMR (500 MHz, CD_2Cl_2, −60°C): 4.08 (s, 6H, −OCH_3), 3.56 (s, 6H, −OCH_3), 1.01 (s, 6H, Pd−CH_3). $^{31}P\{^1H\}$ NMR (202MHz, CD_2Cl_2, −60°C): 20.0. Minor isomer (38%) ^1H NMR (500 MHz, CD_2Cl_2, −60°C): δ 4.18 (s, 6H, −OCH_3), 3.38 (s, 6H, −OCH_3), 0.97 (s, 6H, Pd−CH_3). Inverse-gated $^{31}P\{^1H\}$ NMR (202MHz, CD_2Cl_2, −60°C): δ 20.4. The Ar resonances for these two species are overlapped. The ^1H NMR resonances for bound THF are observed at δ 3.66 and 1.83. Mp: 125.3−129.8°C (dec). Without further purification, **21** was reacted with $AgBF_4$ (10.0mg, 0.0500mmol) using the procedure described for **22** to yield **24** as a tan powder. Yield: 81mg, 94% yield. The labeling scheme for **24** is shown in Figure 101. ^1H NMR (500MHz, CD_2Cl_2, 23°C): δ 8.0 (br s, 2H, Ar), 7.59 (m, 2H, Ar), 7.12 (m, 2H, Ar), 7.01 (m, 2H, Ar), 4.04 (m, 4H, THF), 3.82 (br s, 6H, −OCH_3), 2.02 (m, 4H, THF), 0.89 (s, 3H, Pd−CH_3). $^{13}C\{^1H\}$ NMR (151MHz, CD_2Cl_2, 23°C): δ 160.8 (C−OMe), 135.9 (br, Ar), 134.3 (br, Ar),121.6 (br, Ar), 112.1 (Ar), 69.6 (THF), 57.8 (br s, −OCH_3), 25.4 (THF), 2.6 (br s, Pd−CH_3). $^{11}B\{^1H\}$ NMR (96MHz, CD_2Cl_2, 23°C): δ 24.6 (1B), −4.0 (4B), −6.5 (4B). Inverse-

gated $^{31}P\{^{1}H\}$ NMR (162MHz, CD_2Cl_2, 23°C): δ 21.2. Low-temperature NMR data: ^{1}H NMR (500MHz, CD_2Cl_2, −60°C): δ 8.27 (dd, $^{3}J_{H-H}$ = 8Hz, $^{4}J_{P-H}$ = 12.5Hz, 1H, H^{13}), 7.64 (t, $^{3}J_{H-H}$ = 7.5Hz, 1H, H^{11}), 7.56 (t, J = 7.5Hz, H^{4}), 7.45 (dd, $^{3}J_{P-H}$ = 12.5Hz, J_{H-H} = 8 Hz, 1H, H^{6}), 7.14 (t, J_{H-H} =7 Hz, 1H, H^{12}), 7.08 (t, J_{H-H} = 4, J_{P-H} = 7.5Hz, 1H, H^{10}), 7.04 (t, J_{H-H} = 7.5Hz, 1H, H^{5}), 6.98 (t, J_{H-H} = 4Hz, J_{P-H}= 8Hz, 1H, H^{3}), 4.09 (br m, 4H,THF), 4.05 (s, 3H, H^{7}), 3.73 (s, 3H, H^{14}), 2.01 (br m, 4H, THF), 0.71 (s, 3H, Pd−CH_3). $^{13}C\{^{1}H\}$ NMR (126MHz, CD_2Cl_2, −60°C): δ 160.8 (d, $^{2}J_{P-C}$ = 13Hz, C^{2}), 158.8 (d, $^{2}J_{P-C}$ = 9Hz, C^{9}), 136.4 (C^{13}), 134.3 (C^{11}) 134.2 (C^{4}) 133.5 (C^{16}), 123.2 (C^{5}), 118.8 (d, $^{2}J_{P-C}$ = 10Hz, C^{12}), 115.5 (d, $^{1}J_{P-C}$ = 58Hz, C^{1}) 111.8 (d, $^{2}J_{P-C}$ = 6Hz, C^{3}), 111.1 (d, $^{2}J_{P-C}$ = 8Hz, C^{10}), 108.3 (d, $^{1}J_{P-C}$ = 71Hz, C^{8}), 72.8 (THF), 59.6 (C^{7}), 55.9 (C^{14}), 25.1 (THF), 1.2 (Pd−CH_3). Inverse-gated $^{31}P\{^{1}H\}$ NMR (202MHz, CD_2Cl_2, −60°C): δ 20.8. HRMS: ESI/APCI HRMS (m/z): [M − THF + CH_3CN] − calculated for $C_{18}H_{20}B_9NO_2PCl_9Pd$: 829.8318. Found: 829.8320. Mp: 123.5−135.2°C (dec).

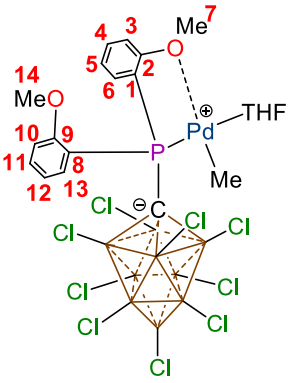

24

*Figure 101. Numbering Scheme for **24**.*

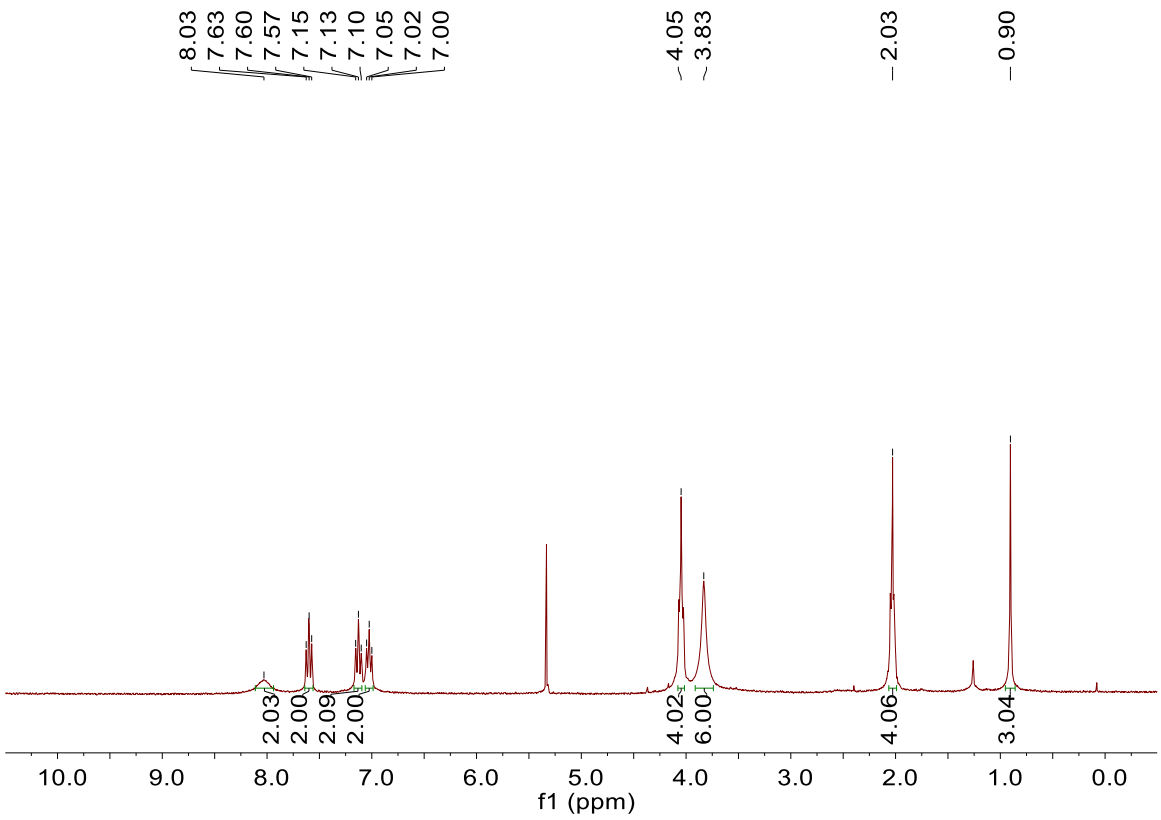

*Figure 102. ^{1}H NMR of **24** (300MHz, CD_2Cl_2).*

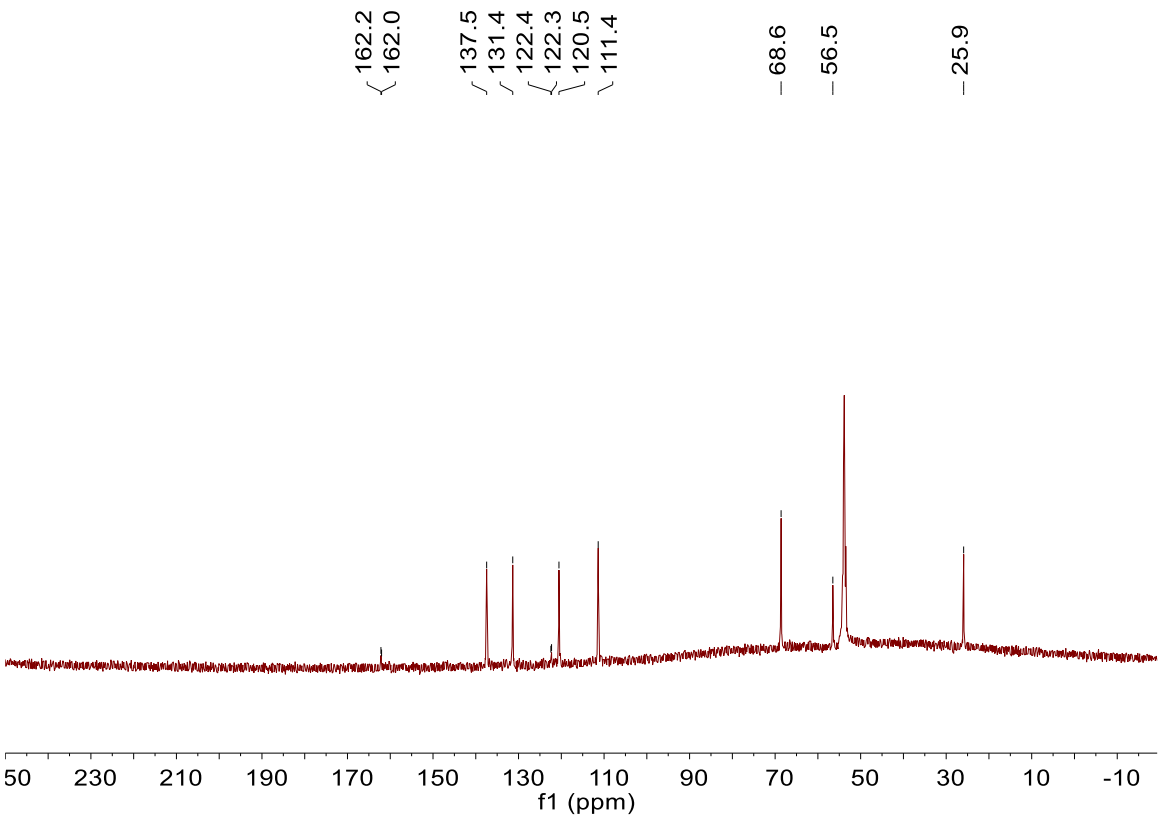

*Figure 103. $^{13}C\{^{1}H\}$ NMR of **24** (162MHz, CD_2Cl_2).*

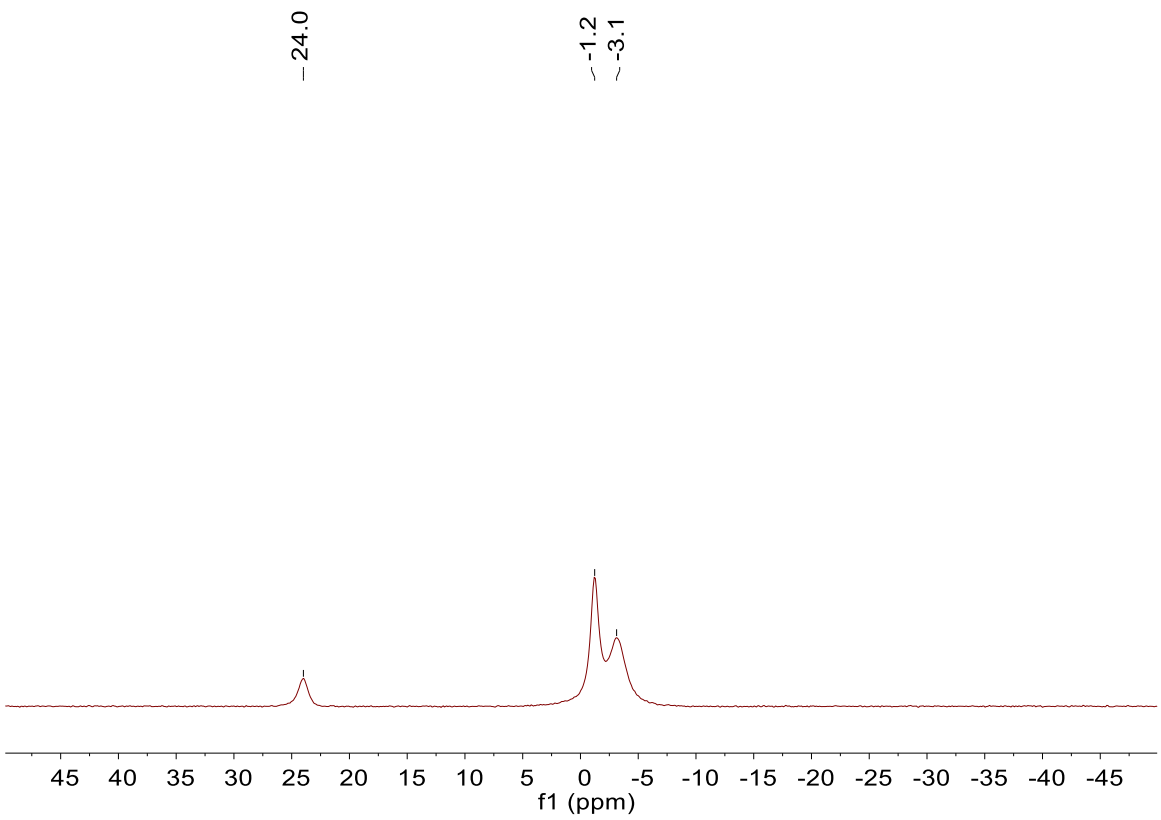

*Figure 104. $^{11}B\{^{1}H\}$ NMR of **24** (96MHz, CD_2Cl_2).*

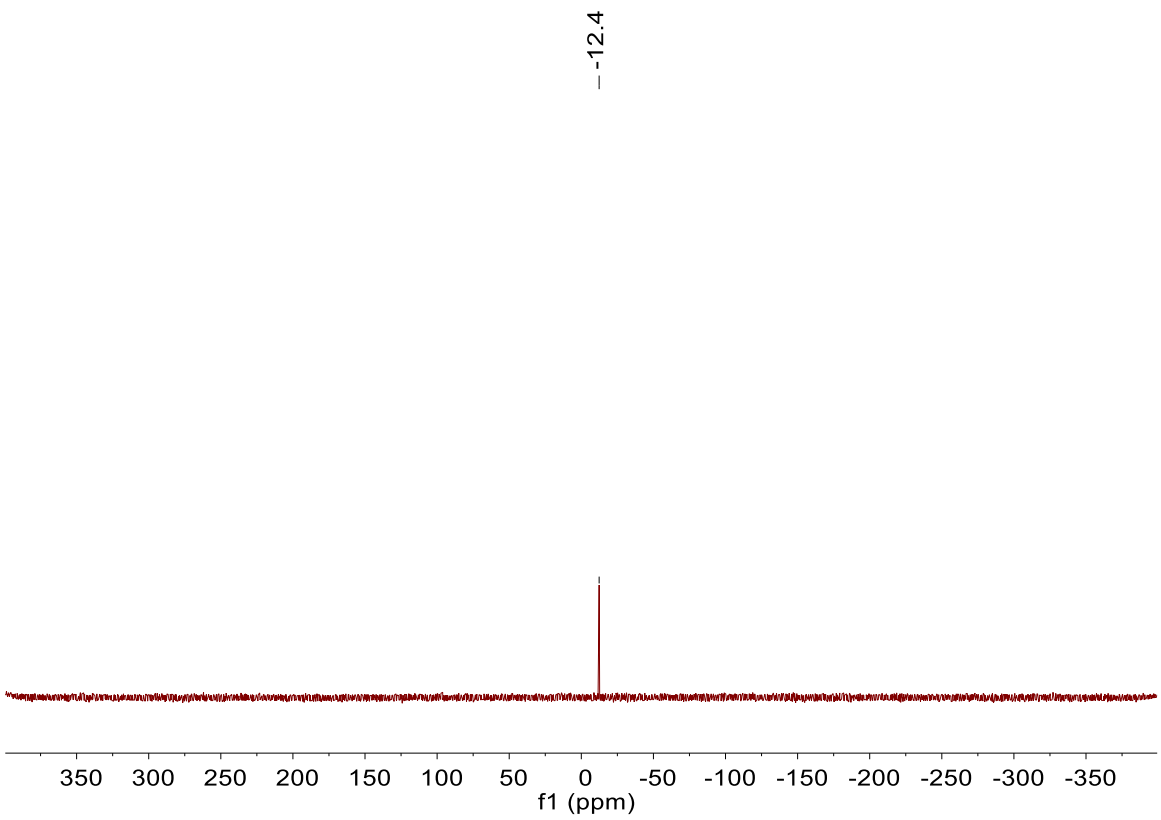

*Figure 105. $^{31}P\{^{1}H\}$ NMR of **24** (121MHz, CD_2Cl_2).*

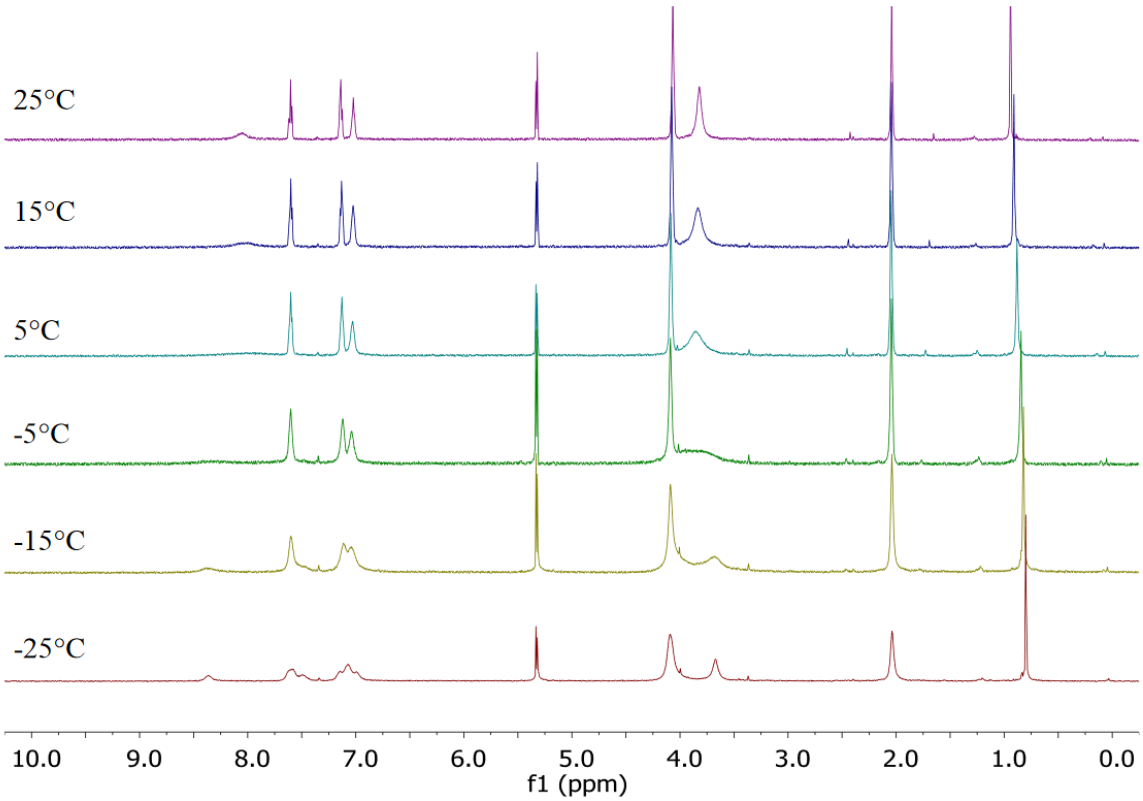

*Figure 107.^{1}H VT NMR of **24** (500MHz, CD_2Cl_2).*

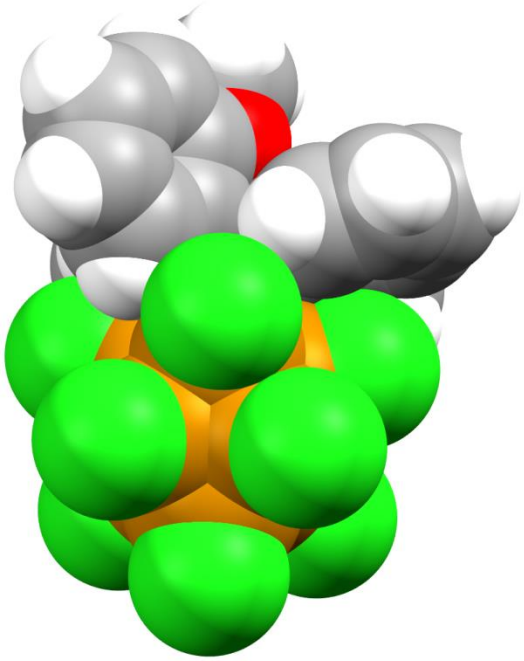

*Figure 106. View of the space-filling model of **24** looking down P-Pd bond.*

Generation of (κ^2-P,O-P(*o*-OMe-Ph)$_2$CB$_9$Cl$_9$)PdMe(η^2- CH$_2$=CH$_2$) (**26**).

A solution of **24** (~5.0 mg) in CD_2Cl_2 was prepared in a J. Young NMR tube. The tube was cooled to −196°C in a liquid nitrogen bath and the desired amount of ethylene was added by vacuum transfer. The tube was allowed to thaw and warm to −78°C to afford a yellow-orange solution. The tube was shaken several times to ensure proper mixing of ethylene into the solvent and then was placed in an NMR probe that had been precooled to −78°C. The numbering scheme for **26** is shown in Figure 57. ^{1}H NMR (CD_2Cl_2 500MHz, −78°C): δ 8.30 (dd, $^3J_{H-H}$ = 8Hz, $^2J_{P-H}$ = 12Hz, 1H, H^{13}), 7.66 (t, $^3J_{H-H}$ = 8Hz, 1H, H^{11}), 7.57 (t, $^3J_{H-H}$ = 7.5Hz, 1H, H^4), 7.43 (dd, $^3J_{H-H}$= 8Hz, $^2J_{P-H}$ = 12Hz, 1H, H^6), 7.18 (t, $^3J_{H-H}$ = 7Hz, 1H, H^{12}), 7.05 (t, $^3J_{H-H}$ =7.5Hz, 2H, H^3 and H^5), 6.99 (dd, $^3J_{H-H}$ = 8Hz, $^2J_{P-H}$ = 8Hz, H^{10}), 5.42 (br d, $^3J_{H-H}$ = 9Hz, 2H, bound ethylene AA′), 5.36 (s, free ethylene), 5.30 (br d, bound ethylene BB′ (overlapped with solvent resonance)), 4.03 (s, 3H, H^7), 3.71 (s, 3H, H^{14}), 3.61 (m, 4H, free THF), 1.74 (m, 4H,free THF), 0.82 (s, $^3J_{P-H}$= 3Hz, 3H, Pd−CH$_3$). ^{13}C{^{1}H} NMR (CD_2Cl_2, 126MHz, −78°C): δ 161.3 (d, $^2J_{P-C}$ = 15Hz, C^9), 158.2 (d, $^2J_{P-C}$ = 10Hz, C^2), 136.8 (C^{13}), 134.5 (C^1), 134.1 (C^4), 134.0 (C^{11}),123.6 (C^5), 122.8 (s, free ethylene), 119.1 (C^{12}), 114.7 (d, $^1J_{P-C}$ = 54Hz, C^1), 112.0 (C^3), 111.4 (C^{10}), 107.0 (d, $^1J_{P-C}$ = 61Hz, C^8), 101.5 (s, bound ethylene), 67.3 (s, free THF), 60.4 (C^7), 56.0 (C^{14}), 25.0 (free THF), 5.9 (Pd−CH$_3$). Inverse-gated ^{31}P{^{1}H} NMR (202MHz, CD_2Cl_2, −78°C): δ 9.8. Chain Growth of **26** at −20 °C. A solution of **24** in CD_2Cl_2 containing excess ethylene (16, 26, or 35eq) was generated in a J. Young NMR tube as described above. The tube was placed in the NMR probe that was pre-chilled to −25°C and equilibrated for 10min. The probe was then warmed to −20°C, and the tube was monitored by ^{1}H NMR for ca. 1h. The resonances for **24**

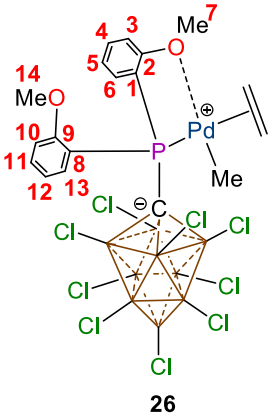

26

*Figure 108. Numbering Scheme for **26**.*

disappeared, and resonances assigned to **27** higher alkyl species grew. ^{1}H NMR data for **27**: δ 4.02 (s, −OCH_3), 3.56 (s,−OCH_3), 2.40 (br s), 2.23 (br s), 1.99 (br s), 1.22 (s, −CH_2−), 1.16 (br m), 0.97 (br m), 0.83 (q, $^{3}J_{H\text{-}H}$ = 7Hz), 0.78 (t, $^{3}J_{H\text{-}H}$ = 8Hz,−CH_3), 0.65 (t, $^{3}J_{H\text{-}H}$ = 7Hz, −CH_3), 0.59 (t, $^{3}J_{H\text{-}H}$ = 8Hz, −CH_3).

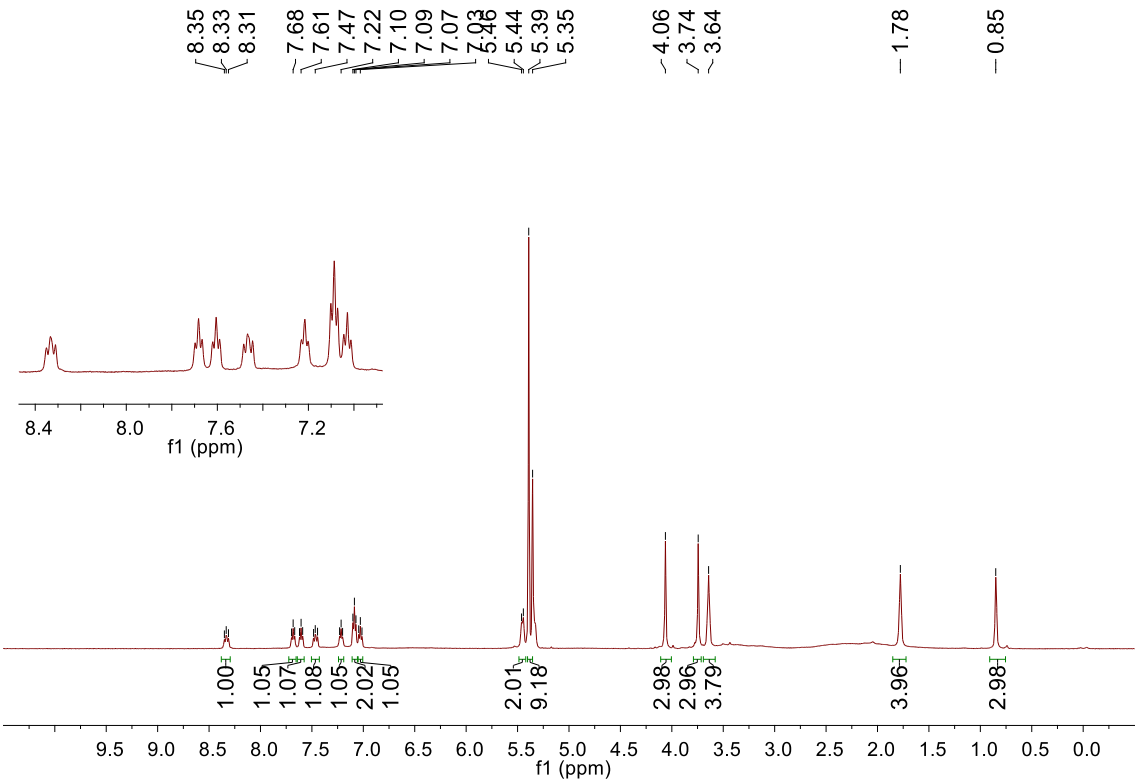

*Figure 109. ^{1}H NMR of **26** generated by the reaction of **24** with 3.5 eq. of ethylene (500MHz,CD_2Cl_2, -78ºC). Note: Free ethylene is shown at 5.46-5.39ppm.*

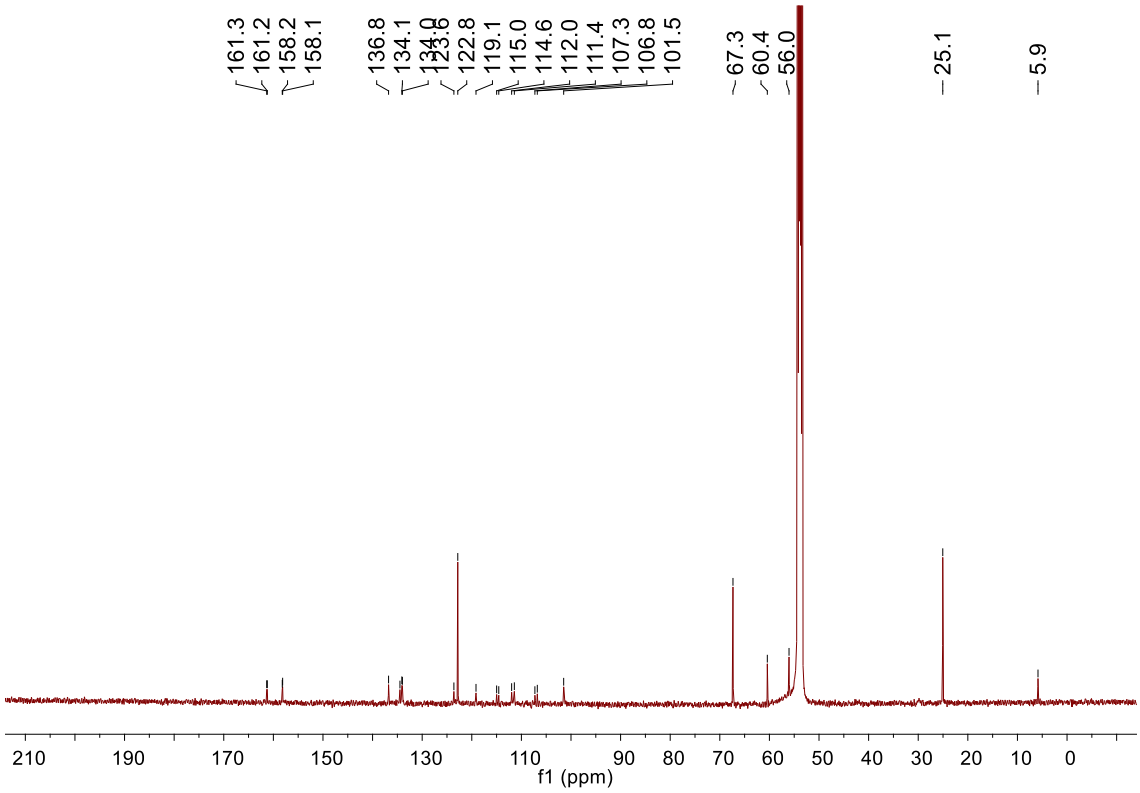

*Figure 110. $^{13}C\{^{1}H\}$ NMR of **26** given by the reaction of **24** with 3.5 equiv. of ethylene (126MHz,CD_2Cl_2, -78ºC).*

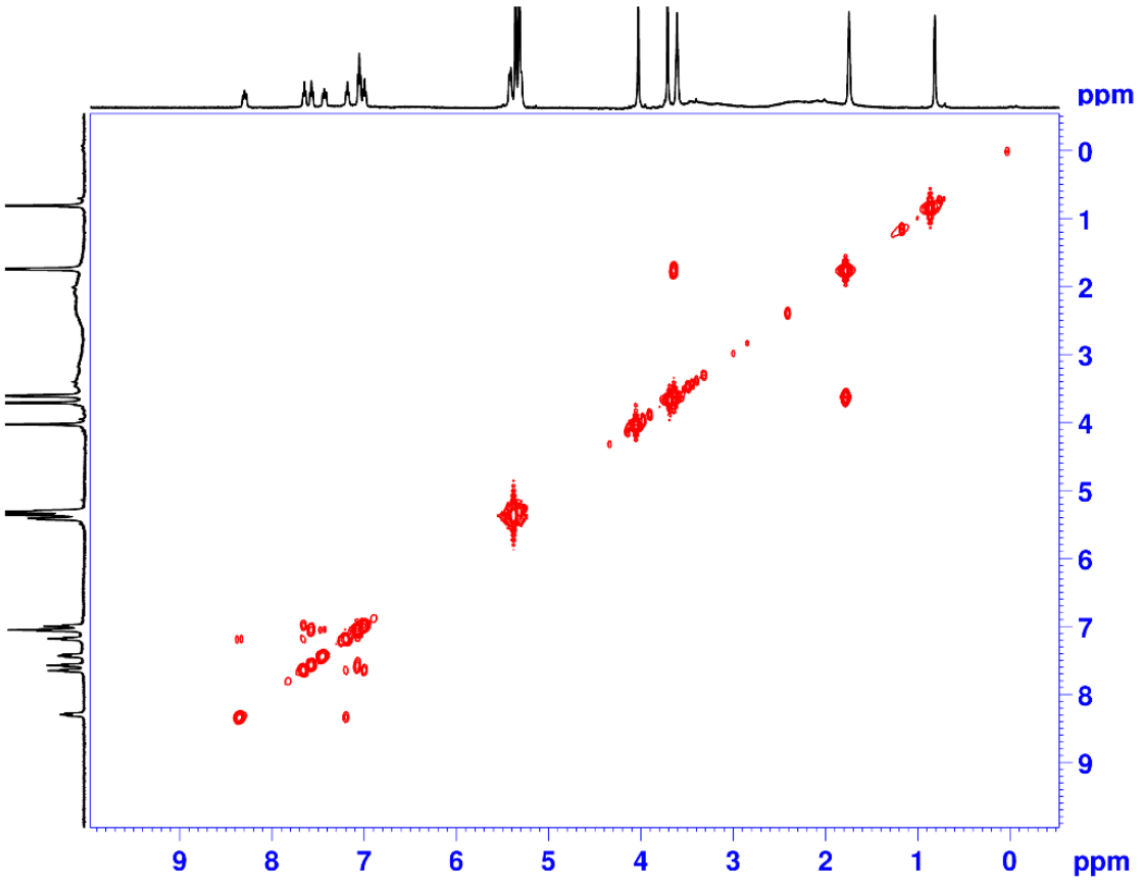

*Figure 111. ^{1}H-^{1}H COSY of **26** given by the reaction of **24** with 3.5 eq. of ethylene (500MHz,CD2Cl2, -78ºC).*

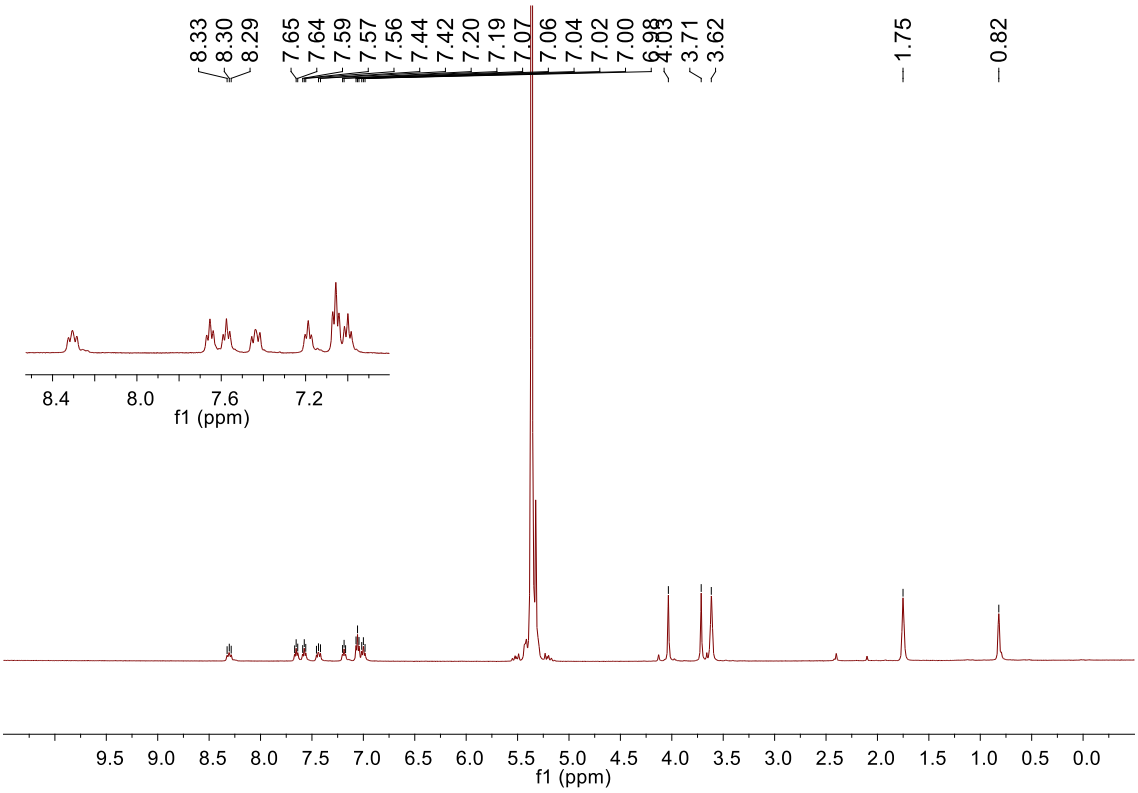

*Figure 112. ^{1}H NMR of **26** given by the reaction of **24** with 35 eq. of ethylene (500MHz, CD_2Cl_2, -78ºC).*

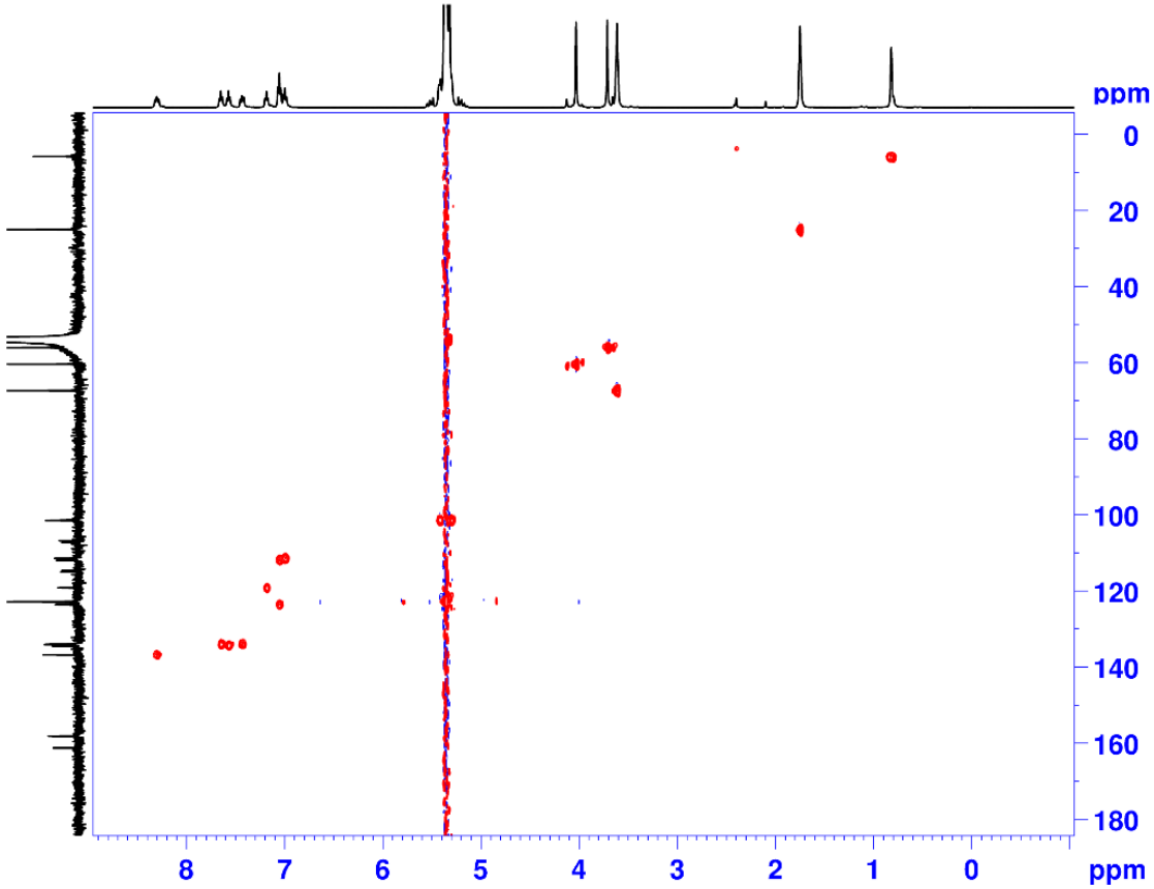

*Figure 113. HSQC of **26** given by the reaction of **24** with 35 eq. of ethylene (500MHz, CD_2Cl_2, -78°C).*

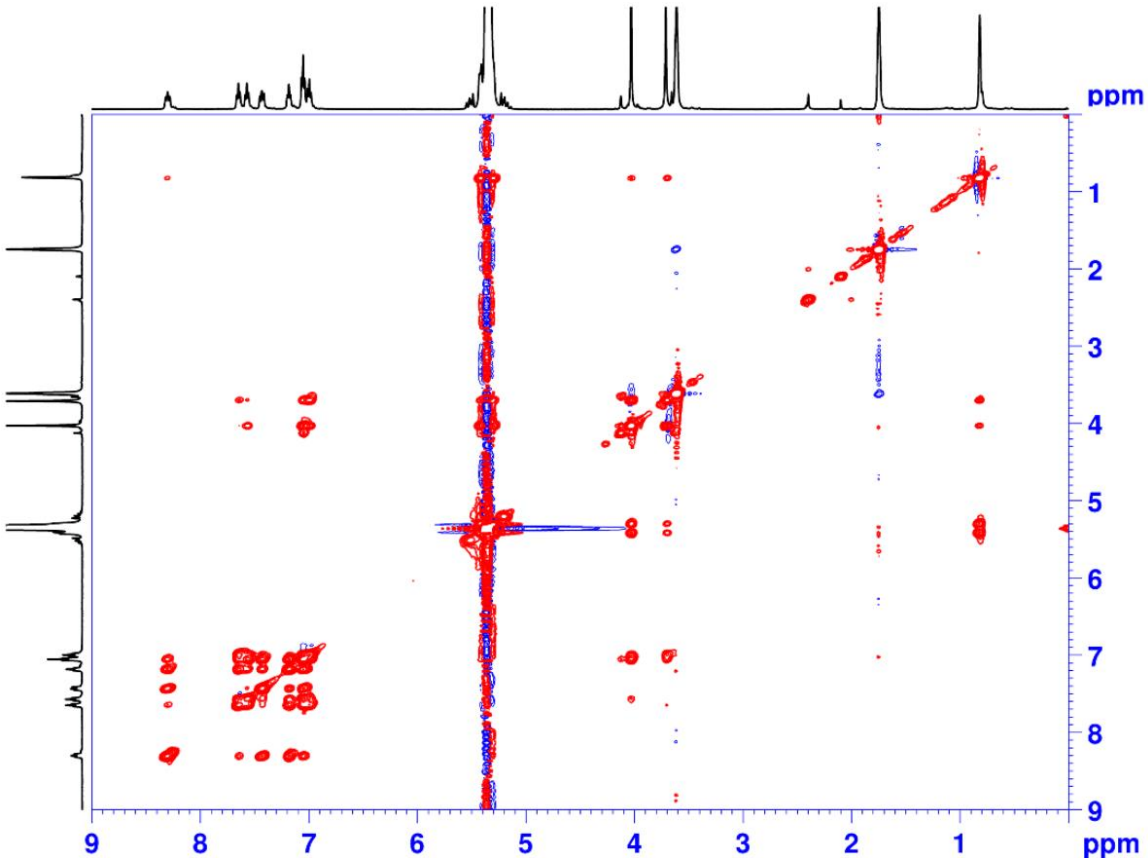

*Figure 114. ^{1}H-^{1}H NOESY of **26** given by the reaction of **24** with 35 eq. of ethylene (500MHz, CD_2Cl_2, -78ºC).*

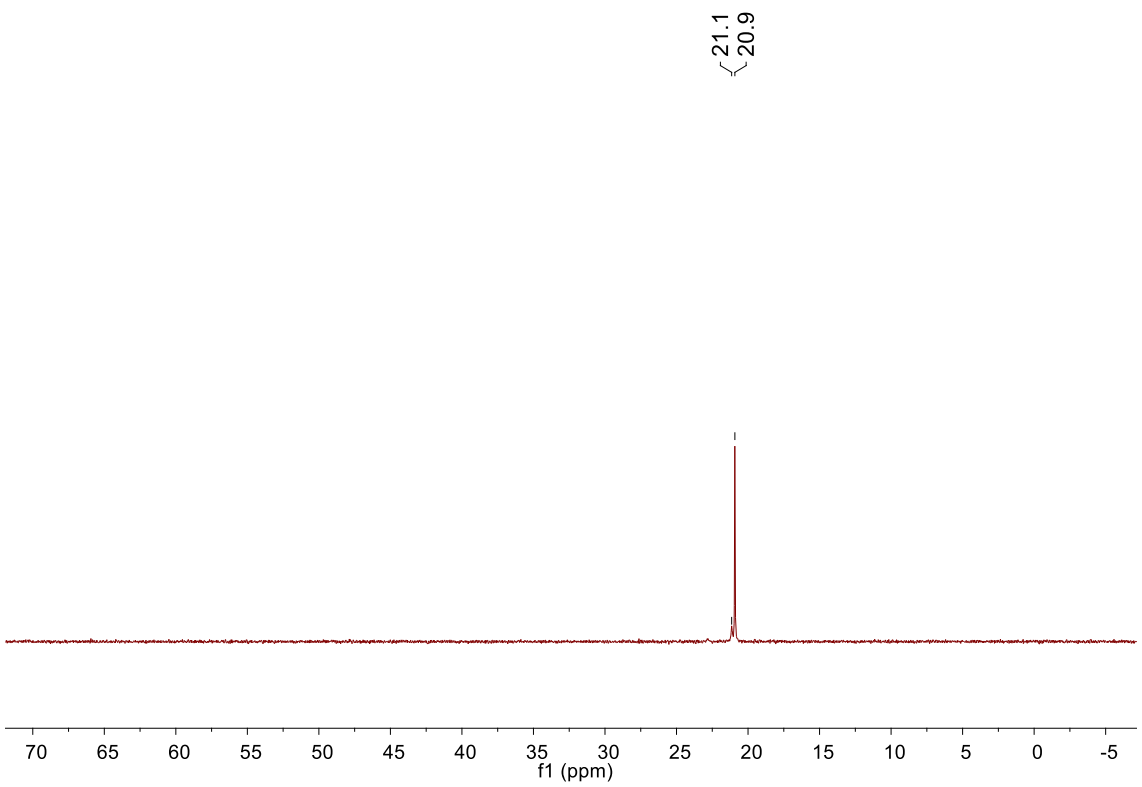

*Figure 115. Inverse-gated $^{31}P\{^{1}H\}$ NMR of **26** with 35 eq. of ethylene (202MHz, CD_2Cl_2, -78ºC). Note: CH_3CN adduct resonance at 21.1ppm.*

Synthesis for (κ^3 -P,S,S-P(*o*-SMe-Ph)$_2$CB$_9$Cl$_9$)PdMe (**25**):

17 (100mg, 0.10mmol) and THF (1mL) were added to a 20mL scintillation vial equipped with a stir bar. (COD)PdMeCl (31.5 mg, 0.10 mmol) was separately dissolved in THF (1mL) in a second vial. The (COD)PdMeCl solution was slowly added to the solution of **17**. The second vial was washed with THF (1mL), and the washing was added to the solution of **17**. The mixture was stirred for 30min and concentrated under vacuum. Pentane was added, and the resulting green precipitate was allowed to settle. The pentane supernatant was decanted off, and the precipitate was washed twice with pentane and dried under vacuum. The solid was then washed with diethyl ether and dried under vacuum to yield **25** as a green solid (75mg, 90% yield). ^{1}H NMR (600MHz, THF-d$_8$, 23°C): δ 8.70 (m, 1H), 7.72 (m, 2H), 7.49 (m, 3H), 7.36 (m, 1H), 7.22 (m, 1H), 3.00 (s, 3H), 2.23 (s, 3H). ^{13}C{^{1}H} NMR (151 MHz, THF-d$_8$, 23°C): δ 144.1 (d, $^1J_{P\text{-}C}$ = 21Hz), 136.8, 136.1, 135.1 (d, $^2J_{P\text{-}C}$ = 14Hz), 132.9, 132.3, 131.6, 130.9, 129.5 (d, $^2J_{P\text{-}C}$ = 16Hz), 128.5, 123.8, 103.6, 23.0, 19.0, 4.4. ^{11}B{^{1}H} NMR (192MHz, THF-d$_8$, 23°C): δ 24.8, −3.4,−5.3. ^{31}P{^{1}H} NMR (243MHz, THF-d$_8$, 23°C): δ 40.8. ESI/APCI HRMS (m/z): [M] − calculated for $PdPS_2Cl_9C_{16}B_9H_{15}$: 827.2059. Found: 827.2075.

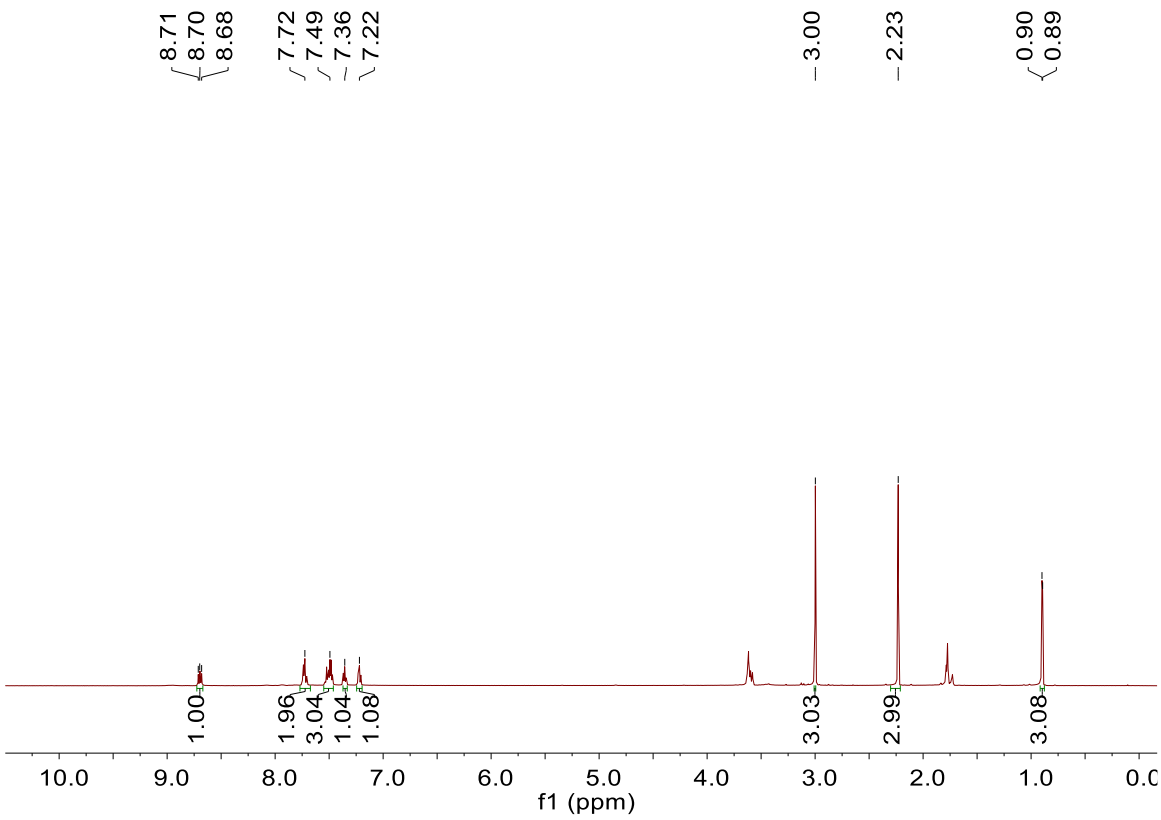

*Figure 116. ^{1}H NMR of **25** (600MHz, THF-d_8, 23°C).*

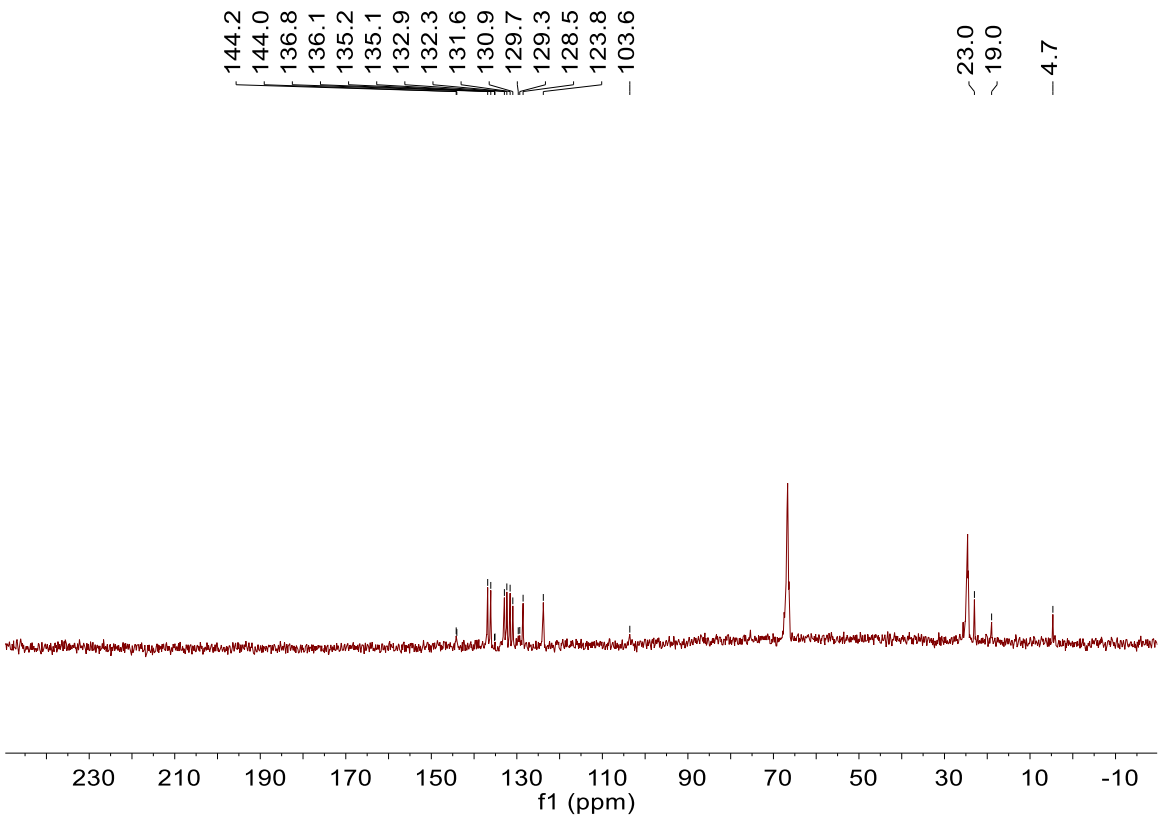

*Figure 117. $^{13}C\{^{1}H\}$ NMR of **25** (151MHz, THF-d_8, 23°C).*

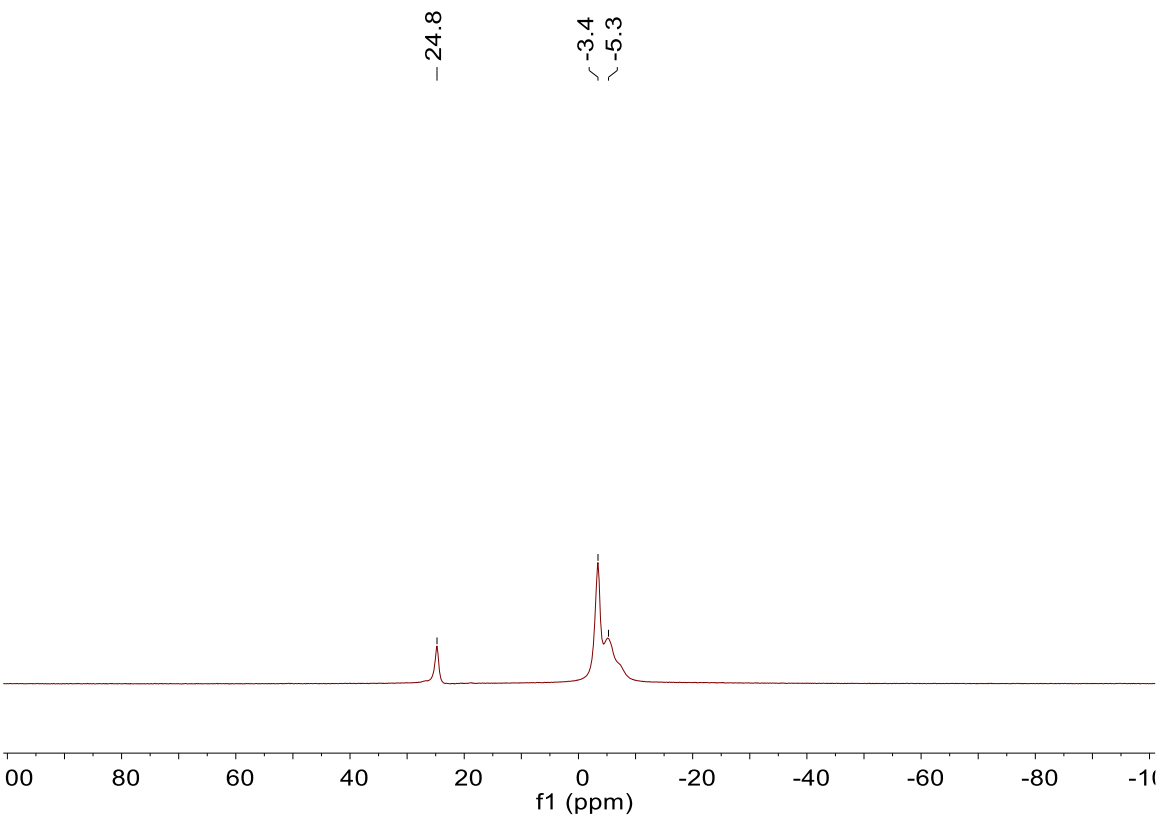

*Figure 118. $^{11}B\{^{1}H\}$ NMR of **25** (128MHz, THF-d_8, 23°C).*

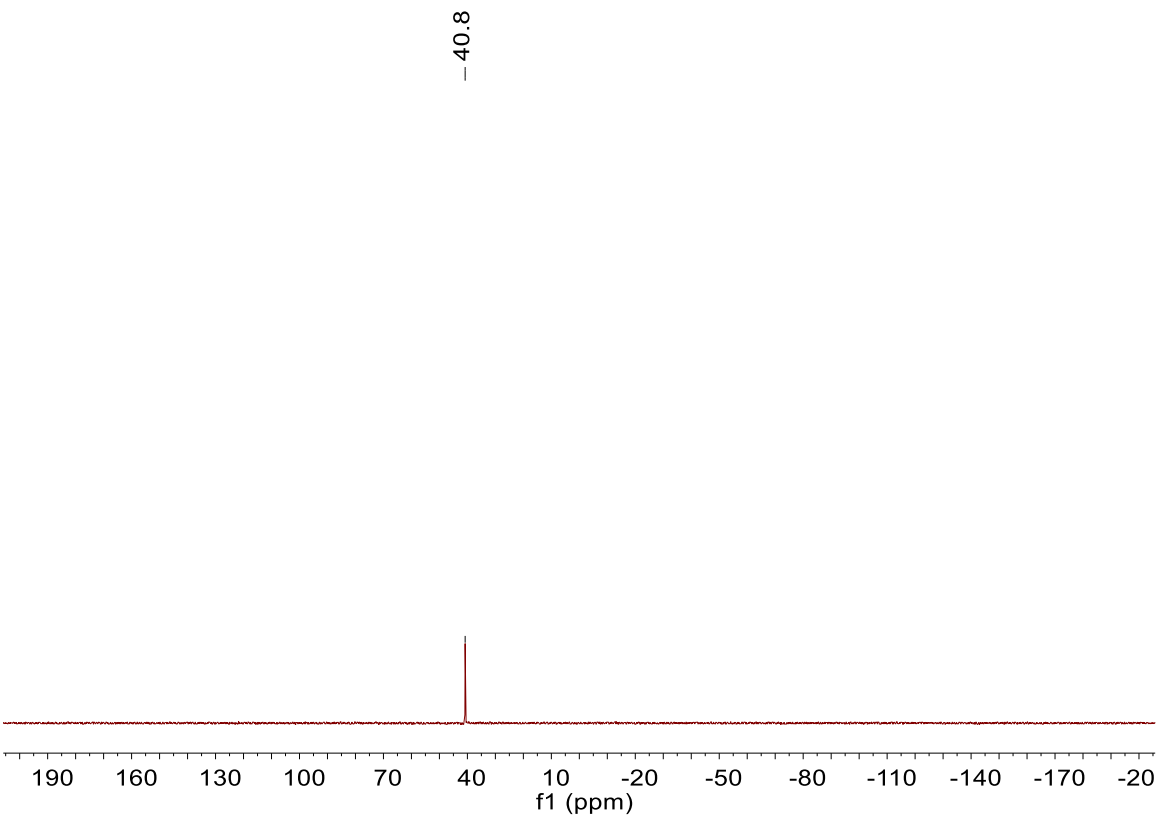

*Figure 119. $^{31}P\{^{1}H\}$ NMR of **25** (243MHz, THF-d_8, 23°C).*

Low-Pressure Ethylene Oligomerization and Polymerization Reactions:

Ethylene oligomerization/polymerization reactions at 2 and 6atm were performed in a 200mL Fischer−Porter bottle equipped with a 2in. long Teflon-coated magnetic stir bar and a stainless-steel pressure head fitted with inlet and outlet needle valves, a septum-capped ball valve for injections, a safety check valve, and a pressure gauge. In a N_2 filled glovebox, the Fischer−Porter bottle was charged with toluene (49mL). The apparatus was removed from the glovebox, connected to a stainless-steel double manifold vacuum/ethylene line, placed in a room temperature water bath or 50°C oil bath, and stirred at 370rpm. The N_2 atmosphere was replaced with ethylene by three

evacuation−refill cycles. The solution was equilibrated at either 2 or 6atm of ethylene pressure for 15min. For the 2atm experiments, a freshly prepared stock solution of catalyst in PhF (1mL) was added via gastight syringe. For the 6atm experiments, the pressure was decreased to 1.4atm, a stock solution of catalyst in fluorobenzene (1mL) added immediately via gastight syringe, and the pressure immediately increased to 6atm. The ethylene pressure was kept constant by feeding ethylene on demand. For catalysts **22** and **23**, ethylene consumption was measured using a Brooks Instruments 5860i Mass Flow Sensor. The total ethylene consumption was determined by numerical integration of the mass flow curve using the LabView software package. Control experiments showed that equilibration of ethylene between the gas and solution phases at 6atm ethylene pressure requires ca. 15min under the reaction conditions (23°C, 370rpm stirring); therefore, the activity for the 6atm experiments was determined using the mass flow curve excluding the first 15min. After 2h, the ethylene line was closed, the Fischer−Porter bottle vented, *o*-xylene (100μL) added as an internal standard, and the solution analyzed by GC-MS using an Aglient6890/5973N GC-MS instrument. The masses of hexene, octene, and decene were determined by GC-MS using predetermined response factors. The mass of butene was calculated by subtracting the masses of the other oligomers from the total mass of ethylene consumed. For catalyst **24**, after the ethylene line was closed and the Fisher-Porter bottle vented, methanol (50mL) was added to precipitate the polymer. The polymer was collected by filtration, washed with methanol (50mL), and dried for 2 days at 70°C in a vacuum oven.

High-Pressure Ethylene Polymerization Reactions:

Ethylene polymerizations at 54atm were performed using a stainless-steel Parr 300mL autoclave, which was equipped with a magnetically driven 1.5in. Diameter four-

blade propeller stirrer, thermocouple, water cooling loop, and a Parr 4842 controller. In a N_2 glovebox, a 200mL glass autoclave liner was charged with toluene (49mL) and a stock solution of the catalyst in fluorobenzene (1mL) and placed in the autoclave. The autoclave was sealed, removed from the glovebox, and attached to the ethylene line. The mixture was stirred (270rpm) at 23°C for 15min and then pressurized to 54atm of ethylene. The ethylene pressure was kept constant by feeding ethylene on demand. After 2h, the ethylene line was closed, and the autoclave was vented. Methanol (50mL) was added to precipitate the polymer, which was characterized as described above. DSC measurements were performed on a TA Instruments 2920differential scanning calorimeter. Samples (5 mg) were annealed by heating to 170°C at 15°C/min and cooling to 0°C at 10°C/min, and analyzed by heating to 170°C at 15°C/min. ^{1}H and $^{13}C\{^{1}H\}$ NMR spectra of PE samples were obtained at 100°C in dry, degassed CD_2Cl_2 solvent using a Bruker Advance 500 NMR instrument. Gel permeation chromatography (GPC) was performed on a Polymer Laboratories PL−GPC 200 instrument at 150°C with 1,2,4-trichlorobenzene (stabilized with 125ppm BHT) as the mobile phase. Three PL gel 10μm Mixed-B LS columns were used. The molecular weights were calibrated using narrow polystyrene standards with a 10-point calibration of M_n from 570Da to 5670kDa and are corrected for linear polyethylene by universal calibration by using the following Mark−Houwink parameters: polystyrene, $K = 1.75 \times 10^{-2} cm^3 g^{-1}$, $\alpha = 0.67$; polyethylene, $K = 5.90 \times 10^{-2} cm^3 g^{-1}$, $\alpha = 0.69$.[167]

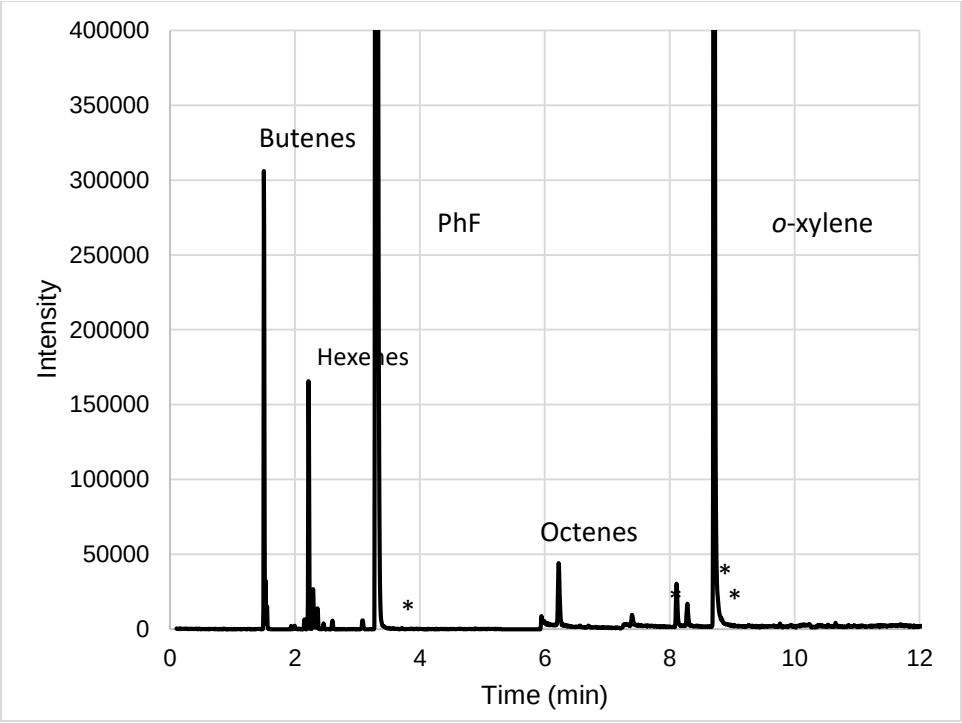

*Figure 120. GC-MS of Oligomers Formed by **22** (Table 2, entry 4) (Impurities from the toluene solvent are labelled by *).*

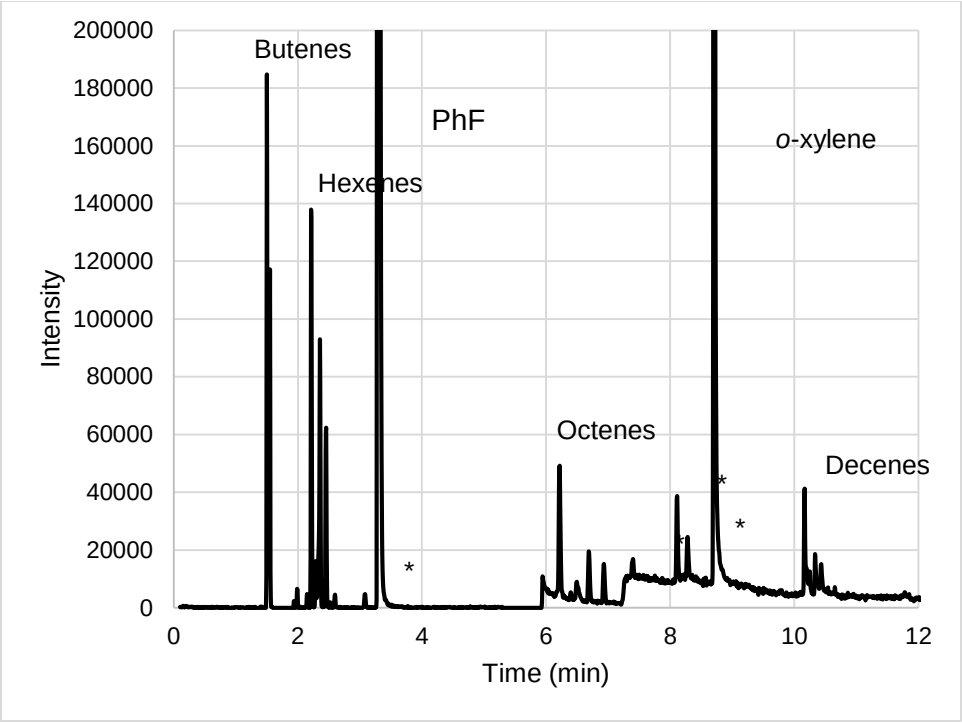

*Figure 121. GC-MS of Oligomers Formed by **23** (Table 2, entry 4) (Impurities from the toluene solvent are labelled by *).*

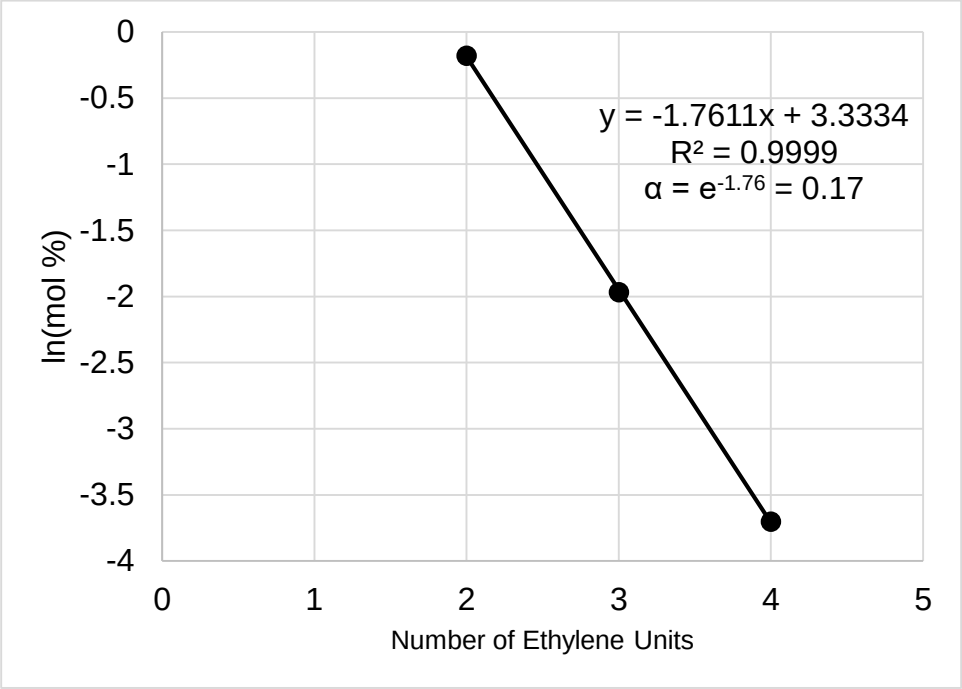

Figure 122. Schulz-Flory Plot of Oligomers Formed by **22** (Table 2, Entry 3)

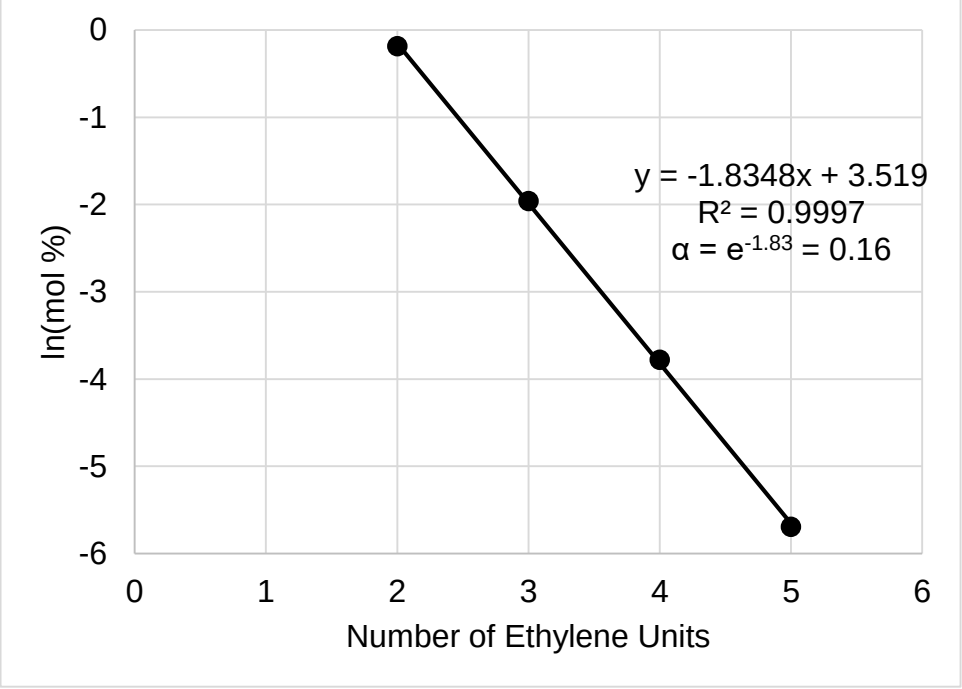

*Figure 123. Schulz-Flory Plot of Oligomers Formed by **23** (Table 2, Entry 6).*

NMR Characterization of the Polyethylene Formed by 20

Figure S57, and Figures S58 and S59 are representative ^{1}H NMR and $^{13}C\{^{1}H\}$ NMR spectra respectively of the polyethylene produced at room temperature and 2 bar (Table 2, entry 1). The triplet at δ 1.05 in ^{1}H NMR is assigned as the homoallylic methyl group of the 3-olefin chain-ends by HMBC (Figure S61 and S62) The broad resonance at δ 1.2 in ^{1}H NMR was assigned as the αB_1 hydrogens by HSQC spectroscopy. (Figure S64)

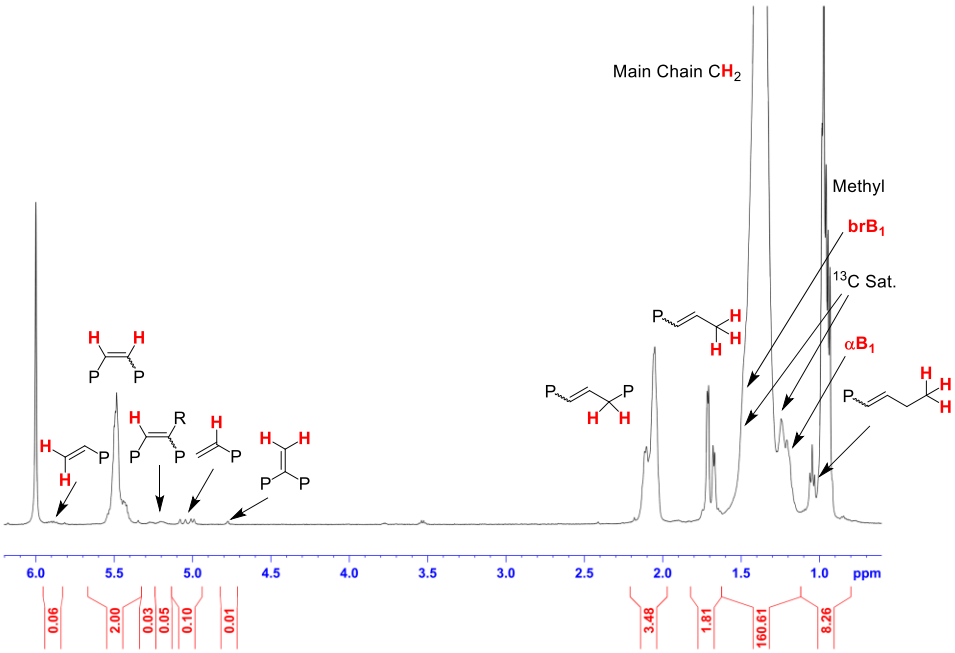

*Figure 124. ^{1}H NMR of Olefin Region of Polyethylene Formed by **24** (Table 3, entry 1) (500MHz, $CDCl_2CDCl_2$, 100ºC).*

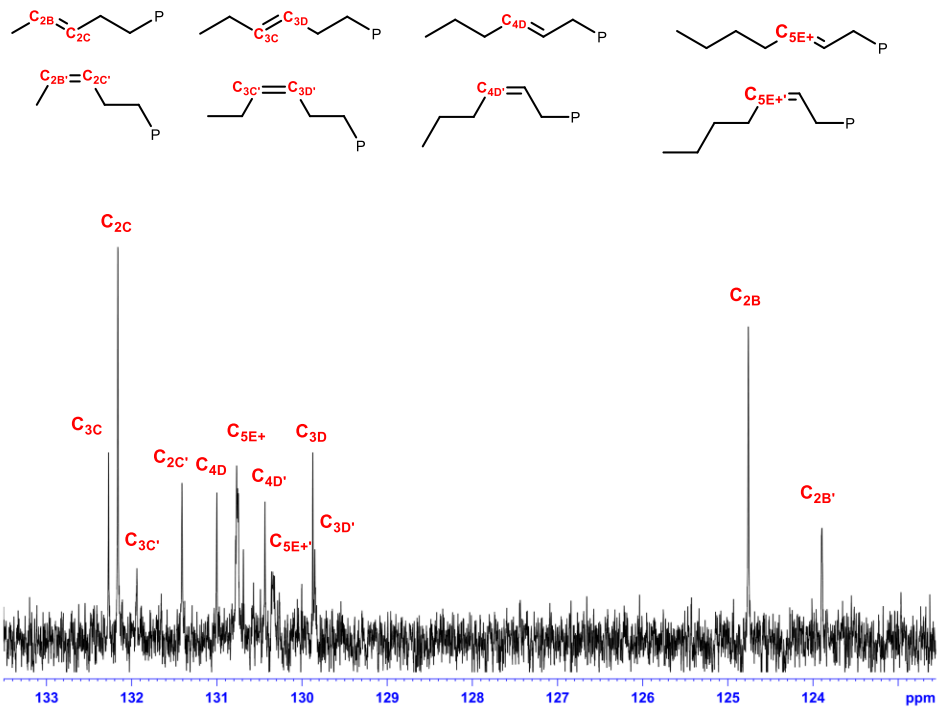

*Figure 125. $^{13}C\{^{1}H\}$ NMR of Olefin Region of Polyethylene Formed by **24** (Table 3, entry 1) (125MHz, $CDCl_2CDCl_2$, 100ºC)*

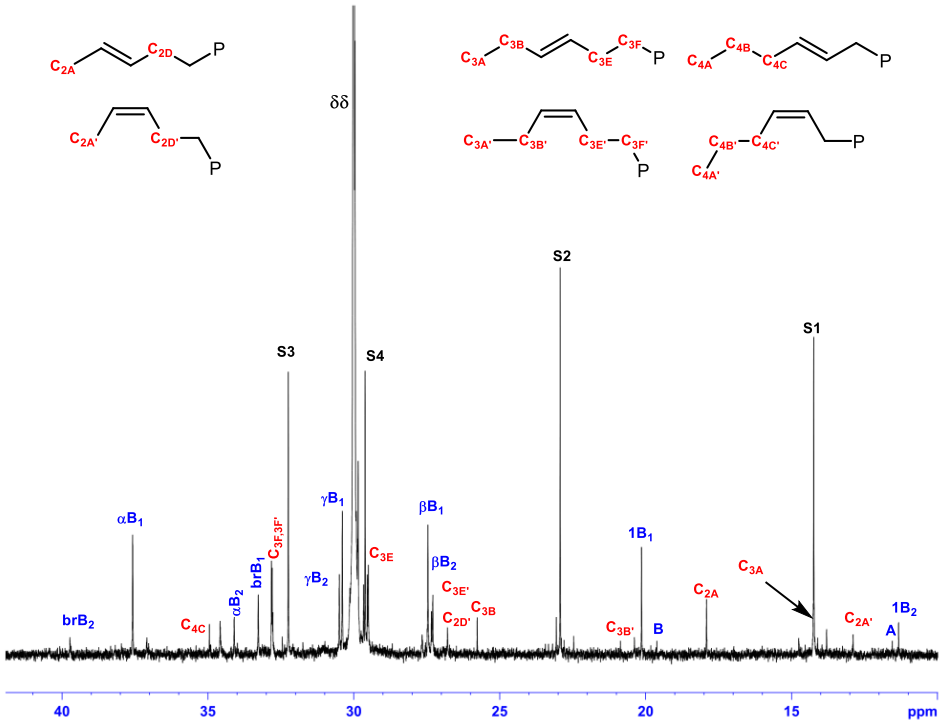

*Figure 126. $^{13}C\{^{1}H\}$ NMR of Aliphatic Region of Polyethylene Formed by **24** (Table 3, entry 1) (125MHz, $CDCl_2CDCl_2$, 100ºC)*

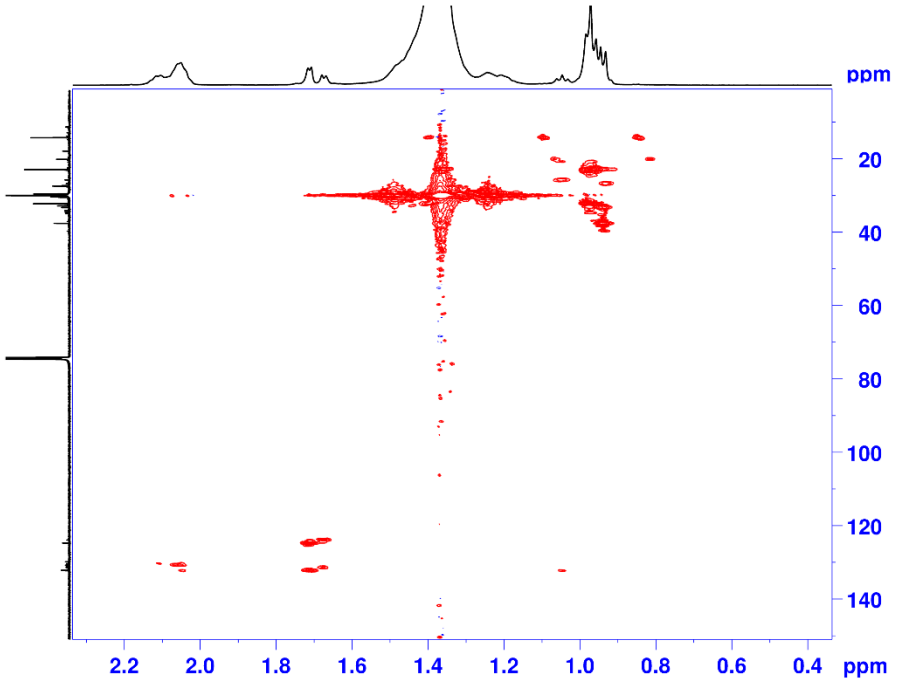

*Figure 127. HMBC of Polyethylene Formed by **24** (Table 3, entry 1) (500MHz, $CDCl_2CDCl_2$, 100ºC)*

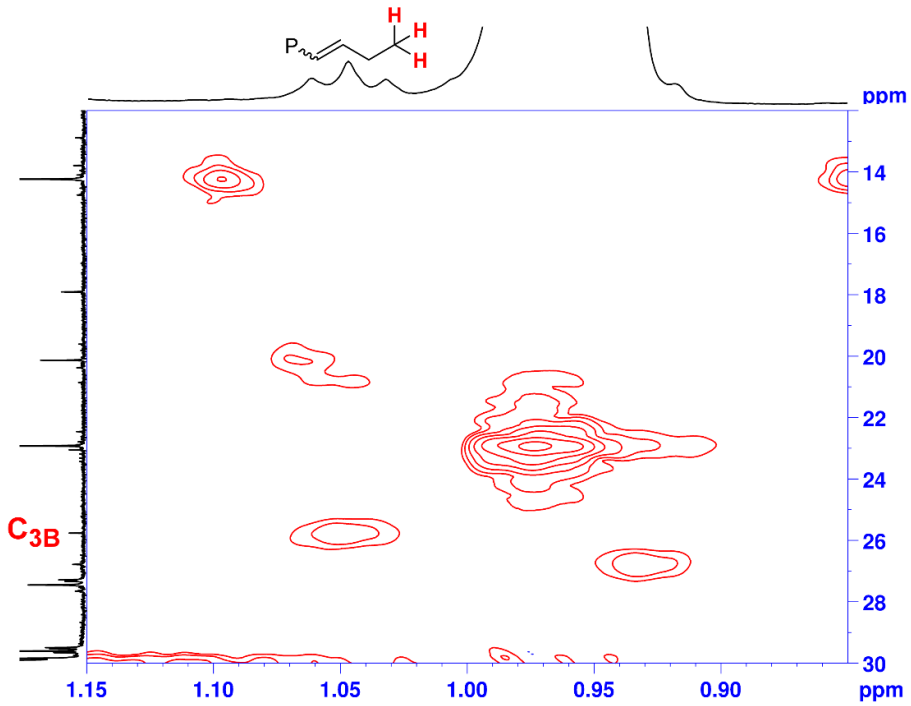

*Figure 128. Expansion of HMBC ((1.15 – 0.85ppm), (30 – 12ppm)) of Polyethylene Formed by **24** (Table 3, entry 1) (500MHz, $CDCl_2CDCl_2$, 100ºC).*

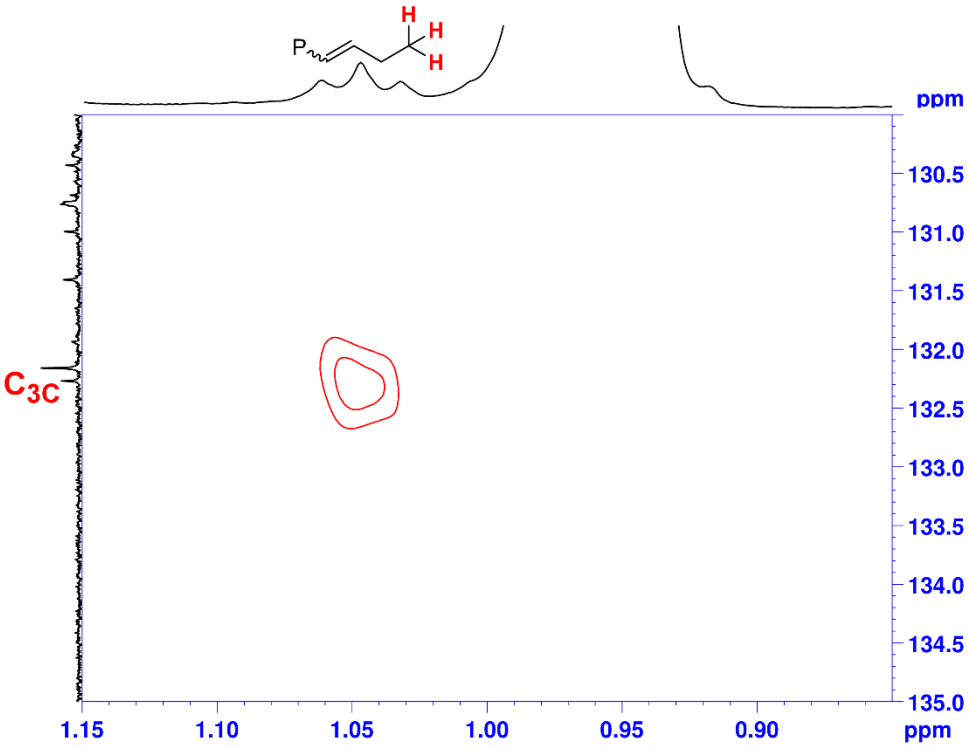

*Figure 129. Expansion of HMBC ((1.15 – 0.85ppm), (135 – 130ppm)) of Polyethylene Formed by **24** (Table 3, entry 1) (500MHz, $CDCl_2CDCl_2$, 100ºC).*

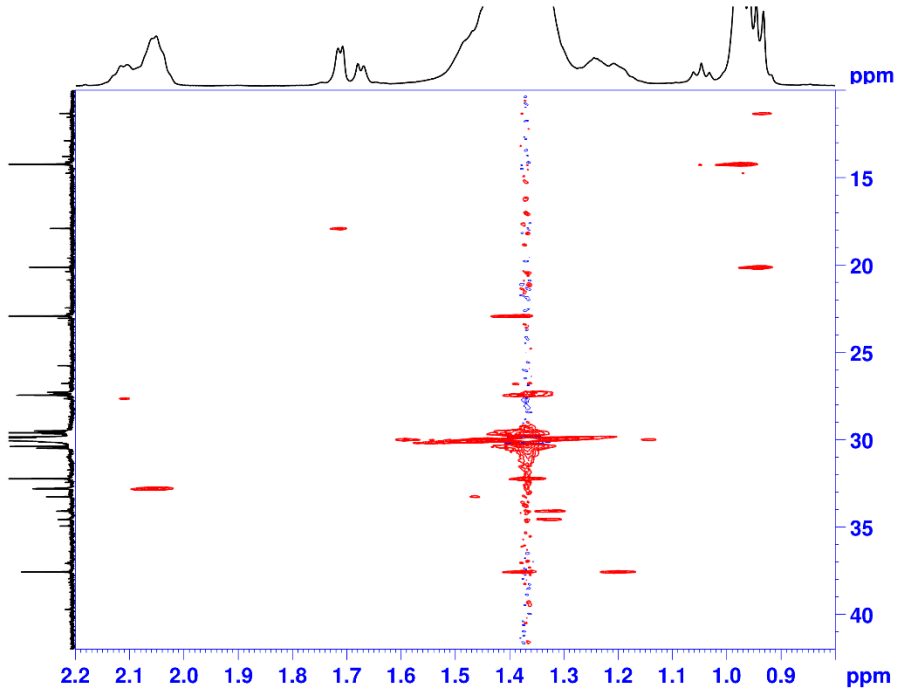

*Figure 130. HSQC of the Polyethylene Formed by **24** (Table 3, entry 1) (500MHz, $CDCl_2CDCl_2$, 100ºC).*

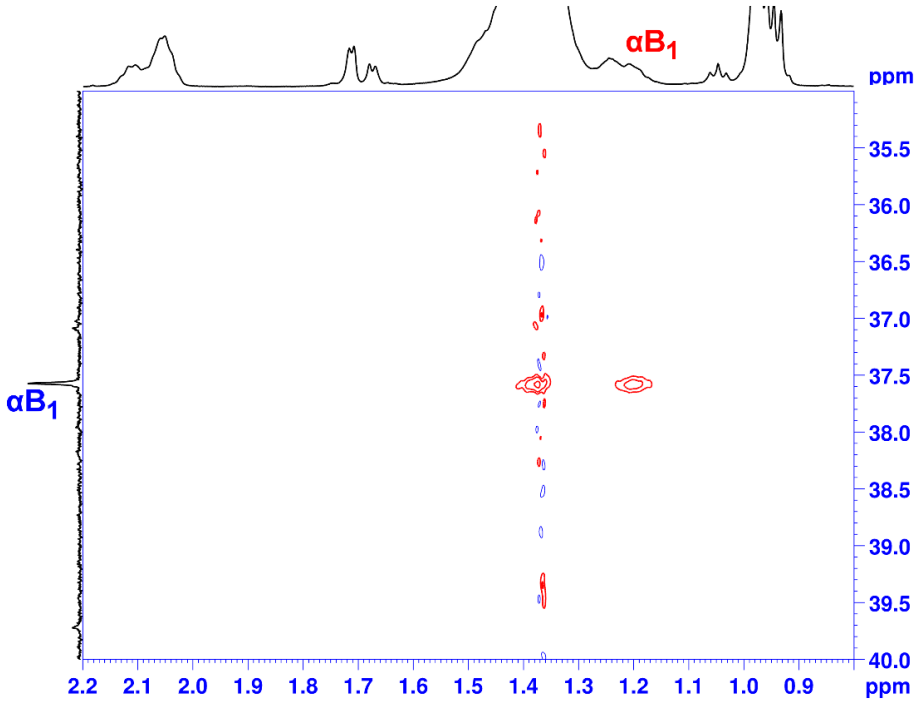

*Figure 131. Expansion of HSQC ((1.50 – 0.70ppm), (40 – 35ppm)) of Polyethylene Formed by **24** (Table 3, entry 1) (500MHz, $CDCl_2CDCl_2$, 100ºC).*

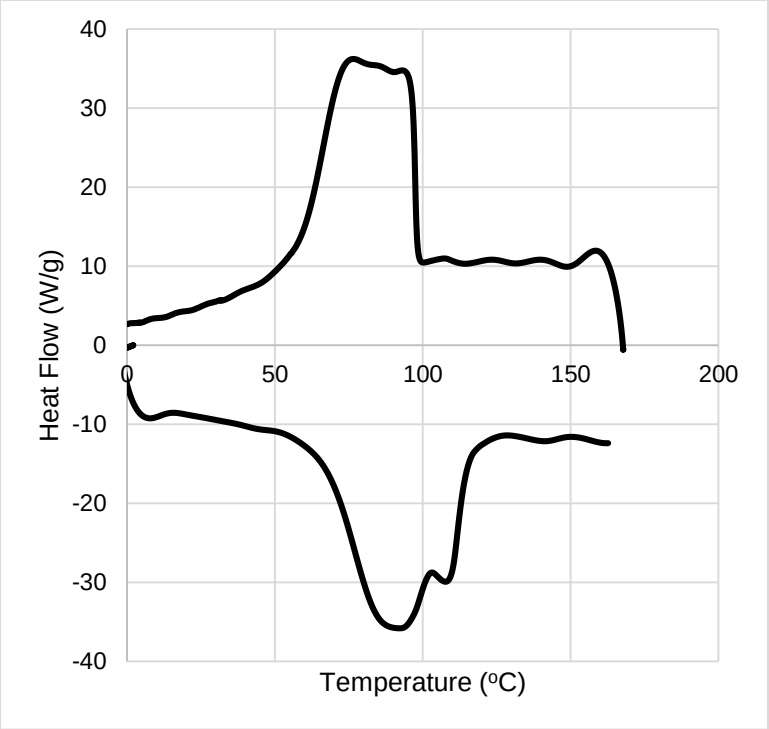

Figure 132. DSC of SasolWax H1.

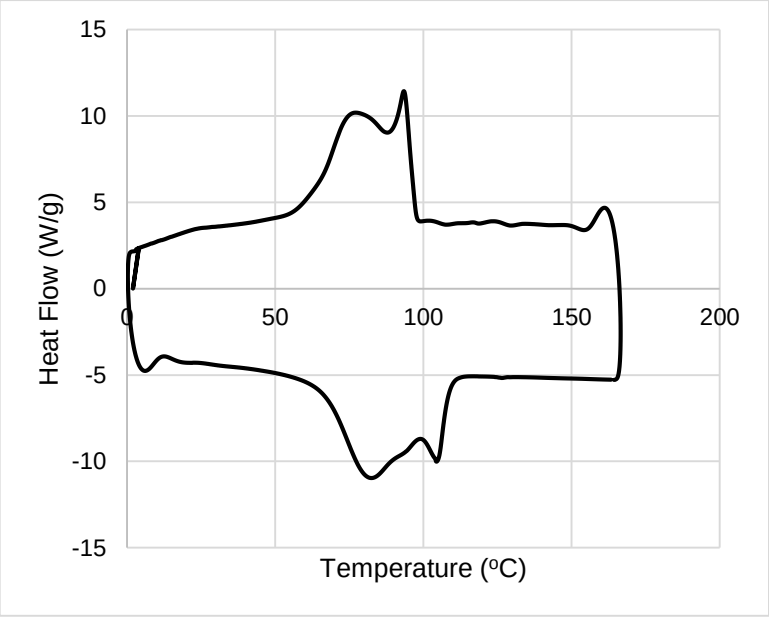

*Figure 133. DCS of polymer product from **24**.*

X-Ray Structure of $[Li(THF)_4]^+[\mu_2\text{-}Cl(\kappa^2\text{-}P,Cl\text{-}P^iPr_2CB_9Cl_9)PdMe)_2]^-$ (**20**):

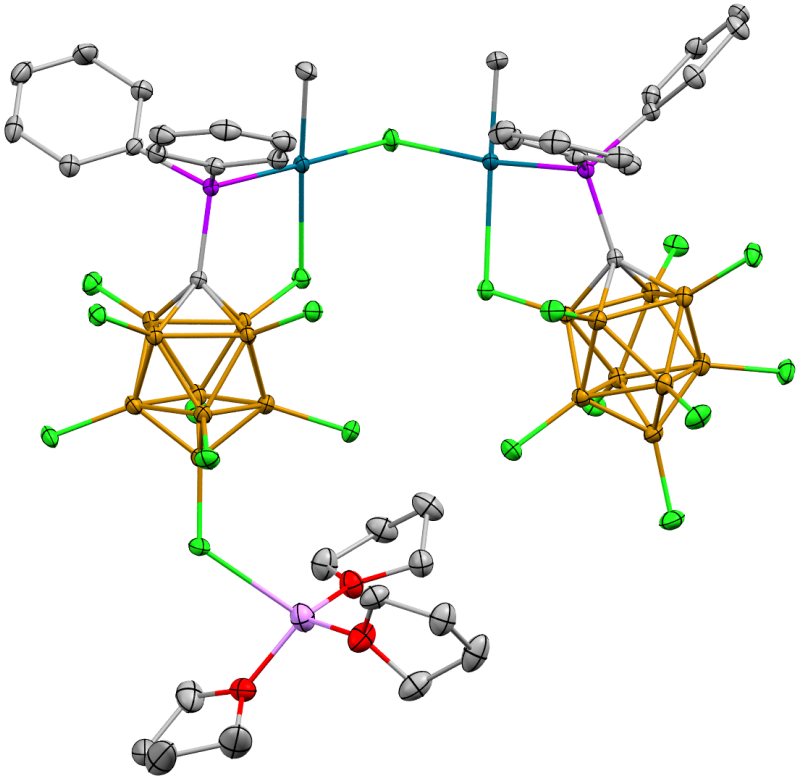

Data collected/Report prepared: Andrew McNeece/Alexander S. Filatov, September/2018 (X-ray Laboratory, Searle B013, Department of Chemistry, the University of Chicago, Chicago, Il).

General information: The diffraction data were measured at 100K on a Bruker D8 VENTURE with PHOTON 100 CMOS detector system equipped with a Mo-target micro-focus X-ray tube (λ = 0.71073 Å). Data were collected using ω and Φ scans to survey a hemisphere of reciprocal space. Data reduction and integration were performed with the Bruker APEX3 software package (Bruker AXS, version 2015.9-0, 2015). Data were scaled and corrected for absorption effects using the multi-scan procedure as implemented in SADABS (Bruker AXS, version 2014/5, Krause, Herbst-Irmer, Sheldrick & Stalke, *J. Appl.*

Cryst. **2015**, *48*, 3-10). The structure was solved by SHELXT (Version 2018/2: Sheldrick, G. M. *Acta Crystallogr*. **2015**, *A**71***, 3-8) and refined by a full-matrix least-squares procedure using OLEX2 (O. V. Dolomanov, L. J. Bourhis, R. J. Gildea, J. A. K. Howard and H. Puschmann. J. Appl. Crystallogr. **2009**, *42*, 339-341) (XL refinement program version 2018/3, Sheldrick, G. M. Acta Crystallogr. **2015**, *C71*, 3-8). Crystallographic data and details of the data collection and structure refinement are listed in Table 1.

Specific details for structure refinement: All elements were refined with anisotropic thermal parameters. Hydrogen atoms were included in idealized positions for structure factor calculations. Several low angle reflections affected by a beamstop were omitted from refinement. All structures are drawn with thermal ellipsoids at 40% probability

Table 1 Crystal data and structure refinement for 0687_reinhart.

Identification code	0687_reinhart
Empirical formula	$C_{40}H_{50}B_{18}Cl_{19}LiO_3P_2Pd_2$
Formula weight	1728.61
Temperature/K	100(2)
Crystal system	triclinic
Space group	P-1
a/Å	11.3936(9)
b/Å	18.2924(15)
c/Å	18.3437(15)
α/°	112.058(2)
β/°	90.830(2)

γ/°	106.104(2)
Volume/Å^3	3373.9(5)
Z	2
ρ_{calc}g/cm^3	1.702
μ/mm^{-1}	1.371
F(000)	1704.0
Crystal size/mm^3	0.327 × 0.311 × 0.271
Radiation	MoKα (λ = 0.71073)
2Θ range for data collection/°	4.186 to 57.522
Index ranges	-15 ≤ h ≤ 15, -24 ≤ k ≤ 24, -23 ≤ l ≤ 24
Reflections collected	135782
Independent reflections	17269 [R_{int} = 0.0358, R_{sigma} = 0.0244]
Data/restraints/parameters	17269/0/768
Goodness-of-fit on F^2	1.049
Final R indexes [I>=2σ (I)]	R_1 = 0.0258, wR_2 = 0.0551
Final R indexes [all data]	R_1 = 0.0351, wR_2 = 0.0580
Largest diff. peak/hole / e Å^{-3}	0.58/-0.40

$R_{int} = \Sigma \mid F_o^2 - \langle F_o^2 \rangle \mid / \Sigma \mid F_o^2 \mid$

$R1 = \Sigma \mid \mid F_o \mid - \mid F_c \mid \mid / \Sigma \mid F_o \mid$

$wR2 = [\Sigma [w (F_o^2 - F_c^2)^2] / \Sigma [w (F_o^2)^2]]^{1/2}$

Goodness-of-fit $= [\Sigma [w (F_o^2 - F_c^2)^2] / (n-p)^{1/2}$

n: number of independent reflections; p: number of refined parameters

X-Ray Structure of (κ^2 -P,Cl-P^{i}Pr$_2$CB$_9$Cl$_9$)PdMe(THF) (**22**):

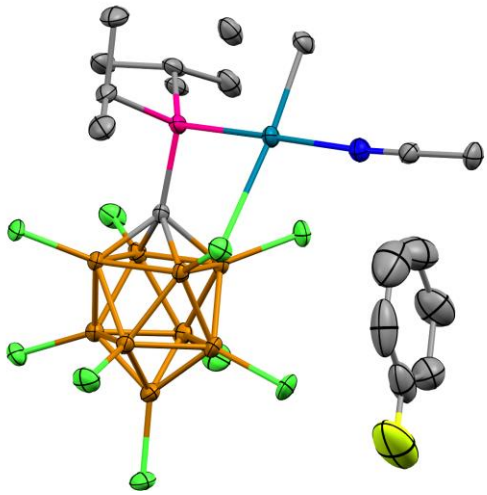

A light yellow needle fragment (0.475 x 0.207 x 0.143 mm^3) was used for the single crystal x-ray diffraction study of $C_{10}H_{20}B_9Cl_9NPPd.[C_6H_5F]_{0.89}$ (sample vL244JKr_0m). The crystal was coated with paratone oil and mounted on to a cryo-loop glass fiber. X-ray intensity data were collected at 100(2) K on a Bruker APEX2 (**ref. 1**) platform-CCD x-ray diffractometer system (fine focus Mo-radiation, λ = 0.71073 Å, 50KV/30mA power). The CCD detector was placed at a distance of 5.0600 cm from the crystal.

A total of 3600 frames were collected for a sphere of reflections (with scan width of 0.3^o in and ω, starting ω and 2σ angles of –30^o, and Φ angles of 0^o, 90^o, 120^o, 180^o, 240^o, and 270^o for every 600 frames, 10 sec/frame exposure time). The frames were integrated using the Bruker SAINT software package (**ref. 2**) and using a narrow-frame integration algorithm. Based on a monoclinic crystal system, the integrated frames yielded a total of 76394 reflections at a maximum 2σ angle of 61.016^o (0.70 Å resolution), of which 9810 were independent reflections (R_{int} = 0.0232, R_{sig} = 0.0132, redundancy = 7.8,

completeness = 100%) and 9259 (94.4%) reflections were greater than 2σ(I). The unit cell parameters were, **a** = 9.4242(3) Å, **b** = 19.9211(6) Å, **c** = 17.3641(5) Å, **σ** = 100.0240(5)°**,** V = 3210.18(17) $Å^3$, Z = 4, calculated density D_c = 1.642 g/cm^3. Absorption corrections were applied (absorption coefficient μ = 1.394 mm^{-1}; max/min transmission = 0.826/0.557) to the raw intensity data using the SADABS program (**ref. 3**).

The Bruker SHELXTL software package (**ref. 4**) was used for phase determination and structure refinement. The distribution of intensities (E^2-1 = 0.909) and systematic absent reflections indicated one possible space group, P2(1)/n. The space group P2(1)/n (#14) was later determined to be correct. Direct methods of phase determination followed by two Fourier cycles of refinement led to an electron density map from which most of the non-hydrogen atoms were identified in the asymmetric unit of the unit cell. With subsequent isotropic refinement, all of the non-hydrogen atoms were identified. There was one molecule of $C_{10}H_{20}B_9Cl_9NPPd$ and one partially occupied C_6H_5F solvent molecule (89% occupied) present in the asymmetric unit of the unit cell. One of the two isopropyl-groups of $C_{10}H_{20}B_9Cl_9NPPd$ was modeled with disorder (disordered site occupancy factor ratio was 81%/19%).

Atomic coordinates, isotropic and anisotropic displacement parameters of all the non-hydrogen atoms were refined by means of a full matrix least-squares procedure on F^2. The H-atoms were included in the refinement in calculated positions riding on the atoms to which they were attached. The refinement converged at R1 = 0.0335, wR2 = 0.0859, with intensity I>2σ (I). The largest peak/hole in the final difference map was 1.206/-0.725 e/$Å^3$. The high difference electron density peak/hole near the Pd atom is probably due to absorption correction errors.

X-Ray Structure of (κ^2 -P,Cl-$PPh_2CB_9Cl_9$)PdMe(THF) (**23**):

A colorless prism fragment (0.437 x 0.272 x 0.103 mm^3) was used for the single crystal x-ray diffraction study of $C_{18}H_{21}B_9Cl_9OPPd$ (sample vL305JK_0m). The crystal was coated with paratone oil and mounted on to a cryo-loop glass fiber. X-ray intensity data were collected at 100(2) K on a Bruker APEX2 (**ref. 1**) platform-CCD x-ray diffractometer system (fine focus Mo-radiation, λ = 0.71073 Å, 50KV/30mA power). The CCD detector was placed at a distance of 5.0600 cm from the crystal.

A total of 3600 frames were collected for a sphere of reflections (with scan width of 0.3° in ω, starting ω and 2σ angles of –30°, and Φ angles of 0°, 90°, 120°, 180°, and 270° for every 600 frames, 10 sec/frame exposure time). The frames were integrated using the Bruker SAINT software package (**ref. 2**) and using a narrow-frame integration algorithm. Based on a monoclinic crystal system, the integrated frames yielded a total of 72659 reflections at a maximum 2σ angle of 61.010° (0.70 Å resolution), of which 9403 were independent reflections (R_{int} = 0.0282, R_{sig} = 0.0163, redundancy = 7.7, completeness = 99.9%) and 8711 (92.6%) reflections were greater than 2□(I). The unit cell parameters were, **a** = 11.3882(4) Å, **b** = 15.4099(5) Å, **c** = 18.1835(6) Å, **σ** = 104.5787(5)°**,** V = 3088.30(18) $Å^3$, Z = 4, calculated density D_c = 1.736 g/cm^3. Absorption corrections were applied (absorption coefficient μ = 1.449 mm^{-1}; max/min transmission = 0.865/0.570) to the raw intensity data using the SADABS program (**ref. 3**).

The Bruker SHELXTL software package (**ref. 4**) was used for phase determination and structure refinement. The distribution of intensities (E^2-1 = 0.944) and systematic absent reflections indicated one possible space group, P2(1)/c. The space group P2(1)/c

(#14) was later determined to be correct. Direct methods of phase determination followed by two Fourier cycles of refinement led to an electron density map from which most of the non-hydrogen atoms were identified in the asymmetric unit of the unit cell. With subsequent isotropic refinement, all of the non-hydrogen atoms were identified. There was one whole molecule disorder of $C_{18}H_{21}B_9Cl_9OPPd$ present in the asymmetric unit of the unit cell. (disordered site occupancy ratio was 90%/10%).

Atomic coordinates, isotropic and anisotropic displacement parameters of all the non-hydrogen atoms were refined by means of a full matrix least-squares procedure on F^2. The H-atoms were included in the refinement in calculated positions riding on the atoms to which they were attached. The refinement converged at R1 = 0.0286, wR2 = 0.0597, with intensity I>2σ (I). The largest peak/hole in the final difference map was 0.611/-0.781 e/Å^3.

X-Ray Structure of (κ^2 -P,O-P(*o*-OMe-Ph)$_2$CB$_9$Cl$_9$)PdMe(THF) (**24**):

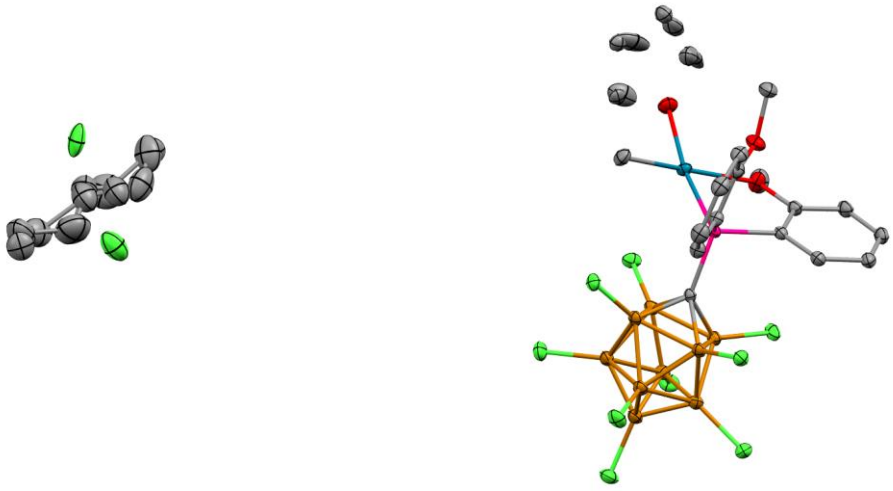

A red prism fragment (0.545 x 0.485 x 0.211 mm^3) was used for the single crystal x-ray diffraction study of $[C_{20}H_{25}B_8Cl_9O_3PPd].[CH_2Cl_2]_{1.04}.[C_5H_{12}]_{0.5}$ (sample vL285JK_0m).

The crystal was coated with paratone oil and mounted on to a cryo-loop glass fiber. X-ray intensity data were collected at 100(2) K on a Bruker APEX2 (**ref. 1**) platform-CCD x-ray diffractometer system (fine focus Mo-radiation, λ = 0.71073 Å, 50KV/30mA power). The CCD detector was placed at a distance of 5.0600 cm from the crystal.

A total of 3600 frames were collected for a sphere of reflections (with scan width of 0.3^o in ω, starting ω and 2σ angles of –30^o, and Φ angles of 0^o, 90^o, 120^o, 180^o, 240^o, and 270^o for every 600 frames, 10 sec/frame exposure time). The frames were integrated using the Bruker SAINT software package (**ref. 2**) and using a narrow-frame integration algorithm. Based on a monoclinic crystal system, the integrated frames yielded a total of 93649 reflections at a maximum 2σ angle of 61.016^o (0.70 Å resolution), of which 12206 were independent reflections (R_{int} = 0.0195, R_{sig} = 0.0111, redundancy = 7.7, completeness = 100%) and 11349 (93.0%) reflections were greater than 2σ(I). The unit cell parameters were, **a** = 35.4349(15) Å, **b** = 10.7750(5) Å, **c** = 21.1647(9) Å, **σ** = 98.2521(6)^o**,** V = 7997.2(6) Å^3, Z = 8, calculated density D_c = 1.647 g/cm^3. Absorption corrections were applied (absorption coefficient μ = 1.273 mm$^{-1;}$ max/min transmission = 0.775 /0.544) to the raw intensity data using the SADABS program (**ref. 3**).

The Bruker SHELXTL software package (**ref. 4**) was used for phase determination and structure refinement. The distribution of intensities (E^2-1 = 0.936) and systematic absent reflections indicated two possible space groups, Cc and C2/c. The space group C2/c (#15) was later determined to be correct. Direct methods of phase determination followed by two Fourier cycles of refinement led to an electron density map from which most of the non-hydrogen atoms were identified in the asymmetric unit of the unit cell. With subsequent isotropic refinement, all of the non-hydrogen atoms were identified. There was one molecule of $C_{20}H_{25}B_8Cl_9O_3PPd$ (where the THF was modeled with

50%/50% disorder), one disordered solvent molecule of CH_2Cl_2 (disordered site occupancy ratio was 57%/43%), partially occupied disordered solvents of C_5H_{12}/CH_2Cl_2 (disordered site occupancy ratio was 50%/4%) present in the asymmetric unit of the unit cell. The partially occupied disordered solvents of C_5H_{12}/CH_2Cl_2 molecules were located at the 2-fold rotation axis parallel to the b-axis.

Atomic coordinates, isotropic and anisotropic displacement parameters of all the non-hydrogen atoms were refined by means of a full matrix least-squares procedure on F^2. The H-atoms were included in the refinement in calculated positions riding on the atoms to which they were attached. The refinement converged at R1 = 0.0212, wR2 = 0.0553, with intensity I>2σ (I). The largest peak/hole in the final difference map was 0.590/-0.444 e/Å^3.

X-Ray Structure of (κ^3 -P,S,S-P(*o*-SMe-Ph)$_2$CB$_9$Cl$_9$)PdMe (**25**):

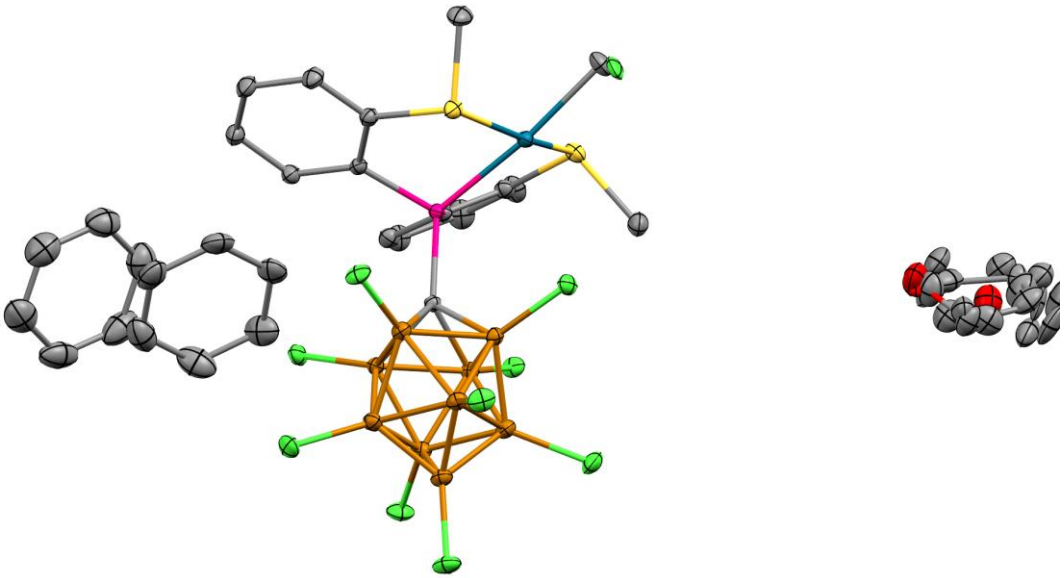

A light brown prism fragment (0.510 x 0.293 x 0.236 mm^3) was used for the single crystal x-ray diffraction study of $C_{16}H_{17}B_9Cl_9PS_2Pd.[C_6H_6]_{2.29}.[C_4H_8O]_{0.71}$ (sample vL316JK_0m). The crystal was coated with paratone oil and mounted on to a cryo-loop glass fiber. X-ray intensity data were collected at 100(2) K on a Bruker APEX2 (**ref. 1**) platform-CCD x-ray diffractometer system (fine focus Mo-radiation, λ = 0.71073 Å, 50KV/30mA power). The CCD detector was placed at a distance of 5.0600 cm from the crystal.

A total of 3600 frames were collected for a sphere of reflections (with scan width of 0.3° in ω, starting ω and 2σ angles of –30°, and Φ angles of 0°, 90°, 120°, 180°, and 270° for every 600 frames, 10 sec/frame exposure time). The frames were integrated using the Bruker SAINT software package (**ref. 2**) and using a narrow-frame integration algorithm. Based on a monoclinic crystal system, the integrated frames yielded a total of 104174 reflections at a maximum 2σ angle of 61.012° (0.70 Å resolution), of which 13438 were independent reflections (R_{int} = 0.0224, R_{sig} = 0.0127, redundancy = 7.8, completeness = 100%) and 12529 (93.2%) reflections were greater than 2□(I). The unit cell parameters were, **a** = 12.4713(8) Å, **b** = 16.2133(11) Å, **c** = 22.0813(15) Å, **β** = 99.5417(10)°**,** V = 4403.1(5) $Å^3$, Z = 4, calculated density D_c = 1.598 g/cm^3. Absorption corrections were applied (absorption coefficient μ = 1.135 mm^{-1}; max/min transmission = 0.776/0.595) to the raw intensity data using the SADABS program (**ref. 3**).

The Bruker SHELXTL software package (**ref. 4**) was used for phase determination and structure refinement. The distribution of intensities (E^2-1 = 0.948) and systematic absent reflections indicated one possible space group, P2(1)/n. The space group P2(1)/n (#14) was later determined to be correct. Direct methods of phase determination followed by two Fourier cycles of refinement led to an electron density map from which most of the

non-hydrogen atoms were identified in the asymmetric unit of the unit cell. With subsequent isotropic refinement, all of the non-hydrogen atoms were identified. There was one disordered molecule of $C_{16}H_{17}B_9Cl_9PS_2Pd$ [disordered site occupancy ratio of CH_3/Cl1D was 89%/11%], two normal benzene molecules, and a partially occupied and disordered benzene/THF molecules present in the asymmetric unit of the unit cell. The benzene partial site occupancy factor of the benzene/THF disorder was 29%. The three different THF side occupancy ratios of the benzene/THF disorder were 34%/22%/15%.

Atomic coordinates, isotropic and anisotropic displacement parameters of all the non-hydrogen atoms were refined by means of a full matrix least-squares procedure on F^2. The H-atoms were included in the refinement in calculated positions riding on the atoms to which they were attached. The refinement converged at R1 = 0.0193, wR2 = 0.0473, with intensity I>2σ (I). The largest peak/hole in the final difference map was 0.466/-0.343 e/Å^3.

CHAPTER 6: Carborane Ligands: Unlocking Unique Pd^{I} Dimer Chemistry

Introduction

Pd chemistry has been a powerful tool for the production of pharmaceuticals, electronics, and even dental amalgam. In 2010, Richard F. Heck, Ei-ichi Negishi, and Akira Suzuki won the Nobel Prize in Chemistry for their development in palladium and nickel based C-C cross coupling catalysis. Since then, there has been an explosion in research investigating Pd catalysis. The first example is the advent of a Pd-Pd dimer where each metal has nine d-electrons, first characterized in 1973 by McCormick *et*. *al*. as a CO complex bearing two bridging halides and a formal Pd-Pd bond, shown in Figure 135.[168] Since its development, numerous groups have probed this class of compound investigating the nature and utility of the Pd metal-metal bond. Ozerov *et. al*. found that a Pd^{I} dimer complex, featuring a PNP pincer-type ligand, could bimolecularly reduce ammonia into the corresponding Pd amide and Pd hydride complexes.[169] Moreover, Pd^{I} dimer chemistry has been well studied in its application to C-C cross coupling catalysis.[170,171]

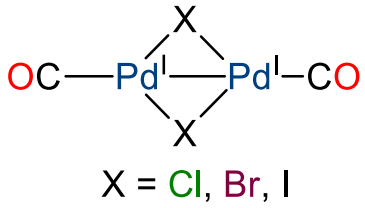

Figure 134. The first characterized Pd^{I} Dimer.

In this report, we wanted to probe what unique chemistry this class of Pd organometallic complex can engage in. The carborane anion is a member of a class of compounds that are some of the most inert chemicals known to science and is known to participate in widely unique chemistry.[9,10,32,49] Therefore, we thought it would aide us in our goal as a ligand substituent. Here, we report some unique chemistry enabled by the carborane anion.

Results and Discussion

Pd^{I} dimers can be produced through a number of ways. Irradiation with ultraviolet light will homolytically cleave a Pd-alkyl bond generating a Pd^{I} dimer complex.[172] However, a more simple approach can be taken thanks to work done by Kurosawa *et. al*.[173] Here, $[Pd_2(MeCN)_6]^{2+}[BF_4]_2^-$ is generated containing labile acetonitrile ligands which can be substituted for more coordinating species. In this report, we coordinate a carboranyl phosphine **16** to this Pd^{I} dimer. As shown in Figure 136, two equivalents of ligand **16** are dissolved in fluorobenzene and added to a fluorobenzene solution containing the orange $[Pd_2(MeCN)_6]^{2+}[BF_4]_2^-$ salt. Immediately upon mixing, the solution turns to a dark, wine red color and produced substantial precipitate.

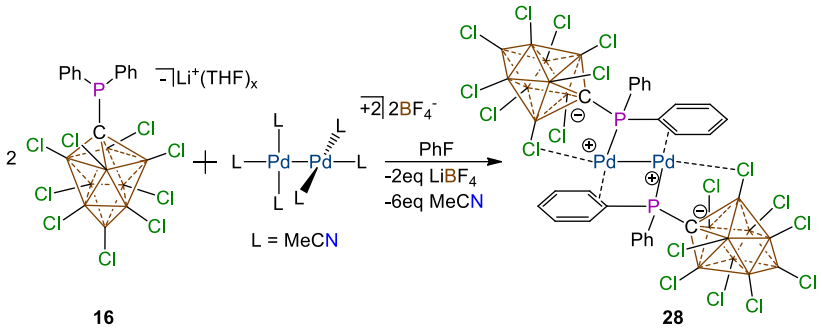

*Figure 135. Synthesis of **28** using $[Pd_2(MeCN)_6]^{2+}[BF_4]_2^-$*

Subsequently, after the filtration of the solvent, $LiBF_4$ is washed away using diethyl ether. The remaining red solid is clean **28**. As mentioned earlier, complexes like **28** can be synthesized by either thermolysis or photolysis of a Pd-Alkyl bond.[172] Therefore, we attempted to decompose complex **23** into **28** by heating and irradiating with UV light in two separate reactions. Indeed, both methods produced **28** as beautiful, dark red crystals which grow from the dichloromethane solution.

Multinuclear magnetic resonance studies were used to elucidate the structure. The ^1H NMR is rather simple displaying only three sets of triplets seen ranging from 8.13-7.86ppm relating to aromatic protons. The most downfield triplet is noticeably broadened

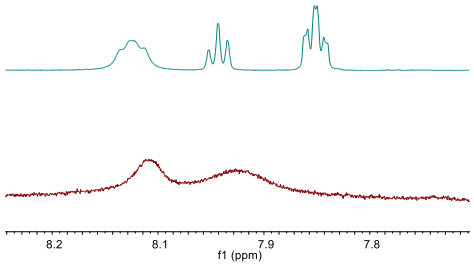

*Figure 136. ^{1}H VT NMR of complex **28** in THF-d_8. Turquoise spectrum is at 23°C. Red spectrum is at -100°C.*

out relative to the other two sets, suggesting π-coordination to one of the Pd centers. To probe this interaction, a variable temperature ^{1}H NMR was carried out. The results from this experiment can be seen in Figure 137. The broadened most downfield triplet completely disappears at -100°C confirming the π-interaction with the *ipso*-H and *ortho*-H on one of the aryl groups. This rotation also broadens out the two upfield triplets and shifts them downfield (Fig. 137). Unfortunately, the solution freezes at the coalescence temperature. This prevented us from isolating the π complex by NMR. The ^{11}B{^{1}H} NMR shows the typical 1:4:4 singlet pattern suggesting that if there is coordination by one of the $Cl_{cluster}$ to the Pd center, this binding mode permits the rapid rotation of the boron cluster retaining its C_{4v} symmetry which freely rotates below that of -100°C. The ^{31}P{^{1}H} NMR shows a downfield shift of roughly 15ppm to 25.1ppm.

A single crystal X-ray diffraction study was then carried out on complex **28**. Crystals suitable for diffraction were grown from layering a solution of THF containing **28** with pentane in an NMR tube. The structure is shown in Figure 137. The Pd-Pd bond distance is 2.6065(2)Å which is typical for Pd metal-metal bonds.[172] Both Pd-$Cl_{cluster}$ interactions are 2.4812(5)Å (Pd1-Cl1)

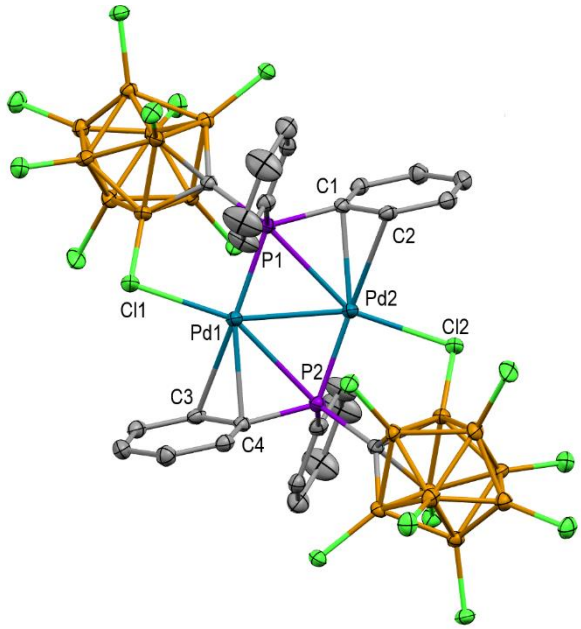

*Figure 137. Crystal Structure of complex **28**.*

and 2.4669(5)Å (Pd2-Cl2), which are fairly similar. This interaction elongates both B-Cl bonds (B1-Cl1: 1.793(2)Å, B2-Cl2: 1.780(2)Å) relative to the average of the B-Cl lengths (1.765Å). What is noteworthy is the seeming bridging phosphine interactions between the Pd centers. Determining whether this interaction is just an artifact from the data processing resulting from the aryl group pulling the phosphine close to its Pd neighbor or is the bond line an actual interaction is difficult. There have been several examples where Pd dimers have μ^2-phosphine coordination modes.[174,175] These distances for **28** are 2.7285(5)Å (Pd2-P1) and 2.7648(5)Å (Pd1-P2) which are quite long. Regardless, the Pd1-P1 (2.2131(5)Å) and Pd2-P2 (2.2169(5)Å) distances are normal for this class of organometallic complex.[170] The π-interaction between the aryl groups and the Pd centers is substantial with Pd1-C3 and Pd1-C4 lengths being 2.460(2)Å and 2.3803(19)Å, respectively. Unsurprisingly, this elongates the C3-C4 bond to 1.417(3)Å which deviates from the average of the non-coordinated C-C aryl bonds (1.393Å). Likewise for the other half of this dimer, the Pd2-C1 and Pd2-C2 lengths are 2.3478(19)Å and 2.489(2)Å, respectively. Again, this elongates the C1-C2 bond substantially to 1.414(3)Å which is significantly longer than the average of the non-coordinated C-C aryl bonds (1.387Å).

With a deeper understanding of **28** in solution and in the solid state, it was time to probe its reactivity and investigate the nature of this interesting metal-metal bond. To start, a cyclic voltammetry experiment was carried out (Fig. 138). Initially scanning

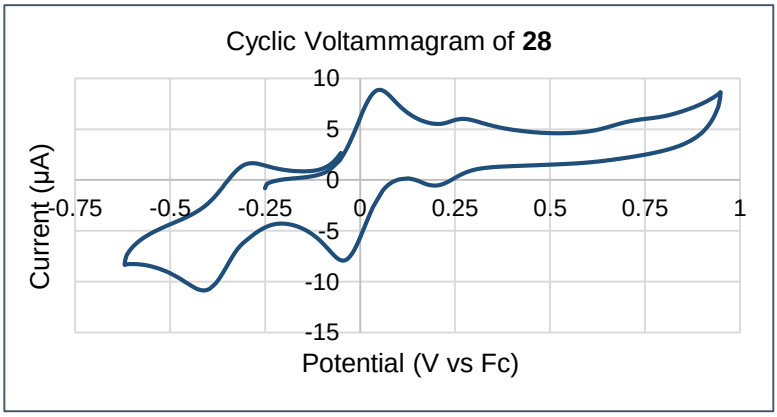

*Figure 138. CV of **28**. THF solution of 0.1 M $[nBu_4N]^+[PF_6]^-$ as electrolyte, scan rate 100 mV/s, potential vs. Fc^+/Fc.*

oxidatively, there is a reversible oxidation event a 0.27V vs Fc. At 0.7V is an irreversible oxidation event. Upon sweeping reductively, a large reversible reduction event is observed at -0.34V vs Fc. With this knowledge in hand, we next sought to identify the species responsible for these reversible oxidation/reduction waves at 0.27 and -0.34V. To do so, we selected a number of appropriate oxidants and reductants to achieve this goal. For the oxidation, we first attempted $[Ag]^+[closo\text{-}HCB_{11}H_5Cl_6]^-$ as our oxidant. Though Ag^+ has a oxidation potential sufficient enough to oxidize **28** (0.41V vs. Fc in THF)[176], no reaction occurred. This is probably a result of the coordinating solvent (1,2-dimethoxyethane) that prevents oxidation to occur by cation sequestriation.[176] Using a stronger oxidant, $[NO]^+[BF_4]^-$, was also attempted. Here, no observable color change had occurred. When characterized by the by multinuclear magnetic resonance and X-ray diffraction, complex **29** was the resulting product (Fig. 140). Here, the NO^+ radical was reduced by the Pd-Pd bond giving a bent NO ligand. Finding more compatible oxidants and reductants is ongoing.

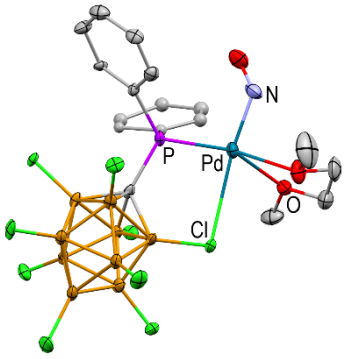

*Figure 139. Crystal Structures for **29**. No discussion of bond lengths and angles can be made from this data.*

We were interested in more than simply the electrochemistry of **28**. Therefore, we probed this complex's reactivity with small molecules. Pd^1 dimers are effective C-C cross coupling catalysts,[171,172] therefore we sought to react **28** with iodobenzene and bromobenzene. Bromobenzene had no reactivity. However, iodobenzene reacted with **28** immediately as

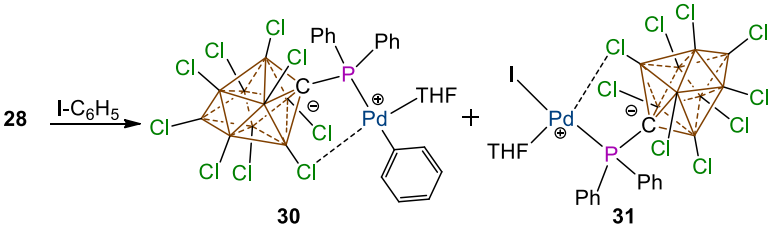

*Figure 140. Proposed structures of **31** and **32**.*

evidenced by two new $^{31}P\{^{1}H\}$ resonances at 42.8 and 41.8ppm. Though no crystal structure is currently available, multinuclear magnetic resonance studies lead us to the proposed structures in Figure 140. In the ^{1}H NMR, nine sets of aromatic protons suggest several distinct aromatic species. One of those sets has an integration ratio of 2:1:2 which corresponds to the aryl group originally from the iodobenzene reagent. Keeping this same integration, the remaining set of aromatic protons integrate to a total of 20 hydrogens and have more complicated splitting resulting from the spin ½ of ^{31}P nucleus (Fig. 123, *Experimental)*. Additionally, $^{11}B\{^{1}H\}$ NMR shows very distinct magnetic environments as there are only 3 peaks in a 1:4:4 ratio, showing that the local C_{4v} symmetry is preserved. This structure is certainly not an unreasonable proposition. Indeed, there have been several reports where Pd dimers bimolecularly oxidatively add across an aryl C-X bond.[170,177,178]

Next, we probed **28**'s reactivity with ethylene. Upon condensing ethylene into a frozen solution of **28** in THF using liquid N_2 and warming the mixture to room temperature, a dramatic color change is observed. The red solution begins to turn mostly colorless with a fine yellow powder that precipitates from solution. When the ethylene atmosphere is removed, the yellow powder begins to leech a red color when in THF. Indeed, when in any solvent without the presence of an ethylene atmosphere, ethylene is slowly released from this mysterious yellow compound and **28** is regenerated. Acetonitrile will immediately displace ethylene. Due to the challenges associated with this compound in solution, we moved to solid state NMR characterization.

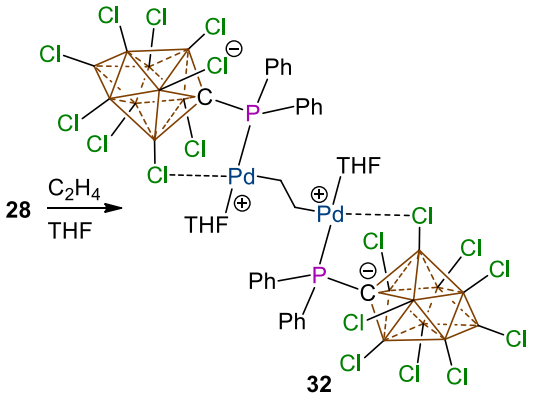

*Figure 141. Proposed structure for complex **32**.*

The most useful NMR performed with this technique was the ^{13}C NMR. Two THF peaks can be seen at 67.7 and 25.9ppm which suggests the presence of coordinated THF to the Pd center(s). The aromatic region show resonances from 134.3-121.4ppm representing the phenyl groups from the ligand. Another resonance is seen at 39.2ppm. Being in the alkyl region, this suggests that the Pd-Pd bond had reduced the ethylene. Combining this information and knowing that the carboranyl ligand tends to bind in a bidentate fashion, the product must be a Pd^{II} species having a k^2-P,Cl carboranyl phosphine ligation with an ethylene bridge connecting the two Pd centers. Two THF molecules must be present to complete the square planar geometry that is typical for d^8 Pd^{II} species. Figure 141 shows reaction scheme of **32**. To unambiguously prove the accuracy of the structure of **32**, crystallographic data is necessary. However, the sensitivity of this complex makes growing single crystals from solution difficult as it is not soluble and readily decomposes in the absence of ethylene atmosphere while suspended in solution.

Nelson *et*. *al*. has shown that microcrystal electron diffraction (MicroED) can be applied to small molecules that are crystalline but whose crystals are too small, too

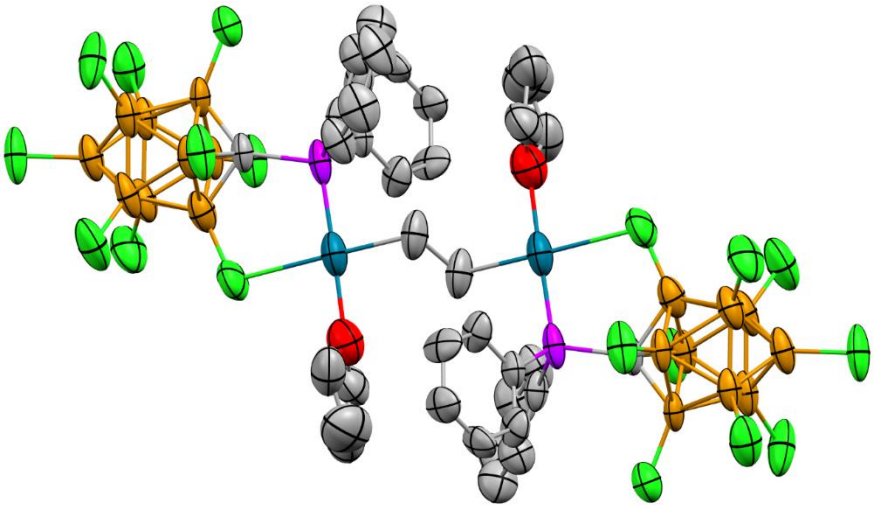

*Figure 142. Crystal structure for Complex **32** by MicroED. Diffraction was collected with 300keV TEM using continuous rotation at ambient temperature. Color codes: blue = Pd; brown = B; green= Cl; grey = C; purple = P; red = O.*

sensitive, or both for X-ray diffraction.[179] MicroED is not a new crystallographic technique. In fact, it has been used for the determination of biological structures such as the famous T4 Bacteriophage elucidated in 1968.[180] Reviews on this technique can be found here.[181,182] We thought that this technique would be a useful tool for determining the structure of our compound. Indeed, observing our compound by TEM showed **32** was nanocrystalline and therefore suitable for electron diffraction. Upon diffraction and data processing, the connectivity of **32** finally could be elucidated. Shown in Figure 142 is the first, new organometallic complex characterized by this technique. Though this technique does not permit a discussion of bond lengths and angles, it unambiguously confirms the proposed structure of **32**. Though there have been reports of a handful of ethylene bridged dimers, none include Pd. Furthermore, these examples do not show that can those species can bimolecularly reductively eliminate ethylene to regenerate the starting material, as **32** can.[183–185] Currently, new reactivity is being explored with this complex.

Conclusion

In this report, we developed a new Pd^{I} dimer ligated by a carboranyl diarylphosphine which was fully characterized by multinuclear magnetic resonance and X-ray crystallography. The redox capacity of the Pd-Pd metal bond was also investigated. Compound **28** rapidly reacts with $I\text{-}C_6H_5$ to generate the oxidative addition products **30** and **31**. Furthermore, the reactivity of **28** was probed where we found unique chemistry involving the reversible bimetallic oxidative addition of ethylene across the Pd-Pd metal bond. In this unique reaction, we used the novel crystallographic technique, MicroED, to elucidate the fascinating structure of **32**.

Experimental

General Considerations: Unless otherwise stated, all manipulations were carried out using standard Schlenk or glovebox techniques (O_2, H_2O < 1ppm) under a dinitrogen or argon atmosphere. Solvents were dried on K or CaH_2 and distilled under argon before use. **23** was prepared according to the literature procedure with modifications.[102] NMR spectra were recorded at room temperature on Bruker Avance 300MHz, Bruker Avance 400MHz, or Bruker Avance 600MHz spectrometers. NMR chemical shifts are reported in parts per million (ppm). ^{1}H NMR and ^{13}C NMR chemical shifts were referenced to residual protio solvent. ^{11}B NMR chemical shifts were externally referenced to BF_3OEt_2. ^{31}P NMR chemical shifts were externally referenced to 80% H_3PO_4 in H_2O. CV experiments were performed using a Pine AFP1 potentiostat. The cell consisted of a glassy carbon working electrode, a Pt wire auxiliary electrode, and a Pt wire pseudo reference electrode. All potentials are referenced versus the ferrocene/ferrocenium couple measured as an internal standard. Crystallographic data for **28** is available free of charge from the Cambridge Crystallographic Data Center under reference number 1850911. This structure can be accessed at: http://www.ccdc.cam.ac.uk/Community/Requestastructure/Pages/DataRequest.aspx.

Modified Synthesis of Complex **18**:

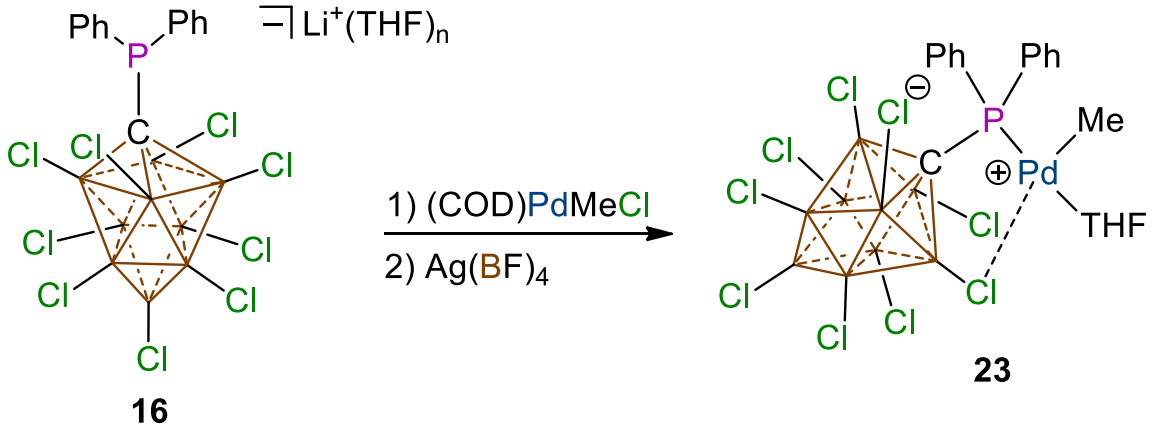

16 **23**

16 is made from literature procedure.[102] **16** (1.00g, 1.10mmol) was added to a glass scintillation vial equipped with a stir bar and PhF (10mL) is added. (COD)PdMeCl (291mg,1.10mmol) is added to a glass scintillation and PhF (5mL) was added. The solution containing CODPdMeCl was then added to the vial containing the solution with **16**. Additional PhF (5mL) was added to wash the vial containing (COD)PdMeCl and was subsequently added to the reaction vial. The reaction was allowed to stir at room temperature for 30 minutes. After 30 minutes, the reaction was filtered through a Hirsch funnel fitted with a glass microfiber filter. The filtrate was pumped to dryness with reduced pressure. The ensuing solid was the washed with portions of pentane (10mL x5) to remove cyclooctadiene. The solid was then left on the vacuum for two hours. The solid was then redissolved in PhF (5mL) and equipped with a stir bar. $AgBF_4$ (107mg, 55.0µmol) was added to a glass scintillation vial and PhF (5mL) was added. The $AgBF_4$ solution was then added to the vial containing the Pd containing solution. The vial containing $AgBF_4$ solution was washed again with PhF (5mL) which was then added to the reaction vial. The reaction was then allowed to stir at room temperature for two hours. After two hours had passed, the reaction was filtered through a Hirsch funnel fitted with a glass microfiber filter and the solid was washed with excess PhF. Diethyl ether was then pass through the filter to

remove $LiBF_4$. The desired compound was then extracted through the filter paper with copious amounts of THF. The THF solution was removed *in vacuo* to produce clean **23**. Yield: 725mg, 93.5µmol, 85%.

Synthesis of Complex **28:**

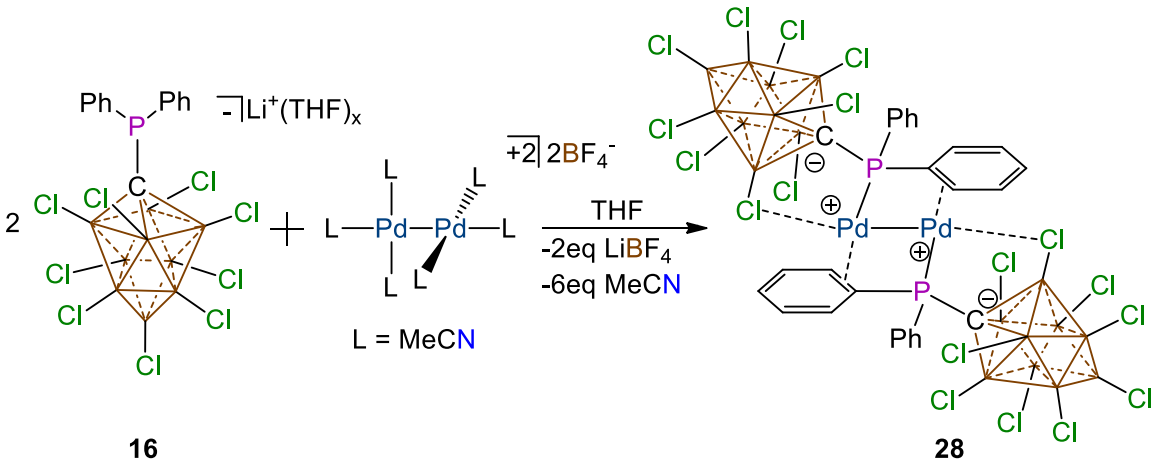

16 **28**

Ligand **16** (500mg, 550µmol) was placed in a 20mL glass scintillation vial that was equipped with a stir bar. Fluorobenzene (5mL) was subsequently added to the white powder and the solution was set to stir. $[Pd_2(MeCN)_6]^+[BF_4]_2^-$ (142mg, 225µmol) was placed in a in a 20mL glass scintillation vial followed by the addition of fluorobenzene (3mL). The vial with the solution containing $[Pd_2(MeCN)_6]^+[BF_4]_2^-$ was added slowly to the stirring solution which immediately turned dark red. The vial containing $[Pd_2(MeCN)_6]^+[BF_4]_2^-$ was washed with flurobenzene (1mL) and added to the red solution. The reaction was left to stir for 24 hours. The next day, the reaction was filtered through a Hirsch funnel fitted with a glass microfiber filter and the solid was washed with excess PhF. Diethyl ether was then pass through the filter to remove $LiBF_4$. The desired compound was then extracted through the filter paper with copious amounts of THF. The THF solution was removed *in vacuo* to produce clean **28**. Yield: 227mg, 158µmol, 70%. Yield: 272mg, 189µmol, 84%. Crystals suitable for an X-ray diffraction study were obtained

by layering a THF solution of **28** with pentane. m.p. = 221°C (dec.); ^{1}H NMR (600MHz, THF-d_8, 25°C): δ = 8.12 (t, $^{3}J(H,H)$ = 9.0Hz, 4H), δ = 8.00 (t, $^{3}J_{H\text{-}H}$ = 7.4Hz, 2H), δ = 7.89-7.86 (dt, $^{3}J_{H\text{-}H}$ = 7.5Hz, $^{4}J_{H\text{-}H}$ = 2.5 Hz, 4H); ^{13}C NMR (151MHz, THF-d_8, 25°C): δ = 137.4, 134.3, 132.3, 117.7; ^{11}B{^{1}H} NMR (192MHz, THF-d_8, 25°C): δ = 24.0, –4.2, –7.4; ^{31}P{^{1}H} NMR (243MHz, THF-d_8, 25°C): δ = 25.1.

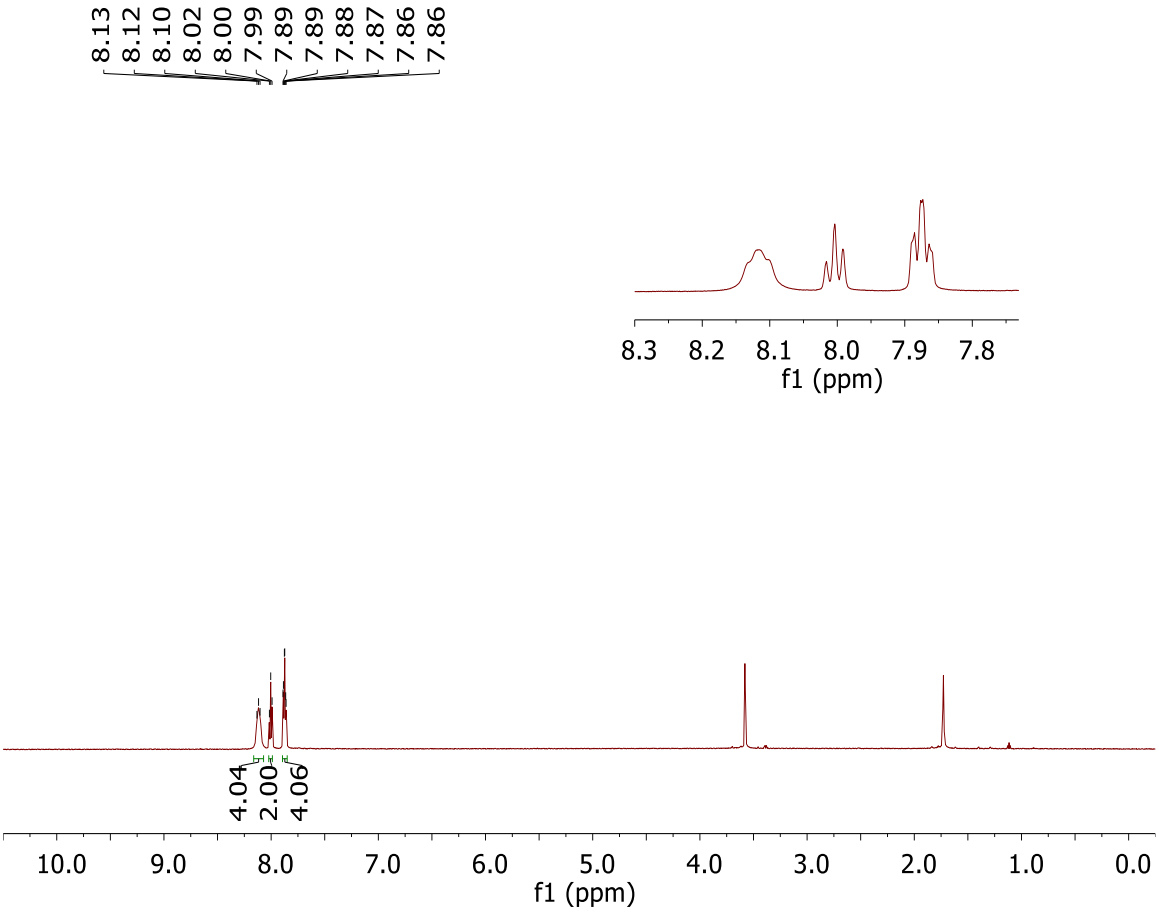

*Figure 143. ^{1}H NMR of **28** (600MHz, THF-d_8, 25°C).*

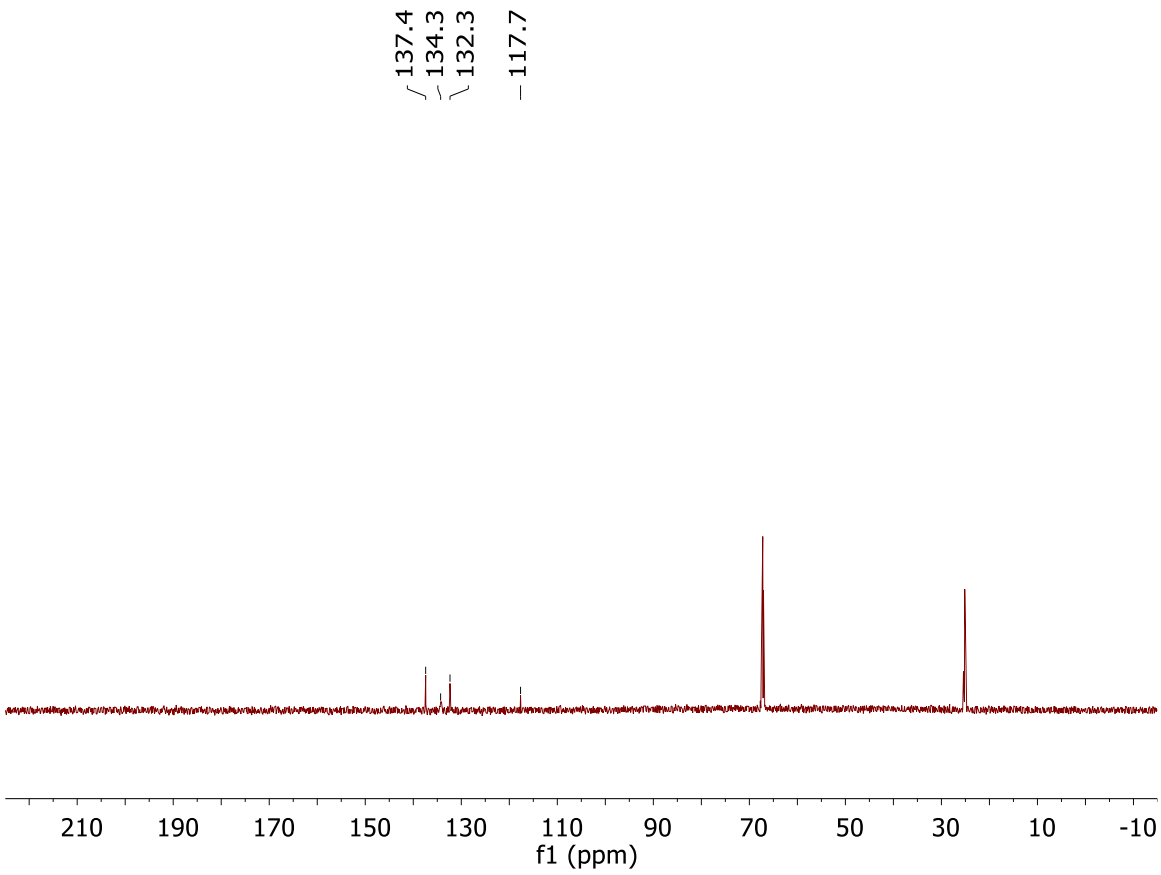

*Figure 144. $^{13}C\{^{1}H\}$ NMR of **28** (151MHz, THF-d_8, 25°C).*

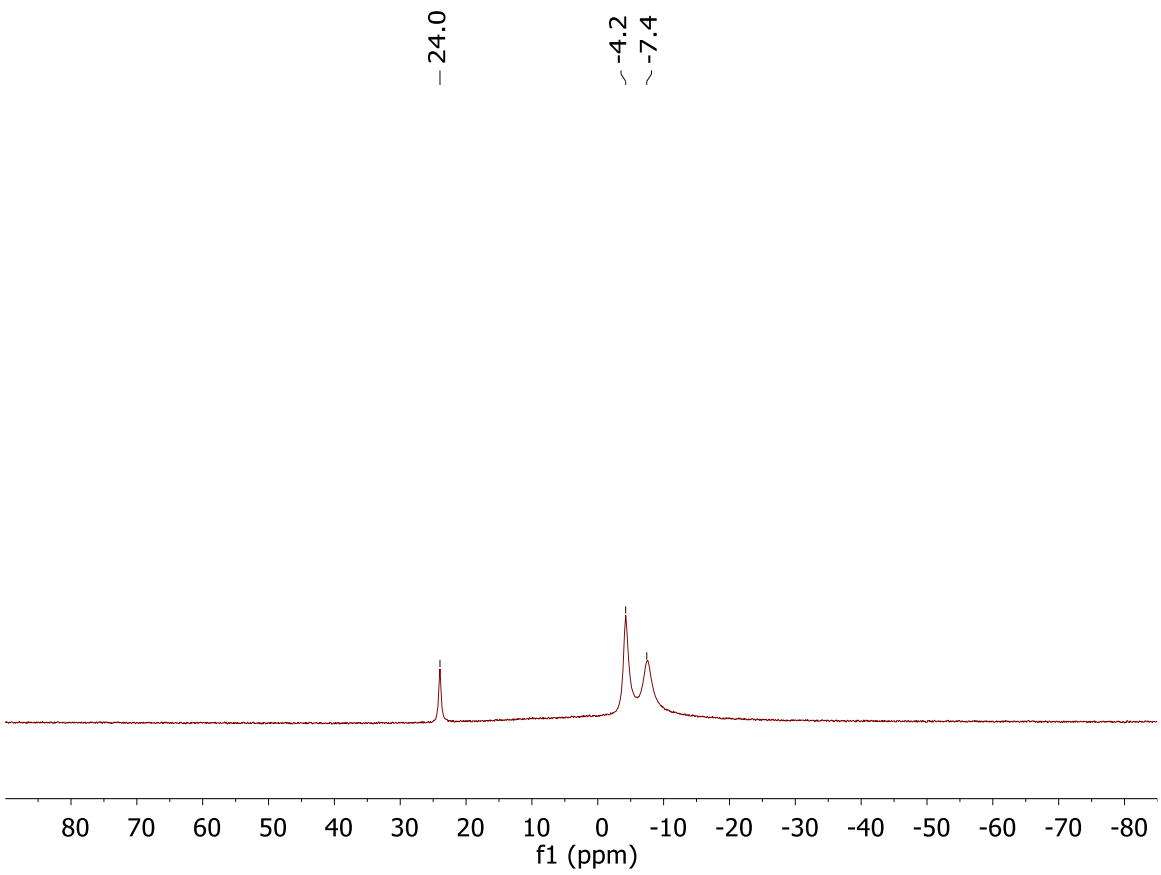

*Figure 145. $^{11}B\{^{1}H\}$ NMR of **28** (192MHz, THF-d_8, 25°C).*

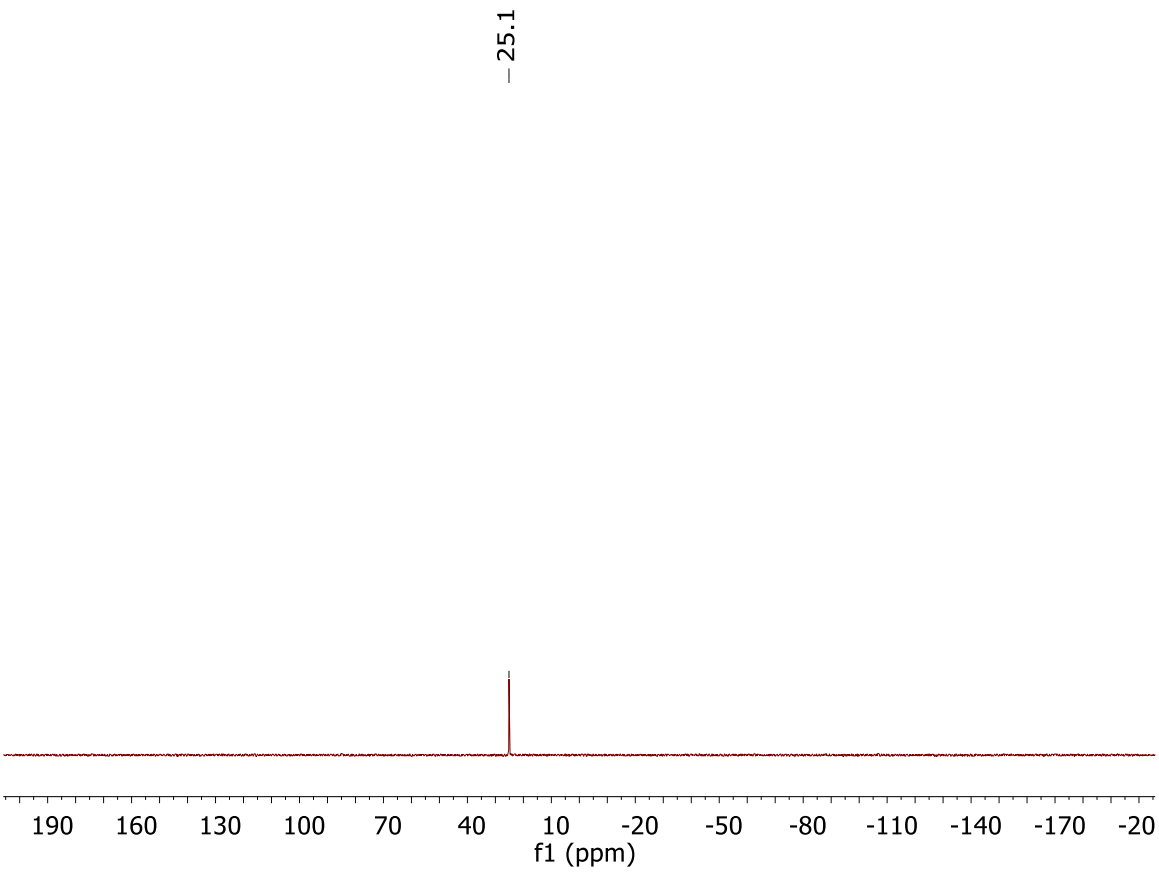

*Figure 146. $^{31}P\{^{1}H\}$ NMR of **28** (243MHz, THF-d_8, 25°C).*

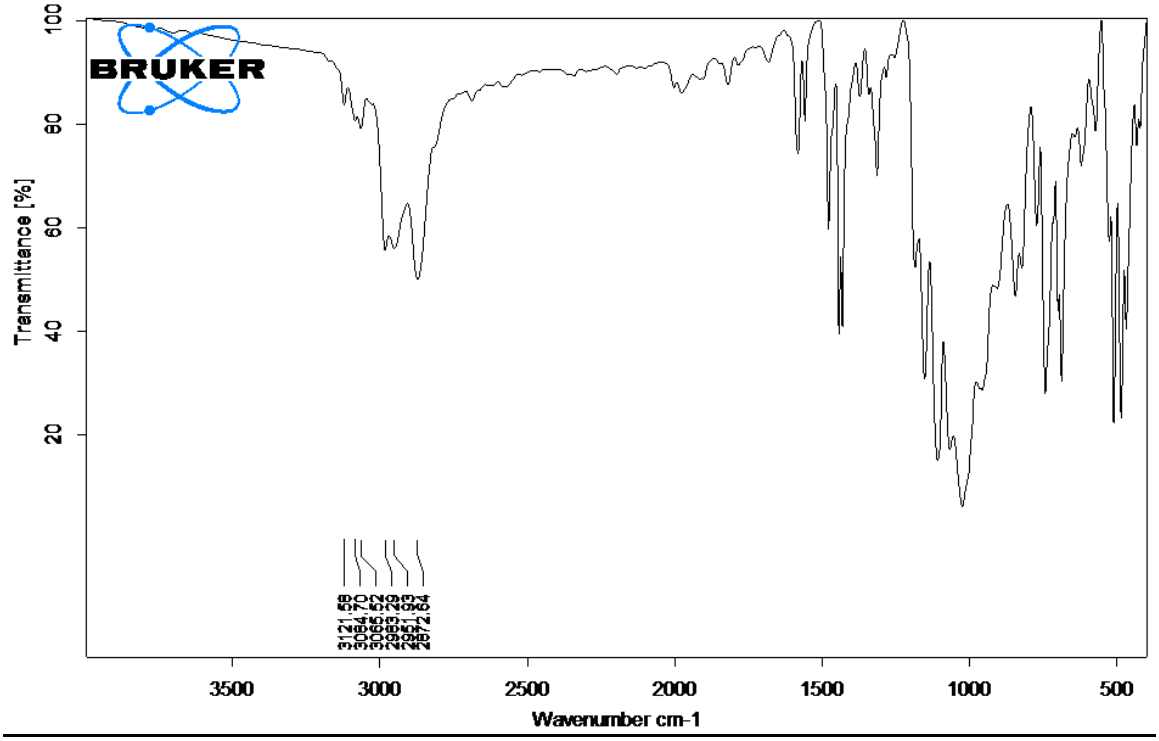

*Figure 147. FTIR spectrum for compound **28** with C-H peaks observable at 2872.64-3121.58cm^{-1}.*

Alternate Synthesis of Complex **28**:

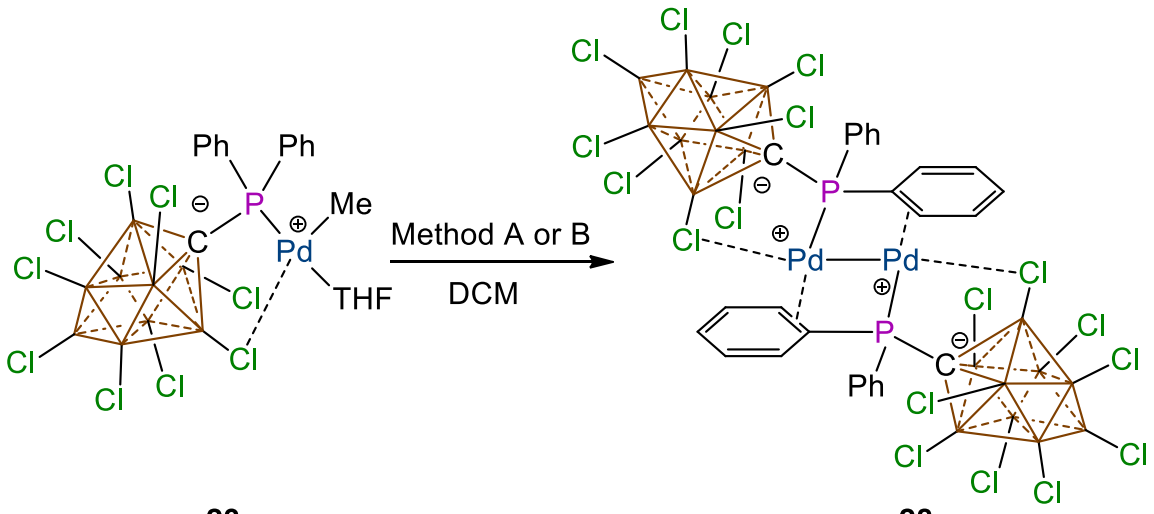

23 **28**

Complex **23** (500mg, 619µmol) was placed in a 200mL flame dried Schlenk flask and was subsequently dissolved in DCM (80mL). The flask was placed on the Schlenk line and placed under UV radiation (Method A) or heated to 40°C (Method B) for 4 days without stirring. After 4 days, the reaction was taken into the glovebox and filtered through a Hirsch funnel fitted with a glass microfiber filter and washed with DCM (5 x 20mL). The washings were discarded. The red solid was then passed through the filter with copious amounts of THF. The THF was then removed *in vacuo* give **28** as a red solid. (Method A: 309mg, 215µmol, 66% yield; Method B: 178mg, 124µmol, 35% yield).

Synthesis of Complex **29**:

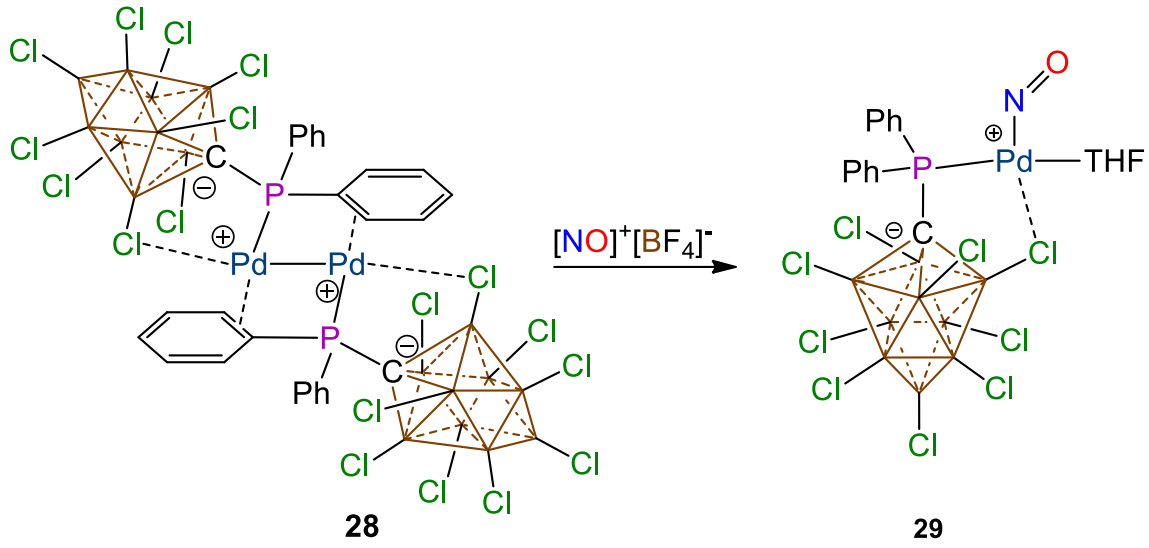

Complex **28** (20mg, 14μmol) was added to a 20mL glass scintillation vial equipped with a stir bar and DME (5mL) was added. $[NO]^+[BF_4]^-$ (1.6mg, 14μmol) was added to a separate 20mL glass scintillation vial and DME (5mL) was added. The solution containing $[NO]^+[BF_4]^-$ was slowly added to the red solution. The vail containing $NO]^+[BF_4]^-$ was washed with DME (1mL) and added to the red solution. The reaction was allowed to stir for 30 minutes. After 30 minutes, the reaction mixture was placed under vacuum to remove DME. The red solid was dissolved in THF and subsequently placed under vacuum. This process was repeated three times giving complex **29**. ^{1}H NMR (300MHz, CD_2Cl2, 25°C): δ = 8.07 (m, 4H), 7.67 (m, 2H), 7.57 (m, 4H); $^{13}C\{^1H\}$ NMR (75MHz, CD_2Cl_2, 25°C): 137.3 ($^3J_{P\text{-}C}$ = 14.3Hz), 133.3, 129.5 ($^3J_{P\text{-}C}$ = 13.4Hz), 72.5; $^{11}B\{^1H\}$ NMR (96MHz, CD_2Cl_2, 25°C): δ = 28.8, 0.3, –2.2; $^{31}P\{^1H\}$ NMR (121MHz, CD_2Cl_2, 25°C): δ = 59.6;

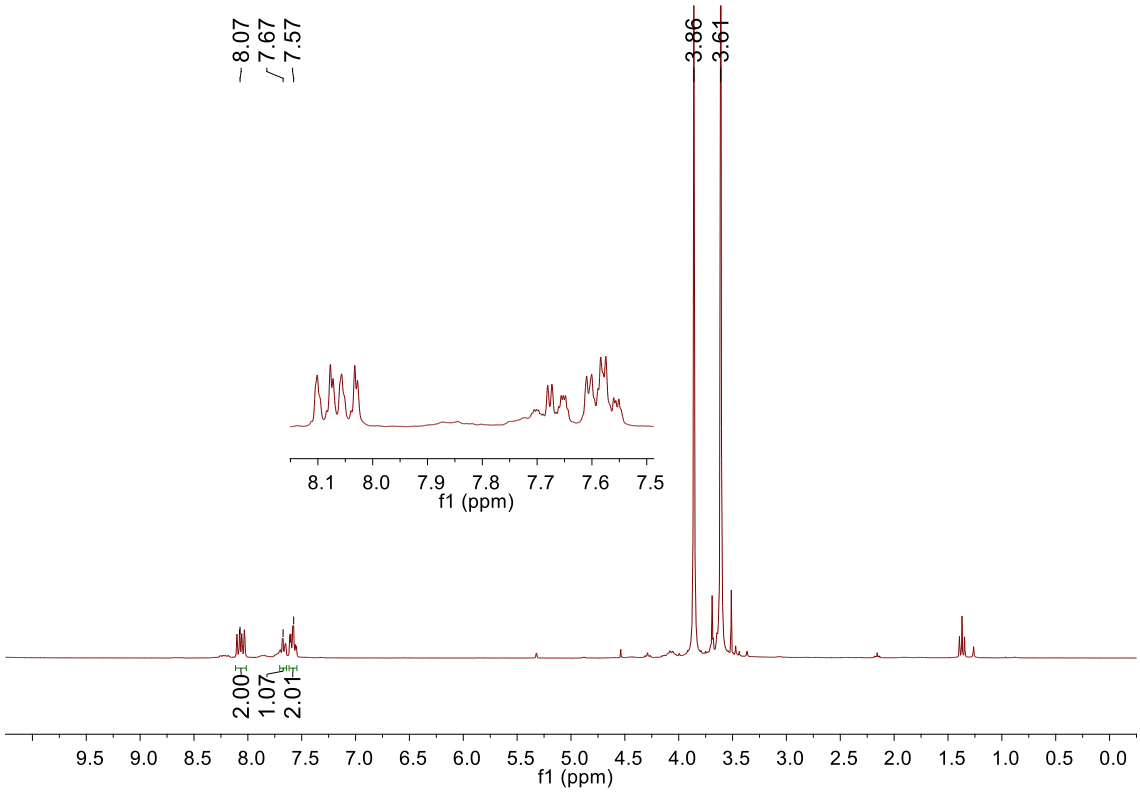

*Figure 148. ^{1}H NMR of **30** (300MHz, CD_2Cl_2, 25°C). Note: DME is seen at 3.86 and 3.61ppm.*

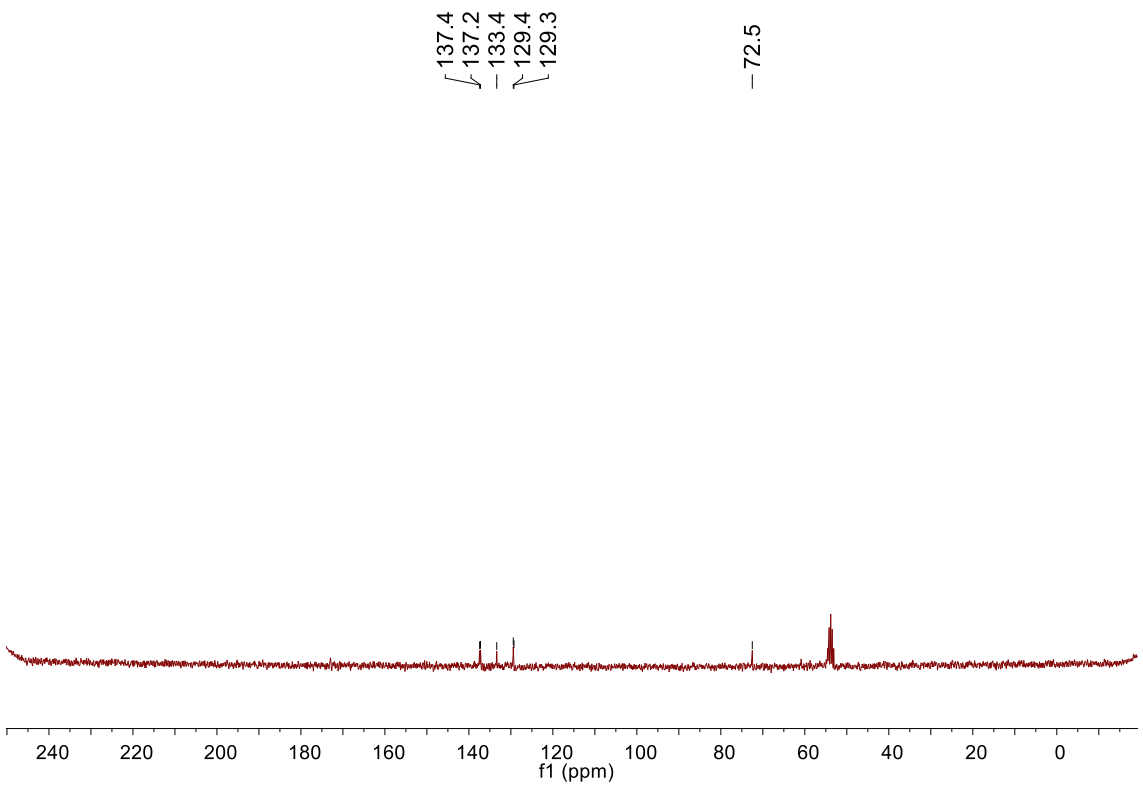

*Figure 149. $^{13}C\{^{1}H\}$ NMR of **30** (75MHz, CD_2Cl_2, 25°C).*

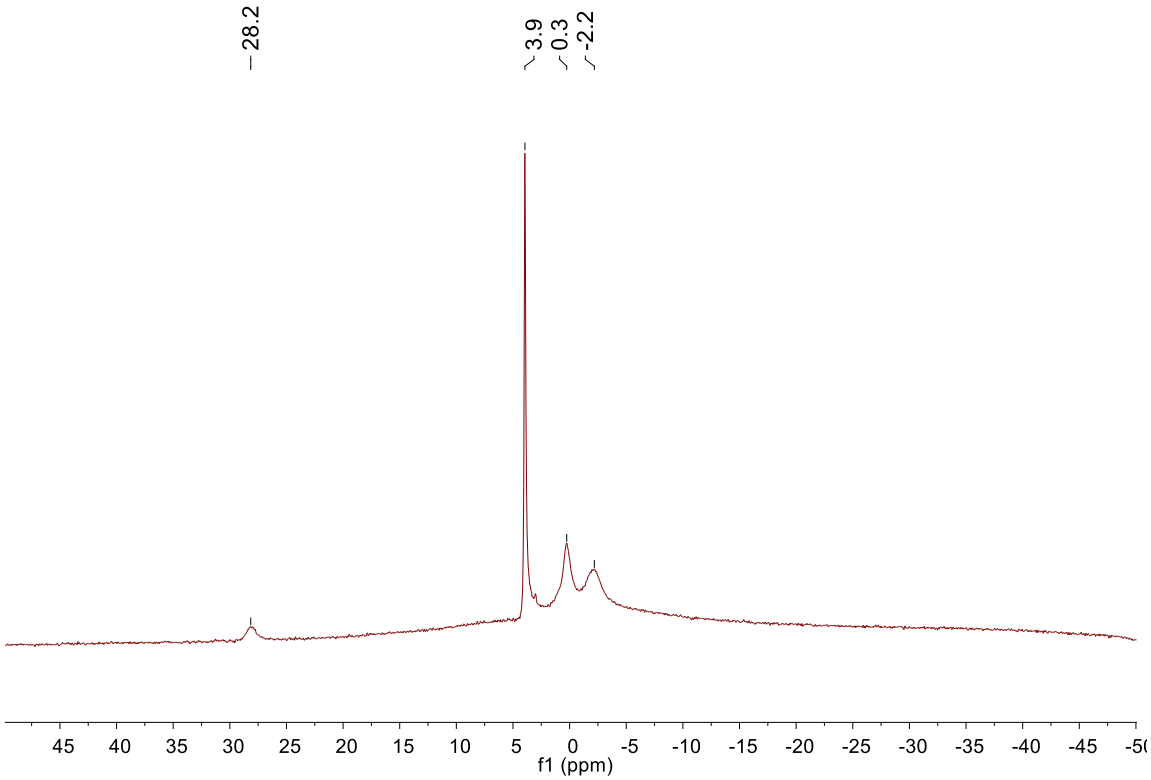

*Figure 150. $^{11}B\{^{1}H\}$ NMR of **30** (96MHz, CD_2Cl_2, 25°C). Note: $[BF_4]^-$ is seen at 3.9ppm.*

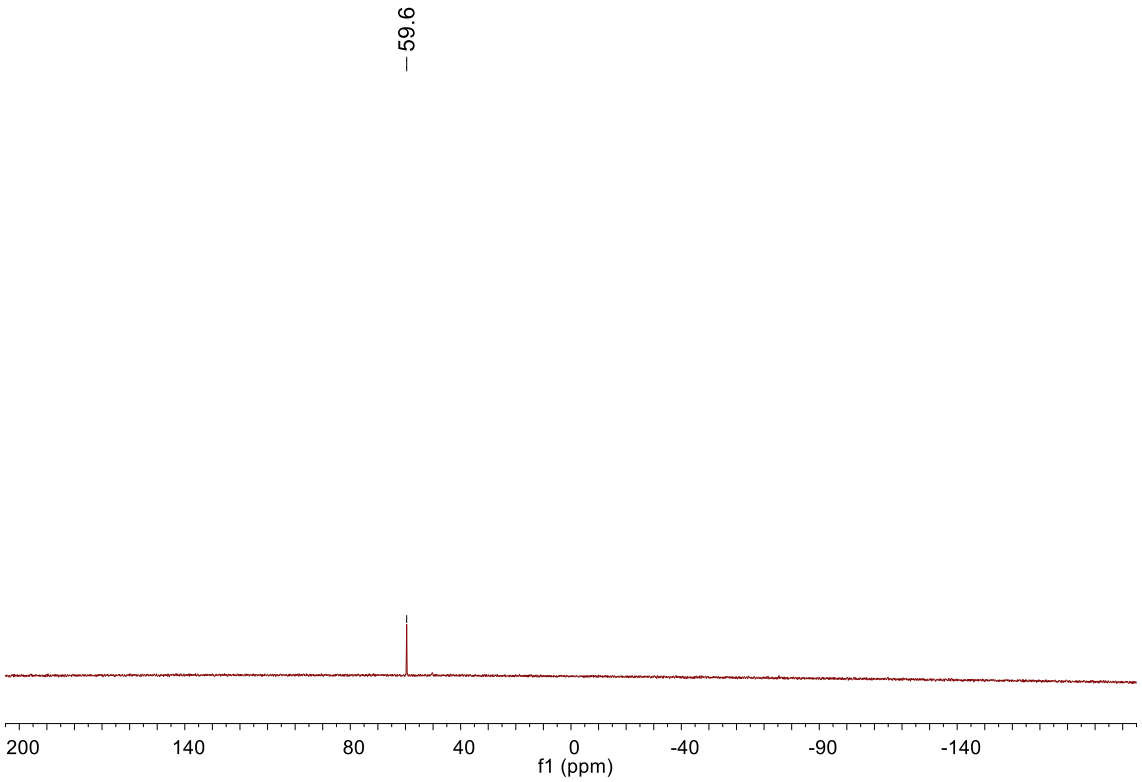

*Figure 151. $^{31}P\{^{1}H\}$ NMR of **30** (121MHz, CD_2Cl_2, 25°C).*

Synthesis of Complex **31** and **32**:

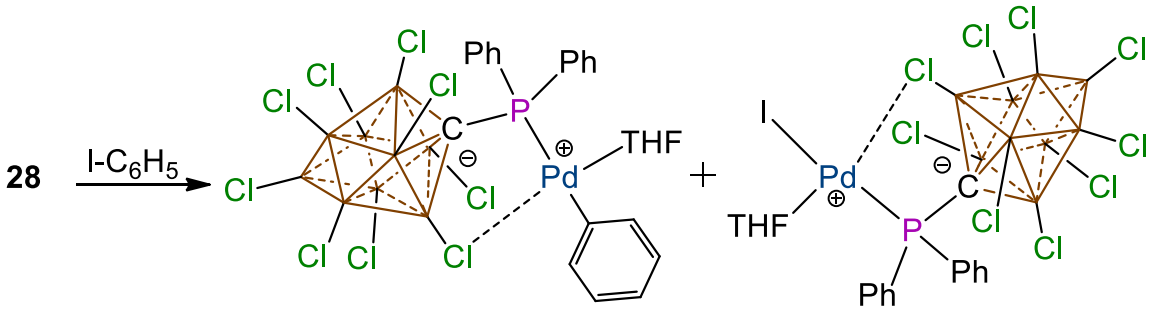

30 **31**

Complex **28** (20mg, 14µmol) was added to a 20mL glass scintillation vial equipped with a stir bar and I-C_6H_5 (5mL) was added. The reaction was allowed to stir for 30 minutes. After 30 minutes, the reaction mixture was dropped into stirring pentane. The red powder was allowed to settle and the pentane was decanted. This process was performed three times giving complex **31**. ^{1}H NMR (300MHz, THF-d_8, 25^{o}C): δ = 8.53 (m, 6H), 7.89 (dd, $^{3}J_{P-H}$ = 14.0Hz, $^{3}J_{H-H}$ = 8.07Hz, 4H), 7.75 (m, 3H), 7.64 (m, 5H), 7.55 (m, 2H), 7.39 (m, 6H) 7.00 (t, $^{3}J_{H-H}$ = 8.0Hz, 2H) 6.84 (t, $^{3}J_{H-H}$ = 7.1Hz, 1H) 6.72 (t, $^{3}J_{H-H}$ = 7.5Hz, 2H). 3.40, 1.62; ^{13}C{^{1}H} NMR (75MHz, THF-d_8, 25^{o}C): 160.6, 149.1, 138.1 (d, $^{2}J_{P-H}$ = 12Hz), 136.3 (d, $^{2}J_{P-H}$ = 12Hz), 134.1, 132.4 (d, $^{3}J_{P-H}$ = 3Hz), 131.9 (d, $^{3}J_{P-H}$ = 4Hz), 128.8 (d, $^{3}J_{P-H}$ = 3Hz), 128.2 (d, $^{2}J_{P-H}$ = 13Hz), 127.9 (d, $^{2}J_{P-H}$ = 14Hz) 125.3, 70.3, 26.7. ^{11}B{^{1}H} NMR (96MHz, THF-d_8, 25^{o}C): δ = 25.4, -2.6, –7.6; ^{31}P{^{1}H} NMR (121MHz, THF-d_8, 25^{o}C): δ = 42.8, 41.8;

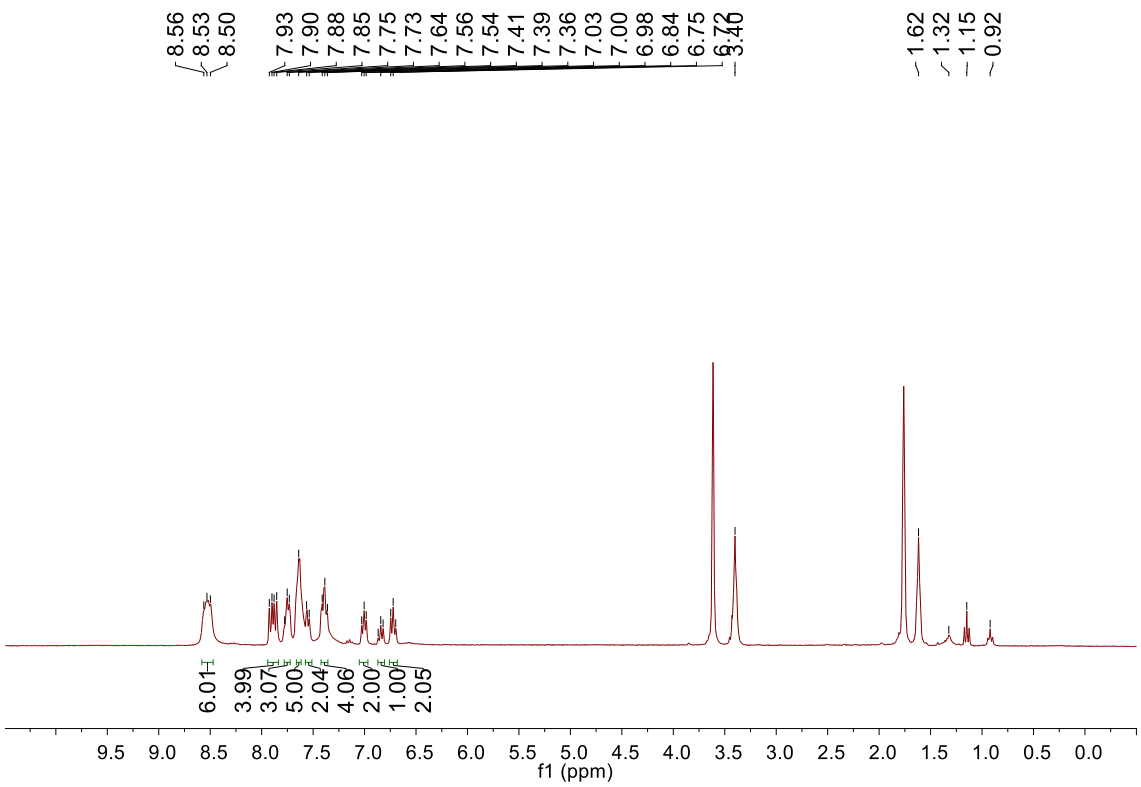

*Figure 152. $^{13}C\{^{1}H\}$ NMR (75MHz, THF-d_8, 25°C) of **30** and **31**.*

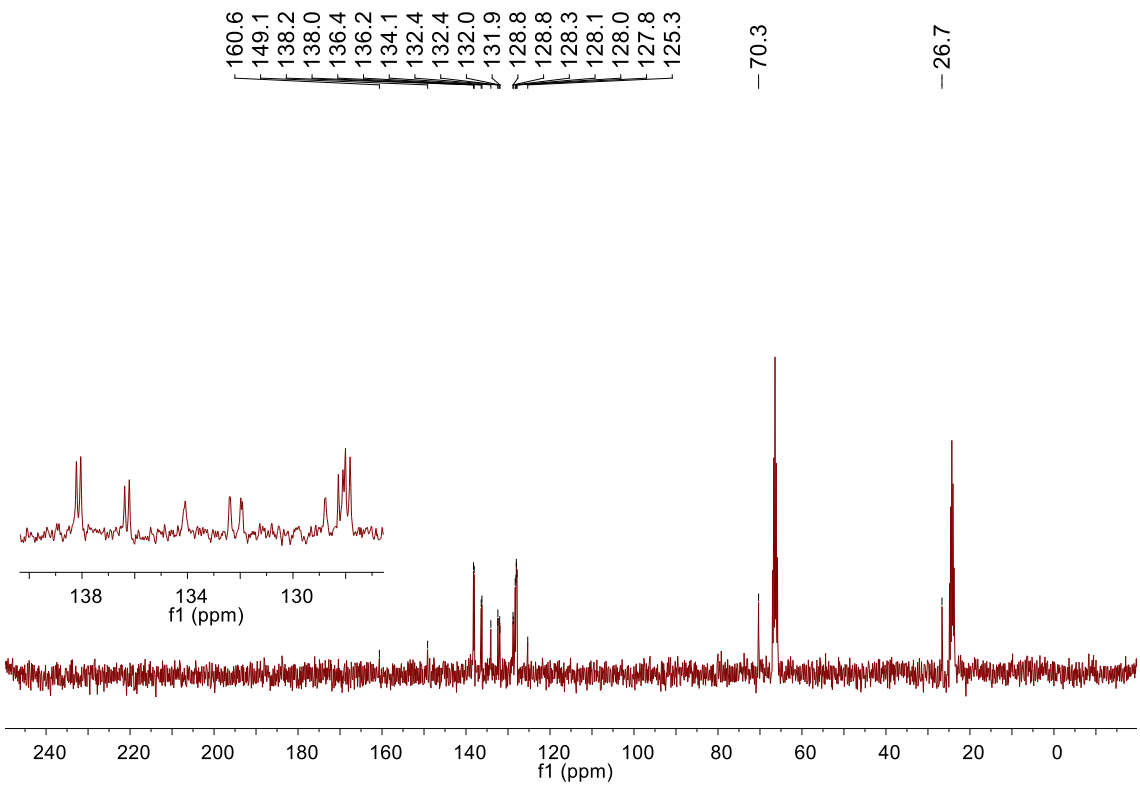

*Figure 153. ^{1}H NMR (300MHz, THF-d_8, 25°C) of **30** and **31**.*

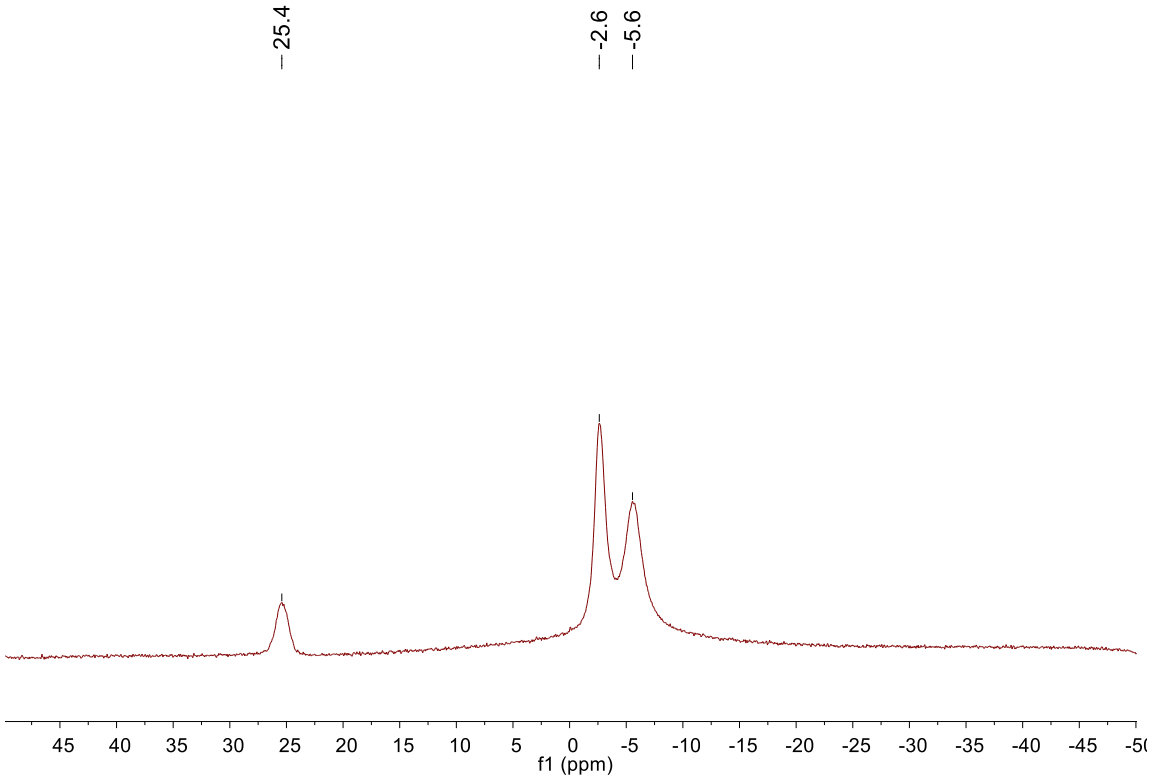

*Figure 154. $^{11}B\{^{1}H\}$ NMR of **30** and **31** (96MHz, THF-d_8, 25°C).*

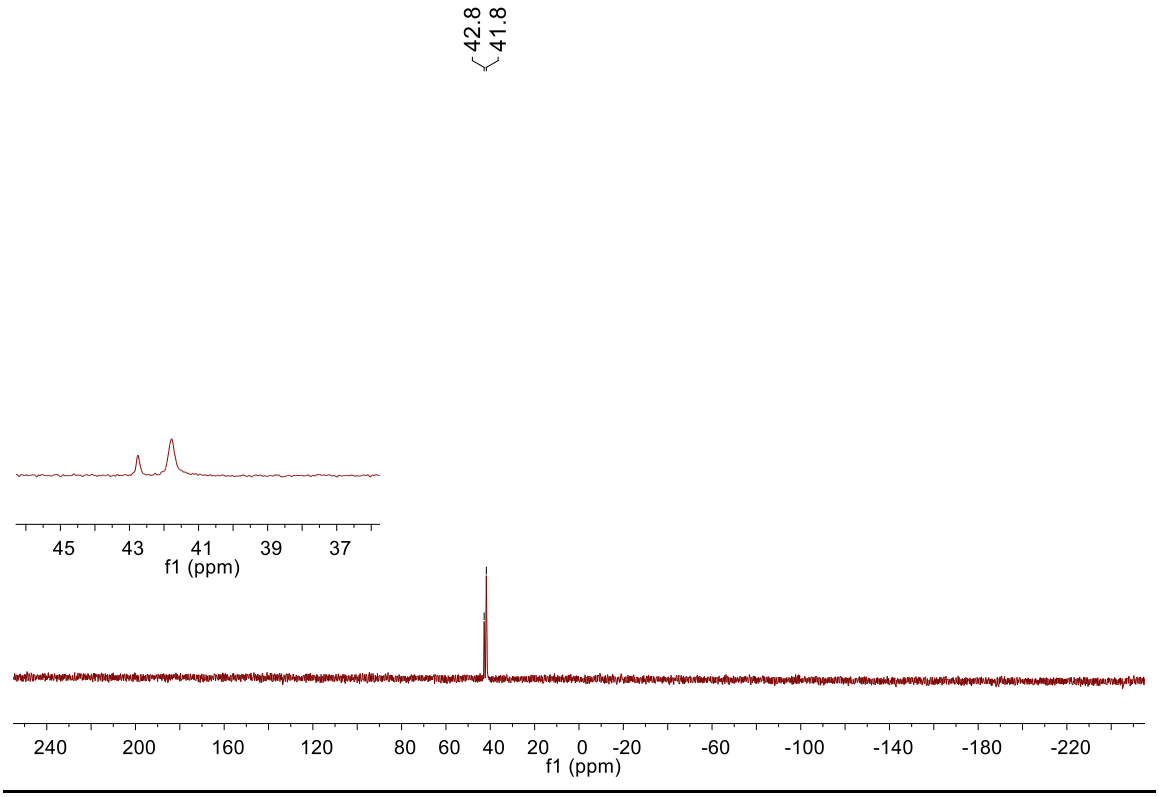

*Figure 155. $^{31}P\{^{1}H\}$ NMR of **30** and **31** (121MHz, THF-d_8, 25^{o}C).*

Synthesis of Complex **32**:

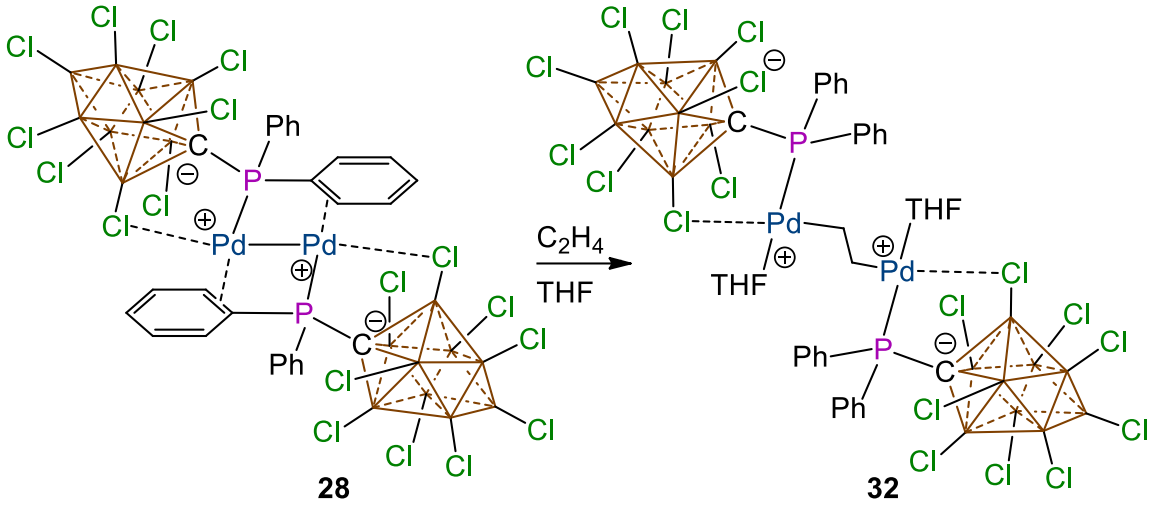

Complex **28** (80mg, 56μmol) was added to a 20mL glass scintillation vial and THF (10mL) was added. The THF solution was then placed in a dried 25mL thick-walled Teflon Schlenk tube. The vial was washed with THF (5mL) and added to the Schlenk tube. The tube was sealed and then a regimen of freeze-pump-thaw was carried out with liquid N_2. Once at room temperature, the Schlenk tube was then back-filled with an ethylene atmosphere and then submerged in liquid N_2 to condense roughly 1cm of liquid ethylene. After sealing the Schlenk, the reaction was allowed to warm to room temperature with the ethylene slowly diffusing into the rest of the THF solution. After 6 hours, the reaction turned clear with a yellow powder settled at the bottom. With constant positive ethylene pressure, the THF was removed via syringe and then the Schlenk was placed under vacuum to remove residual solvent, giving **32**. Yield: 64mg, 44μmol, 72% yield.

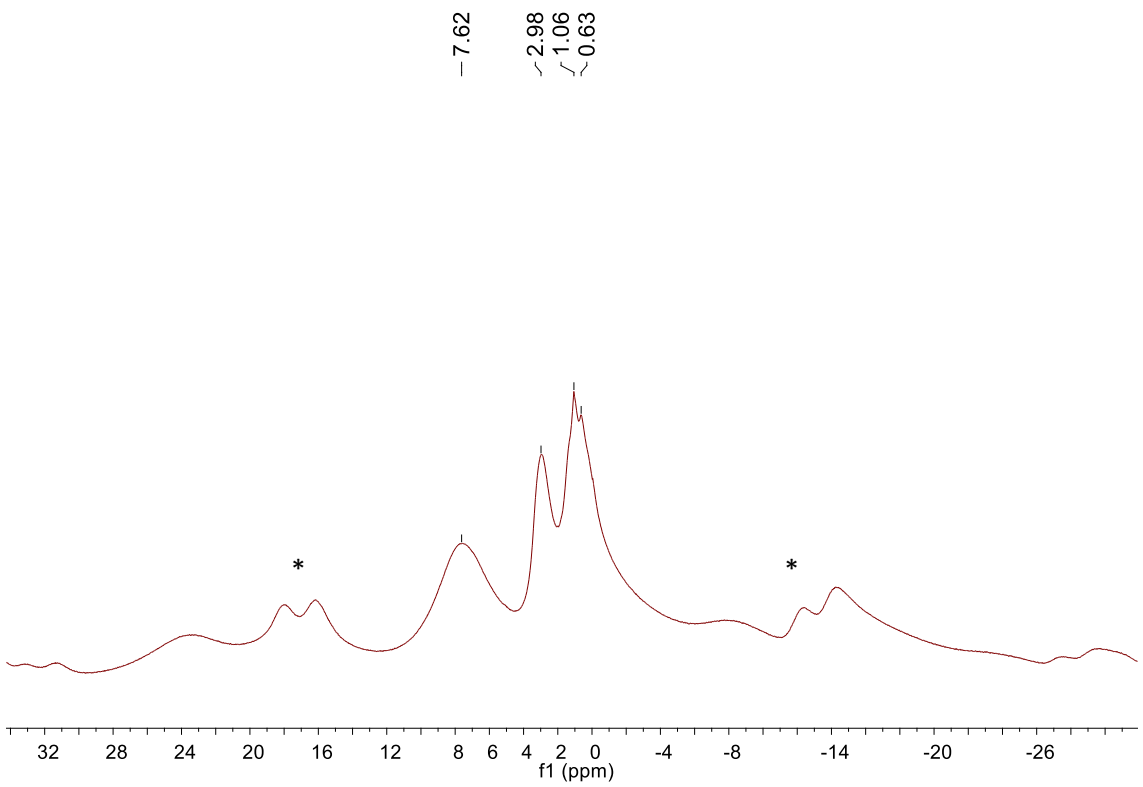

*Figure 156. Solid-state ^{1}H NMR of complex **32**. MAS at 9kHz. Note: * denotes spinning side bands.*

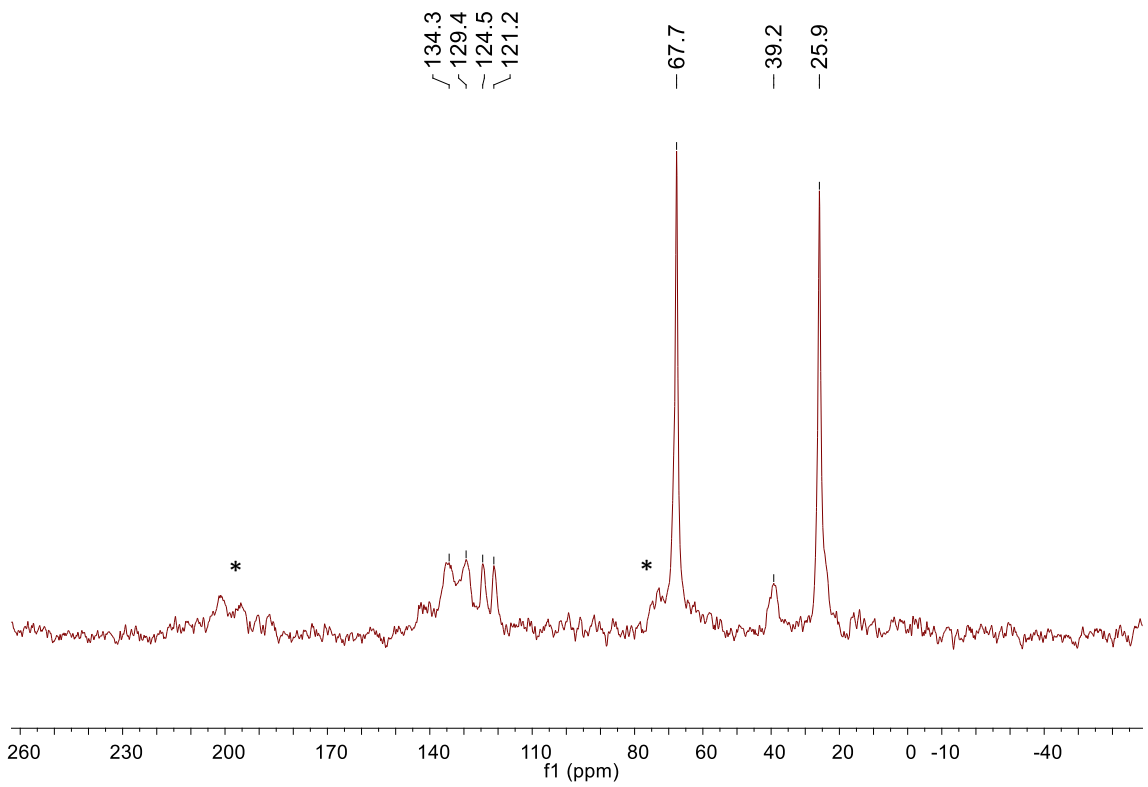

*Figure 157. Solid-state ^{13}C NMR of complex **32**. MAS at 9kHz. The ^{13}C chemical shift for the $PdCH_2CH_2Pd$ carbons is at 37ppm. Note: * denotes spinning side bands.*

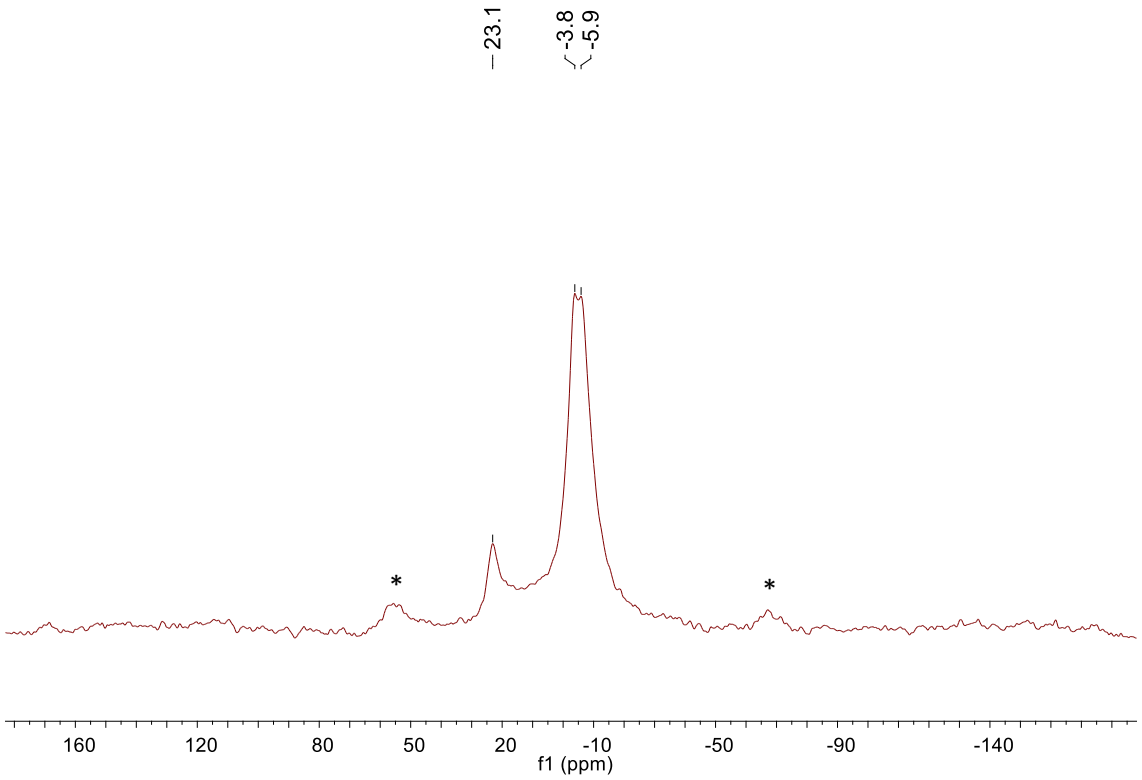

*Figure 158. Solid-state ^{13}B NMR of complex **32**. MAS at 9kHz. Note: * denotes spinning side bands.*

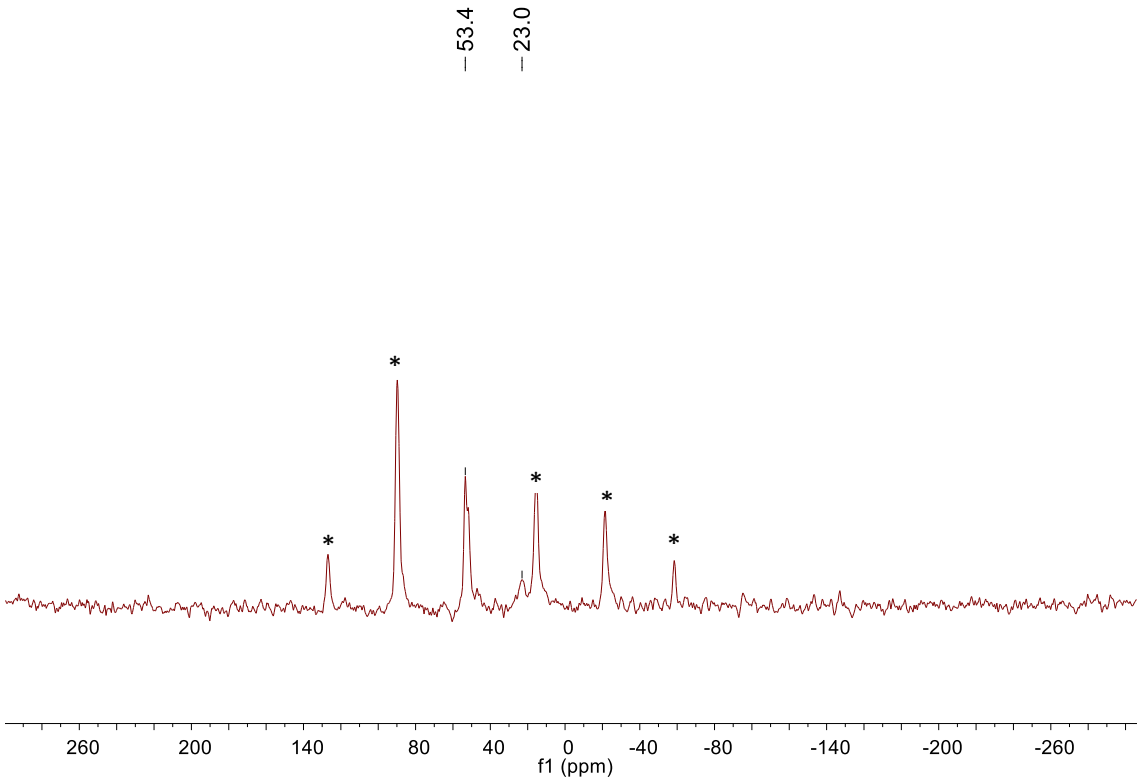

*Figure 159 Solid-state $^{31}P\{^{1}H\}$ NMR of complex **32**. MAS at 9kHz. Note: * denotes spinning side bands.*

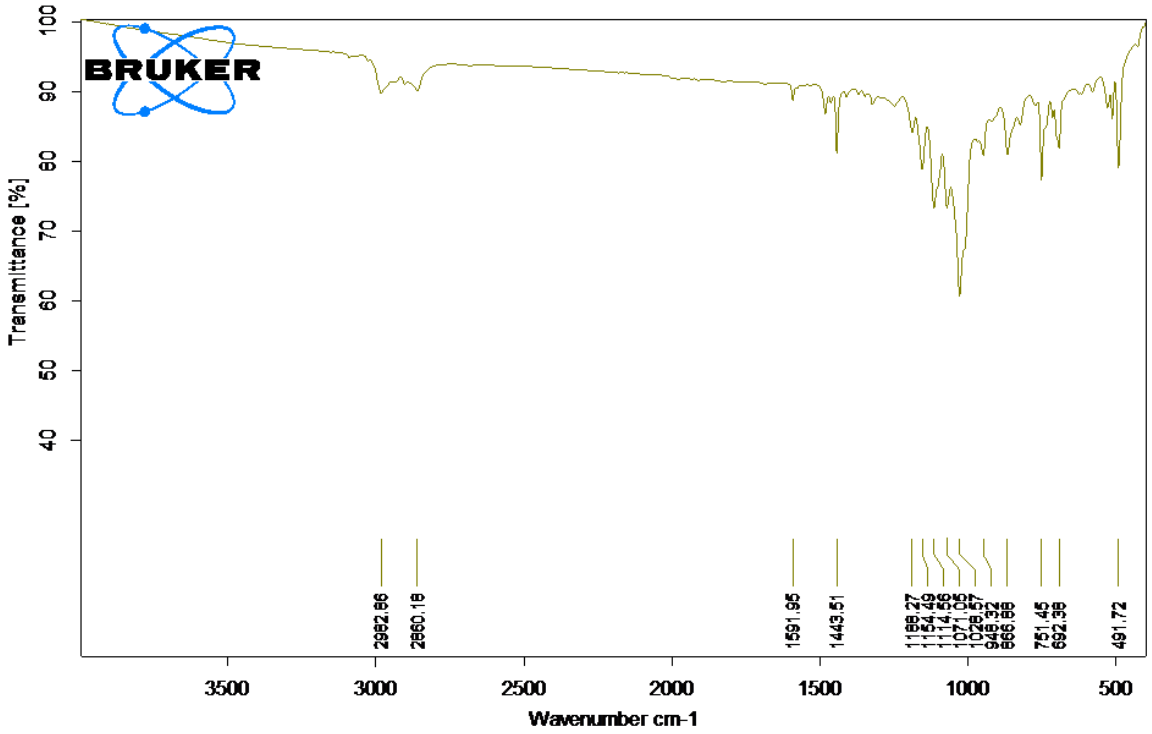

*Figure 160. FTIR spectrum for compound **32** with C-H peaks observable at 2982.86cm^{-1} and 2880.18 cm^{-1}.*

Compound 3	
Stoichiometric Formula	$C_{36}H_{40}B_{18}O_2P_2Cl_{18}Pd_2$
Temperature (K)	~293
Space Group	P-1
Unit cell lengths a, b, c (Å)	13.050 12.040 13.060
angles α, β, γ	107.566 91.152 123.194
Reflections (#)	23883
Unique reflections (#)	3713
Robs	22.5%
Rmeas	23.8%
CC1/2	98.0
Resolution (Å)	0.90
Completeness (%)	80.5%
Total exposure (e Å-2)	~3
R	0.1745
wR2	0.4127
GooF	2.263

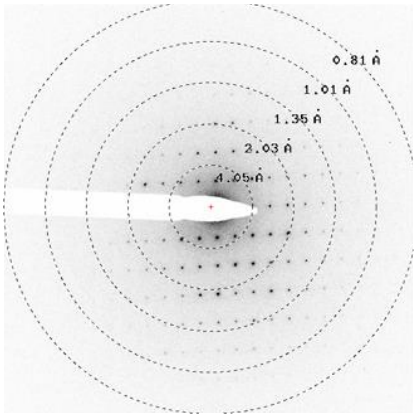

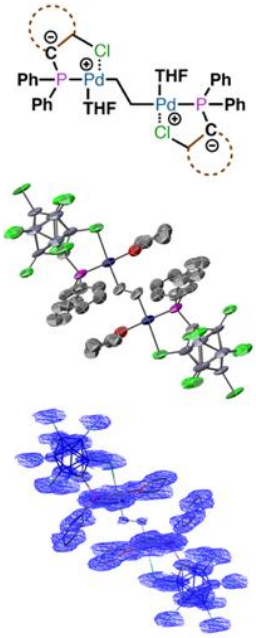

*Figure 161. Data, statistics, sample diffraction pattern and structures for compound **32**.*

Quantum Chemical Calculations:

DFT calculations for complex **32** were performed using the crystal coordinates obtained from MicroED experiments. Hydrogen atoms were optimized from the crystal structure with the B3LYP functional, Pd was described with the LANL2DZ basis set and the associated effective core potentials. All other atoms were described with the 6-31G(d,p) basis set (15). The ^{13}C NMR parameters of complex **32** were calculated using the GIAO method in Gaussian 09, with the PBE functional (16, 17). The calculated shielding of 159 ppm for each carbon was referenced to geometry-optimized tetramethylsilane at the same level of theory (σ_{iso} = 191 ppm). This results in a computed $\delta(^{13}C)$ of 32 ppm, which is close to the experimental value of 37 ppm obtained from ^{13}C CPMAS experiments.

Coordinates:

Pd	2.15767300	-0.85064800	-0.02101400
P	3.27374900	0.89880900	0.06881600
Cl	6.30225900	2.77105100	0.61215500
Cl	5.13230400	-0.38642600	2.84048200
Cl	4.16163000	-2.19219200	-0.50586200
Cl	9.71426700	-1.55817700	-0.07010200
Cl	8.59385200	1.48780600	-1.70379500
Cl	8.40477400	0.64652400	2.31879800
Cl	5.42336400	0.76072400	-2.81310900
Cl	7.07887400	-2.16675900	-2.40680800
Cl	6.87161400	-2.97238200	1.56426600
C	3.00737300	1.96306800	-1.28981700
O	1.12274000	-2.57380700	-0.09882600
C	3.56950300	3.02529100	-1.52279800
H	4.39336800	3.38604400	-0.91847700
C	1.75063000	2.26963300	-3.27967700
H	1.04227300	1.93421400	-4.03139600
C	2.98688000	1.79650300	1.51744100
C	2.14284900	1.77195900	3.64593200
H	1.74795700	1.24458700	4.51350100
C	2.37578800	3.58390100	-3.39232200
H	2.09326300	4.21646600	-4.23038900
B	7.44760500	-0.04802900	1.04614600

B	6.94476100	-1.17324000	-1.11637000
C	3.21963400	3.85819600	-2.58786400
H	3.77149800	4.79790600	-2.64419000
B	6.84252400	-1.52370500	0.67441800
B	7.54155400	0.38404900	-0.72675500
C	2.19801200	3.14379400	3.69996400
H	1.86094900	3.66949600	4.58817900
B	5.44188100	-1.02140100	-0.23147500
C	0.88410500	-3.55966600	1.05101300
H	1.87527500	-3.96454900	1.28232800
H	0.55048800	-2.93321200	1.87727100
C	2.74974400	3.81294900	2.64982600
H	2.84766200	4.89627200	2.72606500
C	0.96103300	-3.15986600	-1.27007500
H	1.91467000	-3.32001100	-1.79543300
H	0.31947200	-2.55555800	-1.92489500
C	3.13152400	3.21375900	1.66558100
H	3.56380300	3.75392400	0.83294400
C	2.03340100	1.51517500	-2.18616500
H	1.58633400	0.53757200	-2.07354000
B	6.38862400	1.27274400	0.27213800
B	5.78286900	-0.28922500	1.23521500
B	8.12882400	-0.80472600	-0.05975800
C	4.94022900	0.42452500	0.03101400

B	5.92717000	0.26483800	-1.20878400
C	0.51924900	0.08983400	0.45622100
H	0.32867800	-0.38650300	1.42805300
H	0.70359500	1.14197700	0.66504200
C	0.27724100	-4.58433800	-0.98651100
H	0.98626200	-5.38530000	-1.20992200
H	-0.61629800	-4.73785300	-1.58710500
C	-0.05330900	-4.56556200	0.58432100
H	-1.09269100	-4.28110400	0.75258900
H	0.12946500	-5.54229500	1.03592900
C	2.46097200	1.12846500	2.58826300
H	2.33910100	0.05238800	2.53811700
C	-0.51966000	-0.09034300	-0.45691300
H	-0.32898300	0.38573400	-1.42887200
H	-0.70433500	-1.14246800	-0.66547500
Pd	-2.15769000	0.85105700	0.02040800
P	-3.27378800	-0.89848700	-0.06842600
Cl	-6.30135700	-2.77103700	-0.61277600
Cl	-5.13273500	0.38583300	-2.84017900
Cl	-4.16166800	2.19251400	0.50625100
Cl	-9.71430600	1.55849900	0.07049200
Cl	-8.59295000	-1.48779200	1.70317400
Cl	-8.40520600	-0.64711700	-2.31849500
Cl	-5.42340200	-0.76040200	2.81349800

Cl	-7.07930600	2.16616600	2.40711000
Cl	-6.87202400	2.97187400	-1.56496000
C	-3.00741000	-1.96274600	1.29020600
O	-1.12277900	2.57412900	0.09921500
C	-3.56954100	-3.02497000	1.52318700
H	-4.39368700	-3.38506300	0.91879700
C	-1.75066700	-2.26931100	3.28006800
H	-1.04237100	-1.93391200	4.03188400
C	-2.98731200	-1.79709700	-1.51713800
C	-2.14196700	-1.77203000	-3.64555800
H	-1.74644700	-1.24504200	-4.51311200
C	-2.37490800	-3.58397200	3.39269800
H	-2.09237600	-4.21673000	4.23056400
B	-7.44764400	0.04835100	-1.04575600
B	-6.94517100	1.17273300	1.11567700
C	-3.22004500	-3.85870400	2.58717100
H	-3.77157900	-4.79853000	2.64341200
B	-6.84164300	1.52363300	-0.67404300
B	-7.54067300	-0.38412100	0.72713000
C	-2.19805100	-3.14347200	-3.69957300
H	-1.86074000	-3.66912600	-4.58775200
B	-5.44231300	1.02080800	0.23177800
C	-0.88453600	3.55907300	-1.05071000
H	-1.87559100	3.96400100	-1.28243700

H	-0.55045200	2.93261000	-1.87676300
C	-2.74976100	-3.81254200	-2.65043200
H	-2.84784400	-4.89583500	-2.72679500
C	-0.96107100	3.16018800	1.27046500
H	-1.91472000	3.32027300	1.79580200
H	-0.31952900	2.55580100	1.92522700
C	-3.13156200	-3.21343700	-1.66519100
H	-3.56336400	-3.75419500	-0.83267900
C	-2.03252000	-1.51524800	2.18654100
H	-1.58543200	-0.53765900	2.07385500
B	-6.38903400	-1.27325200	-0.27283200
B	-5.78290700	0.28954700	-1.23482500
B	-8.12925600	0.80413300	0.06006100
C	-4.94063900	-0.42503300	-0.03170700
B	-5.92720800	-0.26451600	1.20917400
C	-0.27727900	4.58466000	0.98690000
H	-0.98630100	5.38561400	1.21032000
H	0.61624500	4.73812600	1.58751500
C	0.05327100	4.56588400	-0.58393200
H	1.09262000	4.28140900	-0.75231500
H	-0.12976200	5.54243900	-1.03579000
C	-2.46098900	-1.12805800	-2.58886900
H	-2.33963200	-0.05198300	-2.53858100

Reversibility of Ethylene Addition for Compound **28**:

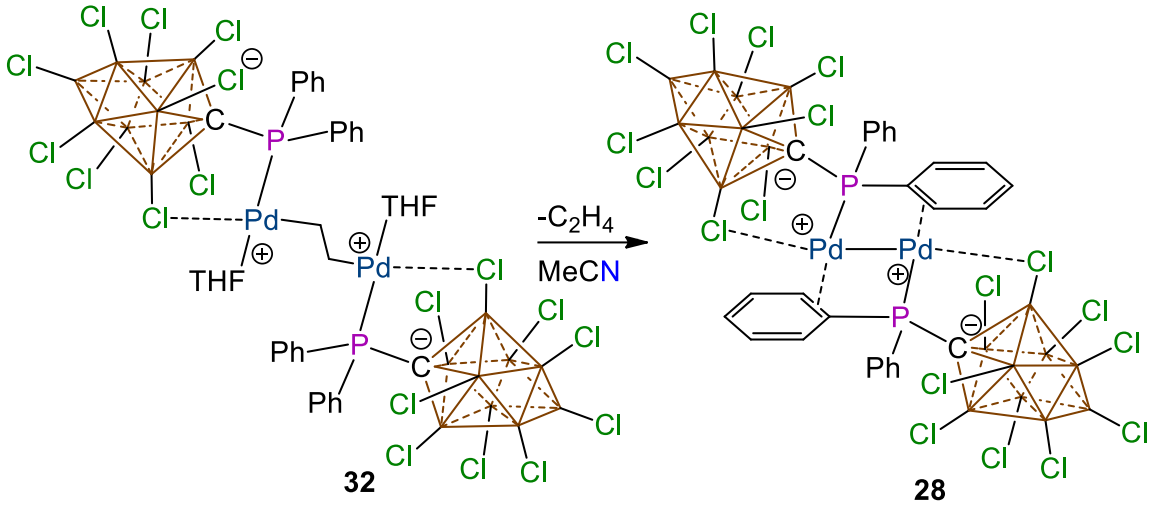

32 (100mg, 62.0µmol) is placed in a 20mL glass scintillation vial and acetonitrile is added. The yellow powder immediately turns to a magenta solution with rapid gas evolution. The acetonitrile is removed under reduced pressure. The solid is dissolved in THF and subsequently placed under reduced pressure again. This process is repeated three times. Yield: 88.4mg, 61.4µmol, 99% yield. ^{1}H NMR (600MHz, THF-d_8, 25°C): δ = 8.13 (dd, $^{3}J_{H\text{-}H}$ = 13.1Hz, $^{3}J_{H\text{-}H}$ = 12.7Hz, 4H), 8.00 (t, $^{3}J_{H\text{-}H}$ = 7.4Hz, 2H), 7.84 (td, $^{3}J_{H\text{-}H}$ = 7.5Hz, $^{4}J_{H\text{-}H}$ = 2.5 Hz, 4H). 2.00; ^{13}C NMR (151MHz, THF-d_8, 25°C): δ = 137.4, 134.3, 132.3, 117.7; ^{11}B{^{1}H} NMR (192MHz, THF-d_8, 25°C): δ = 24.0, –4.2, –7.5; ^{31}P{^{1}H} NMR (243MHz, THF-d_8, 25°C): δ = 25.1.

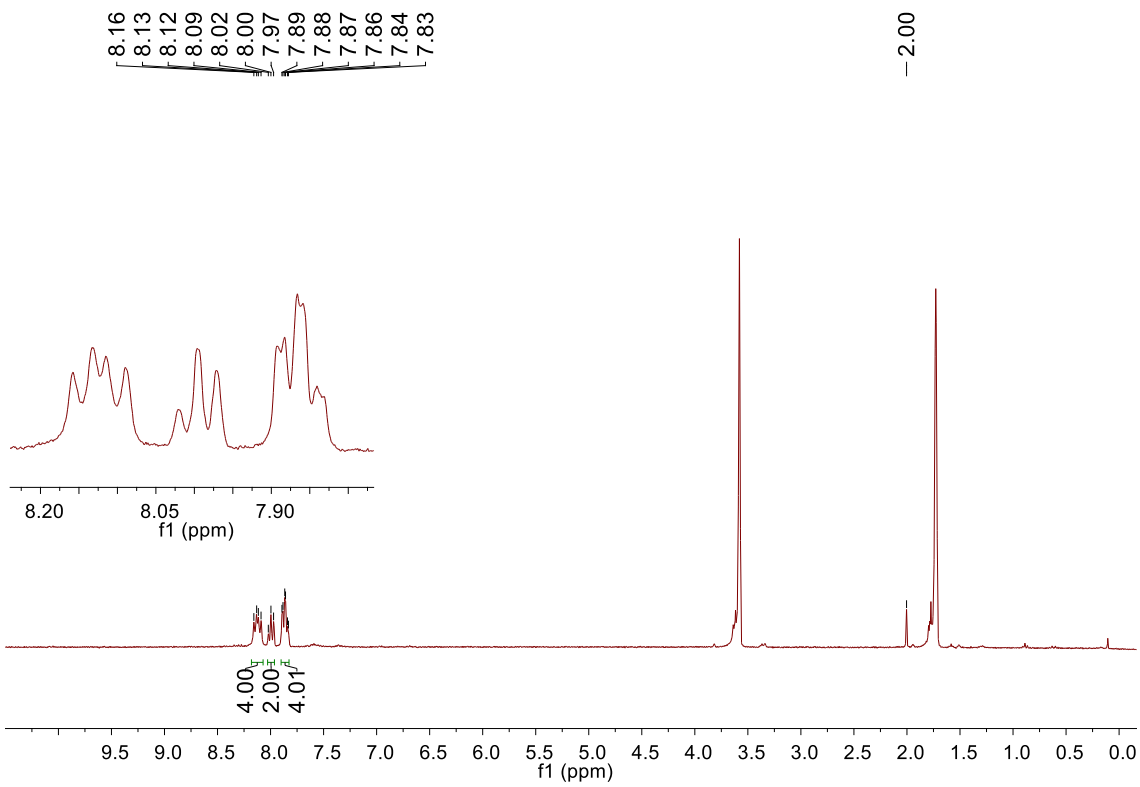

*Figure 162. ^{1}H NMR of **28** (300MHz, THF-d_8, 25°C). Note: peak at 2.00 is acetonitrile.*

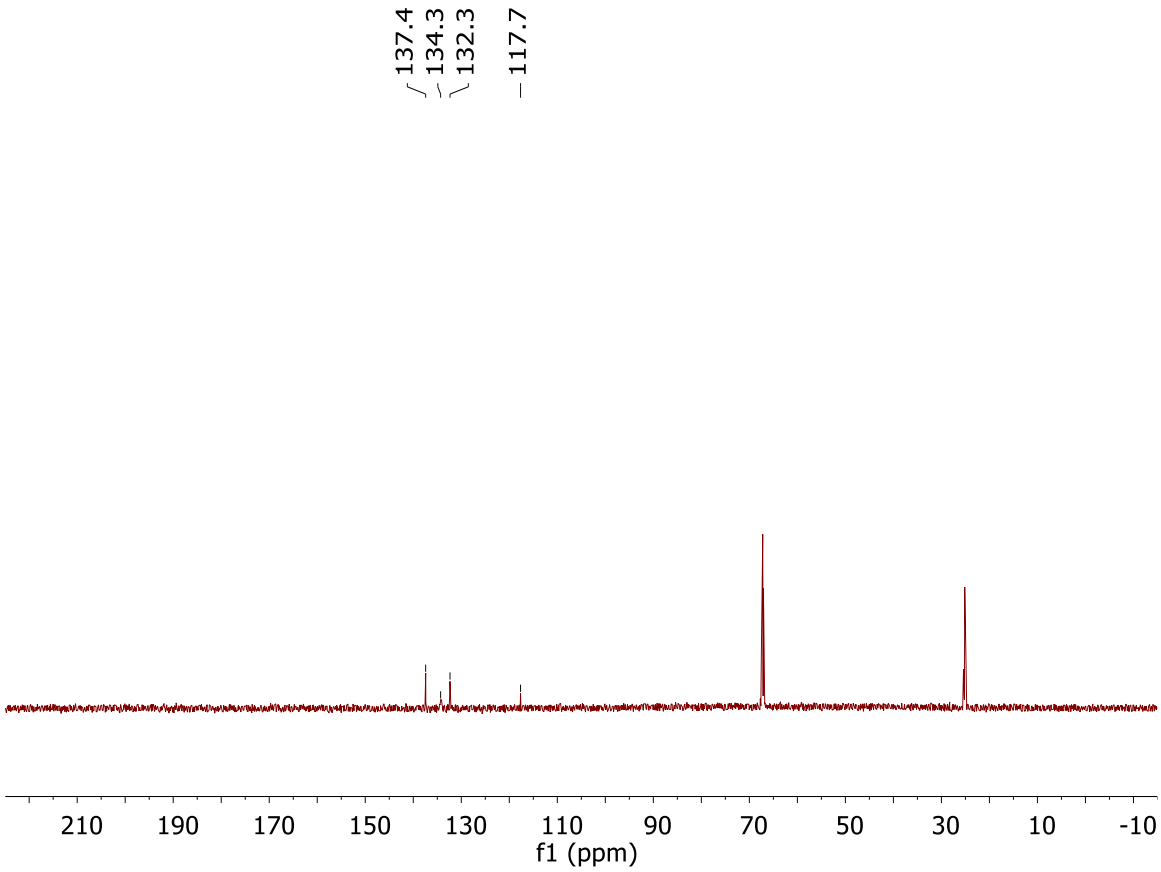

*Figure 163. $^{13}C\{^{1}H\}$ NMR of **28** (151MHz, THF-d_8, 25°C).*

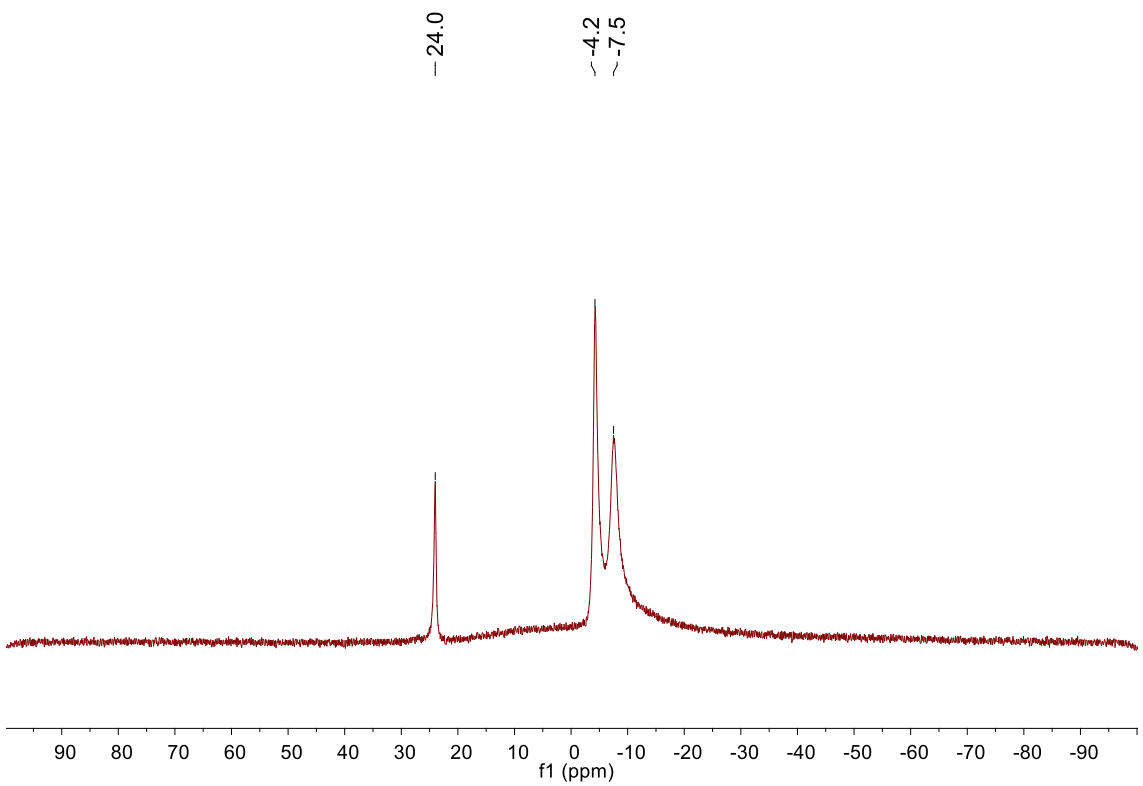

*Figure 164. $^{11}B\{^{1}H\}$ NMR of **28** (192MHz, THF-d_8, 25°C).*

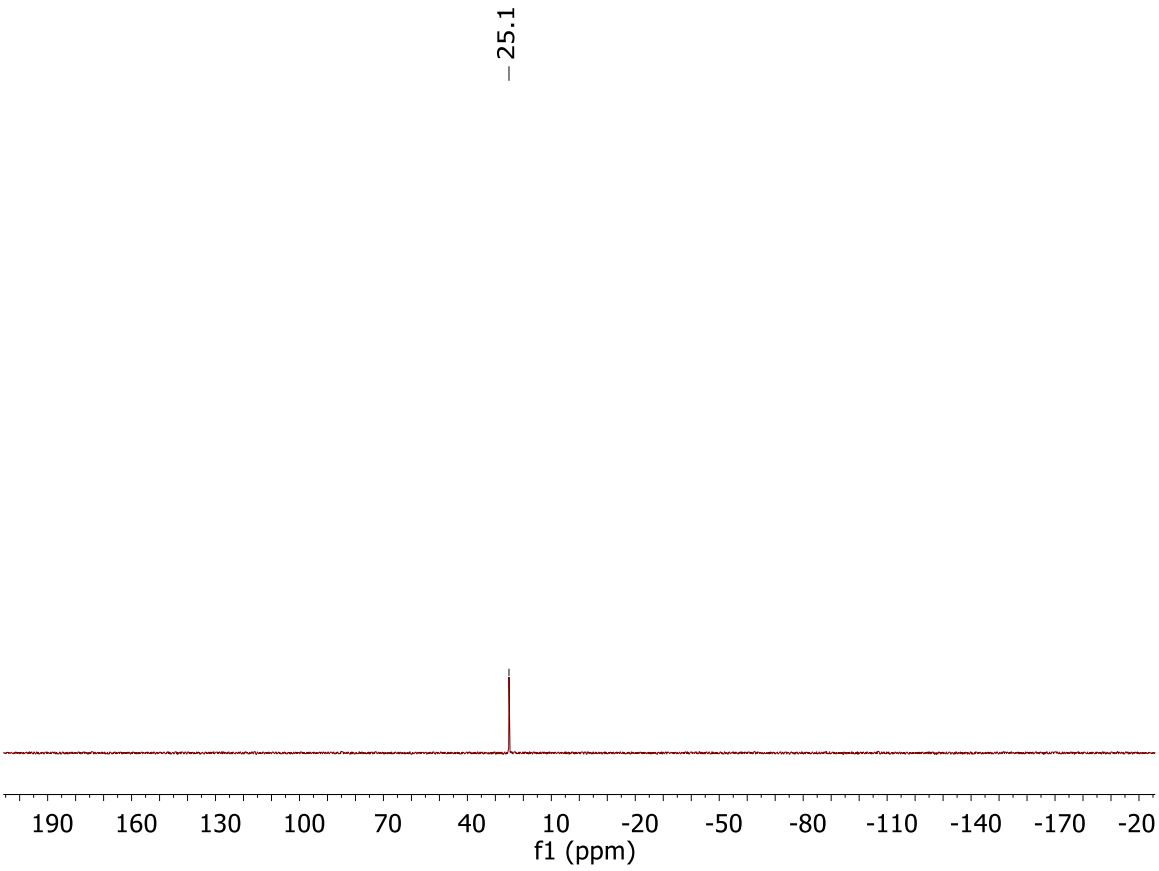

*Figure 165. $^{31}P\{^{1}H\}$ NMR of **28** (243MHz, THF-d_8, 25°C).*

Crystal Structure for Compound **28**:

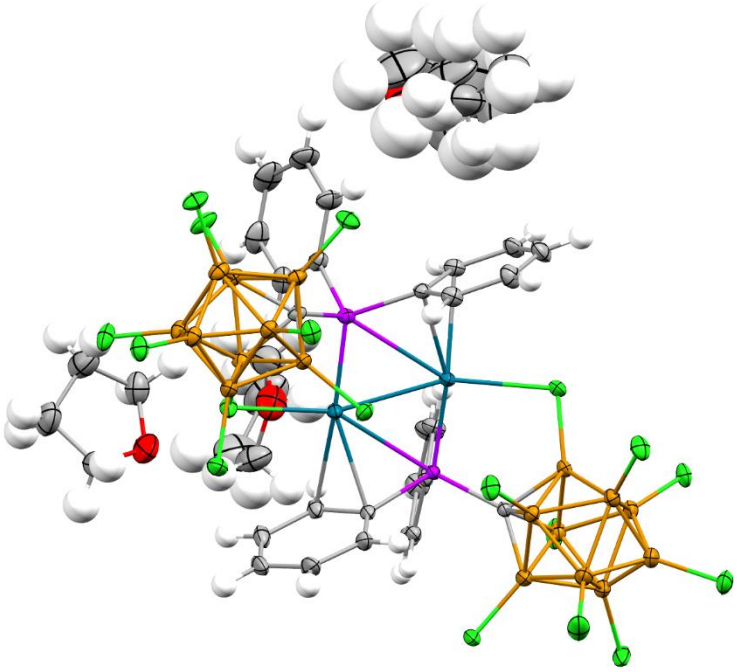

Diffraction data were collected on a Bruker-AXS Apex II diffractometer with an Apex II CCD detector using Mo K_α radiation (λ = 0.71073 Å) from a fine-focus sealed tube source. Data were collected at 100 K by performing 0.5° ω-scans, integrated using SAINT[1], and absorption corrected using SADABS[2]. The structure was solved by direct methods using SHELXT[3] and refined against F^2 on all data by full-matrix least squares with SHELXL-2018/3[4] following established refinement strategies[5]. All non-hydrogen atoms were refined anisotropically. All hydrogen atoms were included into the model at geometrically calculated positions and refined using a riding model. The isotropic displacement parameters of all hydrogen atoms were fixed to 1.2 times the *U* value of the atoms they are linked to (1.5 times for methyl groups). Crystal and data quality details, as well as a summary of the residual refinement values, are listed in the accompanying table.

Compound **28** crystallizes in the monoclinic centrosymmetric space group $P2_1/c$ with one molecule of **28**, two molecules of tetrahydrofuran, and one molecule that was a

mixture of pentane and tetrahydrofuran per asymmetric unit. The ratio of pentane: tetrahydrofuran was refined freely and converged at 51:49. The solvent molecules were refined with the help of similarity restraints on 1,2- and 1,3- distances as well as similarity and rigid-bond restraints for anisotropic displacement parameters. The mixture of solvents result in an empirical formula with non-integer numbers of atoms for C, H, and O.

CHAPTER 7: Conclusion

In this dissertation, we have demonstrated the dynamic and unique chemistry that the carborane anion and its derivatives can participate in. In 1994, Reed showed that the hydridic icosahedral carborane anion is incompatible with the trityl cation.[64] We expanded this work and showed exactly what products it makes and found that it engages in electrophilic aromatic substitution at the anti-podal boron generating a *meta* and *para* substituted carboranyl species. We also demonstrated the reactivity of an anionic biscarboranyl phosphine Au complex towards hydroamination of aryl amines and terminal alkynes. It was also shown that it was not as active as its halogenated, monoligated predecessor. Furthermore, a series of zwitterionic Ru complexes were synthesized which were monoligated with a 10-vertex perhalogenated carboranyl phosphine. In an unusual discovery for these ligand types, the k^2-P,Cl bonding mode of this ligands was so strong that it prevented the free rotation of the cluster, breaking the local C_{4v} symmetry as detected by $^{11}B\{^1H\}$ NMR. Additionally, we probed the activity of a series of 10-vertex perhalogenated carboranyl phosphine PdMe complexes towards ethylene polymerization. Though complexes **22** and **23** could only oligomerize etheylene, complex **24** could polymerize ethylene to make low, molecular weight waxes. Lastly, we demonstrated the unique chemistry that can be unlocked thanks to the carboranyl phosphine with a Pd^I dimer complex. We also showed how useful MicroED can be for the organometallic chemist.

REFERENCES

(1) Longuet-Higgins, H. C.; Bell, R. P. 64. The Structure of the Bron Hyrides. *J. Chem. Soc.* **1943**, No. 0, 250–255. https://doi.org/10.1039/JR9430000250.

(2) Stock, A. Hydrides of Boron and Silicon. *The Journal of Physical Chemistry*. 1933, pp 714–715. https://doi.org/10.1021/j150356a019.

(3) Dequasie, A. *The Green Flame: Surviving Government Secrecy*; American Chemical Society, 1991.

(4) Pitochelli, Anthony R.; Hawthorne, F. M. The Isolation of the Icosahedral $B_{12}H_{12}^{-2}$ Ion. *J. Am. Chem. Soc.* **1960**, *82* (12), 3228–3229. https://doi.org/10.1021/ja01497a069.

(5) Hawthorne, M. F.; Pitochelli, A. R. The Reactions of Bis-Acetonitrile Decaborane with Amines. *J. Am. Chem. Soc.* **1959**, *81* (20), 5519. https://doi.org/10.1021/ja01529a077.

(6) Sivaev, I. B.; Prikaznov, A. V.; Naoufal, D. Fifty Years of the Closo-Decaborate Anion Chemistry. *Collect. Czechoslov. Chem. Commun.* **2010**, *75* (11), 1149–1199. https://doi.org/10.1135/cccc2010054.

(7) Spokoyny, A. M.; MacHan, C. W.; Clingerman, D. J.; Rosen, M. S.; Wiester, M. J.; Kennedy, R. D.; Stern, C. L.; Sarjeant, A. A.; Mirkin, C. A. A Coordination Chemistry Dichotomy for Icosahedral Carborane-Based Ligands. *Nat. Chem.* **2011**, *3* (8), 590–596. https://doi.org/10.1038/nchem.1088.

(8) Sivaev, I. B.; Bregadze, V. I.; Sjöberg, S. Chemistry of Closo-Dodecaborate Anion $[B_{12}H_{12}]^{-2}$: A Review. *Collect. Czechoslov. Chem. Commun.* **2002**, *67* (6), 679–727. https://doi.org/10.1135/cccc20020679.

(9) Reed, C. A. When Triflates Fail: H^+, CH_3^+, and R_3Si^+ Carborane Reagents. *Acc. Chem. Res.* **2010**, *43* (1), 121–128.

(10) Grimes, R. N. *Carboranes*; Academic Press: New York, 2011. https://doi.org/10.1016/B978-0-12-374170-7.00021-5.

(11) Scholz, M.; Hey-Hawkins, E. Carbaboranes as Pharmacophores: Properties, Synthesis, and Application Strategies. *Chem. Rev.* **2011**, *111* (11), 7035–7062. https://doi.org/10.1021/cr200038x.

(12) Duttwyler, S. Recent Advances in B-H Functionalization of Icosahedral Carboranes and Boranes by Transition Metal Catalysis. *Pure Appl. Chem.* **2018**, *90* (4), 733–744. https://doi.org/10.1515/pac-2017-1202.

(13) Farràs, P.; Juárez-Pérez, E. J.; Lepšík, M.; Luque, R.; Núñez, R.; Teixidor, F. Metallacarboranes and Their Interactions: Theoretical Insights and Their Applicability. *Chem. Soc. Rev.* **2012**, *41* (9), 3445–3463. https://doi.org/10.1039/c2cs15338f.

(14) Eleazer, B. J.; Peryshkov, D. V. Coordination Chemistry of Carborane Clusters:

Metal-Boron Bonds in Carborane, Carboranyl, and Carboryne Complexes. *Comments Inorg. Chem.* **2018**, *38* (3), 79–109. https://doi.org/10.1080/02603594.2018.1465939.

(15) Olid, D.; Núñez, R.; Viñas, C.; Teixidor, F. Methods to Produce B-C, B-P, B-N and B-S Bonds in Boron Clusters. *Chem. Soc. Rev.* **2013**, *42* (8), 3318–3336. https://doi.org/10.1039/c2cs35441a.

(16) Popescu, A. R.; Teixidor, F.; Viñas, C. Metal Promoted Charge and Hapticities of Phosphines: The Uniqueness of Carboranylphosphines. *Coord. Chem. Rev.* **2014**, *269* (1), 54–84. https://doi.org/10.1016/j.ccr.2014.02.016.

(17) Körbe, S.; Schreiber, P. J.; Michl, J. Chemistry of the Carba-*closo*-Dodecaborate Anion, $CB_{11}H_{12}^-$. *Chem. Rev.* **2013**, *106* (12), 5208–5249. https://doi.org/10.1021/cr050548u.

(18) Wade, K. The Structural Significance of the Number of Skeletal Bonding Electron-Pairs in Carboranes, the Higher Boranes and Borane Anions, and Various Transition-Metal Carbonyl Cluster Compounds. *J. Chem. Soc. D Chem. Commun.* **1971**, No. 15, 792–793. https://doi.org/10.1039/C29710000792.

(19) Mingos, D. M. P. Polyhedral Skeletal Electron Pair Approach. *Acc. Chem. Res.* **1984**, *17* (9), 311–319. https://doi.org/10.1021/ar00105a003.

(20) Welch, A. J. The Significance and Impact of Wade's Rules. *Chem. Commun.* **2013**, *49* (35), 3615–3616. https://doi.org/10.1039/c3cc00069a.

(21) Knoth, W. H. 1-$B_9H_9CH^-$ and 1-$B_{11}H_{11}CH^-$. *J. Am. Chem. Soc.* **1967**, *89* (5), 1274–1275. https://doi.org/10.1021/ja00981a048.

(22) Reed, C. A. Carboranes: A New Class of Weakly Coordinating Anions for Strong Electrophiles, Oxidants, and Superacids. *Acc. Chem. Res.* **1998**, *31* (3), 133–139. https://doi.org/10.1021/ar970230r.

(23) Reed, C. A.; Bolskar, R. D. Discrete Fulleride Anions and Fullerenium Cations. *Chem. Rev.* **2000**, *100* (3), 1075–1120. https://doi.org/10.1021/cr980017o.

(24) Tsang, C. W.; Yang, Q.; Sze, E. T. P.; Mak, T. C. W.; Chan, D. T. W.; Xie, Z. Synthesis and Structural Characterization of Highly Chlorinated, Brominated, Iodinated, and Methylated Carborane Anions, 1-H-$CB_9X_9^-$, 1-NH_2-$CB_9X_9^-$ (X = Cl, Br, I), and 1-H-$CB_9(CH_3)_9^-$. *Inorg. Chem.* **2000**, *39* (16), 3582–3589. https://doi.org/10.1021/ic000137q.

(25) Kim, K.; Mueller, L. J.; Tham, F.; Lin, L.; Lambert, J. B. Crystallographic Evidence for a Free Silylium Ion. *Science (80-.).* **2012**, *825* (2002), 825–828. https://doi.org/10.1126/science.1073540.

(26) Kato, T.; Reed, C. A. Putting Tert-Butyl Cation in a Bottle. *Angew. Chemie - Int. Ed.* **2004**, *43* (22), 2908–2911. https://doi.org/10.1002/anie.200453931.

(27) Form, P.; Form, R. This Space Reserved for 2D Barcode. **2014**, 1–4. https://doi.org/10.1021/ac101812x.

(28) Kato, T.; Stoyanov, E.; Geier, J.; Grützmacher, H.; Reed, C. A. Alkylating Agents Stronger than Alkyl Triflates. *J. Am. Chem. Soc.* **2004**, *126* (39), 12451–12457. https://doi.org/10.1021/ja047357d.

(29) Juhasz, M.; Hoffmann, S.; Stoyanov, E.; Kim, K. C.; Reed, C. A. The Strongest Isolable Acid. *Angew. Chemie - Int. Ed.* **2004**, *43* (40), 5352–5355. https://doi.org/10.1002/anie.200460005.

(30) Reed, C. A. Carborane Acids. New "Strong yet Gentle" Acids for Organic and Inorganic Chemistry. *Chem. Commun.* **2005**, No. 13, 1669–1677. https://doi.org/10.1039/b415425h.

(31) Reed, C. A.; Fackler, N. L. P.; Kim, K. C.; Stasko, D.; Evans, D. R.; Boyd, P. D. W.; Rickard, C. E. F. Isolation of Protonated Arenes (Wheland Intermediates) with BAr(F) and Carborane Anions. A Novel Crystalline Superacid. *J. Am. Chem. Soc.* **1999**, *121* (26), 6314–6315. https://doi.org/10.1021/ja981861z.

(32) Müller, T.; Juhasz, M.; Reed, C. A. The X-Ray Structure of a Vinyl Cation. *Angew. Chemie - Int. Ed.* **2004**, *43* (12), 1543–1546. https://doi.org/10.1002/anie.200352986.

(33) Reed, C. A.; Xie, Z.; Bau, R.; Benesi, A. Closely Approaching the Silylium Ion. *Science.* **1993**, *262* (5132), 402–404. https://doi.org/10.1126/science.262.5132.402.

(34) Xie, Z.; Manning, J.; Reed, R. W.; Mathur, R.; Boyd, P. D. W.; Benesi, A.; Reed, C. A. Approaching the Silylium (R_3Si^+) Ion: Trends with Hexahalo (Cl, Br, I) Carboranes as Counterions . *J. Am. Chem. Soc.* **2002**, *118* (12), 2922–2928. https://doi.org/10.1021/ja953211q.

(35) Olah, G. A.; Li, X.-Y.; Wang, Q.; Rasul, G.; Prakash, G. K. S. Trisilyloxonium Ions: Preparation, NMR Spectroscopy, *ab Initio* IGLO Studies, and Their Role in Cationic Polymerization of Cyclosiloxanes. In *Across Conventional Lines*; World Scientific Series in 20th Century Chemistry; World Scientific Publishing Company, 2003; pp 725–729. https://doi.org/doi:10.1142/9789812791405_0132.

(36) Stasko, D.; Reed, C. A. Optimizing the Least Nucleophilic Anion. A New, Strong $Methyl^+$ Reagent. *J. Am. Chem. Soc.* **2002**, *124* (7), 1148–1149. https://doi.org/10.1021/ja0118800.

(37) Fisher, Steven P.; Tomich, Anton W.; Lovera, Sergio; Kleinsasser, Jack F.; Guo, Juchen; Asay, Matthew; Nelson, Hosea; Lavallo, V. Non-Classical Applications of Closo-Carborane Anions: From Main Group Chemistry and Catalysis to Energy Storage. *Chem. Rev.* **2019**, *ASAP*. https://doi.org/10.1021/acs.chemrev.8b00551.

(38) Jelínek, T.; Baldwin, P.; Scheidt, W. R.; Reed, C. A. New Weakly Coordinating Anions. 2. Derivatization of the Carborane Anion $CB_{11}H_{12}^-$. *Inorg. Chem.* **1993**, *32* (10), 1982–1990. https://doi.org/10.1021/ic00062a018.

(39) Zhang, J.; Xie, Z. Synthesis, Structure, and Reactivity of 13- and 14-Vertex Carboranes. *Acc. Chem. Res.* **2014**, *47* (5), 1623–1633. https://doi.org/10.1021/ar500091h.

(40) Spokoyny, A. M. New Ligand Platforms Featuring Boron-Rich Clusters as Organomimetic Substituents. *Pure Appl. Chem.* **2013**, *85* (5), 903–919. https://doi.org/10.1351/PAC-CON-13-01-13.

(41) Engesser, T. A.; Lichtenthaler, M. R.; Schleep, M.; Krossing, I. Reactive P-Block Cations Stabilized by Weakly Coordinating Anions. *Chem. Soc. Rev.* **2016**, *45* (4), 789–799. https://doi.org/10.1039/c5cs00672d.

(42) Krossing, I.; Raabe, I. Noncoordinating Anions - Fact or Fiction? A Survey of Likely Candidates. *Angew. Chemie - Int. Ed.* **2004**, *43* (16), 2066–2090. https://doi.org/10.1002/anie.200300620.

(43) Strauss, S. H. The Search for Larger and More Weakly Coordinating Anions. *Chem. Rev.* **1993**, *93* (3), 927–942. https://doi.org/10.1021/cr00019a005.

(44) Douvris, C.; Ozerov, O. V. Hydrodefluorination Of. *Science.* **2008**, *321* (August), 1188–1190.

(45) Shao, Brian; Bagdasarian, Alex L.; Popov, Stasik; Nelson, H. M. Arylation of Hydrocarbons Enabled by Organosilicon Reagents and Weakly Coordinating Anions. *Science.* **2017**, *355*, 1403–1407.

(46) Allemann, O.; Duttwyler, S.; Romanato, P.; Baldridge, K. K.; Siegel, J. S. Ok Friedel-Crafts Coupling of Fluoroarenes. *Science.* **2011**, *332* (April 2011), 574–577. https://doi.org/10.1126/science.1202432.

(47) Klis, T.; Powell, D. R.; Wojtas, L.; Wehmschulte, R. J. Synthesis and Characterization of Bulky Cationic Arylalkylaluminum Compounds. *Organometallics* **2011**, *30* (9), 2563–2570. https://doi.org/10.1021/om200120y.

(48) Cummings, S.; Hratchian, H. P.; Reed, C. A. The Strongest Acid: Protonation of Carbon Dioxide. *Angew. Chemie - Int. Ed.* **2016**, *55* (4), 1382–1386. https://doi.org/10.1002/anie.201509425.

(49) Reed, C. A.; Toyanov, E. S.; Stoyanova, I. V.; Tham, F. S. Dialkyl Chloronium Ions. *J. Am. Chem. Soc.* **2010**, *3*, 4062–4063. https://doi.org/10.1021/ja100297b.

(50) Núñez, R.; Tarrés, M.; Ferrer-Ugalde, A.; De Biani, F. F.; Teixidor, F. Electrochemistry and Photoluminescence of Icosahedral Carboranes, Boranes, Metallacarboranes, and Their Derivatives. *Chem. Rev.* **2016**, *116* (23), 14307–14378. https://doi.org/10.1021/acs.chemrev.6b00198.

(51) Fisher, S. P.; El-Hellani, A.; Tham, F. S.; Lavallo, V. Anionic and Zwitterionic Carboranyl N-Heterocyclic Carbene Au(I) Complexes. *Dalt. Trans.* **2016**, *45* (24), 9762–9765. https://doi.org/10.1039/c6dt00551a.

(52) Chan, A. L.; Estrada, J.; Kefalidis, C. E.; Lavallo, V. Changing the Charge: Electrostatic Effects in Pd-Catalyzed Cross-Coupling. *Organometallics* **2016**, *35* (19), 3257–3260. https://doi.org/10.1021/acs.organomet.6b00622.

(53) Hailmann, M.; Wolf, N.; Renner, R.; Schäfer, T. C.; Hupp, B.; Steffen, A.; Finze, M. Unprecedented Efficient Structure Controlled Phosphorescence of Silver(I) Clusters Stabilized by Carba-c*loso*-Dodecaboranylethynyl Ligands. *Angew.*

Chemie - Int. Ed. **2016**, *55* (35), 10507–10511. https://doi.org/10.1002/anie.201604198.

(54) Estrada, J.; Woen, D. H.; Tham, F. S.; Miyake, G. M.; Lavallo, V. Synthesis and Reactivity of a Zwitterionic Palladium Allyl Complex Supported by a Perchlorinated Carboranyl Phosphine. *Inorg. Chem.* **2015**, *54* (11), 5142–5144. https://doi.org/10.1021/acs.inorgchem.5b00576.

(55) Estrada, J.; Lee, S. E.; McArthur, S. G.; El-Hellani, A.; Tham, F. S.; Lavallo, V. Resisting B-H Oxidative Addition: The Divergent Reactivity of the *o*-Carborane and Carba-*closo*-Dodecaborate Ligand Substituents. *J. Organomet. Chem.* **2015**, *798*, 214–217. https://doi.org/10.1016/j.jorganchem.2015.05.008.

(56) Asay, M. J.; Fisher, S. P.; Lee, S. E.; Tham, F. S.; Borchardt, D.; Lavallo, V. Synthesis of Unsymmetrical N-Carboranyl NHCs: Directing Effect of the Carborane Anion. *Chem. Commun.* **2015**, *51* (25), 5359–5362. https://doi.org/10.1039/c4cc08267b.

(57) El-Hellani, A.; Lavallo, V. Fusing N-Heterocyclic Carbenes with Carborane Anions. *Angew. Chemie - Int. Ed.* **2014**, *53* (17), 4489–4493. https://doi.org/10.1002/anie.201402445.

(58) Lavallo, V.; Wright, J. H.; Tham, F. S.; Quinlivan, S. Perhalogenated Carba-*closo*-Dodecaborate Anions as Ligand Substituents: Applications in Gold Catalysis. *Angew. Chemie - Int. Ed.* **2013**, *52* (11), 3172–3176. https://doi.org/10.1002/anie.201209107.

(59) Himmelspach, A.; Finze, M.; Raub, S. Tetrahedral Gold(I) Clusters with Carba-Closo-Dodecaboranylethynido Ligands: [{12-(R3PAu)2Ci??C-Closo-1-CB 11H11}2]. *Angew. Chemie - Int. Ed.* **2011**, *50* (11), 2628–2631. https://doi.org/10.1002/anie.201007239.

(60) Ringstrand, B.; Kaszynski, P. Functionalization of the [*closo*-1-CB_9H_{10}]$^-$ Anion for the Construction of New Classes of Liquid Crystals. *Acc. Chem. Res.* **2013**, *46* (2), 214–225. https://doi.org/10.1021/ar300081b.

(61) McArthur, S. G.; Jay, R.; Geng, L.; Guo, J.; Lavallo, V. Below the 12-Vertex: 10-Vertex Carborane Anions as Non-Corrosive, Halide Free, Electrolytes for Rechargeable Mg Batteries. *Chem. Commun.* **2017**, *53* (32), 4453–4456. https://doi.org/10.1039/c7cc01570d.

(62) McArthur, S. G.; Geng, L.; Guo, J.; Lavallo, V. Cation Reduction and Comproportionation as Novel Strategies to Produce High Voltage, Halide Free, Carborane Based Electrolytes for Rechargeable Mg Batteries. *Inorg. Chem. Front.* **2015**, *2* (12), 1101–1104. https://doi.org/10.1039/c5qi00171d.

(63) Boeré, R. T.; Bolli, C.; Finze, M.; Himmelspach, A.; Knapp, C.; Roemmele, T. L. Quantum-Chemical and Electrochemical Investigation of the Electrochemical Windows of Halogenated Carborate Anions. *Chem. - A Eur. J.* **2013**, *19* (5), 1784–1795. https://doi.org/10.1002/chem.201202475.

(64) Xie, Z.; Jelínek, T.; Bau, R.; Reed, C. A. New Weakly Coordinating Anions. III.

Useful Silver and Trityl Salt Reagents of Carborane Anions. *J. Am. Chem. Soc.* **1994**, *116* (5), 1907–1913. https://doi.org/10.1021/ja00084a034.

(65) Wiersema, R. J.; Hawthorne, M. F. Electrochemistry and Boron-11 Nuclear Magnetic Resonance Spectra of Monocarbon Carboranes. *Inorg. Chem.* **1973**, *12* (4), 785–788. https://doi.org/10.1021/ic50122a016.

(66) Himmelspach, A.; Reiss, G. J.; Finze, M. Microwave-Assisted Kumada-Type Cross-Coupling Reactions of Iodinated Carba-*closo*-Dodecaborate Anions. *Inorg. Chem.* **2012**, *51* (4), 2679–2688. https://doi.org/10.1021/ic202638k.

(67) Ingleson, M. J.; Kociok-Köhn, G.; Weller, A. S. B-C Activation in Highly Alkylated Carborane Monoanions Partnered with Cationic Transition Metal Fragments: Observations and Comments. *Inorganica Chim. Acta* **2005**, *358* (5 SPEC. ISS.), 1571–1580. https://doi.org/10.1016/j.ica.2004.09.048.

(68) Bullen, N. J.; Franken, A.; Kilner, C. A.; Kennedy, J. D. Polyhedral Monocarbaborane Chemistry. Routes to Neutral, Monoanionic and Dianionic Carbo-Carbaborane Rods. *Chem. Commun.* **2003**, *3* (14), 1684–1685. https://doi.org/10.1039/b303589a.

(69) Franken, A.; Kilner, C. A.; Thornton-Pett, M.; Kennedy, J. D. Polyhedral Monocarbaborane Chemistry. The C,B-Para-Diphenyl Monocarbadodecaborane Anion [1,12-Ph2-Closo-1-CB11H10]-. *J. Organomet. Chem.* **2002**, *657* (1–2), 176–179. https://doi.org/10.1016/S0022-328X(02)01539-5.

(70) Grüner, B.; Janoušek, Z.; King, B. T.; Woodford, J. N.; Wang, C. H.; Všetečka, V.; Michl, J. Synthesis of 12-Substituted 1-Carba-*closo*-Dodecaborate Anions and First Hyperpolarizability of the 12-$C_7H_6^+$-$CB_{11}H_{11}$- Ylide. *J. Am. Chem. Soc.* **1999**, *121* (13), 3122–3126. https://doi.org/10.1021/ja982368q.

(71) Janoušek, Z.; Lehmann, U.; Častulík, J.; Císařová, I.; Michl, J. Li^+-Induced σ-Bond Metathesis: Aryl for Methyl Exchange on Boron in a Methylated Monocarbadodecaborate Anion. *J. Am. Chem. Soc.* **2004**, *126* (13), 4060–4061. https://doi.org/10.1021/ja0387857.

(72) Kitazawa, Y.; Takita, R.; Yoshida, K.; Muranaka, A.; Matsubara, S.; Uchiyama, M. "naked" Lithium Cation: Strongly Activated Metal Cations Facilitated by Carborane Anions. *J. Org. Chem.* **2017**, *82* (4), 1931–1935. https://doi.org/10.1021/acs.joc.6b02677.

(73) Grimes, R. N. Carboranes in the Chemist's Toolbox. *Dalt. Trans.* **2015**, *44* (13), 5939–5956. https://doi.org/10.1039/c5dt00231a.

(74) Spokoyny, A. M. New Ligand Platforms Featuring Boron-Rich Clusters as Organomimetic Substituents. *Pure Appl. Chem.* **2013**, *85* (5), 903–919. https://doi.org/10.1351/PAC-CON-13-01-13.

(75) Vinas, C.; Nuez, R.; Teixidor, F.; Sillanpa, R.; Kivekos, R. Formation of B-P Bonds through the Reaction of *nido*-Monophosphinocarboranes with Palladium(II) Complexes. The First Example of a Chelating R_2P-C-B-PR_2 Diphosphine. *Organometallics* **1999**, *18* (23), 4712–4717. https://doi.org/10.1021/om990599f.

(76) Teixidor, F.; Casabó, J.; Romerosa, A. M.; Vinas, C.; Rius, J.; Miravitlles, C.; Casabó, J. Simultaneous Conversion of Pd-PPh_3 and B-H to B-PPh_2 under Exceedingly Mild Conditions. Crystal and Molecular Structure of $PdPPh_3Cl${7-SMe 8-Me-11-PPh_2-7,8-$C_2B_9H_{10}$}. *J. Am. Chem. Soc.* **1991**, *113* (26), 9895–9896. https://doi.org/10.1021/ja00026a049.

(77) Estrada, J.; Lugo, C. A.; McArthur, S. G.; Lavallo, V. Inductive Effects of 10 and 12-Vertex *closo*-Carborane Anions: Cluster Size and Charge Make a Difference. *Chem. Commun.* **2015**, *52* (9), 1824–1826. https://doi.org/10.1039/c5cc08377j.

(78) El-Hellani, A.; Kefalidis, C. E.; Tham, F. S.; Maron, L.; Lavallo, V. Structure and Bonding of a Zwitterionic Iridium Complex Supported by a Phosphine with the Parent Carba- Closo-Dodecaborate $CB_{11}H_{11}^-$ Ligand Substituent. *Organometallics* **2013**, *32* (23), 6887–6890. https://doi.org/10.1021/om401001p.

(79) Estrada, J.; Lavallo, V. Fusing Dicarbollide Ions with N-Heterocyclic Carbenes. *Angew. Chemie - Int. Ed.* **2017**, *56* (33), 9906–9909. https://doi.org/10.1002/anie.201705857.

(80) Alyabyev, S. B.; Beletskaya, I. P. Gold as a Catalyst. Part I. Nucleophilic Addition to the Triple Bond. *Russ. Chem. Rev.* **2017**, *86* (8), 689–749. https://doi.org/10.1070/RCR4727.

(81) Gooßen, L. J.; Huang, L.; Arndt, M.; Gooßen, K.; Heydt, H. Late Transition Metal-Catalyzed Hydroamination and Hydroamidation. *Chem. Rev.* **2015**, *115* (7), 2596–2697. https://doi.org/10.1021/cr300389u.

(82) McWhannell, M. A.; Rosair, G. M.; Welch, A. J. 1-[Chloro(Diphenylphosphino)Gold(I)-*P*]-2-Phenyl-1,2-Dicarba-*closo*-dodecaborane(12). *Acta Crystallogr. Sect. C Cryst. Struct. Commun.* **1998**, *54* (1), 13–15. https://doi.org/10.1107/S0108270197013048.

(83) Ramirez-Contreras, Rodgrigo; Ozerov, O. V. Convenient C-Alkylation of the $[HCB_{11}Cl_{11}]^-$ Carborane Anion. *Dalt. Trans.* **2012**, *41*, 7842–7844. https://doi.org/10.1039/c2dt30639e.

(84) Shanbhag, G. V.; Kumbar, S. M.; Joseph, T.; Halligudi, S. B. Heterogeneous Intermolecular Hydroamination of Terminal Alkynes with Aromatic Amines. *Tetrahedron Lett.* **2006**, *47* (2), 141–143. https://doi.org/10.1016/j.tetlet.2005.11.001.

(85) Imamoto, T.; Iwadate, N.; Yoshida, K. Enantioselective Hydrogenation of Acyclic Aromatic N-Aryl Imines Catalyzed by an Iridium Complex Of. *Org. Lett.* **2006**, *8* (11), 2289–2292.

(86) Brunet, J. J.; Chu, N. C.; Diallo, O. Intermolecular Highly Regioselective Hydroamination of Alkenes with Ligandless Platinum(II) Catalysts in Ionic Solvents: Activation Role of n-Bu4PBr. *Organometallics* **2005**, *24* (13), 3104–3110. https://doi.org/10.1021/om040142s.

(87) Lorber, C.; Choukroun, R.; Vendier, L. Hydroamination of Alkynes Catalyzed by Imido Complexes of Titanium and Vanadium. *Organometallics* **2004**, *23* (8), 1845–

1850. https://doi.org/10.1021/om0342762.

(88) Bruker AXS Inc. APEX 2, Version 2014.1-1. Madison, Wisconsin, USA 2014.

(89) Bruker AXS Inc. SAINT, Version V8.34A. Madison, Wisconsin, USA 2012.

(90) Bruker AXS Inc. SADABS, Version 2012/1. Madison, Wisconsin, USA 2012.

(91) Bruker AXS Inc. SHELXTL, Version 2013/4. Madison, Wisconsin, USA 2013.

(92) Heckelsberg, L. F.; Banks, R. L.; Bailey, G. C. A Tungsten Oxide on Silica Catalyst for Phillips' Triolefin Process. *Ind. Eng. Chem. Prod. Res. Dev.* **1968**, *7* (1), 29–31. https://doi.org/10.1021/i360025a007.

(93) Nguyen, S. B. T.; Johnson, L. K.; Grubbs, R. H.; Ziller, J. W. Ring-Opening Metathesis Polymerization (ROMP) of Norbornene by a Group VIII Carbene Complex in Protic Media. *J. Am. Chem. Soc.* **1992**, *114* (10), 3974–3975. https://doi.org/10.1021/ja00036a053.

(94) Schwab, Peter; France, B., Marcia; Ziller, W., Joseph; Grubbs, H., R. A Series of Well-Defined Metathesis Catalysts–Synthesis of and Its Reactions. *… Int. Ed. …* **1995**, *34* (18), 2039–2041.

(95) Hartwig, J. F. Organotransition Metal Chemistry. 2010. https://doi.org/10.1039/9781847551597.

(96) Ivin, K. J. Kenneth J. J. M. *Olefin Metathesis and Metathesis Polymerization*; Mol, J. C., Ed.; Academic Press: San Diego, 1997.

(97) Dias, E. L.; Nguyen, S. B. T.; Grubbs, R. H. Well-Defined Ruthenium Olefin Metathesis Catalysts: Mechanism and Activity. *J. Am. Chem. Soc.* **1997**, *119* (17), 3887–3897. https://doi.org/10.1021/ja963136z.

(98) Daumann, L. J.; Tatum, D. S.; Snyder, B. E. R.; Ni, C.; Law, G. L.; Solomon, E. I.; Raymond, K. N. New Insights into Structure and Luminescence of Eu^{III} and Sm^{III} Complexes of the 3,4,3-LI(1,2-HOPO) Ligand. *J. Am. Chem. Soc.* **2015**, *137* (8), 2816–2819. https://doi.org/10.1021/ja5116524.

(99) Brellochs, B.; Bačkovský, J.; Štíbr, B.; Jelínek, T.; Holub, J.; Bakardjiev, M.; Hnyk, D.; Hofmann, M.; Císarová, I.; Wrackmeyer, B. New Ways to a Series of Parent Representatives of the Eight-, Nine-, and Ten-Vertex Monocarbaborane Family. *Eur. J. Inorg. Chem.* **2004**, *14* (18), 3605–3611. https://doi.org/10.1002/ejic.200400125.

(100) Ringstrand, B.; Bateman, D.; Shoemaker, R. K.; Janoušek, Z. Improved Synthesis of [*closo*-1-CB_9H_{10}]$^-$ Anion and New C-Substituted Derivatives. *Collect. Czechoslov. Chem. Commun.* **2009**, *74* (3), 419–431. https://doi.org/10.1135/cccc2008151.

(101) Anions, M. C.; Cl, X. X.; Tsang, C.; Yang, Q.; Sze, E. T.; Mak, T. C. W.; Chan, D. T. W.; Xie, Z. Synthesis and Structural Characterization of Highly Chlorinated , Brominated , Iodinated ,. **2000**, *9* (c), 3582–3589.

(102) Kleinsasser, J. F.; Reinhart, E. D.; Estrada, J.; Jordan, R. F.; Lavallo, V. Ethylene Oligomerization and Polymerization by Palladium(II) Methyl Complexes Supported by Phosphines Bearing a Perchlorinated 10-Vertex *closo*-Carborane Anion Substituent. *Organometallics* **2018**, *37* (24), 4773–4783. https://doi.org/10.1021/acs.organomet.8b00772.

(103) McCormick, F. B.; Cox, D. D.; Gleason, W. B. Synthesis, Structure, and Disproportionation of Labile $(\eta^6\text{-}C_6H_6)Ru(CH_3CN)_2Cl^+$ Salts. *Organometallics* **1993**, *12* (3), 610–612. https://doi.org/10.1021/om00027a006.

(104) Roh, S. W.; Choi, K.; Lee, C. Transition Metal Vinylidene- and Allenylidene-Mediated Catalysis in Organic Synthesis. *Chem. Rev.* **2019**, *119*, 4293–4356. https://doi.org/10.1021/acs.chemrev.8b00568.

(105) Péron, D.; Romero, A.; Dixneuf, P. H. Functional Ruthenium(II) Allenylidene and Diynyl (Arene) Derivatives Formed by Activation of a Diyne via a $Ru=C=C=C=CR_2$ Intermediate. *Organometallics* **1995**, *14* (7), 3319–3326. https://doi.org/10.1021/om00007a036.

(106) Picquet, M.; Touchard, D.; Bruneau, C.; Dixneuf, P. H. Room Temperature Operating Allenylidene Precatalyst $[L_nRu=C=C=CR_2]^+X^-$ for Olefin Metathesis: Dramatic Influence of the Counter Anion X-. *New J. Chem.* **1999**, *23* (2), 141–143. https://doi.org/10.1039/a808859d.

(107) Antonucci, A.; Bassetti, M.; Bruneau, C.; Dixneuf, P. H.; Pasquini, C. Allenylidene to Indenylidene Rearrangement in Cationic P-Cymene Ruthenium(II) Complexes: Solvent, Counteranion, and Substituent Effects in the Key Step toward Catalytic Olefin Metathesis. *Organometallics* **2010**, *29* (20), 4524–4531. https://doi.org/10.1021/om100654z.

(108) Fürstner, A.; Liebl, M.; Lehmann, C. W.; Picquet, M.; Kunz, R.; Bruneau, C.; Touchard, D.; Dixneuf, P. H. Cationic Ruthenium Allenylidene Complexes as Catalysts for Ring Closing Olefin Metathesis. *Chem. - A Eur. J.* **2000**, *6* (10), 1847–1857. https://doi.org/10.1002/(SICI)1521-3765(20000515)6:10<1847::AID-CHEM1847>3.0.CO;2-1.

(109) Picquet, M.; Bruneau, C.; Dixneuf, P. H.; Cl, C. N. C. N. C. R. L. Cationic Ruthenium Allenylidene Complexes as a New Class of Performing Catalysts for Ring Closing Metathesis. *Chem. Commun.* **1998**, *95* (76), 1315–1316.

(110) Castarlenas, R.; Vovard, C.; Fischmeister, C.; Dixneuf, P. H. Allenylidene-to-Indenylidene Rearrangement in Arene-Ruthenium Complexes: A Key Step to Highly Active Catalysts for Olefin Metathesis Reactions. *J. Am. Chem. Soc.* **2006**, *128* (12), 4079–4089. https://doi.org/10.1021/ja0579762.

(111) Thurier, C.; Fischmeister, C.; Bruneau, C.; Olivier-Bourbigou, H.; Dixneuf, P. H. Ethenolysis of Methyl Oleate in Room-Temperature Ionic Liquids. *ChemSusChem* **2008**, *1* (1–2), 118–122. https://doi.org/10.1002/cssc.200700002.

(112) Owalude, S. O.; Tella, A. C.; Odebunmi, E. O.; Eke, U. B.; Golen, J. E.; Rheingold, A. L.; Mahlaka, T. J.; Meijboom, R. Synthesis of New Ruthenium(II) Complexes Derived from Labile Nitrile Ligands: An Alternative Route to the Preparation of *Trans*-Dichlorotetrakis(Diphenylphosphine)Ruthenium(II). *J. Coord. Chem.* **2017**, *70* (7), 1260–1269. https://doi.org/10.1080/00958972.2017.1297806.

(113) Nakamura, A.; Anselment, T. M. J.; Claverie, J.; Goodall, B.; Jordan, R. F.; Mecking, S.; Rieger, B.; Sen, A.; Van Leeuwen, P. W. N. M.; Nozaki, K. Ortho-Phosphinobenzenesulfonate: A Superb Ligand for Palladium-Catalyzed Coordination-Insertion Copolymerization of Polar Vinyl Monomers. *Acc. Chem. Res.* **2013**, *46* (7), 1438–1449. https://doi.org/10.1021/ar300256h.

(114) Ito, S.; Nozaki, K. Coordination-Insertion Copolymerization of Polar Vinyl Monomers by Palladium Catalysts. *Chem. Rec.* **2010**, *10* (5), 315–325. https://doi.org/10.1002/tcr.201000032.

(115) Nakamura, Akifumi; Ito, Shingo; Nozaki, K. Coordination – Insertion Copolymerization of Polar Vinyl Monomers By. *Chem. Rev.* **2009**, *109*, 5215–5244. https://doi.org/10.1002/tcr.201000032.

(116) Sui, X.; Dai, S.; Chen, C. Ethylene Polymerization and Copolymerization with Polar Monomers by Cationic Phosphine Phosphonic Amide Palladium Complexes. *ACS Catal.* **2015**, *5* (10), 5932–5937. https://doi.org/10.1021/acscatal.5b01490.

(117) Zhang, Y.; Cao, Y.; Leng, X.; Chen, C.; Huang, Z. Cationic Palladium(II) Complexes of Phosphine-Sulfonamide Ligands: Synthesis, Characterization, and Catalytic Ethylene Oligomerization. *Organometallics* **2014**, *33* (14), 3738–3745. https://doi.org/10.1021/om5004094.

(118) Mitsushige, Y.; Carrow, B. P.; Ito, S.; Nozaki, K. Ligand-Controlled Insertion Regioselectivity Accelerates Copolymerisation of Ethylene with Methyl Acrylate by Cationic Bisphosphine Monoxide-Palladium Catalysts. *Chem. Sci.* **2015**, *7* (1), 737–744. https://doi.org/10.1039/c5sc03361f.

(119) Noda, S.; Nakamura, A.; Kochi, T.; Lung, W. C.; Morokuma, K.; Nozaki, K. Mechanistic Studies on the Formation of Linear Polyethylene Chain Catalyzed by Palladium Phosphine-Sulfonate Complexes: Experiment and Theoretical Studies. *J. Am. Chem. Soc.* **2009**, *131* (39), 14088–14100. https://doi.org/10.1021/ja9047398.

(120) Contrella, N. D.; Sampson, J. R.; Jordan, R. F. Copolymerization of Ethylene and Methyl Acrylate by Cationic Palladium Catalysts That Contain Phosphine-Diethyl Phosphonate Ancillary Ligands. *Organometallics* **2014**, *33* (13), 3546–3555. https://doi.org/10.1021/om5004489.

(121) Kim, Y.; Jordan, R. F. Synthesis, Structures, and Ethylene Dimerization Reactivity of Palladium Alkyl Complexes That Contain a Chelating Phosphine-Trifluoroborate Ligand. *Organometallics* **2011**, *30* (16), 4250–4256. https://doi.org/10.1021/om200472x.

(122) Johnson, A. M.; Contrella, N. D.; Sampson, J. R.; Zheng, M.; Jordan, R. F. Allosteric Effects in Ethylene Polymerization Catalysis. Enhancement of Performance of

Phosphine-Phosphinate and Phosphine-Phosphonate Palladium Alkyl Catalysts by Remote Binding of $B(C_6F_5)_3$. *Organometallics* **2017**, *36* (24), 4990–5002. https://doi.org/10.1021/acs.organomet.7b00815.

(123) Gutsulyak, D. V.; Gott, A. L.; Piers, W. E.; Parvez, M. Dimerization of Ethylene by Nickel Phosphino-Borate Complexes. *Organometallics* **2013**, *32* (11), 3363–3370. https://doi.org/10.1021/om400288u.

(124) Wucher, P.; Goldbach, V.; Mecking, S. Electronic Influences in Phosphinesulfonato Palladium(II) Polymerization Catalysts. *Organometallics* **2013**, *32* (16), 4516–4522. https://doi.org/10.1021/om400297x.

(125) Gott, A. L.; Piers, W. E.; Dutton, J. L.; McDonald, R.; Parvez, M. Dimerization of Ethylene by Palladium Complexes Containing Bidentate Trifluoroborate-Functionalized Phosphine Ligands. *Organometallics* **2011**, *30* (16), 4236–4249. https://doi.org/10.1021/om2004095.

(126) Spokoyny, A. M.; Lewis, C. D.; Teverovskiy, G.; Buchwald, S. L. Extremely Electron-Rich, Boron-Functionalized, Icosahedral Carborane-Based Phosphinoboranes. *Organometallics* **2012**, *31* (24), 8478–8481. https://doi.org/10.1021/om301116x.

(127) Riley, L. E.; Krämer, T.; McMullin, C. L.; Ellis, D.; Rosair, G. M.; Sivaev, I. B.; Welch, A. J. Large, Weakly Basic Bis(Carboranyl)Phosphines: An Experimental and Computational Study. *Dalt. Trans.* **2017**, *46* (16), 5218–5228. https://doi.org/10.1039/c7dt00485k.

(128) King, A. S.; Ferguson, G.; Britten, J. F.; Valliant, J. F. Sterically Hindered and Robust Pnictogen Ligands Derived from Carboranes: Synthesis and X-Ray Structure Determination of Tris(1′ -Methyl(1,2-Dicarba-*closo*-Dodecaboran-1-Yl))Phosphine, Tris(1′ -Methyl(1,2-Dicarba-*closo*-Dodecaboran-1-Yl))Arsine and Chloro(T. *Inorg. Chem.* **2004**, *43* (11), 3507–3513. https://doi.org/10.1021/ic049947i.

(129) Yao, Z. J.; Jin, G. X. Transition Metal Complexes Based on Carboranyl Ligands Containing N, P, and S Donors: Synthesis, Reactivity and Applications. *Coord. Chem. Rev.* **2013**, *257* (17–18), 2522–2535. https://doi.org/10.1016/j.ccr.2013.02.004.

(130) Hosmane, N. S. . *Boron Science: New Technologies and Applications*, 1st ed.; CRC Press: Raton, Florida, USA, 2011.

(131) Dodge, T.; Curtis, M. A.; Russell, J. M.; Sabat, M.; Finn, M. G.; Grimes, R. N. Titanium and Zirconium $Et_2C_2B_4H_4^-$ Metal-Phosphine Complexes: Synthesis, Characterization, and Ethylene Polymerization Activity. *J. Am. Chem. Soc.* **2000**, *122* (43), 10573–10580. https://doi.org/10.1021/ja001366e.

(132) Boring, E.; Sabat, M.; Finn, M. G.; Grimes, R. N. Alkene and Alkyne Insertion Reactions with Tantalum Metallacarborane Complexes: The $Et_2C_2B_4H_4^{-2}$ Carborane Ligand as a Spectator and Participant1. *Organometallics* **1998**, *17* (18), 3865–3874. https://doi.org/10.1021/om980242w.

(133) Yinghuai, Z.; Nong, L. C.; Zhao, L. C.; Widjaja, E.; Hwei, C. S.; Cun, W.; Tan, J.; Van Meurs, M.; Hosmane, N. S.; Maguire, J. A. Synthesis, Characterization, and Polymerization of a Neutral Tantalacarborane Sandwich Complex Derived from a Pentaanionic Exo-Polyhedrally Linked Bis(C_2B_{10}-Carborane) Ligand. *Organometallics* **2009**, *28* (1), 60–64. https://doi.org/10.1021/om800516x.

(134) Yinghuai, Z.; Yulin, Z.; Carpenter, K.; Maguire, J. A.; Hosmane, N. S. Syntheses and Catalytic Activities of Group 4 Metal Complexes Derived from C(Cage)-Appended Cyclohexyloxocarborane Trianion. *J. Organomet. Chem.* **2005**, *690* (11), 2802–2808. https://doi.org/10.1016/j.jorganchem.2005.01.047.

(135) Paxson, T. E.; Hawthorne, M. F. Preparation of Hydridometallocarboranes and Their Use as Homogeneous Catalysts. *J. Am. Chem. Soc.* **1974**, *96* (14), 4674–4676. https://doi.org/10.1021/ja00821a054.

(136) Hewes, J. D.; Kreimendahl, C. W.; Marder, T. B.; Hawthorne, M. F. Metal-Promoted Insertion of an Activated Alkene into a B-H Bond of an Exopolyhedral *nido*-Rhodacarborane: Rhodium-Catalyzed Hydroboration. *J. Am. Chem. Soc.* **1984**, *106* (19), 5757–5759. https://doi.org/10.1021/ja00331a072.

(137) Long, J. A.; Marder, T. B.; Behnken, P. E.; Hawthorne, M. F. Metallacarboranes in Catalysis. 3. Synthesis and Reactivity of Exo-*nido*-Phosphinerhodacarboranes. *J. Am. Chem. Soc.* **1984**, *106* (10), 2979–2989. https://doi.org/10.1021/ja00322a039.

(138) Behnken, P. E.; Busby, D. C.; Delaney, M. S.; King, R. E.; Kreimendahl, C. W.; Marder, T. B.; Wilczynski, J. J.; Hawthorne, M. F. Metallacarboranes in Catalysis. 7. Kinetics and Mechanism of Acrylate Ester Hydrogenation Catalyzed by *closo*-Rhodacarboranes. *J. Am. Chem. Soc.* **1984**, *106* (24), 7444–7450. https://doi.org/10.1021/ja00336a025.

(139) Crowther, D. J.; Baenziger, N. C.; Jordan, R. F. Group 4 Metal Dicarbollide Chemistry. Synthesis, Structure, and Reactivity of Electrophilic Alkyl Complexes (Cp*)($C_2B_9H_{11}$)M(R) (M = Hf, Zr). *J. Am. Chem. Soc.* **1991**, *113* (4), 1455–1457. https://doi.org/10.1021/ja00004a080.

(140) Kreuder, C.; Jordan, R. F.; Zhang, H. Early Metal Carborane Chemistry. Generation and Reactivity of (C_5Me_5)(η-$C_2B_9H_{11}$)TiMe. *Organometallics* **1995**, *14* (6), 2993–3001. https://doi.org/10.1021/om00006a050.

(141) Soloway, A. H.; Tjarks, W.; Barnum, B. A.; Rong, F.-G.; Barth, R. F.; Codogni, I. M.; Wilson, J. G. The Chemistry of Neutron Capture Therapy. *Chem. Rev.* **1998**, *98* (4), 1515–1562. https://doi.org/10.1021/cr941195u.

(142) Xie, Z. Cyclopentadienyl-Carboranyl Hybrid Compounds: A New Class of Versatile Ligands for Organometallic Chemistry. *Acc. Chem. Res.* **2003**, *36* (1), 1–9. https://doi.org/10.1021/ar010146i.

(143) Piche, L.; Daigle, J. C.; Rehse, G.; Claverie, J. P. Structure-Activity Relationship of Palladium Phosphanesulfonates: Toward Highly Active Palladium-Based Polymerization Catalysts. *Chem. - A Eur. J.* **2012**, *18* (11), 3277–3285. https://doi.org/10.1002/chem.201103694.

(144) McGuinness, D. S.; Wadsley, A. W.; Malinowski, R.; Britovsek, G. J. P.; Nobbs, J. D.; Tomov, A. K.; Young, C. T. Ethylene Oligomerization beyond Schulz–Flory Distributions. *ACS Catal.* **2015**, *5* (11), 6922–6925. https://doi.org/10.1021/acscatal.5b02203.

(145) Ittel, S. D.; Johnson, L. K.; Brookhart, M. Late-Metal Catalysts for Ethylene Homo- and Copolymerization. *Chem. Rev.* **2000**, *100* (4), 1169–1203. https://doi.org/10.1021/cr9804644.

(146) Seger, M. R.; Maciel, G. E. Quantitative ^{13}C NMR Analysis of Sequence Distributions in Poly(Ethylene-Co-1-Hexene). *Anal. Chem.* **2004**, *76* (19), 5734–5747. https://doi.org/10.1021/ac040104i.

(147) Roesle, P.; Göttker-Schnetmann, I.; Voit, G.; Wiedemann, T.; Tchernook, A.; Mecking, S. Monofunctional Hyperbranched Ethylene Oligomers. *J. Am. Chem. Soc.* **2014**, *136* (5), 2078–2085. https://doi.org/10.1021/ja411945n.

(148) Azoulay, J. D.; Bazan, G. C.; Galland, G. B. Microstructural Characterization of Poly(1-Hexene) Obtained Using a Nickel α-Keto-β-Diimine Initiator. *Macromolecules* **2010**, *43* (6), 2794–2800. https://doi.org/10.1021/ma9025543.

(149) Liu, W.; Rinaldi, P. L.; McIntosh, L. H.; Quirk, R. P. Poly(Ethylene-Co-1-Octene) Characterization by High-Temperature Multidimensional NMR at 750 MHz. *Macromolecules* **2001**, *34* (14), 4757–4767. https://doi.org/10.1021/ma001792k.

(150) Hansen, E. W.; Blom, R.; Bade, O. M. N.m.r. Characterization of Polyethylene with Emphasis on Internal Consistency of Peak Intensities and Estimation of Uncertainties in Derived Branch Distribution Numbers. *Polymer (Guildf).* **1997**, *38* (17), 4295–4304. https://doi.org/10.1016/S0032-3861(96)01027-0.

(151) Kolbert, A. C.; Didier, J. G.; Xu, L. Mechanochemical Degradation of Ethylene-Propylene Copolymers: Characterization of Olefin Chain Ends. *Macromolecules* **1996**, *29* (27), 8591–8598. https://doi.org/10.1021/ma961099q.

(152) Prasad, A.; Mandelkern, L. Equilibrium Dissolution Temperature of Low Molecular Weight Polyethylene Fractions in Dilute Solution. *Macromolecules* **1989**, *22* (2), 914–920. https://doi.org/10.1021/ma00192a065.

(153) Kanazawa, M.; Ito, S.; Nozaki, K. Ethylene Polymerization by Palladium / PhosphineÀSulfonate. *Organometallics* **2011**, 6049–6052.

(154) Anselment, T. M. J.; Wichmann, C.; Anderson, C. E.; Herdtweck, E.; Rieger, B. Structural Modification of Functionalized Phosphine Sulfonate-Based Palladium(II) Olefin Polymerization Catalysts. *Organometallics* **2011**, *30* (24), 6602–6611. https://doi.org/10.1021/om200734x.

(155) Skupov, K. M.; Piche, L.; Claverie, J. P. Linear Polyethylene with Tunable Surface Properties by Catalytic Copolymerization of Ethylene with N -Vinyl-2-Pyrrolidinone and N -Isopropylacrylamide . *Macromolecules* **2008**, *41* (7), 2309–2310. https://doi.org/10.1021/ma800240p.

(156) Reynhardt, E. C. Temperature Dependence of the Cell Parameters of Fischer-

Tropsch Waxes: Hard Wax and Oxidised Hard Wax. *J. Phys. D. Appl. Phys.* **1986**, *19* (10), 1925–1938. https://doi.org/10.1088/0022-3727/19/10/017.

(157) Ciesińska, W.; Liszyńska, B.; Zieliński, J. Selected Thermal Properties of Polyethylene Waxes. *J. Therm. Anal. Calorim.* **2016**, *125* (3), 1439–1443. https://doi.org/10.1007/s10973-016-5706-1.

(158) Mpanza, H. S.; Luyt, A. S. Influence of Different Waxes on the Physical Properties of Linear Low-Density Polyethylene. *South African J. Chem. Tydskr. Vir Chemie* **2006**, *59*, 48–54.

(159) Moller, M.; Cantow, H.; Drotloff, H.; Emeis, D.; Lee, K.; Wegnef, G. Phase Transitions and Defect Structures in the Lamellar Surface of Polyethylene and N-Alkane Crystallites Magic Angle Spinning I3C NMR Studies. *Makromolecular Chem.* **1986**, *1252*, 1237–1252. https://doi.org/10.1016/j.jnucmat.2016.01.026.

(160) Luyt, A. S.; Krupa, I. Thermal Behaviour of Low and High Molecular Weight Paraffin Waxes Used for Designing Phase Change Materials. *Thermochim. Acta* **2007**, *467* (1–2), 117–120. https://doi.org/10.1016/j.tca.2007.11.001.

(161) Mandelkern, Leo; Price, J., M.; Gopalan, M.; Fatou, J., G. Sizes and Interfacial Free Energies of Crystallites Formed from Fractionated Linear Polyethylene. *J. Polym. Sci. Part B Polym. Phys.* **1966**, *4*, 385–400.

(162) Guo, X.; Pethica, B. A.; Huang, J. S.; Prud'homme, R. K. Crystallization of Long-Chain n-Paraffins from Solutions and Melts as Observed by Differential Scanning Calorimetry. *Macromolecules* **2004**, *37* (15), 5638–5645. https://doi.org/10.1021/ma035848x.

(163) Benn, R. Dynamic ^{1}H NMR Spectroscopy of H_2-ethylene Transition Metal Complexes. *Org. Magn. Reson.* **1983**, *21* (12), 723–726. https://doi.org/10.1002/omr.1270211204.

(164) Number, I. A.; Date, I. F. Wo 00/21663 20. **2000**, *16* (21).

(165) Gu, W.; Mcculloch, B. J.; Reibenspies, J. H.; Ozerov, O. V. Improved Methods for the Halogenation of the $[HCB_{11}H_{11}]^-$ Anion. *Chem. Commun.* **2010**, *46*, 2820–2822. https://doi.org/10.1039/c001555e.

(166) Rulke, Richard, E.; Ernsting, Jan, M.; Spec, Anthony, L.; Elsevier, Cees, J.; van Leeuwen, Plet, W., N., M.; Vrieze, K. NMR Study on the Coordination Behavior of Dissymmetric Terdentate Trinitrogen Ligands on Methylpalladoum(II) Compounds. *Inorg. Chem.* **1993**, *32*, 5769–5778.

(167) Grinshpun, V.; Rudin, A. Measurement of Mark-Houwink Constants by Size Exclusion Chromatography with a Low Angle Laser Light Scattering Detector. *Die Makromol. Chemie, Rapid Commun.* **1985**, *6* (4), 219–223. https://doi.org/10.1002/marc.1985.030060401.

(168) Colton, R.; Farthing, R. H.; McCormick, M. J. Carbonyl Halides of the Group VIII Transition Metals. *Aust. J. Chem.* **1973**, *26*, 2607–2614.

(169) Fafard, C. M.; Adhikari, D.; Foxman, B. M.; Mindiola, D. J.; Ozerov, O. V. Addition of Ammonia, Water, and Dihydrogen across a Single Pd-Pd Bond. *J. Am. Chem. Soc.* **2007**, *129* (34), 10318–10319. https://doi.org/10.1021/ja0731571.

(170) Inatomi, T.; Koga, Y.; Matsubara, K. Dinuclear Nickel(I) and Palladium(I) Complexes for Highly Active Transformations of Organic Compounds. *Molecules* **2018**, *23* (1). https://doi.org/10.3390/molecules23010140.

(171) Colacot, T. J. A Highly Active Palladium(I) Dimer for Pharmaceutical Applications. *Platin. Met. Rev.* **2009**, *53* (4), 183–188. https://doi.org/10.1595/147106709X472147.

(172) Inatomi, T.; Koga, Y.; Matsubara, K. Dinuclear Nickel(I) and Palladium(I) Complexes for Highly Active Transformations of Organic Compounds. *Molecules* **2018**, *23* (1). https://doi.org/10.3390/molecules23010140.

(173) Murahashi, T.; Nagai, T.; Okuno, T.; Matsutani, T.; Kurosawa, H. Synthesis and Ligand Substitution Reactions of a Homoleptic Acetonitrile Dipalladium(I) Complex. *Chem. Commun.* **2000**, *4* (17), 1689–1690. https://doi.org/10.1039/b004726k.

(174) Deborde, V.; Sauthier, M.; Guennic, B. Le; Réau, R.; Halet, J. F.; Toupet, L. COMMUNICATIONS A Rare Phosphane Coordination Mode : Dinuclear Palladium(I) Complex. *Angew. Chem.* **2001**, *7870* (1), 228–231.

(175) Nohra, B.; Rodriguez-Sanz, E.; Lescop, C.; Réau, R. Chemistry of Bridging Phosphanes: Cui Dimers Bearing 2,5-Bis(2-Pyridyl)Phosphole Ligands. *Chem. - A Eur. J.* **2008**, *14* (11), 3391–3403. https://doi.org/10.1002/chem.200701423.

(176) Connelly, N. G.; Geiger, W. E. Chemical Redox Agents for Organometallic Chemistry. *Chem. Rev.* **1996**, *96* (2), 877–910. https://doi.org/10.1021/cr940053x.

(177) Proutiere, F.; Aufiero, M.; Schoenebeck, F. Reactivity and Stability of Dinuclear Pd(I) Complexes: Studies on the Active Catalytic Species, Insights into Precatalyst Activation and Deactivation, and Application in Highly Selective Cross-Coupling Reactions. *J. Am. Chem. Soc.* **2012**, *134* (1), 606–612. https://doi.org/10.1021/ja209424z.

(178) Senol, E.; Scattolin, T.; Schoenebeck, F. Selenolation of Aryl Iodides and Bromides Enabled by a Bench-Stable Pd I Dimer. *Chem. Eur. J.* **2019**, *25*, 1–5. https://doi.org/10.1002/chem.201900951.

(179) Jones, C. G.; Martynowycz, M. W.; Hattne, J.; Fulton, T. J.; Stoltz, B. M.; Rodriguez, J. A.; Nelson, H. M.; Gonen, T. The CryoEM Method MicroED as a Powerful Tool for Small Molecule Structure Determination. *ACS Cent. Sci.* **2018**, *4* (11), 1587–1592. https://doi.org/10.1021/acscentsci.8b00760.

(180) Klug, A.; De Rosier, D. J. Reconstruction of Three Dimensional Structures from Electron Micrographs. *Nature* **1968**, *217*, 130–134.

(181) Barringer, R. Illuminating the Secrets of Crystals: Microcrystal Electron Diffraction in Structural Biology. *Biosci. Horizons Int. J. Student Res.* **2019**, *11*, 1–12. https://doi.org/10.1093/biohorizons/hzy013.

(182) Martynowycz, M. W.; Gonen, T. From Electron Crystallography of 2D Crystals to MicroED of 3D Crystals. *Curr. Opin. Colloid Interface Sci.* **2018**, *34*, 9–16. https://doi.org/10.1016/j.cocis.2018.01.010.

(183) Zhai, H.; Bunn, A.; Wayland, B. Formation and Ethene Substrate Reactions of Iridium(II) Porphyrin Metal-Centered Dπ Radicals. *Chem. Commun.* **2001**, No. 14, 1294–1295. https://doi.org/10.1039/b104301n.

(184) Hoth, D. C.; Atwood, J. D. Reaction of [PPN][Re(CO)5] with [Mn(CO)5(C 2H4)][BF4], a Rapid Two-Electron, Ethylene Transfer Reaction, PPN=bis(Triphenylphosphine)Nitrogen(1+). *Inorganica Chim. Acta* **2002**, *334*, 71–76. https://doi.org/10.1016/S0020-1693(02)00793-4.

(185) de Bruin, B.; Thewissen, S.; Yuen, T.-W.; Peters, T. P. J.; Smits, J. M. M.; Gal, A. W. Formation of Ethylene-Bridged Dinuclear Ir III Species via M−C Coupling of Ir(II) and Ir(II)(Ethene). *Organometallics* **2002**, *21* (21), 4312–4314. https://doi.org/10.1021/om020476m.